

# Characterisation of Fibre–Forming Peptides and Proteins by Means of Atomic Force Microscopy

---

*Rhiannon Coralie Guinevere McInnes Lloyd Creasey*

*Supervised by*

**Professor Nicolas H Voelcker** (School of Chemical and Physical Sciences)

*Co-supervised by*

**Dr Christopher T Gibson** (School of Chemical and Physical Sciences)

**Dr Shiwani Sharma** (Discipline of Ophthalmology)

**Dr Jamie E Craig** (Discipline of Ophthalmology)



**Flinders**  
UNIVERSITY

Adelaide, South Australia

*Submitted on the 14<sup>th</sup> of December 2011*

*in fulfilment of the requirements for the degree of Doctor of Philosophy*

*Accepted on the 9<sup>th</sup> of May 2012*

## **Declaration**

I certify that this thesis does not incorporate without acknowledgment any material previously submitted for a degree or diploma in any university; and that to the best of my knowledge and belief it does not contain any material previously published or written by another person except where due reference is made in the text.

Rhiannon G. Creasey

## Acknowledgements

I would like to first thank my supervisor, Professor Nicolas Voelcker, for trying to teach me proper English, for endless hours of technical discussions on every aspect of the project, and for finding the funding for me to carry out the research herein. He has been an inspiring mentor, and this work would not be possible without him.

I also sincerely thank my co-supervisors; in particular, Shiwani and Chris, who have always taken the time to answer questions, demonstrate techniques, and correct drafts. In addition, thank you to Voelcker lab members who were always available to answer questions and assist in any way possible, especially Steve for keeping the lab running.

Special thanks go to my collaborators, for their fresh insights and technical advances, and especially to my Austrian and Western Australian collaborators for kindly hosting me at their institutions, sharing their knowledge and facilities, and making me feel welcome. Also to Carolyn, for spending many hours sharing her experiences with me. Specific technical acknowledgements are outlined in respective appendices.

Personal thanks to all my family and friends who have supported me through this journey; my cousin Trixi for making me feel at home in WA; my parents for their endless encouragement and financial support; my officemate Kerrilee for keeping me going (but not quite sane); my sister for keeping me well fed and entertained, and all the rest simply for sticking with me.

Above all, thank you to my husband Matthew, for everything.

## Abstract

Atomic force microscopy (AFM) is a high-resolution microscopic technique highly suitable for investigating biological entities. Chapter 1 reviews the use of AFM for investigating fibre-forming peptides and proteins, followed by the application of AFM to peptide-based dendrimers in chapter 2, fungus-based proteins in chapter 3 and whole human tissue in chapter 4. This investigation is supported by more traditional analytical techniques such as optical, electron and fluorescence microscopy, dynamic light scattering and circular dichroism spectroscopy.

In chapter 2, the aggregation properties of peptide-based dendrons and dendrimers were investigated using AFM. 3<sup>rd</sup>- and 4<sup>th</sup>-generation dendrons made from L-lysine showed gelation via a unique vesicle-driven pathway, confirmed by transmission electron microscopy, forming a dense network of nanofibres. The symmetrical dendrimers also formed nanofibre-based gels, which could be polymerised using UV irradiation to form tightly-packed gels with altered optical, Raman and fluorescence properties. UV irradiation through a photomask allowed the generation of crosslinked gel patterns. Gels from dendrons and dendrimers may be suitable for use in biomaterial applications for cell seeding assays, tissue engineering, or for drug delivery.

Chapter 3 dealt with the aggregation of fungal proteins. The recent identification of genes encoding three arabinogalactan-like (AGL) proteins of the fungi *G. intraradices* suggests that AGL proteins may be involved in the formation of the symbiotic interface between a common fungus and plant roots. Currently, the nature of cell wall modifications in this interface is unknown. Here, AFM was applied to investigate the self-assembly of the fungal proteins rAGL1 and rAGL3 and the growth of nanofibres and microtubules was

observed and described. Peptides based on the repeat regions seen in the AGL sequences were also observed to form fibres as seen by AFM and optical microscopy. The secondary structure of the proteins and peptides – hypothesised to be responsible for creating the interface of root apoplasts and fungi – were found to be primarily disordered or polyproline II helices by circular dichroism spectroscopy. Understanding of the structural properties of these proteins is vital to the process of *G. intraradices* symbiosis. Self-assembling peptides based on these proteins may find applications as innovative self-assembling biomaterials.

Protein aggregation is of significant interest to various disciplines including ophthalmology. One ocular disease hallmarked by protein aggregation is known as pseudoexfoliation (PEX) syndrome. This condition is caused by the formation of insoluble aggregates in the eye, and is clinically characterised by the deposition of proteinaceous material on the anterior lens capsule. The ultrastructure of PEX material is poorly characterised, despite numerous proteomic and genomic studies. The novel application of AFM-based antibody recognition imaging is applied in chapter 4 for determination of the molecular nature of PEX material on lens capsules in their native state. Topographical AFM images and antibody recognition images were obtained simultaneously to determine the specific location of clusterin, lysyl oxidase-like 1, and elastin proteins in and around PEX aggregates using antibody-modified AFM probes. Multiple AFM-based techniques were tested, and TREC was found to be the most suitable technique for recognition on whole unprocessed tissue samples. Future studies into AFM-antibody recognition techniques, such as quantitative nanomechanical mapping, may lead to interesting data combinations of mechanical and compositional information.

# Table of Contents

<b>Declaration</b> .....	<b>i</b>
<b>Acknowledgements</b> .....	<b>ii</b>
<b>Abstract</b> .....	<b>iii</b>
<b>Table of Contents</b> .....	<b>v</b>
<b>List of Figures</b> .....	<b>viii</b>
<b>List of Tables</b> .....	<b>x</b>
<b>List of Abbreviations</b> .....	<b>xi</b>
<b>1 Introduction</b> .....	<b>1</b>
1.1 Summary .....	2
1.2 Atomic Force Microscopy .....	3
1.2.1 Atomic Force Microscope Operation .....	4
1.2.2 Molecular Recognition Imaging .....	20
1.2.3 Combination with Non-Atomic Force Microscope Techniques .....	30
1.3 Fibre-Forming Peptides and Proteins .....	32
1.3.1 Secondary Structures .....	32
1.3.2 Protein Aggregation.....	34
1.4 Conclusions and Future Perspectives.....	61
<b>2 Characterisation of Organogels Formed by Peptide-Based Dendrons and Dendrimers</b> .....	<b>64</b>
2.1 Summary .....	65
2.2 Introduction.....	67
2.3 Materials and Methods.....	72
2.3.1 Dendron and Dendrimer Synthesis .....	72
2.3.2 Preparation of Gels.....	73
2.3.3 Characterisation of Gels.....	75
2.4 Results & Discussion .....	78
2.4.1 Characterisation of Organogel Formation from Dendrons .....	78
2.4.2 Characterisation of Organogel Formation from Dendrimers .....	83

2.5	Conclusions and Future Perspectives.....	89
<b>3</b>	<b>Characterisation of Fibres Formed by Fungal Proteins and Peptides.....</b>	<b>90</b>
3.1	Summary.....	91
3.2	Introduction.....	92
3.3	Methods and Materials.....	97
3.3.1	<i>Expression of Recombinant AGL Proteins in Escherichia coli</i> .....	97
3.3.2	<i>Peptide Preparation</i> .....	97
3.3.3	<i>Characterisation of Protein and Peptide Samples</i> .....	98
3.4	Results.....	101
3.4.1	<i>Secondary Structure and Self-Assembly of Recombinant AGLs</i> .....	101
3.4.2	<i>Characterization of Synthetic Peptides Based on P- and G-rich Repeats of AGL Proteins</i> .....	104
3.5	Discussion.....	115
3.5.1	<i>Secondary Structure</i> .....	115
3.5.2	<i>Self-Assembly of Recombinant Proteins</i> .....	119
3.5.3	<i>Self-Assembly of Repeat Regions into Fibrous Structures</i> .....	123
3.6	Conclusions and Future Perspectives.....	128
<b>4</b>	<b>Characterisation of Pseudoexfoliation Syndrome Deposits using AFM-Based Antibody Recognition Imaging.....</b>	<b>129</b>
4.1	Summary.....	130
4.2	Introduction.....	130
4.2.1	<i>The Human Eye</i> .....	131
4.3	Materials and Methods.....	140
4.3.1	<i>Tissue Samples</i> .....	140
4.3.2	<i>Atomic Force Microscopy</i> .....	140
4.3.3	<i>Immunofluorescence Labelling</i> .....	146
4.4	Results & Discussion .....	148
4.4.1	<i>Pilot Study: Detection of Clusterin</i> .....	148
4.4.2	<i>AFM-Based Antibody Recognition Imaging: Technique Comparison for the Detection of LOXLI</i> .....	164

4.4.3	<i>The Biological Significance of TREC results.....</i>	176
<b>5</b>	<b>Conclusions and Future Perspectives.....</b>	<b>191</b>
<b>6</b>	<b>Reference list .....</b>	<b>196</b>
<b>7</b>	<b>Appendices.....</b>	<b>I</b>
	Appendix A.....	II
	<i>Supporting data for dendrons and dendrimers .....</i>	<i>II</i>
	<i>Acknowledgements.....</i>	<i>XV</i>
	Appendix B .....	XVI
	<i>Supporting data for fungal proteins.....</i>	<i>XVI</i>
	<i>Acknowledgements.....</i>	<i>XXIII</i>
	Appendix C .....	XXIV
	<i>Supporting figures for Pseudoexfoliation syndrome.....</i>	<i>XXIV</i>
	<i>Acknowledgements.....</i>	<i>XXVIII</i>

## List of Figures

Figure caption	Page
Figure 1:1 – Basic schematic of AFM operation showing laser-based detection of cantilever deflection.	4
Figure 1:2 – A typical deflection vs. z-piezo displacement curve, tracking the deflection of a cantilever as it approaches towards (blue line) and retracts from (red line) a surface.	8
Figure 1:3 – SEM images of AFM probes. Images acquired by L. Green and A. Slattery, adapted with permission from C. T. Gibson.	13
Figure 1:4 – A common coupling scheme for linking an antibody (red) to a 3-aminopropyltriethoxysilane-functional AFM tip (grey)	15
Figure 1:5 – ‘Broadening’ artefacts arising from tip convolution	18
Figure 1:6 – AFM TM images acquired with contaminated or damaged probes, leading to ‘tip doubling’ artefacts.	19
Figure 1:7 – AFM force–volume images using lysozyme adsorbed onto a mica surface and HyHEL5 antibody attached to the probe. Adapted from [62].	25
Figure 1:8 – PeakForce QNM images showing topography and stiffness of bacteriorhodopsin protein layers. Adapted from [113].	27
Figure 1:9 – AFM PeakForce QNM images of $\beta$ -lactoglobulin amyloid fibrils on mica. Adapted from [94].	29
Figure 1:10 – Diagrammatic representation of some of the common ordered (and ‘random’) secondary structures observed for protein segments. Adapted from [124].	33
Figure 1:11 – Schematic of some of the many conformational states that can be adopted by polypeptide chains.	34
Figure 1:12 – Time-lapse (denoted beneath each image series) series of TM AFM height images showing protofibril elongation. Adapted from [163].	40
Figure 1:13 – AFM height mode images of prion aggregates formed in buffer containing 0.4 M GdnHCl (a) and 2.0 M GdnHCl (b). Adapted from [165].	43
Figure 1:14 – Time course showing fibrillar surface structures on Scrapie-infected N2a cells (ScN2a) derived at 1, 2, 4 and 5 days after plating (columns). Adapted from [168].	44
Figure 1:15 – TM AFM height images of $\alpha$ S annular particles, induced by the presence of calcium and cobalt ions. Adapted from [185].	49
Figure 1:16 – AFM height and phase images of detergent-treated glial cytoplasmic inclusions, displaying annular nanoparticles. Adapted from [188].	50
Figure 1:17– TREC AFM images acquired on a mouse endothelial cell surface treated with 50 $\mu$ M of nocodazole for 80 minutes and subsequently fixed with glutaraldehyde. Adapted from [199].	53
Figure 1:18 – AFM height images of the self-assembly of KFE8 peptide in aqueous solution. Adapted from [213].	55
Figure 1:19 – AFM height image of peptides deposited on mica. Adapted from [220].	58
Figure 2:1 – Basic schematic of synthetic pathways leading to creation of a dendrimer with a (blue) core, (green) ‘inner’ shell and (purple) ‘outer’ shell.	68
Figure 2:2 – Synthesis of dendrons 2a and 2b.	72
Figure 2:3 – Synthesis of dendrimers 5a and 5b from dendrons 2a and 2b, respectively, and synthesis of dendrons 3 and 4 from dendron 2a.	73
Figure 2:4 – AFM height images in TM of non-gelled sample deposited on mica.	78
Figure 2:5 – EM micrographs of vesicles from dendrons 3 and 4.	80
Figure 2:6 – AFM and SEM images of gels formed from dendrons 3 and 4.	82
Figure 2:7 – Photographs of the gel formed by 5a in inverted tubes (a) before UV irradiation, (b) after 5 minutes and (c) 15 minutes of UV irradiation.	83

Figure 2:8 – AFM height images in TM of (a) a gel of 5a and (c) a gel of 5b, and (b, d) gels after UV irradiation, respectively.	84
Figure 2:9 – Fluorescence microscopy images of the gels 5a and 5b, and the Raman spectra of 5b, before and after UV irradiation.	86
Figure 3:1 – Arbuscular mycorrhizal fungi colonization of roots, and cell wall proteins. Figure prepared by C. Schultz.	94
Figure 3:2 – CD spectra of rAGL1 at 25°C (a), and rAGL3 (b) at 25°C (dashed line) and 5°C (solid line). Figure prepared by C. Schultz.	102
Figure 3:3 – Characterisation of rAGL protein fibre formation	.103
Figure 3:4 – CD spectra of synthetic peptides under different conditions. Figure prepared by C. Schultz.	106
Figure 3:5 – Synthetic peptide self-assembly in high salt conditions.	111
Figure 3:6 – Synthetic peptide self-assembly in low salt conditions.	113
Figure 4:1 – Basic structure of the human eye.	131
Figure 4:2 – TM AFM images acquired in PBS of (a–c) control and (d–f) PEX-affected lens capsules, at increasing magnification.	150
Figure 4:3– AFM images of control lens capsule mounted on a glass slide using MAC mode in PBS.	154
Figure 4:4 – AFM images of PEX lens capsule on glass using MAC mode in PBS.	155
Figure 4:5– Frequency distribution histogram of TREC recognition spots observed across control and PEX lens capsule samples measured as a unit of area (nm <sup>2</sup> ).	156
Figure 4:6 – AFM images of normal lens capsule mounted on a glass slide using MAC mode in PBS with injection of anti-clusterin antibody (150 µg/ml) to block surface-bound clusterin.	158
Figure 4:7 – Confocal microscopy images of the anterior side of a control lens capsule and a PEX-affected lens capsule immunolabelled with the anti-clusterin primary antibody and labelling detected with Alexa fluor-488 conjugated anti-rabbit IgG secondary antibody.	161
Figure 4:8 – Force spectroscopy detection of adhesion between sample and functionalised probe.	165
Figure 4:9 – AFM (a) topography and (b) recognition images of a lens capsule from a PEX patient acquired using an anti-LOXL1 antibody functionalised tip.	167
Figure 4:10 – AFM (a) topography and (b) phase images of a lens capsule from a PEX patient acquired in TM in PBS, using (i) a non-functionalised tip, (ii) a functionalised tip and (iii) the same tip after blocking of surface LOXL1 sites with free anti-LOXL1 antibody in solution.	169
Figure 4:11 –AFM (a) topography and (b) adhesion map images with 32 x 32 pixel resolution, using (i) a non-functionalised tip, (ii) an anti-LOXL1 antibody functionalised tip and (iii) the same tip after blocking of LOXL1 epitopes on the tissue surface with anti-LOXL1 antibody in solution.	172
Figure 4:12 – AFM topography images of (a, b) control and (c, d) PEX-affected lens capsules acquired using an anti-clusterin antibody functionalised tip, masked with TREC recognition in blue.	177
Figure 4:13 – AFM topography images of (a, b) control and (c, d) PEX-affected lens capsules acquired using an anti-LOXL1 antibody functionalised tip, masked with TREC recognition in blue.	180
Figure 4:14 – AFM topography images of (a) control and (b – d) PEX-affected lens capsules acquired using an anti-elastin antibody functionalised tip, masked with TREC recognition.	182

## List of Tables

Table caption	Page
Table 1:1 – Brief comparison of microscopy techniques for characterizing single proteins.	3
Table 1:2 – Comparison of AFM techniques capable of antibody recognition imaging.	21
Table 2:1 – Gelation of dendrons (3, 4) or dendrimers (5a, 5b) in a variety of solvents.	74
Table 3:1 – Properties of synthetic peptides.	97
Table 3:2 – Secondary structure predictions of synthetic peptides at different temperatures and in different buffers.	107
Table 3:3 – Mode of particle size determined by DLS of synthetic peptides at two salt concentrations; high salt (100mM / 10 mM) and low salt (10mM / 1 mM).	109
Table 4:1 – Antibodies used for functionalisation of AFM probes.	142
Table 4:2 – Comparison of recognition spot sizes between control and PEX-affected lens capsules seen for clusterin, elastin and LOXL1 proteins.	185

## List of Abbreviations

Abbreviation	Expansion
$\alpha$ S	Alpha-Synuclein
AFM	Atomic Force Microscope/y
AGL	Arabinogalactan-Like
AM	Arbuscular Mycorrhizal
APTES	3-Aminopropyltriethoxysilane
A $\beta$	Beta-Amyloid
CD	Circular Dichroism
CM	Contact Mode
CR	Congo Red
DCC	Dicyclohexylcarbodiimide
DLS	Dynamic Light Scattering
DNA	Deoxyribonucleic Acid
<i>E. Coli</i>	Escherichia Coli
EM	Electron Microscope/y
<i>G. Intraradices</i>	Glomus Intraradices
HOPG	Highly Ordered Pyrolytic Graphite
hr	Hour
LOX	Lysyl-Oxidase Like
min	Minute
MS	Mass Spectrometry
NHS	N-hydroxysuccinimide
PBS	Phosphate Buffered Saline
PDA	Polydiacetylene
PEG	Polyethylene Glycol
PEX	Pseudoexfoliation
PPII	Polyproline II
PrP	Prion Protein
QNM	Quantitative Nanomechanical Mapping
SEM	Scanning Electron Microscope/y
SPM	Scanning Probe Microscope/y
TEA	Triethylamine
TEM	Transmission Electron Microscope/y
ThT	Thioflavin T
TM	Tapping mode
TMEDA	N,N,N',N'-tetramethylethylenediamine
TREC	Topography and Recognition imaging
UV	Ultraviolet
Z	Benzyloxycarbonyl group

# Chapter 1

---

## **1 Introduction**

This chapter forms the basis of the following publication:

R. G. Creasey, C. T. Gibson, and N. H. Voelcker, 'Characterization of Fiber-Forming Peptides and Proteins by Means of Atomic Force Microscopy',  
*Current Protein and Peptide Science*, **2012** (*in press*).

## **1.1 Summary**

The atomic force microscope (AFM) is widely used in biological sciences due to its ability to perform imaging experiments at high-resolution in a simulated physiological environment, without special sample preparation such as fixation or staining. AFM is ideal for single molecule information of mechanical properties and molecular recognition to be gathered. Herein, methodological applications of AFM for characterization of fibre-forming proteins and peptides are identified. The basics of AFM operation are detailed, with in-depth information for any life scientist to get a grasp on AFM capabilities. It also briefly describes antibody recognition imaging and mapping of nanomechanical properties on biological samples.

Subsequently, examples of AFM application to fibre-forming natural proteins, and fibre-forming synthetic peptides are given. Here, AFM is used primarily for structural characterization of fibres combined with other techniques, such as circular dichroism and fluorescence spectroscopy. More recent developments in antibody recognition imaging to identify constituents of protein fibres formed in human disease are explored. This review, as a whole, seeks to highlight the manifold capabilities of this technique, and introduce the concepts pertaining to AFM applied throughout the thesis.

## 1.2 Atomic Force Microscopy

AFM is a scanning probe technique developed by Binnig *et al.* [1]. The technique relies on the piezo-driven movement of a sharp probe tip across a sample surface, generating deflections in the cantilever attached to the probe. These deflections for each x,y pixel on the scanned area are then generated into a topographical map. Because this microscope does not rely on light or electron beams as optical and electron microscopes do, resolution in AFM is not limited by diffraction, and true 3D information can be gathered (Table 1:1) [2]. Furthermore, the AFM does not require a vacuum to function effectively and can therefore be operated under a variety of environments, including liquid and in particular aqueous milieu (Table 1:1) [3]. Consequently, the AFM has become an invaluable tool for the life scientist interested in surface investigations at the nanoscale [3–10]. In particular, the biophysical characterization of proteins benefits from access to AFM-related techniques.

Table 1:1. Brief comparison of microscopy techniques for characterizing single proteins.

	Electron Microscopy		Optical Microscopy		Atomic Force Microscopy
	Scanning	Transmission	Brightfield	Fluorescence	
Lateral Resolution	<1 nm	<1 nm	200 nm	200 nm	<1 nm
Structural Information	✓	✓	X	X	✓
Mechanical Information	X	X	X	X	✓
Physiological Conditions	X	X	✓	✓	✓
Molecular Recognition	✓	✓	✓	✓	✓
3D Information	✓ <sup>^</sup>	✓ <sup>*</sup>	X	X	✓
	<sup>^</sup> qualitative only		<sup>*</sup> using tomography		

### 1.2.1 Atomic Force Microscope Operation

The most common AFM setup utilises an optical detection system [2], [8]. A laser is aimed at the end of a cantilever where the probe tip is mounted (Figure 1:1).

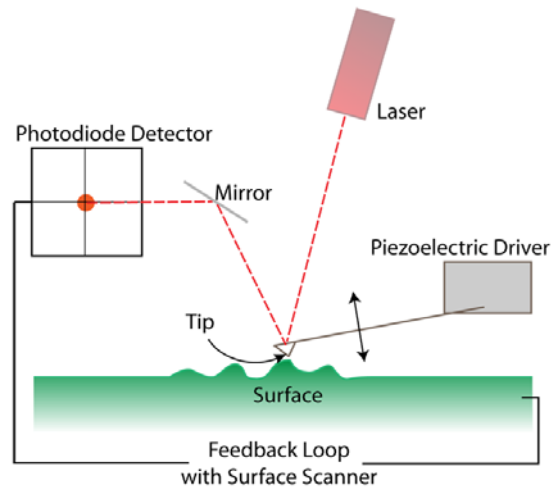


Figure 1:1 – Basic schematic of AFM operation showing laser-based detection of cantilever deflection.

This laser reflects onto a position-sensitive photodiode, typically consisting of four quadrants. As the cantilever deflects due to the probe's interaction with the surface, the photodiode signal due to the laser spot in each quadrant will change. This change is monitored by the controller. Cantilever movement is calculated from the change in voltage of the photodiode. The cantilever or the surface itself can be moved with accuracy by a piezo scanner in 3D. Alternative detectors are available, based on optical interferometry, electrical capacitance, electron tunnelling, and piezoelectric cantilevers [2]. However, due to the simple and robust operating principle of photodiode laser detection, alternative detectors are rare.

### ***1.2.1.1 Atomic Force Microscope Imaging***

#### **1.2.1.1.1 Contact Mode**

There are various modes of operation available for imaging using an AFM [2], the simplest being contact mode (CM), where the probe is brought into contact with the surface, then ‘dragged’ laterally across the substrate. The force between the cantilever and the surface is maintained by keeping the deflection (setpoint) of the cantilever constant. In addition to topographical information, CM also provides frictional information as the probe ‘drags’ more heavily on areas of high friction and is subjected to torsional effects, which can be detected by the position-sensitive detector. In CM imaging, three basic channels of information can be acquired during the imaging process: height, deflection, and friction. The height image represents the topography of the sample, converted from piezo movement as it maintains the deflection setpoint. Typically, the z-height scale is represented as a colour bar, where the colours of the pixels in the height image represent different physical heights.

When imaging, the setpoint is subtracted from the photodiode reading and this deviation is known as the ‘error-signal’. This signal can be optimized in order to be quite large on steep gradients, but minimized on flatter areas. By mapping the cantilever deflection directly, the finer details of a surface can become visible in the ‘deflection channel’. In this way, coarse details on rough samples can be sacrificed in order to visualize fine surface details. An example of deflection images is seen in Figure 1:14, where CM was applied to scrapie infected cells to observe the finer structural details of the cell surface. However, the z-scale in these images is not representative of true topography.

Finally, the friction channel records horizontal deflections of the cantilever. As the probe maintains constant contact with the surface, a higher friction between the probe and surface will result in increased torsional twisting of the cantilever, measured by the lateral photodiode quadrants. To avoid topographical artefacts, the comparison of topographic and lateral force images acquired in the same direction can be performed. A more common method seen is the subtraction of the forward and backward scanning direction from each other. However, correction for the nonlinear behaviour of the piezoelectric transducer must be taken into account [11].

### **1.2.1.1.2 Intermittent and Non-Contact Modes**

In tapping mode (TM) [12], the cantilever is oscillated near resonant frequency, and one of the components of oscillation, such as amplitude, is monitored for changes due to surface interactions. This mode of operation reduces the chances of damaging the probe or the surface, as the probe is only in intermittent contact with the surface. In TM imaging, three basic channels of information can be acquired while imaging: height, amplitude error, and phase. As with CM imaging, the height image represents the topography of the image. Further, the amplitude error maps the ‘error-signal’ of the amplitude oscillation adjustments as a voltage from the photodiode measurements [2], [12], [13]. This channel can be equated to CM’s deflection, and is useful for observing finer details on rough samples, as seen in Figure 3:5 e and Figure 3:6 e – f.

## *Introduction*

The phase channel essentially produces a map of how the probe interacts with the surface [2], [12], [14], [15]. The phase lag of the probe's oscillation is measured with reference to the excitation oscillatory signal while the amplitude is maintained at a constant value. There are a variety of physical interactions that may cause phase lag of the probe. These include surface stiffness, viscoelasticity, adhesion or large topographical variations. Phase imaging may provide further structural or compositional information than can be derived from a topography image of a substrate. An example of the additional information that can be gained from the phase channel is seen in Figure 1:6 c, Figure 2:6 b and Figure 3:3 e. However, interpretation of the phase signal is not straightforward and care must be taken when analysing phase images.

These modes are by no means the only imaging modes. Non-contact AFM, for example, was the first AFM mode to provide atomic resolution on a silicon surface [16]. In this mode, the probe never contacts the surface as it oscillates, avoiding sample or tip deformations [16], [17]. The mapping of physical properties (based upon force spectroscopy, described in Section 1.2.1.2) is also available [2], [12], [18]. Furthermore, within each mode are alternative methods of cantilever excitation and detection, leading to a vast array of methods of extracting information from samples using AFM. Nevertheless, due to the gentle yet robust operational characteristics of TM, this mode is generally employed for initial investigations into biological surfaces [2], [5], [10], [19].

1.2.1.2 Force Spectroscopy

Force spectroscopy is an AFM-based technique in which nanomechanical information can be obtained on the sample (Table 1:1) [20], [21]. After positioning the AFM probe to the desired x,y position, the probe is brought into contact with the surface using the z-piezo, until the cantilever deflects, and it is then pulled away again. The cantilever deflection is graphed against the position of the z-axis, as seen in Figure 1:2.

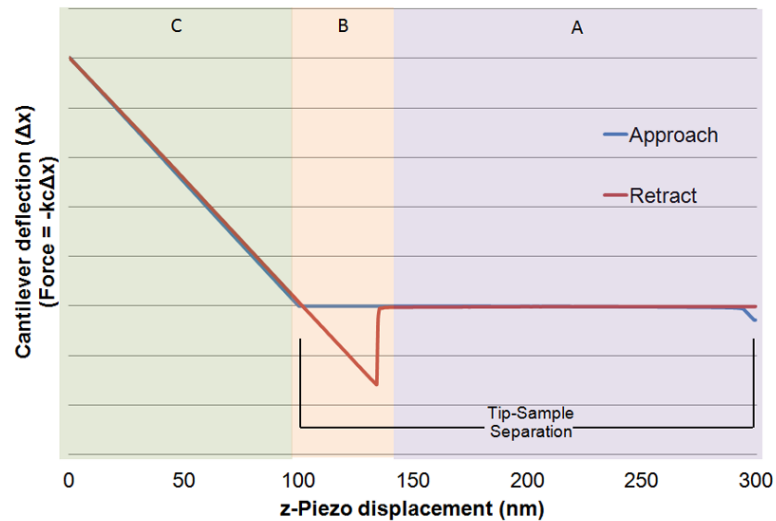


Figure 1:2 – A typical deflection vs. z-piezo displacement curve, tracking the deflection of a cantilever as it approaches towards (blue line) and retracts from (red line) a surface. In Region A, no deflection occurs. In Region B, the probe adheres to the surface on retraction and in Region C the probe is in contact with surface and the cantilever deflects upon further approach.

Initially, there are no forces acting on the cantilever, as it is too distant from the surface (Region A). As the probe approaches the surface, the atoms of the probe will interact with the atoms on the surface to create either an attractive or repulsive force due to van der Waals and electrostatic interactions in Region B. There is often a ‘snap-on’ effect seen when approaching in Region B, where the probe becomes close enough to the surface to be attracted by van der Waals forces [22]. In Region C, the probe is in contact with the surface, causing the

## *Introduction*

cantilever to bend away from the surface due to the repulsive force of the electron orbital overlap between probe and sample. Sample and probe may undergo elastic and/or plastic deformations at this time, providing nanomechanical information of the surface. The cantilever is deflected up to a maximum loading value as set by the user, before reversing the z-direction to retract from the surface. When the probe is retracted (red line), adhesion between the probe and the surface often occurs, giving rise to a hysteresis effect (Region B). Finally, the probe ‘snaps off’ and loses contact with the surface (Region A).

If the properties of the cantilever are determined, then probe–sample forces can be quantitatively studied [23], [24] on the basis of Hooke’s Law (Equation 1).

Equation 1– Hooke's law of motion of a spring.

$$F = -k_c x$$

Where  $F$  is the force applied,  $x$  is the deflection of the cantilever, and  $k_c$  is its spring constant. Once the spring constant has been adequately calibrated (see Section 0), the deflection–displacement curve can be converted to a force curve, in which the force applied to the cantilever is graphed against the probe’s actual separation from the surface (tip–sample separation, denoted in Figure 1:2). Forces detected from the approach of a force curve include van der Waals, repulsive double–layer electrostatic, repulsive hydration, and the solvation forces. The adhesion and hydrophobic forces between the probe and sample can be calculated from the retract curve [25]. As discussed above, the nanomechanical properties, such as stiffness (Young’s modulus) of the sample,

can be extrapolated from the contact forces (Region C) of a deflection–displacement curve. In the case of a probe indenting into the sample, the surface properties can be described by the Hertz model (Equation 2).

Equation 2 – Hertz equation of surface deformation.

$$F = \delta^{3/2} 2E \sqrt{\frac{R}{3(1-\nu^2)}}$$

Where  $\delta$  is the indentation of the surface,  $E$  its Young’s modulus, and  $\nu$  is its Poisson’s value, and  $R$  is the radius of the probe. However, this case does not take into account adhesion, which requires further calculations as provided by the Derjaguin–Müller–Toporov (DMT) [26], [27] and Johnson–Kendall–Roberts (JKR) [28] theories. In biological samples, the surface is much softer than the probe; hence the JKR theory is usually applied for determination of sample deformation. The interested reader is referred to detailed reviews on the application of JKR and DMT theories [21], [25], [29], [30]. However, state-of-the-art AFM instruments contain modules enabling the life scientist to easily measure surface stiffness, deformation and adhesion properties of biological samples. Some examples of force spectroscopy used for investigating fibre-forming peptides and proteins are included in Section 0.

### *1.2.1.3 Cantilever Calibration*

The cantilever deflection can be measured with high precision using a position-sensitive photodiode. The calibration of the position-sensitive photodiode is usually done by performing force distance curves on a flat clean surface with a stiffness much greater than that of the cantilever. The average

## Introduction

slope of the force distance curves, when the tip is in contact with the surface, will give the position-sensitive photodiode calibration factor or, as it is commonly known, sensitivity. For most AFM cantilevers, glass or silicon is sufficient. For stiffer cantilevers (with a stiffness greater than 100 N/m), sapphire may be more appropriate. Once the deflection of the cantilever is calibrated the spring constant must also be accurately determined. One of the earliest reliable methods utilised for the spring constant calibration of AFM cantilevers involved the addition of a known mass to a cantilever, resulting in a shift in the cantilever resonant frequency [31]. However, the addition of the mass, usually a small tungsten or gold sphere, is time consuming and potentially damaging to the cantilever and tip. Two non-destructive and relatively simple methods are more commonly used for measuring the spring constants of AFM cantilevers; the so-called ‘thermal method’ and ‘Sader Hydrodynamic method’. The first derivation of the ‘thermal method’ was made by Hutter *et al.* [32] utilising the thermal fluctuations of the cantilever, relating the stiffness via the equipartition theorem, assuming the cantilever acts as a simple harmonic oscillator.

Equation 3 – Spring constant calibration using the ‘thermal method’.

$$k_z = \frac{k_B T}{p}$$

where  $k_B$  is the Boltzmann constant,  $T$  is the temperature of the cantilever, and  $p$  is the area of the power spectrum of the thermal fluctuations (available experimentally). [33] Hence, this method is suitable to most AFM systems, as the temperature can be input easily and all other factors can be measured.

## Introduction

However, the accuracy of this method is estimated to be between 10 – 20% [23], [34] due to the assumption that the cantilever acts as a perfect simple harmonic oscillator. A more accurate method reported to be as low as 5% [29], but usually closer to 10% [34] was developed by Sader *et al.* [35]. The ‘Sader Hydrodynamic method’ utilises precise measurements of the cantilever dimensions, Q factor and resonant frequency ( $f_r$ ), and can be used for calibration of a cantilever in fluid.

Equation 4 – Spring constant calibration using the ‘Sader method’ for rectangular ( $k_{rect}$ ) and ‘V’-shaped ( $k_v$ ) cantilevers.

$$k_{rect} = 0.1906 lQ(\omega 2\pi f_r)^2 \rho_f \Gamma_i(v_k)$$

$$k_v = \frac{\epsilon \omega t_c^3}{2l^3} \cos\alpha \left[ 1 + \frac{4\omega^3}{b_c^3} (3\cos\alpha - 2) \right]^{-1}$$

Where Q is the quality factor of the cantilever,  $\rho_f$  is the density of the fluid the cantilever is immersed into, l and  $\omega$  are the length and width of the cantilever respectively, and  $\Gamma_i$  is the imaginary part of the so-called ‘hydrodynamic function’. This technique is only applicable to rectangular nbeam shaped cantilevers. Sader also derived an expression for V shaped cantilevers that is based on Euler beam equations [31] and is given in the second equation. In the second equation, the angle between the ‘arms’ of the V-shaped cantilever ( $\alpha$ ), and the thickness of the cantilever ( $t_c$ ), the Young’s modulus of the cantilever  $\epsilon$  and the case width of the cantilever ( $b_c$ ) must be taken into account, as this equation is derived from the parallel beam theory [33]. An example of a rectangular and V-shaped cantilever can be seen in Figure 1:3 a and c.

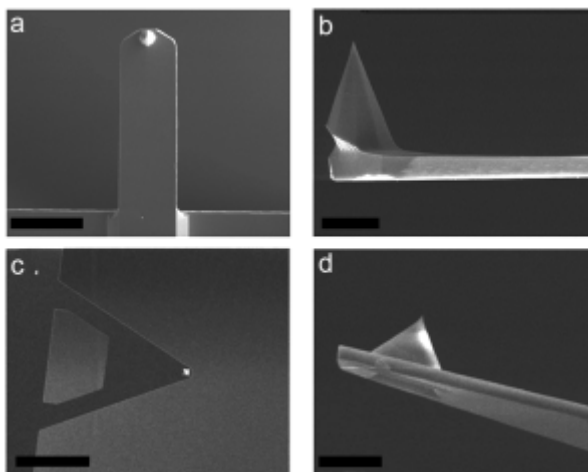


Figure 1:3 – SEM images of AFM probes. (a) and (b) are NSC probes (Mikromasch) showing the rectangular cantilever (x-scales = 50  $\mu\text{m}$ ), and (c) and (d) are OTR8 probes (Bruker) showing the V-shaped cantilever (x-scales = 5  $\mu\text{m}$ ). Images acquired by L. Green and A. Slattery, adapted with permission from C. T. Gibson.

There are various calibration methods further to the ones discussed above [24], [36], such as the use of reference cantilevers of measured dimensions, radiation pressure, capacitive sensors, and a differential pressure resulting from a known fluid flow rate [37]. The choice of which calibration method to use is not a trivial one. For most biological applications, the Sader or the thermal method are deemed adequate.

#### *1.2.1.4 Probe Functionalisation*

Force spectroscopy can be utilised for molecular recognition, by attaching a ligand to a probe. Although molecular recognition is possible using immunorecognition by means of other microscopy methods (Table 1:1), force spectroscopy allows for true single molecule identification and measurement. Probe functionalisation has developed into a versatile procedure allowing hosts of ligands, including antibodies for specific molecular recognition to be attached to the probes without loss of biological activity [38–42]. Once an antibody is stably bound to the probe, force spectroscopy can be used to

## Introduction

measure the specificity of the interaction with the corresponding protein. Data such as the binding kinetics, rupture forces and protein conformation can be investigated [18], [25], [43–46]. For more information on the use of functionalised probes in single molecule recognition force spectroscopy, reviews by Willemsen *et al.* [47], Leckband *et al.* [48], Kienberger *et al.* [49] and Hinterdorfer *et al.* [50] are recommended to the interested reader.

To functionalise a probe for molecular recognition, a biomolecule must be attached to the probe. This can be done via a linker, such as a biotin–streptavidin bridge [51–55], or glutaraldehyde crosslinking [56]. Alternatively, the biomolecule and the probe can be tethered via a defined covalent bond with a rupture force greater than the rupture force of the interaction being investigated [57]. This can be done using an amylose [57–60] or polyethylene glycol (PEG) chain [39], [50], [61–69] between an amine–reactive tip [70–74] and a biomolecule with available amino groups. A schematic used for linking antibodies to tips using a PEG linker is shown in Figure 1:4.

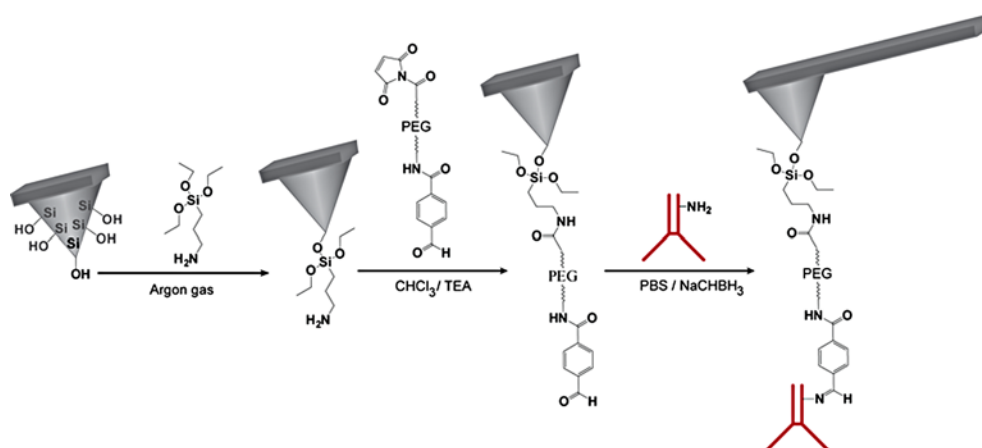


Figure 1:4 – A common coupling scheme for linking an antibody (red) to a 3-aminopropyltriethoxysilane-functional AFM tip (grey). After amine-functionalisation, a PEG chain is attached via its NHS-ester. The aldehyde residues on the free end of the PEG chain can be conjugated to the amino groups of the lysine residues of the protein. Reaction of antibody and aldehyde results in the formation of Schiff base, which is subsequently fixed by reduction with  $\text{NaCNBH}_3$ .

In the example in Figure 1:4, used for example by Chitchevlova *et al.* [75] and Creasey *et al.* [76], a probe is amine-functionalised using gas-phase silanisation with 3-aminopropyltriethoxysilane. An amide bond between the amine-activated tip and the activated carboxy group of an N-hydroxysuccinimide (NHS) ester end of a heterobifunctional aldehyde-PEG-NHS ester crosslinker is formed. Finally, the lysine residues of an antibody are coupled via the aldehyde residue of the crosslinker. Reduction with sodium cyanoborohydride stabilizes the Schiff base formed between the antibody and the aldehyde moiety. A variety of other chemistries are available for biomolecule immobilization on AFM tips. See also reviews by Ebner *et al.* [38] and Lee *et al.* [77], and a recent compilation of protocols published by Bergkvist and Cady [78], for in-depth information on probe functionalisation.

#### 1.2.1.5 Choice of Atomic Force Microscope Probe

A critical parameter in any AFM measurements, regardless of mode, is the choice of cantilever and probe to be used. Several factors influence this

## *Introduction*

decision such as the sharpness of the probe tip (its radius of curvature) determining lateral resolution, the aspect ratio of the tip, the cantilever spring constant (or stiffness), and cantilever reflectivity [2]. Due to tip convolution (discussed further in Section 1.2.1.6), a sharp tip is generally preferred for imaging of samples, [79] such as those seen in Figure 1:3 b and d. However, for quantitative nanomechanical measurements of a surface, a nanoparticle attached to the tip is often employed [29] to provide a defined contact area, which is large enough to reduce the pressure and minimize damage to the sample. High-aspect ratio probes are required to image high-aspect ratio features on the sample. Harder silicon probes are employed for use in TM in air, and softer silicon nitride probes are employed for TM experiments in fluid or CM measurements. The cantilever and the tip are usually fabricated out of the same material. However, diamond tips [80] or carbon nanotubes [81] are at times mounted on silicon or silicon nitride cantilevers.

In CM imaging, due to the lateral motion of the probe, a V-shaped cantilever is preferred as it will have reduced torsional stress. In TM imaging, a rectangular cantilever is typically chosen which is oscillated at frequencies above 50 kHz. This allows a minimum amount of force to be exerted on the sample to reduce deformation and damage, while keeping the probe stiff enough to prevent it from sticking to the surface due to capillary forces [2], [12]. When using TM in fluid, a softer V-shaped cantilever oscillating at a lower frequency of less than 20 kHz is typically employed as the fluid causes drag.

A highly reflective coating such as aluminium or gold may be used to ensure differentiation of reflection off the cantilever from reflection from the sample. In turn, magnetic coatings allow the cantilever to be driven magnetically. Magnet driving is suited for imaging in fluid, as the fluid is not disturbed by large oscillations due to acoustic drivers, and very small cantilever oscillations are possible to reduce the forces exerted on the sample [82].

### *1.2.1.6 Resolution*

The z-resolution of the AFM is limited only by the electronic and thermal noise inherent in the cantilever detection system. 3D information in the range of Angstroms is typically achievable, and sub-Angstrom measurements can be realized on well-calibrated equipment. Height measurements can be affected by adhesion and deformation, particularly when investigating biological samples [2], [73], [83]. Although a range of methods and calculations have been investigated for true height determination [12], [24], [84], TM employing minimal peak forces will minimize this deformation sufficiently for most investigations [12], [84].

Lateral (x,y-plane) resolution is influenced by a range of factors. The tip's shape and size limit the geometrical topographies that can be observed due to 'convolution' [24]. As seen in Figure 1:5, a tip with an aspect ratio greater than the sample to be imaged will result in a 'broadening' artefact. This artefact is also observed if the tip is blunt or otherwise broadened due to contamination or damage.

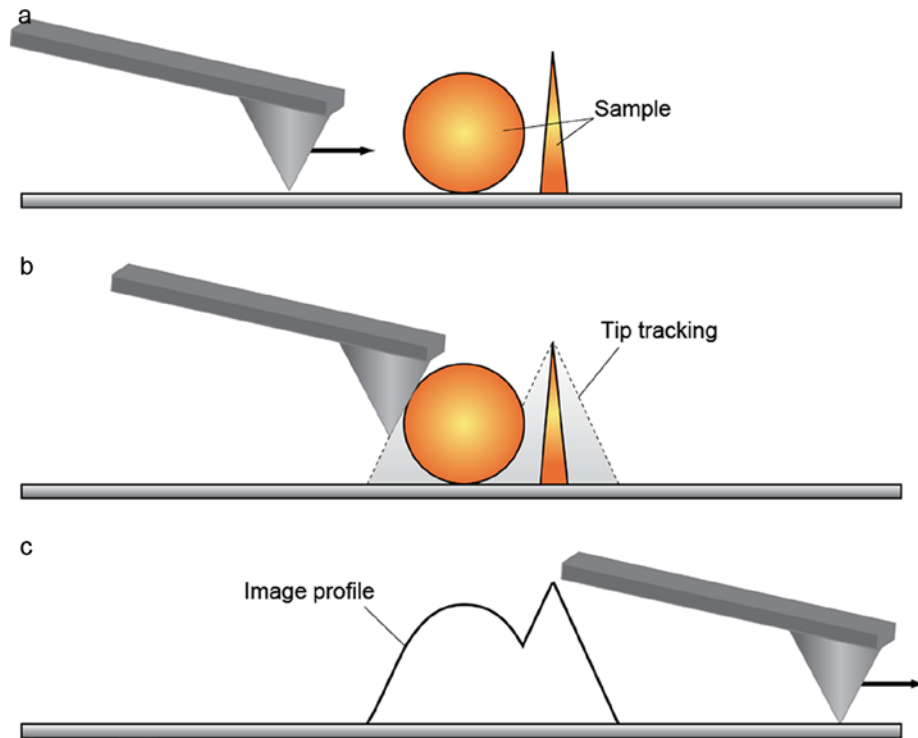


Figure 1:5 – ‘Broadening’ artefacts arising from tip convolution, where (a) shows the actual sample profile, (b) highlights the way the probe interacts with the sample resulting in (c) the line profile obtained.

It follows that the sample topography is also going to affect the imaging resolution, as regions which are inaccessible by the probe will not be visible. Furthermore, tip-sample interactions, such as long-range repulsive forces or sample deformation can also change the apparent features observed [85]. During imaging, probes may become contaminated by sample material, leading to ‘tip doubling’ artefacts (as seen in Figure 1:6), resulting in the observation of repeated shapes reflecting the shape of the tip. Probes may be cleaned using ozone, plasma, or solvents, and if successful will remove the contamination to allow further imaging.

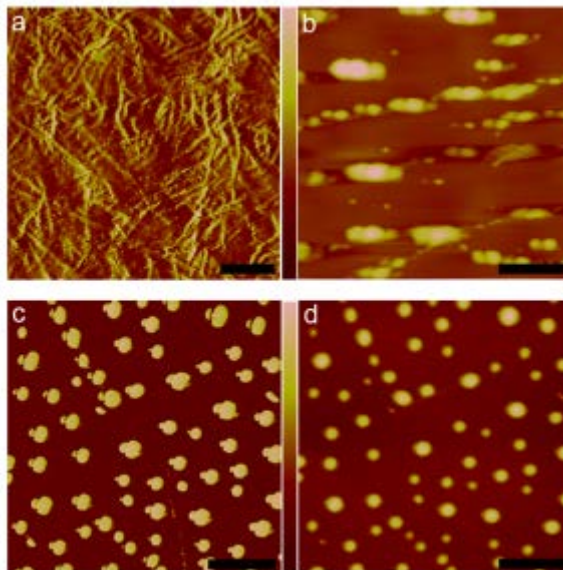


Figure 1:6 – AFM TM images acquired with contaminated or damaged probes, leading to ‘tip doubling’ artefacts. (a) Phase image of a PEX-affected lens capsule (chapter 4), showing double fibre features (x-scale = 1  $\mu$ m). (b) Height image of an rAGL1 protein (chapter 3) on a HOPG surface, showing horizontal tip doubling and tripling (x-scale = 250 nm). (c) and (d), phase and height images, respectively, of rAGL3 protein (chapter 3) on a HOPG surface, showing how the phase channel shows tip doubling despite it not being visible in the height channel (x-scales = 250 nm).

Such artefacts can be minimized by a judicious choice of probe (Section 1.2.1.5), and true surface features can be calculated by deconvolution algorithms. In this respect, the most accurate calculation is the Legendre function [86], which is, however, a rather cumbersome procedure. For most investigations, geometric deconvolution using the probe shape and radius of curvature is typically sufficient for determining true surface feature widths [86, 87]. Determination of the probe’s shape and radius of curvature can be done using a test sample surface of known geometries [86, 88], available from most probe suppliers, and most commercial AFM software provides deconvolution packages.

### **1.2.2 Molecular Recognition Imaging**

A further development of AFM, beyond morphology and mechanical characterization, is the so-called chemical force microscopy [89], [90]. In this technique, the AFM probe displays certain chemical functionality or ligands to measure the interactions with molecules carrying functional groups or receptors on a surface. Probe functionalisation is discussed in Section 1.2.1.4, with reference to single molecule force spectroscopy. Here, probe-surface interactions are mapped to obtain information about the lateral distribution of molecular recognition events. Antibody functionalisation of the probe is particularly popular for AFM based immunorecognition imaging or antibody recognition imaging.

A series of key developments have underpinned antibody recognition imaging at the nanoscale [50]. A comparison of the common antibody recognition imaging techniques is presented in Table 1:2. Phase imaging and force-volume imaging have been available for some years [12], [52], [91], [92]. More recent developments, including *HarmoniX*<sup>TM</sup>, *PeakForce QNM*<sup>TM</sup> (Quantitative Nanomechanical property Mapping) and *picoTREC*<sup>TM</sup> (simultaneous Topography and REcognition imaging; TREC), are also included [63], [93–95].

Table 1:2. Comparison of AFM techniques capable of antibody recognition imaging.

	Phase Imaging	Force–Volume Imaging	HarmoniX™	PeakForce QNM™	PicoTREC™
Real–time adhesion mapping	Yes	No (offline)	Yes	Yes	Yes
Proof of recognition specificity	Block	Force curve analysis / Block	Block	Block	Amplitude modulation / Block
Simultaneous topography and recognition	Yes	No	Yes	Yes	Yes
Lateral resolution	<5 nm	<100 nm	<5 nm	<5 nm	<5 nm
Ease of use / analysis	Easy / Moderate	Moderate / Moderate	Easy / Easy	Easy / Easy	Easy / Moderate
Specialized probes required	No	No	Yes	No	Yes
Time to obtain 1µm <sup>2</sup> image (512x512 pixels)	<5 min	>18 hr	<5 min	<5 min	<5 min

The functionalisation strategies and detection methods used in these areas have been extensively reviewed [7], [38], [50], [96]. However, the following includes a brief review of the working principles of molecular recognition imaging and antibody recognition imaging in particular, and highlights some of the significant applications to biological sciences.

### 1.2.2.1 Force–Volume Imaging

One of the features of force spectroscopy is that conformational changes of protein unfolding can be detected. The technique provides a platform for high throughput screening of environmental conditions [25], [97], [98] at which proteins may interact. Further, mechanical properties of cells and even cellular responses to physical stimuli can be investigated [99]. However, no information can be gained about the size and shape of potential aggregates, only the force of interaction between proteins, and structural changes resulting from these single molecule interactions. In order to compare the topographical features of a sample and localize the data obtained by force spectroscopy in the

## *Introduction*

x–y axis, force–volume imaging was developed [100]. By mapping the adhesion measured by force spectroscopy using a probe functionalised with antibodies or other proteins across a topographical area, using force–volume imaging, the location and identity of proteins can be inferred at a sub–micron level. This method is inherently slow since each pixel requires a full force curve to be acquired. Furthermore, the CM image of the area must be acquired separately to the force curve. Over the timeframe of the experiment, drift in the x,y,z position is difficult to exclude, and this severely limits the resolution of the technique. Some offline calculations must be done to ensure the mapped adhesion is due to antibody recognition, and not due to non–specific interactions [97]. A blocking step must also be incorporated in order to reduce or eliminate signal due to receptor–ligand interactions, to prove molecular recognition specificity.

Dupres *et al.* [101] used a functionalised tip to map the adhesins on living bacterial cells using force–volume imaging. The blocking used in this experiment included addition of free heparin to block the surface sites of adhesin, shown by a reduction in binding events. This combination of force spectroscopy and adhesion imaging of the surface is a powerful technique, and has been applied to systems such as bacteria [102] and lipid membranes [103], [104], among others [105], [106]. The resolution of force–volume imaging is generally limited by the amount of time it takes to collect a force–distance curve at each point on the surface.

#### **1.2.2.2 Phase Imaging**

In TM imaging, the phase lag of the tip oscillation relative to the external driving oscillation can be monitored, as discussed in Section 1.2.1.1.2. A phase lag results from surface-dampened harmonic oscillations. This signal is sensitive to short-range interactions such as adhesive forces and visco-elastic forces as well as long-range interactions such as magnetic and electric fields [12], [13], [92]. By utilising a functionalised probe, the adhesion of the probe will be increased in areas where the corresponding ligand is located, resulting in increased phase contrast. However, due to the number of potential interactions leading to a phase response, it is difficult to map adhesion using this method alone. Li *et al.* [107] were able to identify angiotensin-II type 1 (AT1) receptors on a fixed neuronal membrane using an anti-AT1 antibody functionalised probe by employing ‘interleaving’ [108]. Interleaving involves scanning each line once in TM to detect topography, then again with a ‘lift-up’ to minimize surface contact for phase signal acquisition. Following data acquisition, a low-pass filter can be used to remove low-frequency topographical data from the phase channel. A disadvantage of interleaving is the increase in image acquisition time. Furthermore, although interleaving can be used to separate the topographical information, the phase response may still be affected by other tip-sample interactions, and a blocking step as described for force-volume imaging should be applied for proof of specificity.

#### **1.2.2.3 TREC**

TREC operation relies on the use of a receptor-functionalised tip on a magnetic-coated cantilever oscillated by a magnetic field (Magnetic AC (MAC) mode). The receptor must be attached via a long, flexible crosslinker.

## *Introduction*

As the receptor binds to ligands while imaging, this crosslinker will stretch during the ‘upswing’ of the oscillation, stunting the full amplitude. The lower region of the oscillation is only affected by the sample topography. Hence, the probe oscillation trace is split into lower and upper regions with respect to the probe’s resting position by the TREC equipment. Due to the nature of the data collection, TREC is capable of full–amplitude or half–amplitude feedback to eliminate topography signal from interfering in recognition data. Also, proof of recognition can be obtained without introduction of a free receptor or ligand by amplitude modulation inhibition of the crosslinker stretching [109].

TREC has been applied to a variety of biological systems, such as localization of streptavidin–based probes on bacterial S–layers [110], detection of human ergotoxin–1 on embryonic kidney cells [111] and recognition of cystic fibrosis transmembrane conductance regulator on human erythrocyte membranes [112]. Stroh *et al.* [63] analysed lysozyme adsorbed on a surface using a HyHEL5 antibody–modified tip. Force curves were first obtained to confirm antibody specificity, before acquiring recognition images using both force–volume and TREC imaging (Figure 1:7).

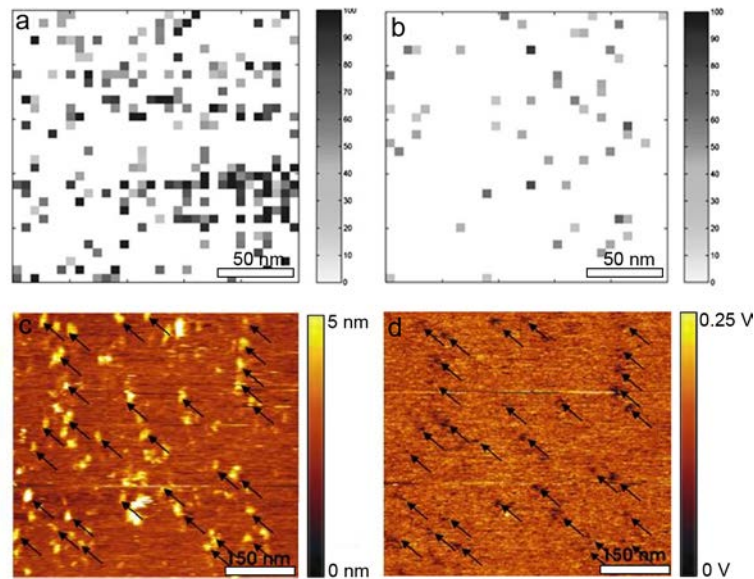


Figure 1:7 – (a, b) AFM force–volume images using lysozyme adsorbed onto a mica surface and HyHEL5 antibody attached to the probe. Binding sites on the lysozyme layer were detected in a, and blocked with free HyHEL5 antibody in solution in b. The unbinding forces in the pixels are scaled in grey scale values (0–100 pN). (c, d) Simultaneously acquired topography (c) and recognition (d) images using a HyHEL5 antibody–coated tip on mica surface with adsorbed lysozyme. The correlation between topography and recognition image is indicated with black arrows, showing that at least two–thirds of the lysozyme molecules are detected in the recognition image at the same position. Adapted from [63].

It is clear from Figure 1:7 that the resolution of TREC exceeds that of force–volume imaging. At the same scan size, whilst the force–volume image took 14 minutes at a resolution of 64 x 64 pixels, the TREC image was captured within 8 minutes at 512 x 512 pixel resolution.

Preiner *et al.* [109] investigated the optimal imaging conditions of TREC using a model protein interaction. Single avidin molecules were detected on mica using a biotinylated–IgG–functionalised tip. Minimization of topographical crosstalk was achieved by resonating the cantilever at a very low frequency. The modulation of the amplitude of oscillation was investigated to determine the optimal amplitude for a reliable recognition signal. The authors found that molecular recognition can be proven *in situ* by increasing the amplitude to a range higher than the crosslinker is capable of stretching. Blocking

experiments as described for force–volume imaging that contaminate the tip and/or the sample are not required.

These examples of TREC imaging clearly demonstrate the usefulness of TREC to visualize, identify and quantify binding sites on biological surfaces. Comparison between the simultaneously acquired topography and recognition images yields high–resolution maps, acquired in relatively short timeframes, on isolated proteins and fixed cell systems. TREC is still a relatively new technique, with continuing advances in methodology. The greatest advantage TREC has over other AFM antibody–recognition imaging is the ability to prove that adhesion is due to the antibody–mediated molecular recognition by modulating the amplitude of oscillation until crosslinker stretching is no longer causing a recognition signal [109]. This avoids contamination of the sample or the probe resulting from blocking experiments, and allows reuse of probe and sample.

Unfortunately, due to the need to use a long crosslinker, there is some lateral resolution loss due to tip broadening artefacts. Additionally, the use of specialized magnetically coated probes can increase the cost of running samples.

### *1.2.2.4 Other Molecular Recognition Techniques*

PeakForce QNM<sup>TM</sup> is a recent technique developed by Bruker (previously Veeco) [94], [95], [113]. It utilises a patent–pending algorithm designed specifically for the fast analysis of cantilever deflections when approaching and

## Introduction

retracting from the surface. The instantaneous peak force is detected and minimized to avoid damaging the sample or probe, and calculations of the sample properties such as Young's modulus, deformation, dissipation and adhesion are *ad hoc*. Rico *et al.* [114] utilised PeakForce QNM to image the plasma membrane protein bacteriorhodopsin of *Halobacterium salinarum*, mapping the flexibility of membrane proteins at sub-molecular resolution. Stiffness measurements of the protein subunits were correlated with their secondary structures as shown in Figure 1:8.

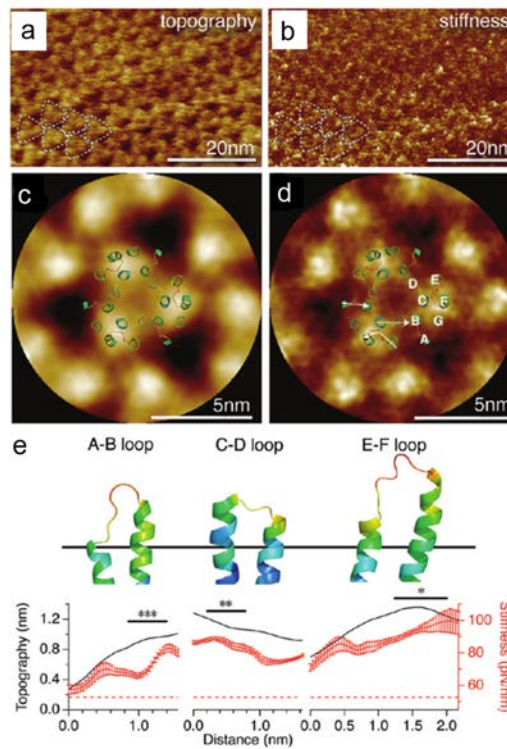


Figure 1:8 – PeakForce QNM images showing topography (a, z-axis = 1.5 nm) and stiffness (b, z-axis = 39 – 109 pN/nm) of bacteriorhodopsin protein layers, with individual trimers encircled in (c, z-axis = 1.5 nm) and (d, z-axis = 39 – 109 pN/nm). Individual loops are labelled. (e) Correlation of averaged topography and stiffness with loop structures calculated from 13 bacteriorhodopsin trimers from a and b and overlaid with the atomic structure [115]. Lateral view of the atomic structure coloured by B-factors (top) of each cytoplasmic loop, and cross-sectional profiles (bottom) of topography (black) and stiffness ( $\pm$ standard error of the mean, red) along the arrows shown in d. The red dashed line shows the average stiffness of the lipidic region in d. Adapted from [114].

## Introduction

By correlating the high-resolution images seen in Figure 1:8 with mechanical maps, Rico *et al.* were able to identify which proteins contribute to structure and which contribute to function.

Another relevant technique recently developed by Bruker is HarmoniX<sup>TM</sup>. This system utilises specially designed ‘hammer-head’ shaped probes, oscillated at higher harmonic modes beyond the resonant frequency of the cantilever. The torsional amplitudes are monitored, and the harmonics are converted back to the time domain to provide tapping force curves from lateral deflection signals. As the tip geometry and spring constant are known, maps of elasticity or adhesion can be extrapolated from the data [84]. To date, only two publications have utilised HarmoniX for biological applications. Husale *et al.* [116] imaged unlabelled DNA and RNA on a thiolated gold surface in order to determine the stiffness of single-stranded *versus* double-stranded molecules. The hybridized DNA strands were softer than their single stranded counterparts, double-stranded DNA having a stiffness of ~3.8 GPa compared with ~5 GPa for single-stranded DNA. Using these nanomechanical properties, it was possible to map the location of hybridized and un-hybridized DNA and RNA across a surface in a label-free manner.

Sweers *et al.* [94] used nanoindentation, HarmoniX and PeakForce QNM in their comparative study of  $\alpha$ -synuclein amyloid fibres. PeakForce QNM was able to gather mechanical data across the fibril images with more automation than nanoindentation, and less image artefacts than HarmoniX. The elastic moduli obtained by the three methods were corrected by accounting for the tip

## Introduction

and fibril shape and size, and the values were comparable (1.3 – 2.1 GPa) for all techniques. Nanoindentation remains the most accurate method for biomechanical measurements at the nanoscale, but mapping techniques such as HarmoniX and PeakForce QNM are faster and simpler to use, and may consequently find application for screening purposes.

Adamcik *et al.* [95] applied PeakForce QNM to analyse the height, elastic modulus and deformation of amyloid fibrils from  $\beta$ -lactoglobulin (Figure 1:9), a protein present in milk which can form amyloid fibres under low pH and/or high temperature conditions.

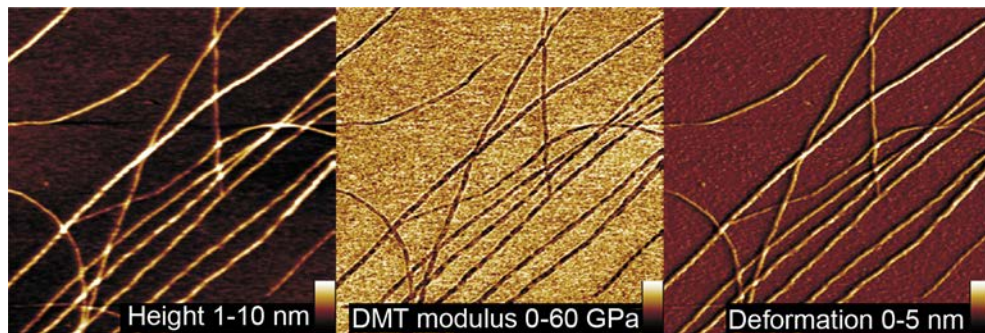


Figure 1:9 –  $1.3 \times 1.3 \mu\text{m}^2$  AFM PeakForce QNM images of  $\beta$ -lactoglobulin amyloid fibrils on mica. From left to right, data displayed are, respectively, topography (z-scale 10 nm), elasticity using a Derjaguin–Mueller–Toporov fit (z-scale 60 GPa), and deformation (z-scale 5 nm). Adapted from [95].

The values found for elastic modulus of individual fibres supported indirect calculations by means of topological statistical analysis (utilising polymer physics [117]) on fibrils structural conformations.

With the development of new AFM methodologies such as Peakforce QNM, nanomechanical data such as elasticity and deformation can be gathered quickly at the same time as morphological characterization. To my knowledge,

PeakForce QNM and HarmoniX have not been used for antibody recognition imaging in the literature. Antibody blocking would need to be carried out in order to prove antibody binding, contaminating the sample and probe. It would nevertheless be interesting to see how the results compare against TREC and other antibody recognition imaging techniques.

### **1.2.3 Combination with Non-Atomic Force Microscope Techniques**

Other microscopic (such as those seen in Table 1:1) or spectroscopic techniques can be combined with AFM on biological samples to acquire a more comprehensive understanding. Examples of relevant techniques that can be applied to samples prepared in parallel are circular dichroism (CD) spectroscopy for determination of protein secondary structure, dynamic light scattering (DLS) for determining size of proteins aggregates and fluorescence assays of fibre formation with Thioflavin T (ThT) and Congo Red (CR). Fluorescence microscopy can be combined with the AFM, as similar environmental conditions are achievable for both techniques. It is possible to attach a tip scanning AFM system on an inverted microscope to allow visualization of optically transparent samples, such as a monolayer of cells [118], [119]. This combination of fluorescence microscopy and AFM has also been demonstrated for molecular recognition AFM. Duman *et al.* [120] have combined TREC imaging and fluorescence microscopy to determine density, distribution and localization of yellow fluorescent protein-labelled cluster of differentiation 1 molecules on  $\alpha$ -galactosylceramide ( $\alpha$ GalCer)-loaded human acute monocytic cells with a natural killer T-cell receptor modified AFM tip.

## *Introduction*

A variety of other techniques useful for investigating protein samples, such as Raman microscopy [121], [122], and infrared microscopy [123], have also been coupled to AFM systems for simultaneous measurements of topography and chemical functional groups.

## **1.3 Fibre-Forming Peptides and Proteins**

### **1.3.1 Secondary Structures**

The 'secondary structure' of a biopolymer (such as proteins and DNA) describes the three-dimensional form of localized segments of the molecule; the overall three-dimensional structure of a protein, relating the atomic coordinates in space, is known as 'tertiary structure' and will not be discussed herein.

In proteins, the pattern of hydrogen bonds between the amide backbone and carboxyl groups defines the secondary structure. These inter-residue bonds give rise to 'turns' and 'bridges', repeating elements of which are known as 'helices' and 'ladders', respectively. The result of laterally joined ladders is a 'sheet'. The geometric structure, resulting from torsion and curvature of the peptide backbone, is used for definition of secondary structures observed in proteins [124].

The most commonly observed secondary structures in proteins are  $\alpha$ -helices and  $\beta$ -sheets, consisting of right-handed helices with 3.6 residues per turn and adjacent peptide strands of 3 – 10 amino acids connected by bridges, respectively [124], [125]. PPII helices have also been observed, consisting of right-handed helices of 3.3 residues per turn left-handed helices of 3 residues per turn for polyproline I and II respectively [126], [127]. Often overlooked is the very common random coil configuration, which is not a structure as such but a description of randomly oriented amino acids forming hydrogen bonds

with random adjacent residues. Visual representations of these secondary structures are shown in Figure 1:10, below.

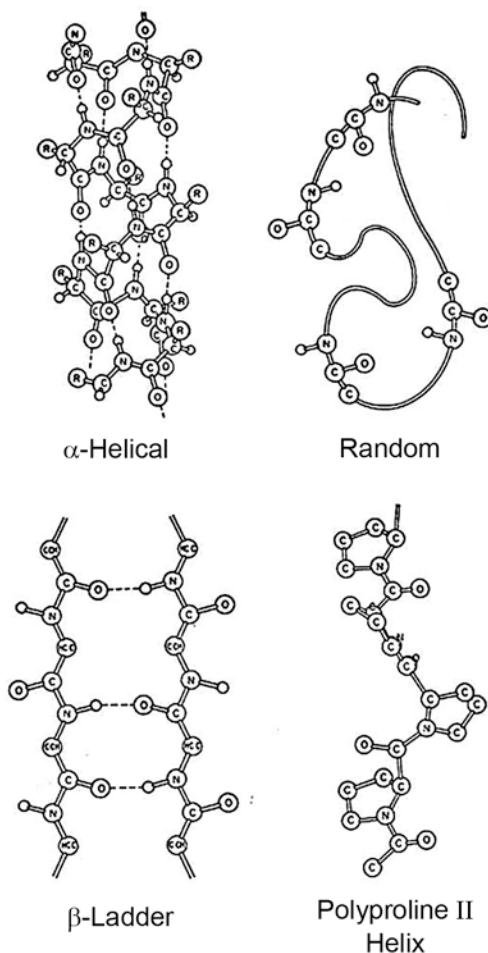


Figure 1:10 – diagrammatic representation of some of the common ordered (and ‘random’) secondary structures observed for protein segments. Adapted from [125].

Ordinarily, a protein contains multiple secondary structures, the approximate ratios of which may be estimated effectively using spectroscopic techniques such as solid state nuclear magnetic resonance (ssNMR) and CD [125], [128], [129]. The AFM can be used to identify morphological properties of proteins, which – in conjunction with spectroscopic techniques – allows for complete structural investigations of protein aggregates.

### 1.3.2 Protein Aggregation

Protein aggregation occurs when peptides or proteins assemble into clusters of proteins, due to non-covalent interactions, which will eventually phase-separate. Such aggregates can be amorphous, crystalline or have ordered superstructures such as filaments or fibres, and can occur in intra- and extra-cellular environments [130], [131]. A typical protein folding pathway is shown in Figure 1:11, in which a native protein is partially misfolded, exposing regions which are normally hidden. These regions are often hydrophobic, driving aggregate formation in physiological environments due to the hydrophobic effect. In the schematic shown in Figure 1:11, there are four possibilities for the partially unfolded protein; it can revert to a native protein, completely unfold, or it can form aggregates [132], [133].

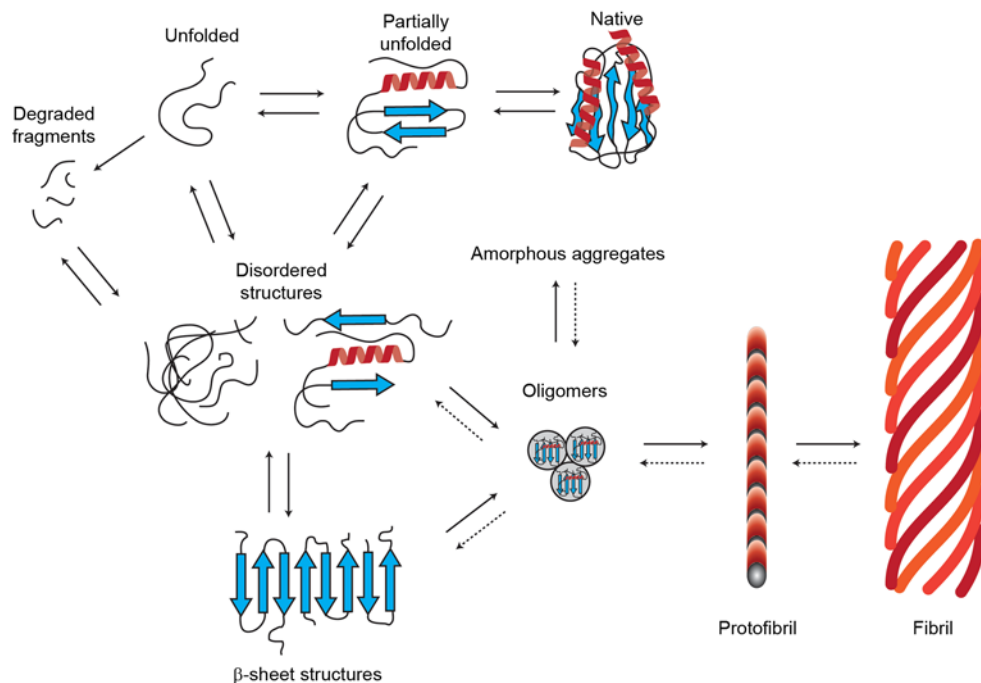


Figure 1:11 – Schematic of some of the many conformational states that can be adopted by polypeptide chains. All of these different conformational states and their interconversions are carefully regulated by the biological environment.

## *Introduction*

In general, fibre formation occurs via an aggregation pathway as in Figure 1:11. Peptide chain subunits fold into disordered, partially ordered, or native states. These secondary structures may then assemble to form oligomers. After a nucleation event, elongation via the addition of further oligomers or monomers leads to the formation of protofibrils. It is generally agreed that the step at which protofibril growth from oligomers occurs is due to a nucleation event [134], [135], and the time it takes for the nucleation event to occur is known as the lag phase or induction time. The nucleation step does not occur for all systems in which fibrils are formed from protofibrils; fibril formation can occur as a result of the breakdown and re-structuring of the protofibrils, or the bundling of multiple protofibrils [136], [137]. In the literature, the nomenclature of fibrillar structures is not always clear; in this review, protofibrils refers to a fibre-like structure known to precede a fibril. Further ambiguity results from the use of the term, 'fibre,' which in common usage can refer to any elongated structure [138], and is often used interchangeably with 'fibril' in the literature. Again, for the purposes of this review, a fibre is considered the mature form of the protein or peptide aggregation, and may be formed of fibril subunits.

### *1.3.2.1 Amyloid Fibres*

In terms of ordered protein aggregates, the most common form in nature is the group of amyloids. Amyloid deposits are implicated in over 40 different diseases, known collectively as amyloidoses. They also function in non-pathological roles, such as in spider silk [133]. These are polypeptide-based fibres characterized by a cross- $\beta$  sheet structure as seen by X-ray diffraction,

having a characteristic diffraction pattern with a sharp reflection at 4.7 Å along the same direction as the fibre, and a more diffuse reflection at between 10 and 11 Å perpendicular to the fibre direction [139]. Amyloid proteins do not necessarily share homology of peptide sequence, and it is the cross-β sheet conformation, which is the accepted biophysical hallmark of an amyloid fibre [140].

The mean aggregation properties and configuration of amyloid fibres have been studied using a variety of methods, including DLS, neutron scattering, CD spectroscopy, Fourier transform infrared (FTIR) spectroscopy, electron diffraction, electron paramagnetic resonance, and ssNMR [128], [139]. Clinical diagnosis of amyloidosis, however, is usually carried out using a CR stain, by polarized microscopy, or by immuno-gold EM, to detect amyloid plaques in tissue sections [133], [140], [141]. Amyloidic fibres display a range of ultrastructural polymorphisms, which are best investigated using high-resolution microscopic techniques, such as AFM. Furthermore, high structural stability and resistance to degradation make these structures ideal candidates for nanomaterial design. It is therefore not surprising that peptides mimicking this aggregation pathway have also been extensively studied.

In the following two chapters, the use of AFM for morphological and mechanical characterization of amyloid fibres will be reviewed, with a focus on three disease-causing proteins; α-synuclein (αS), β-amyloids (Aβ) and prions.

## Introduction

$\alpha$ S is the main causative agent in the pathogenesis of Parkinson's disease [142]. The protein can form several aggregation states; these include a natively unfolded monomer, oligomers rich in  $\beta$ -sheets (protofibrils) and stable amyloid fibrils [143], [144]. Amyloid structures interact with the neurons' cell membranes, resulting in destabilised cellular ionic homeostasis [145]. The AFM has been used to observe  $\alpha$ S aggregation states, including non-fibrillar oligomers [146], spheroids, and fibril formation under a variety of conditions *in vitro* [147], [148].

A $\beta$  is a peptide of 39–43 amino acids that is processed from the so called amyloid precursor protein [149]. As the name implies, A $\beta$  peptides form amyloidic rod-like fibres held together by  $\beta$ -sheets. The occurrence of A $\beta$  fibrils, protofibrils and oligomers in amyloidic plaques within brain tissue is a hallmark of Alzheimer's disease [133], [150]. Soluble A $\beta$  peptide fragments found in cerebrospinal fluid from patients diagnosed with Alzheimer's disease are most commonly composed of amino acids 1 – 40 and 1 – 42 [151].

Prions are a unique form of infectious agent, consisting of misfolded proteins rather than organisms with a DNA/RNA code. The prions act as a template to induce the misfolding of normal proteins in neurological tissue, leading to amyloid inclusions [152]. Specifically, the cellular Prion Protein (PrP<sup>C</sup>) is misfolded into an abnormal isoform (PrP<sup>SC</sup>), which is insoluble and protease-resistant. PrP<sup>SC</sup> is responsible for transmissible spongiform encephalopathies such as Scrapie and Creutzfeldt–Jakob syndrome, for which there is currently no effective treatment and which are invariably fatal [153].

As mentioned above, amyloid protein aggregates have become infamous for their involvement in neurodegenerative diseases such as Parkinson's and Alzheimer's disease [133], [154], but are also implicated in a wide range of other disorders such as type II diabetes and cataracts. The reader is referred to an excellent in-depth review about protein misfolding in human disease by Chiti and Dobson [133].

### 1.3.2.1.1 Morphological Characterization of Amyloid Fibres

AFM offers a perspective on the mechanisms of assembly of amyloid fibres with nanoscale resolution under physiological conditions. Since the first papers to observe amyloid fibres by AFM in the 1990s, fibril growth and polymorphisms have been extensively investigated [144], [155], [156]. The ultrastructural characteristics of amyloid fibres, including the length and width, polymorphisms (curvature and persistence), periodicity and higher-order assembly have been described for amyloid fibres from a range of sources [117], [139], [140], [156]. In general, amyloid fibres are observed to be long (up to several microns), straight and mostly unbranched. The diameter of the fibres varies between 5 – 25 nm [139], [140] depending on the number of protofibrils twisted together to form a fibril. The fibril shape and contour depends on the number of protofibrils and overlapping  $\beta$ -sheets [87], [139], [140], [150], [157].

Stine *et al.* [155] observed A $\beta$ (1–40) protofibrils using both CM and TM in air on mica and graphite. Protofibrils with an axial periodicity of around 25 nm

## Introduction

were seen alongside smooth protofibrils of similar dimensions. The authors discuss some of the effects that sample compression and tip convolution can have on AFM measurements, and utilise both an internal calibration of plasmid DNA and an external calibration of A $\beta$  measured by electron microscopy. Protofibrils were estimated to be 6 – 10 nm thick after taking into account AFM artefacts. These values are in the expected range for amyloid protofibrils.

Bocharova *et al.* [158] were able to induce PrP<sup>SC</sup>-like aggregates from recombinant mouse full-length PrP<sup>C</sup>. Anderson *et al.* [159] then used AFM and TEM to characterize the ultrastructure of the aggregated prion protein fibres. Interestingly, several different morphologies were observed based on AFM topography measurements. The major sub-types of polymorphisms identified were straight or slightly curvy ribbons, rod-shape protofibrils and bundles, protofibrils with a beaded nature, and ribbon-shaped protofibrils composed of laterally aligned sub-cords. Also described were protofibrils with a diverse range of twisting patterns, although these are far less commonly seen. The polymorphisms described were consistent with features seen in EM images of proteins isolated from Scrapie infected tissue, indicating that the PrP<sup>SC</sup> are able to assemble into a certain range of conformations regardless of pathological *in vivo* or *in vitro* conditions. Petty *et al.* [160] synthesized peptide sequences based on the most amyloidogenic residues (109 – 122) of a prion protein found in healthy Syrian hamster. AFM imaging showed that modification of the amino acid present at residue 117 resulted in altered alignment of the peptides, either forming the long twisted rods expected of amyloid fibrils, producing smooth thin protofibrils, or preventing aggregation as seen for the wildtype

PrP<sup>C</sup>. This residue impacted on the assembly process of peptide fibres by affecting the strand alignment and  $\beta$ -sheet crosslinking of adjacent peptides. Such studies may be useful in designing peptides or peptidomimetics to arrest prion aggregation.

Since the growth of fibrils is slow with respect to AFM imaging, time-lapse AFM can be used to observe the fibrillization process [161–163]. Goldsbury *et al.* [164] investigated the growth of A $\beta$ (1–40) fibrils using TM AFM in neutral buffer (Figure 1:12).

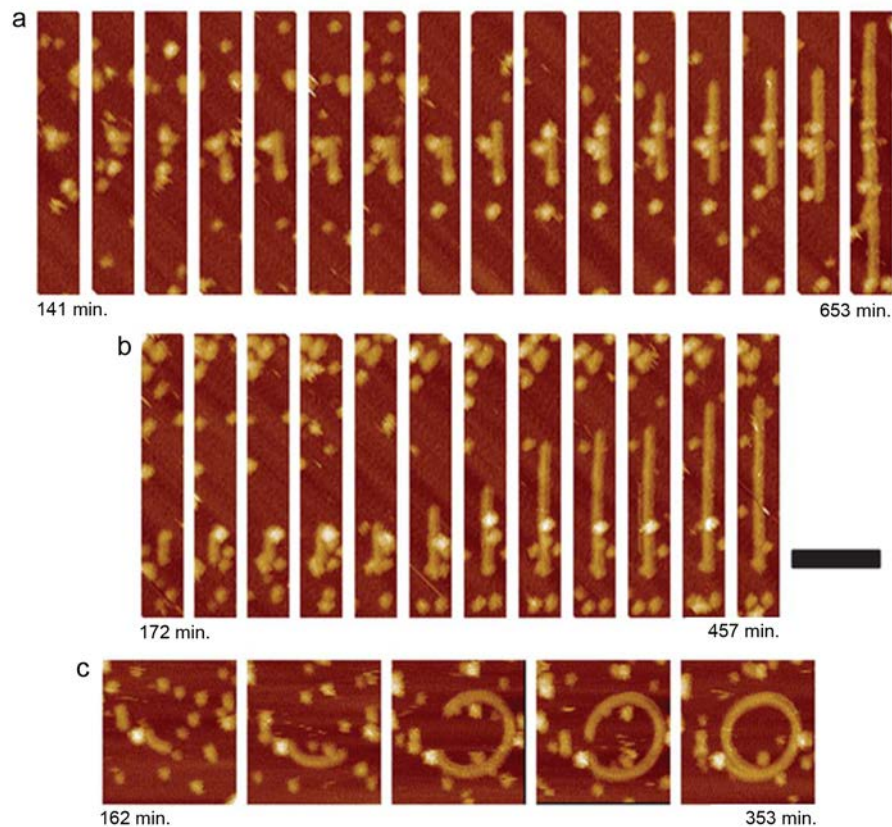


Figure 1:12 – Time-lapse (denoted beneath each image series) series of TM AFM height images showing protofibril elongation. Protofibril elongation was both bi-directional (a) and uni-directional ((b) and (c)). The scale bar = 200 nm. Adapted from [164].

## Introduction

Monomers and high molecular weight oligomers were immediately observed on the mica surface, indicating the effectiveness of mica for adsorbing A $\beta$  in fluid conditions. After 2 hours, protofibrils of width  $6 \pm 0.5$  nm began to form on the surface. If A $\beta$  fibrils were pre-adsorbed to mica instead of using clean mica, new protofibrils and oligomers were observed immediately, suggesting a seeding effect for pre-formed fibrils. As the A $\beta$  peptide was consumed from solution by fibrillization, fibrils formed on the mica with heights of  $10.7 \pm 2.3$  nm in two different discrete elongation steps: the first of which the authors interpret as the addition of protofibril subunits; the second possibly resulting from assembly of discrete independent peptides, morphologically resembling loosely twisted ribbons with  $\sim 80 - 130$  axial cross-over spacings. Due to the constraints of fibril growth on surfaces, there may be additional pathways for fibril growth in solution which are not observed in this system.

A $\beta$ (1–40) and A $\beta$ (1–42) were also investigated using time-lapse AFM by Harper *et al.* [165] utilising TM AFM in air. Here, A $\beta$ (1–40) aggregation occurred within one week, yielding protofibrils of height  $3.1 \pm 0.3$  nm. This time course was accelerated for A $\beta$ (1–42), requiring only a day to form protofibrils of height  $7.8 \pm 0.5$  nm. Over time, larger (at least double the height) fibrils appeared, effectively consuming the protofibrils (and not necessarily growing from them). Harper *et al.* [144] were able to speed up the growth of fibrils by adding pre-formed protofibril ‘seeds’. The final fibres, consisting of a helical twisted structure, were compared with the fibres isolated from Alzheimer’s tissue as well as other published amyloid fibres such as prions and found to have a similar morphology. This work demonstrated that

## *Introduction*

the critical nucleation step is the transition from protofibril to fibril, and that seeding can effectively decrease the lag phase of fibril formation without affecting the final morphology.

The role of chaotropic denaturing agents in initiating amyloid fibril growth has been investigated by Polano *et al.* [166] who studied the aggregation of recombinant mouse prion protein (RecMoPrP(89–230)) previously shown to form prion fibrils when prepared in buffers containing guanidine hydrochloride (GdnHCl). GdnHCl is commonly used in diagnostic amyloid seeding assays [167], [168]. At low concentration (0.4 M) of GdnHCl, only protofibrils or oligomers were observed by AFM. However, an increased concentration (2 M) led to the formation of amyloid fibrils as seen in Figure 1:13 below.

## Introduction

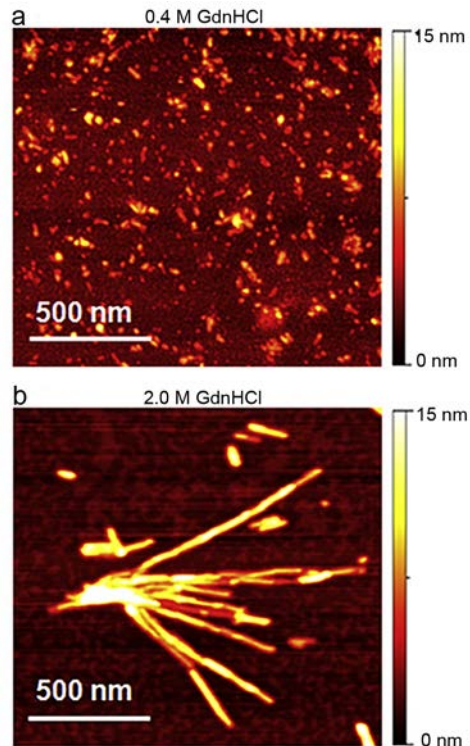


Figure 1:13 – AFM height mode images of prion aggregates formed in buffer containing 0.4 M GdnHCl (a) and 2.0 M GdnHCl (b). Adapted from [166].

The nucleation event of aggregation of prion proteins into fibrils is affected by the hydrogen bond disrupting–GdnHCl, with an increased concentration of denaturing agent leading to the formation of more amyloid fibres. However, the ultrastructures observed by AFM at high concentrations of GdnHCl did not closely mimic those seen in purified disease prion aggregates. Instead of featuring many polymorphisms, like the PrP<sup>SC</sup> fibres from disease tissue, Polano observed a dominant morphology of rod–like fibres with height 5.7 nm (Figure 1:13), which indicated that this model system of aggregation may not reflect pathological conditions. Instead, Wegmann *et al.* [169] postulated that investigation of infected cells may reveal more relevant insights into the structure of prion proteins involved in disease pathology. In this study, AFM and light microscopy were used simultaneously on a culture of mouse

neuroblastoma (N2a) cells infected with prions isolated from the brains of mice with Scrapie, as shown in Figure 1:14.

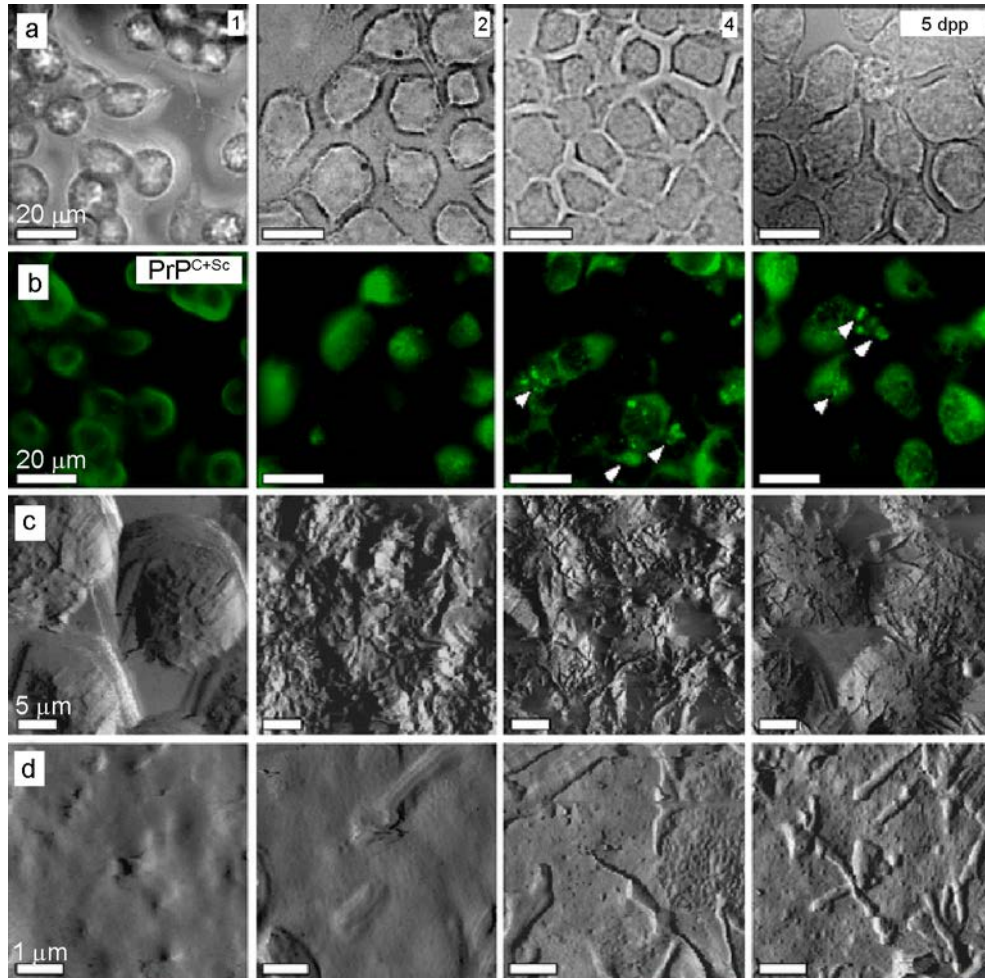


Figure 1:14 – Time course over 5 days, showing fibrillar surface structures on Scrapie–infected N2a cells (ScN2a) derived at 1, 2, 4 and 5 days after plating (columns). (a) Phase contrast microscopy images, and (b) immunofluorescence detection of PrP<sup>C+Sc</sup> with x–scale = 20 μm. (c and d) AFM deflection images of fixed ScN2a cells, showing an increase in fibrillar structures at 5 days after plating (c; x–scale = 5 μm, and d; x–scale = 1 μm). Adapted from [169].

Immunofluorescence microscopy was used to identify infected cells, so that AFM could be applied on those as seen in Figure 1:14 to analyse structures on the cell surfaces. After 5 – 6 days, extensive fibrillar structures were observed, similar to those obtained from diseased tissue. Further investigations utilising a cell culture system like that above could be used to investigate the

environmental conditions of aggregation, and effectiveness of therapeutical drug targets.

Ku *et al.* [170] studied peptides based on one of the most amyloidogenic regions in the human prion protein (residues 106 – 127). Peptides were immobilized on NHS-ester activated glass or self-assembled monolayer-coated gold slides and analysed by AFM and  $\beta$ -sheet binding dyes CR and ThT. Rod-like amyloid protofibrils formed from peptides in solution on these surfaces in more uniform morphologies and at a greatly increased rate compared to solution-based aggregation. This was thought to be due to the immobilized peptides having a seeding effect, rather than being a surface artefact. Although the system is arguably not the best mimic for the diseased state, it may nevertheless be useful for designing advanced diagnostic assays for disease detection. Also exploiting an NHS-ester surface, Ha and Park [171] immobilised A $\beta$  monomers, oligomers and fully grown fibrils as seeds for A $\beta$ (1–42) growth. Utilising TM AFM in air, they studied the frequency and morphology of mature fibres. Pre-aggregated oligomers were found to be the most efficient at seeding by serving as a sink to soluble A $\beta$  in solution. The use of functionalised surfaces for *ex situ* fibre formation is a highly effective method and reveals the effects of surfaces on amyloid aggregation. Further surface effects have been investigated as protein aggregation inducing factors. Giacomelli *et al.* [172] observed the influence of Teflon on A $\beta$  fibril formation by inserting 100 nm Teflon nanoparticles into a solution of A $\beta$ (1–40) peptide. Using a pH 10 buffer, A $\beta$  was mostly observed as random coil and  $\beta$ -sheet structure in solution (by means of CD spectroscopy), converting to primarily

$\alpha$ -helices upon introduction of Teflon particles. As the peptide concentration increased,  $\beta$ -sheet structures re-formed across the Teflon nanoparticle surfaces. Ideally, flat Teflon surfaces incubated with amyloid-forming peptides would be analysed by AFM, since the morphology of the aggregates could then also be observed.

Zhu *et al.* [173] studied amyloid fibre formation on mica since this is a commonly used ultraflat substrate for AFM studies. They observed that the lag phase for protofibril formation was shortened due to incubation in the presence of mica, and protofibril formation occurred at lower concentrations than incubation in the solution phase followed by deposition onto mica. Kowalewski and Holtzman [174] applied *in situ* TM AFM in pH 7.4 buffer to compare aggregation of A $\beta$ (1–42) on mica and graphite. On mica, highly mobile globular aggregates of 5 nm height were observed with a tendency to coalesce to protofibrillar aggregates over a 20 minute period. In contrast, graphite was covered with elongated parallel sheet structures at 120° angles to each other within minutes of being introduced to the surface. These were interpreted as  $\beta$ -sheets, with extended peptide chains perpendicular to the long axis of the aggregates stabilized by the hydrophobic interactions between graphite and the peptides' hydrophobic residues. Wang *et al.* [175] observed a similar phenomenon for A $\beta$ (1–42) peptides in a citrate buffer (pH 4) on a graphite surface. The authors also observed beaded protofibrils with a right-handed axial periodicity, for which self-assembly was suggested to be via a joining of bead-like aggregates, leading to elongated protofibrils of A $\beta$  peptide, followed by the protofibrils intertwining into fibrils. This

hydrophobically-driven self-assembly on graphite has also been observed by STM [176].

Gorman *et al.* [177] also investigated A $\beta$  fibril formation on mica and graphite. Here, the shorter A $\beta$ (1–40) peptide was used in a buffer of pH 6. Aggregation on mica was observed over a similar timeframe as described by Kowalewski and Holtzman [174]. However, large amorphous aggregates of 150 – 500 nm height were observed on the graphite surface. These large aggregates were transient, disappearing after longer incubation times. The main experimental differences between the work by Kowalewski and Holtzman and that of Gorman *et al.* are that Gorman *et al.* used a solution phase incubation before allowing aggregates to deposit onto the substrates, and that imaging was performed in air. Hence the differences observed between substrates by Gorman *et al.* are likely to reflect differences in the propensity of aggregates of varying hydrophobicities to adhere to the substrates, rather than result from surface-induced morphological differences on A $\beta$  aggregation.

In order to observe the aggregation of amyloid fibres on more physiologically relevant substrates, solid supported lipid bilayer membranes have been employed. Quist *et al.* [145] monitored the interactions between amyloid forming proteins, including A $\beta$ (1–40) and  $\alpha$ S, reconstituted into 1,2-dioleoyl-sn-glycero-3-phosphocholine (DOPC) liposomes formed into lipid bilayers supported on mica. Individual pore-like structures were seen to form in the bilayer, with pores of 1 nm and 2 nm diameter, for  $\alpha$ S and A $\beta$ , respectively, which the authors suggest may support an ion channel function of the protein

## Introduction

aggregates. Green *et al.* [178] also investigated A $\beta$ (1–40) interactions with lipid bilayers of 1–palmitoyl–2–oleoyl–*sn*–glycero–3–phosphocholine (POPC) and 1–palmitoyl–2–oleoyl–*sn*–glycero–3–phosphoglycerol (POPG) (3:1) supported on mica in a pH 7.4 Tris buffer. In this case, pore–like structures were not observed, and instead the authors described expanding lesions caused by the adsorption of A $\beta$ (1–40) to lipid bilayer defects. As the peptides were incubated onto the pre–formed lipid bilayers instead of being reconstituted into the liposomes prior to lipid bilayer formation, this suggests that the peptides do not span solid–supported lipid bilayers. Green *et al.* also suggest a toxicity mechanism for A $\beta$ (1–40), but one involving membrane thinning rather than ion channel formation by protein aggregates. Indeed, the precursors of amyloid fibres are often identified as the cytotoxic element of amyloidosis [179–185]. Lowe *et al.* [186] have demonstrated that calcium and cobalt ions induce the formation of potentially pore–forming annular  $\alpha$ S oligomers (Figure 1:15). The structure and properties of aggregation of  $\alpha$ S in the presence of various metal ions is now well documented, with various mechanistic insights being provided [187], [188].

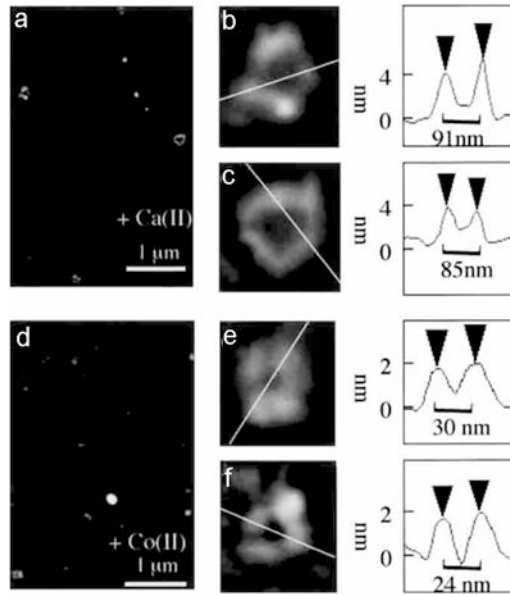


Figure 1:15 – TM AFM height images of  $\alpha$ S annular particles, induced by the presence of calcium (a – c) and cobalt ions (d – f) after incubation at 4 °C for 1 day. Height cross-sections of  $\alpha$ S particles are shown on the right. Adapted from [186].

Pountney *et al.* [189] performed antibody recognition imaging utilising a covalently bound organic crosslinker (trimethoxy-3-bromoacetamidopropylsilane) to functionalise the AFM probe with anti- $\alpha$ S antibodies. These probes were used to image annular nanoparticles formed after incubation of  $\alpha$ S containing glial inclusions purified from diseased brain tissue and treated with mild detergents (Figure 1:16).

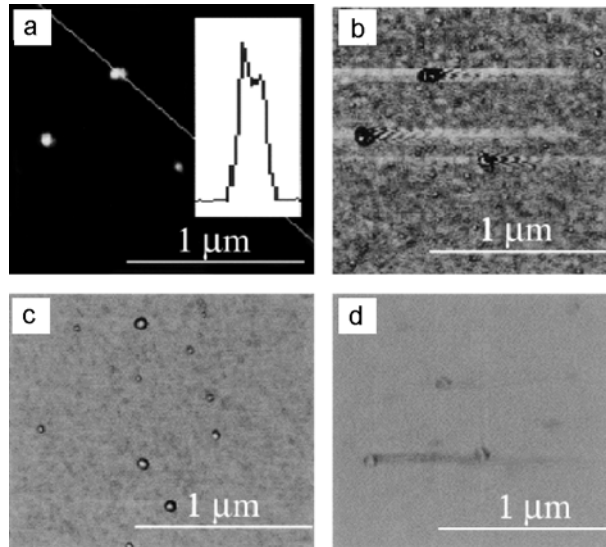


Figure 1:16 – AFM (a) height and (b – d) phase images of detergent–treated glial cytoplasmic inclusions, displaying annular nanoparticles. (a, b) Anti– $\alpha$ S conjugated probe, with inset, height cross–section of individual particle. (b) Corresponding phase image, showing a strong phase response to indicate presence of  $\alpha$ S. (c) Anti–SUMO–1 antibody–functionalised probe (phase image). (d) Bovine serum albumin–functionalised probe (phase image). Adapted from [189].

Control experiments using probes modified with antibodies not found in the sample showed significantly smaller phase signals than using the anti– $\alpha$ S antibody–functionalised probe. Further controls to remove any phase effects due to tip morphology variations, such as a system in which multiple proteins are present on the same surface or introduction of free antibody/protein to block molecular recognition, would further confirm  $\alpha$ S recognition.

More recently, Chen *et al.* [190] determined that incubation of  $\alpha$ S with D–ribose resulted in significantly increased aggregation. The resulting aggregates were 20 nm high. When their frequency increased, fibril formation was inhibited. Fibril formation was also inhibited by the addition of hydroquinone and dopamine, as demonstrated by means of AFM by Li *et al.* [191]. However, small spherical  $\alpha$ S oligomers were still observed after incubation with these compounds, suggesting that the fibril formation is inhibited due to stabilization

## Introduction

of pre-fibril structures. Indeed, Hong *et al.* [192] made similar observations when incubating  $\alpha$ S with hydroquinone and nicotine, which resulted in greatly reduced fibril formation by stabilizing three types of small oligomer, with heights 16, 10 and 4 nm. Whilst Li *et al.* argued for a mechanism involving dopamine driven stabilization of  $\alpha$ S oligomers in the brain, Hong *et al.* claimed that compounds in cigarette smoke have potential as a treatment to prevent  $\alpha$ S plaque formation in Parkinson's disease for a similar reason. However, given the recent spur of research strongly suggesting that  $\alpha$ S oligomers are toxic [184], [185], [193], cigarette smoke may actually be contraindicated in Parkinson's disease.

Similar to  $\alpha$ S, research into the oligomeric or pre-fibrillar structure of PrP<sup>SC</sup>, as seen with other amyloidic aggregations, also suggests a toxic intermediate prior to fibril formation. Silveira *et al.* [194] showed that the most infectious PrP<sup>SC</sup> aggregates are composed of only 14 – 28 molecules, with molecular weights of 300 – 600 kDa and an outer diameter of 17 – 27 nm.

In general, PrP aggregation literature focusses on the infectious nature of prion disease, with less emphasis on research into the toxicity mechanism. Some research suggests it is the pre-fibrillar structures that should be the focus of therapeutic interventions to prevent cytotoxicity of neural cells [195], [196], although investigations into dismantling the amyloidic fibres are undoubtedly also important for treatment of brain tissue inclusions [197] and are also highly infectious. The interested reader is referred to further work on the topic of the

toxicity of amyloid species [145], [166], [185], [193], [195], [196], [198], [199].

### *1.3.2.2 Molecular Recognition of Protein Fibres*

The use of molecular recognition on amyloid fibres seems to be absent from the literature. However, some interesting applications of TREC to non-amyloid fibres from the literature will be described in the following.

Chitchevlova *et al.* [75], [200] functionalised an AFM probe with vascular endothelial-cadherin antibody fragments and performed TREC on endothelial mouse cells. Recognition was observed, as seen in Figure 1:17 below, primarily along the actin filaments on the cell surface. The cells were treated with glutaraldehyde to make the cell surface stiffer, and with nocodazole to depolymerise microtubules, hence actin filaments were easily observed on the cell surface.

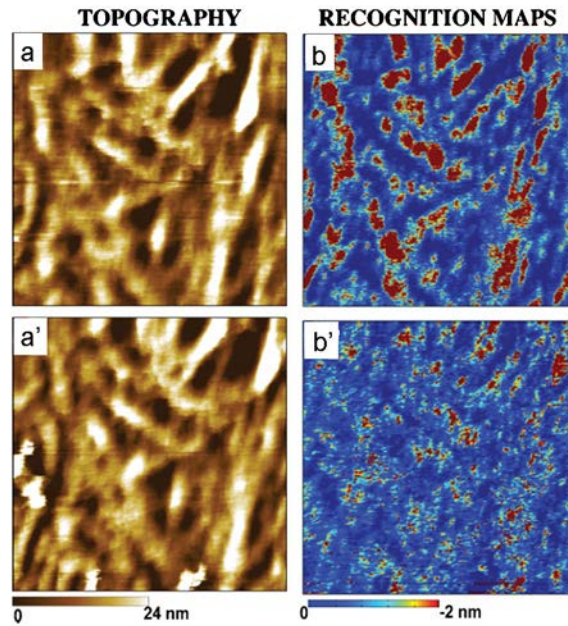


Figure 1:17– TREC AFM images acquired on a mouse endothelial cell surface treated with 50  $\mu\text{M}$  of nocodazole for 80 minutes and subsequently fixed with glutaraldehyde, displaying topography (a, z-scale = 24 nm) and recognition images (b, z-scale = 2 nm). After addition of 5 mM EDTA in the fluid cell, the recognition spots (dark red domains) were reduced (b'). Blocking experiments did not affect the membrane topography (a'). Adapted from [200].

Recognition was shown to occur via a calcium-mediated dimerisation of vascular endothelial-cadherin, and could be blocked via the addition of ethylenediaminetetraacetic acid (EDTA) to remove free calcium ions (Figure 1:17 B).

### 1.3.2.3 Synthetic Fibre-Forming Peptides

Natural systems such as cells have been successfully building nanostructures since the beginning of life. Therefore, it makes sense to research and emulate the bottom-up construction employed by nature. The study of self-assembling systems and biological nanostructures is critical for nano- and biomaterial research [201]. In particular, fibre-forming molecules are receiving increased attention for use in cell scaffolds, biosensors, bio-reactive materials, and as nanowires [202–205]. There has been an explosion of research exploiting

## *Introduction*

synthetic peptide molecules resulting in fibre formation [136], [202], [205] and 3D gel scaffolds [206], [207]. The adsorption of peptide fibre solution to a flat surface allows morphological analysis by AFM under a variety of conditions, not only as an endpoint but also during the self-assembly process. AFM is an ideal method for the analysis of fibrous nanomaterials due to the low interaction forces leading to sensitive mechanical measurements [208], and the high-resolution of the technique affording important structural information [10].

The laboratory of Shuguang Zhang [201], [202] has focused on ionic self-complementary peptides to form amyloid nanofibres. Following observations of the rapid and stable self-assembly of a lysine, phenylalanine and glutamic acid-based peptide sequence (FKFEFKFE) [209], AFM revealed the helical structure of KFE8 peptide oligomers as seen in Figure 1:18(a) below [210]. Using a combination of AFM, CD spectroscopy, and molecular modelling,  $\beta$ -sheet formation of protofibrils and fibrils over time was deduced.

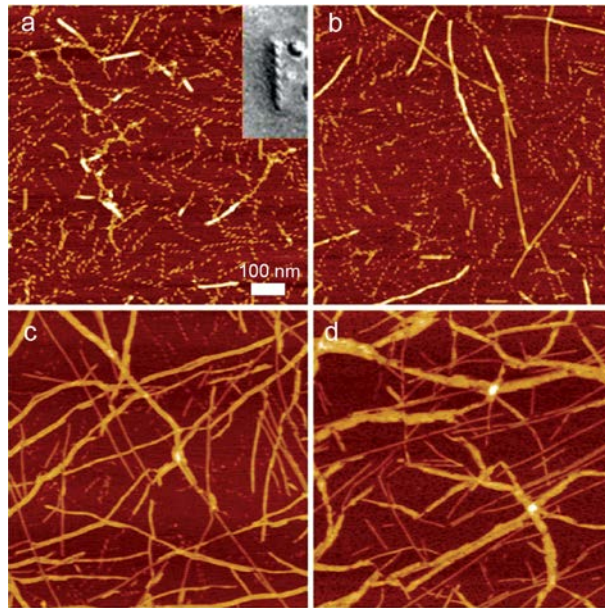


Figure 1:18 – AFM height images of the self-assembly of KFE8 peptide in aqueous solution (a) 8 min (Inset: EM image of a sample of peptide solution obtained using the quick-freeze deep-etch technique), (b), 35 min (c), 2 h and (d), 30 h after preparation. Scale bar = 100 nm. Adapted from [210].

The helical oligomers observed at shorter timeframes decreased in frequency after ~2 hours, being replaced instead with smooth protofibrils of ~8 nm height, which then bundled together to form fibrils of increasing thickness but similar length. During these experiments, the authors made an effort to eliminate artefacts that can affect the assembly of the peptides—including sample-substrate interactions—by observing fibril formation on three different substrates, and by rinsing the adsorbed peptide aggregates with pure water before drying for imaging. Zhang and Luo *et al.* [211] studied the aggregation of alanine- and glycine-based ‘two-tail’ peptides, containing a hydrophilic centre and two hydrophobic ‘tails’. These peptides were denoted ‘AXG’, where the X was replaced with aspartic acid, lysine or arginine. The effect of peptide concentration, temperature, ionic strength and buffer pH was studied. In the absence of salt, peptide aggregation was not observed by AFM, despite DLS showing a wide size range of nanoparticles (100 – 80 nm) in solution. By

adding NaCl or upon incubation in phosphate buffered saline, superstructures such as nano-layer networks and nanofibres were observed by AFM, while CD spectroscopy indicated a reduction in  $\beta$ -sheet structure in the peptide secondary structure. The authors posit that more experiments are required to understand the relationship between the primary structure of two-tail peptides and their aggregation properties under various environmental conditions, and thus do not fully reconcile the CD spectroscopy and AFM results.

The effect of temperature on peptide self-assembly was studied by Tiné *et al.* [212] using an arginine, tryptophan and aspartic acid-based peptide sequence (RWDW). AFM revealed a dense entanglement of fibres at lower temperatures (15°C and 25°C), whilst the physiologically relevant results acquired at 35°C incubation revealed distinct, shorter protofibrils along with round aggregates. These results were interpreted in terms of changes in enthalpy of peptide aggregation as determined by isothermal titration calorimetry and differential scanning calorimetry.

Hydrogels formed by highly networked fibres can ideally be applied as a tissue engineering scaffold. Studying an arginine, alanine and aspartic acid-based peptide (RADA-16), Zhang and Yokoi *et al.* [213] observed the assembly and disassembly of nanofibres scaffolds. The RADA-16 peptides aggregated to form a hydrogel immediately in aqueous solution which consisted of fibres ranging from 100 nm to several microns lengths. By sonicating the self-assembled hydrogel, the peptide building blocks could be disassembled. Over a time period of only 2 minutes, short fibres of 20 – 100 nm length were

observed by the AFM, elongating to their pre-sonication length of over 100 nm after 2 hours of incubation. A further observation from the AFM images was that the order of packing seen upon reassembly had a more ordered overall structure than the initial assembly. This assembly and disassembly cycle could be repeated multiple times on the same sample, showing the repeatability and durability of the peptide assembly process for use as a dynamic tissue engineering scaffold as well as adding interesting insights to the formation of and resistance to treatment of amyloid protein based diseases.

Likewise, Zhang and Luo *et al.* [214] investigated nanofibre formation of a glutamic acid, alanine and lysine-based peptide (EAK-16) for use as a scaffold. The formation of nanofibres of 10 nm height was observed by TM AFM in air on mica. Using CD, the secondary structure of these fibres at neutral pH was shown to be primarily  $\beta$ -sheet. At very low or high pH, fibres were not readily observed and the secondary structure changed from  $\beta$ -sheet to  $\alpha$ -helix. The authors also observed that L-amino acid-based peptide assemblies resisted protease degradation, while the corresponding D-amino acid-based peptide assemblies were more stable at high temperatures. Considering the otherwise identical nature of opposite chirality peptide sequences, this may reflect a slight difference in inter-molecular bonding based on the chirality of amino acid residues. The stability of scaffolds for tissue engineering could therefore be manipulated using the stereochemistry of the peptide building blocks. Indeed, Sun and Zheng [215] investigated a lysine, leucine and aspartic acid-based (KLD-12) peptide sequence for use as an injectable cell scaffold. In pure water, KLD-12 existed in monomeric form.

## Introduction

However, self-assembly into a hydrogel composed of thin, anfractuous, highly networked nanofibres was triggered by introducing salt [216]. The authors suggested that the assembly of KLD-12 occurred via  $\beta$ -sheet interactions. However, no spectroscopic method was used to confirm this. An aqueous solution KLD-12 was used for injection into a mesenchymal stem cell culture, where the physiologically relevant ionic strength of the cell media caused the formation of the gel, encapsulating stem cells to create a 3D scaffold.

Wang *et al.* [217] formed fibres from random coil peptides based on an alanine, glutamic acid, tyrosine and lysine-based sequence (AEAEYAKAK), which formed dense, directional fibres (Figure 1:19) formed by a ‘Lego-type assembly’. No characteristic ordered secondary structure motif was identified in the assembled fibres.

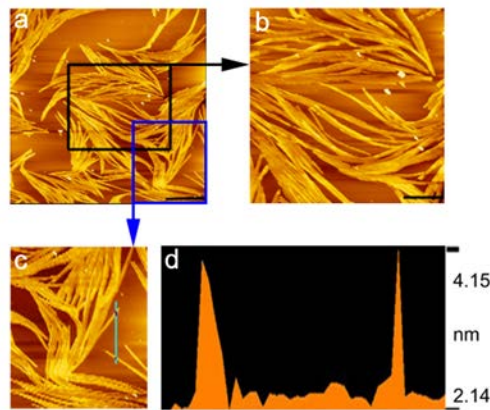


Figure 1:19 – AFM height image of peptides deposited on mica (a, x-scale = 2  $\mu\text{m}$ ). (b, c) Higher magnification of (a) (x-scale = 1  $\mu\text{m}$ ). (d) Line profile through the directional fibres as noted in (c), indicating a height of approximately 2.1 nm. Adapted from [217].

Kogan *et al.* [218] investigated fibre formation of peptides based on the maize storage protein,  $\gamma$ -zein. The valine, histidine, leucine, and proline sequence (VHLPPP) resulted in PPII helices, which then assembled into long nanorods

when placed on a hydrophobic surface. The self-assembly process involved micellar aggregation in aqueous solution as confirmed by X-ray scattering and TEM [219]. Unfortunately, the authors did not study the effect of the wettability of the underlying substrate surface.

Synthesized peptide sequences are the first step to designer biomaterials. Arguably, an important next step is the design of novel peptide-based molecules. A class of highly branched macromolecules, called dendrimers, is one way of combining the biological relevance of amino acids and the tunability of synthetic chemistry [206], [219]. Dendrimers are of particular interest due to the definition of functional motifs on the surface combined with tunability of mass and size in a monodisperse manner [220], [221].

Haridas *et al.* [222] synthesized lysine-based peptide dendrons and dendrimers and studied their assembly into fibres and gels by means of AFM. The symmetrical 2<sup>nd</sup> and 3<sup>rd</sup> generation dendrons formed vesicles in organic solution, which coalesced into a dense network of fibres upon addition of a non-solvent, persisting in aqueous buffer. Self-assembling diacetylene-core dendrimers were also prepared which could be crosslinked under UV irradiation. The supramolecular organization of peptide-based synthetic chemicals such as dendrimers can be exploited to form fibrous hydrogels for drug delivery, tissue engineering scaffolds, biosensors, and novel biomaterials [220], [223], [224].

## *Introduction*

Biologically inspired peptide self-assemblies with a wide range of envisioned applications are constantly being developed, with the AFM being the critical tool for characterisation of the resulting nanostructures [225] such as nanobelts [226] and nanotubes [227], [228]. This review focused on the most recent or critical developments in fibre forming peptides investigated by AFM and left aside a plethora of interesting work on other structural elements.

## **1.4 Conclusions and Future Perspectives**

The AFM is a scanning probe technique, capable of ‘feeling’ the 3D topography of surfaces at the nanoscale, as well as affording information on the nanomechanical and compositional properties of a range of samples. Due to its ability to perform experiments in a physiological environment without special sample preparation, AFM is perfectly suited for biological investigations. In this review, AFM operating conditions and modes were described with particular relevance to the investigation of proteins and their aggregates. Methodologies for molecular recognition mapping using the AFM including force–volume imaging and TREC were also highlighted. These techniques have strong potential for nanoscale compositional analysis of biological samples.

In the second part of the review, recent and key examples of using AFM for the characterisation of amyloid fibres were highlighted. The AFM is able to structurally characterise the polymorphisms of fibres, indicating potential pathways of aggregation. In concert with techniques such as fluorescence microscopy, EM, and spectroscopic tools such as CD spectroscopy, the basic mechanisms of aggregation are being elucidated. Time–lapse AFM can be used to investigate kinetics of fibre growth, and the effects of environmental conditions, seeding, and choice of substrate surface can be parsed out. Oligomers have been identified as an integral part of amyloidosis, potentially forming the cytotoxic species of diseases such as Alzheimer’s and Parkinson’s.

## *Introduction*

TREC was shown to be an effective molecular recognition imaging technique on cells for detection of fibres in physiological environments.

Research on synthetic fibre-forming peptides where the AFM underpinned the investigation into the structural properties of self-assembling fibres and fibre networks were subsequently reviewed. Peptide self-assembly was seen to occur for  $\beta$ -sheet,  $\alpha$ -helix and PPII secondary structures, and peptide fibres used as scaffolds for tissue engineering and as drug delivery vehicles. Unique morphologies and self-assembly mechanisms were designed and AFM used as the main tool to explore the resulting structures.

In terms of future perspectives, it is clear that the AFM based investigation of fibre-forming proteins has key applications in clinical screening, drug optimisation and drug discovery, particularly where the morphological and toxicological characterization of amyloid aggregates can be used to identify therapeutic targets, to investigate the influence of environmental factors on amyloid aggregation, and to study the efficacy of therapeutic drugs designed to disrupt aggregates. At the same time, AFM analysis underpins the design of novel peptide-based fibre forming molecules for applications in tissue engineering scaffolds and drug delivery.

The potential of AFM-based antibody-recognition imaging has thus far been underutilised, and the use of this high-resolution technology for discovering the pathogenesis of protein aggregation diseases such as Alzheimer's and PEX syndrome has significant potential. Further advances in AFM technology including high speed scanners or high throughput AFM have not been

## *Introduction*

reviewed here, but these advances will no doubt have a bearing on the implementation of molecular recognition imaging.

In summary, the AFM is an invaluable asset to the life scientist interested in the studying the fascinating phenomenon of protein aggregation.

## Chapter 2

---

### **Characterisation of Organogels Formed by Peptide–Based Dendrons and Dendrimers**

This work forms the basis of the peer–reviewed publication:

V. Haridas, Y. Sharma, R. Creasey, S. Sahu, C. T. Gibson, and N. H. Voelcker,  
‘Gelation and topochemical polymerization of peptide dendrimers’, *New Journal of Chemistry*, **2011**, 35 / 2, 303 – 309.

## **2.1 Summary**

The push for synthetic molecules and materials with functional properties has been increasing since the first plastics in the 1850s. The disciplines of organic chemistry, materials sciences and biology have become amalgamated in the pursuit of novel classes of molecules for biological application. In this chapter, a new class of peptide-based dendrons and dendrimers is presented, adding to the structural repertoire available for synthetic chemists interested in peptide-based structures.

Organogelation of lysine-based dendrons is shown to be via vesicle fusion; however, this does not result in hollow nanotubes as seen previously. Therefore, the gelation pathways presented are unique to the best of my knowledge. The vesicles observed by AFM, and confirmed as hollow by TEM, are relatively monodisperse, primarily occurring at 100 nm. The organogels formed by the lysine-based dendrons and dendrimers presented are a dense network of nanofibres, as seen by AFM and SEM.

The diacetylene moieties incorporated into the lysine-based dendrimers were crosslinked using photopolymerisation. Polydiacetylene (PDA) formation was seen following UV irradiation, confirmed by colour change and tighter-packing of fibres in AFM. Fluorescence microscopy and Raman microspectroscopy were also used to validate PDA formation.

*Characterisation of Organogels Formed by Peptide-Based Dendrons and Dendrimers*

Lithography was possible utilising a UV mask, leading to potential applications for these organogels primarily in patterned biomaterials for cell culture arrays, stem cell differentiation, or tissue engineering scaffolds. Further applications such as drug delivery agents are also discussed.

## **2.2 Introduction**

The design of new building blocks with defined and robust connectivities is a formidable challenge, which relies heavily on an in-depth understanding of structure–activity relationships. Self-assembly of carefully designed molecular building blocks into complex functional architectures has enabled the discovery of new materials with programmable properties [229]. Hence, dendrimers have become an exciting tool for materials scientists working across the disciplines of organic chemistry, surface science and biology [230].

The word dendrimer comes from the Greek word for ‘tree’ (*δένδρον*, pronounced ‘*dendron*’), and ‘unit’ (*meros*) [231]. Dendrimers are a highly branching polymer architecture, first described in 1978 by Buhleier *et al.* [232]. A dendrimer consists of a focal point, or ‘core’, from which repeating chemical units expand outwards in ‘generations’. The final generation of chemicals is the ‘outer’ shell, containing the terminal functionality. The intermediate generations, or ‘inner’ shell, control the host–guest properties of the dendrimer. The result is a spherical branched structure as seen in Figure 2:1. Also shown in Figure 2:1 are two basic synthetic pathways for dendrimer formation; the divergent pathway (used by Buhleier *et al.* [232]) and the convergent pathway (first used by Hawker *et al.* [233]).

*Characterisation of Organogels Formed by Peptide-Based Dendrons and Dendrimers*

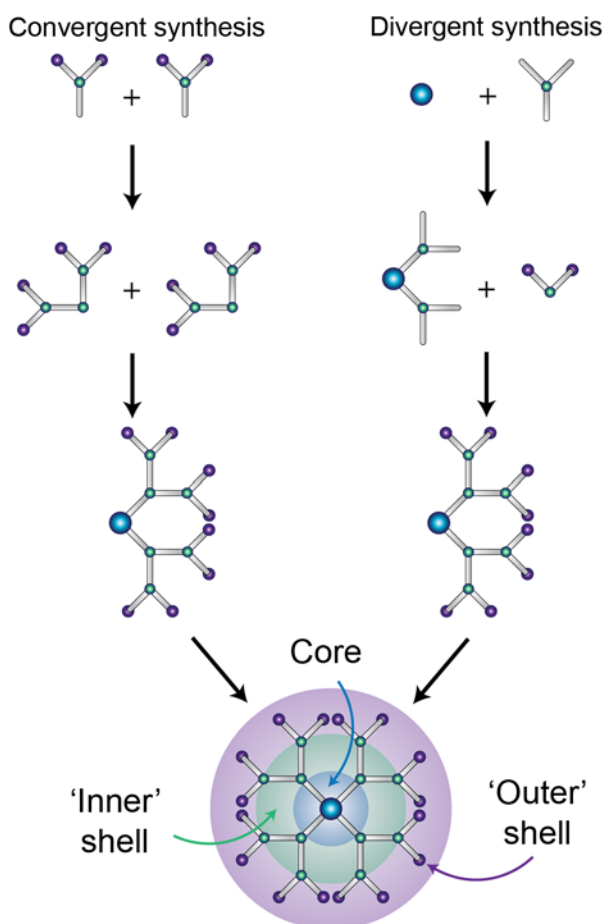


Figure 2:1 – Basic schematic of synthetic pathways leading to creation of a dendrimer with a (blue) core, (green) ‘inner’ shell and (purple) ‘outer’ shell.

The convergent synthesis of dendrimers actually begins with what will be the outer shell. Functional groups are linked together to form dendron ‘wedges’ until the desired number of generations are incorporated, when a suitable core can be used to converge the dendrons into a complete dendrimer.

As the name suggests, divergent synthesis begins at the core, and each functional group is added in steps so that the generations diverge from the core. Due to the exponential increase of functional groups, the growth of high generation dendrimers increases deletions and defects in the final product. These defective dendrimers are of similar molecular mass to the desired product, and are therefore difficult to purify. Hence, while divergent synthesis

### *Characterisation of Organogels Formed by Peptide-Based Dendrons and Dendrimers*

is capable of producing larger molecular mass dendrimers, convergent synthesis results in dendrimer products that are easier to purify from synthesis side products, as defective dendrons will have significantly altered molecular mass. Furthermore, the introduction of multiple functional groups onto the outer shell is possible by combining alternate dendrons in the final convergence.

There is a current push in research into producing dendrimers of high purity, high molecular mass and high yield – hence a number of synthetic pathways that differ slightly from the basic pathways described above exist, such as ‘double exponential’ and ‘mixed growth’ [230], [234–237]. For example, Haridas *et al.* [238] recently combined convergent synthesis with ‘click’ chemistry to create dendrimers with yield 65 – 92% and high purity. Click chemistry involves carbon–heteroatom bonds, in this case using 1,3–dipolar cycloaddition, and allows for fast and reliable modular reactions [239]. The chemoselectivity and versatility of combining these methods allowed the synthesis of a variety of peptide– and carbohydrate–based functional dendrimers.

Due to the highly controlled synthetic pathway of dendrimers, the supramolecular properties of the final molecule can be finely tuned by altering the core, inner shell and outer shell functional groups. The molecular weight is determined by the number of generations. Dendrimers have found a variety of applications, from chemical sensing, utilising the functional specificity of the outer shell, to drug delivery utilising the host–guest capacity of the inner shell

[234], [235], [240]. Furthermore, dendrimers in the nanometre size range are able to pass the biological barriers such as the blood–brain barrier, and are therefore ideal candidates for organ–targeted drugs [241].

In order to be used in a biomedical application, dendrimers must be biocompatible. By incorporating amino acids into the dendrimer structure, the functionality of amino acids combined with the multivalency of dendrimers can be exploited in a biological setting [242]. For example, peptide–based gels are of interest for use as synthetic matrices in tissue engineering, as proliferating cell cultures can be encapsulated into the gel, creating a 3D cell scaffold [215], [243]. Synthetic matrices are also useful for studying the differentiation of stem cells for tissue engineering applications [244], and patterned biomaterials are of particular interest in high–throughput screening of cell culture assays [245]. Self–assembling nanostructures incorporating peptides and crosslinkable moieties also find applications as biosensors, for peptides, toxins, bacteria and virus analytes, to name a few [246–249].

In this chapter, the characterisation of a new class of peptide dendrons and dendrimers, based on left–handed lysine, and their gel forming properties are reported. These molecules display a unique vesicle–driven organogelation. Furthermore, the crosslinking of diacetylene–based dendrimers in the gel state produces strongly fluorescent PDAs. As AFM is an ideal technique for nanoscale characterisation, it was employed to analyse both the dendrimers in solution, and follow the process of gelation. It was also used to compare gels before and after photopolymerisation with UV light. To best understand the

*Characterisation of Organogels Formed by Peptide-Based Dendrons and Dendrimers*

mechanism of gelation, complementary techniques were also employed such as TEM, to identify vesicles, and Confocal Raman spectroscopy and fluorescence microscopy, to confirm photopolymerisation via acetylene moieties. SEM was also used to confirm the structural features observed by AFM. These techniques have all been well established for the analysis of dendrimer supramolecular assembly [206], [250], [251]. The crosslinked gels crafted from peptide dendrimers may find practical use in various applications, including as scaffold materials in tissue engineering, cell microarrays, and for drug delivery [222].

## 2.3 Materials and Methods

### 2.3.1 Dendron and Dendrimer Synthesis

Dendrons and dendrimers were prepared by V. Haridas, Yogesh K. Sharma and Srikantu Sahu as described [222]. BocLys(Boc)-OH was reacted with propargyl amine in the presence of N-hydroxysuccinimide (NHS) and dicyclohexylcarbodiimide (DCC), yielding **2a**. The use of the benzyloxycarbonyl group (Z) as a protecting group produced **2b** (Figure 2:2).

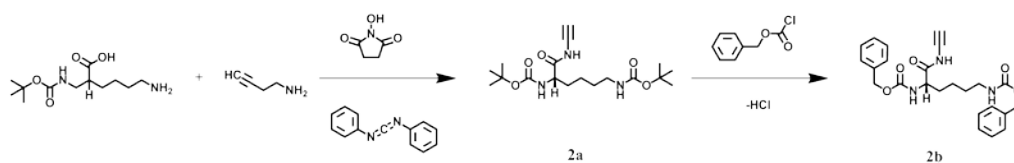


Figure 2:2 – Synthesis of dendrons 2a and 2b

The deprotection of Boc groups from **2a** using 50% TFA in CH<sub>2</sub>Cl<sub>2</sub> and a further reaction with BocLys(Boc)-OH using N-hydroxysuccinimide/DCC coupling conditions produced dendron **3**. Further deprotection using 50% TFA in CH<sub>2</sub>Cl<sub>2</sub> and coupling with BocLys(Boc)-OH resulted in the formation of dendron **4** [252]. The oxidative coupling of the dendrons with terminal alkyne units in the presence of catalytic amounts of copper(I) chloride and N,N,N',N'-tetramethylethylenediamine (TMEDA) afforded symmetrical dendrimers **5a** and **5b** in good yields from **2a** and **2b**, respectively (Figure 2:3).

## Characterisation of Organogels Formed by Peptide-Based Dendrons and Dendrimers

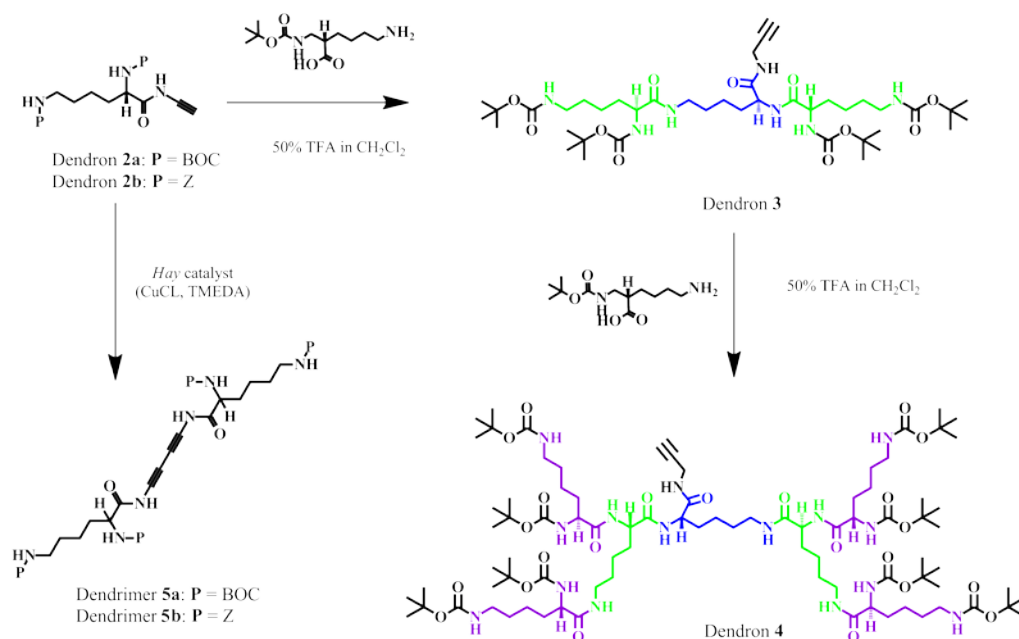


Figure 2:3 – Synthesis of dendrimers **5a** and **5b** from dendrons 2a and 2b, respectively, and synthesis of dendrons 3 and 4 from dendron 2a. In the structure of dendrons 3 and 4, the generations of left-handed lysine are highlighted in blue (first), green (second) and purple (third).

Further characterisation by NMR, MS, and differential scanning calorimetry as performed by Haridas *et al.* [222] is available in Appendix A to confirm dendron and dendrimer structure.

### 2.3.2 Preparation of Gels

The samples were dissolved in the more polar solvent and the less polar non-solvent was then added to initiate gel formation as seen in Table 2:1 below.

*Characterisation of Organogels Formed by Peptide-Based Dendrons and Dendrimers*

Table 2:1 – Gelation of dendrons (**3**, **4**) or dendrimers (**5a**, **5b**) in a variety of solvents. The symbol ✓ in the table corresponds to formation of the gel and X denotes that no gel formation in that particular solvent has taken place. This table shows only mixtures of solvents, because none of the compounds gelled in a single solvent. Further solvents not resulting in gelation are shown in Table A1 (Appendix A).

Solvent	Sample			
	<b>3</b>	<b>4</b>	<b>5a</b>	<b>5b</b>
Ethyl acetate + hexane (2:3)	✓	X	✓	X
Methanol + ethyl acetate (1:9)	X	✓	X	X
Methanol + chloroform + hexane (1:2:2)	X	X	X	✓

Gel preparation was performed as follows, and confirmed by inversion of the sample vial and observation of colour changes.

#### Gel from **3**

Compound **3** (10 mg) was dissolved in 200 µL of ethyl acetate and to this was added 300 µL hexane to form the gel.

#### Gel from **4**

Compound **4** (20 mg) was dissolved in 40 µL of methanol with heating. After cooling, 360 µL of ethyl acetate was added to form the gel.

#### Gel from **5a**

Compound **5a** (10 mg) was dissolved in 200 µL of ethyl acetate with heating. After cooling, 300 µL of hexane was added to form the gel.

#### Gel from **5b**

Compound **5b** (10 mg) was dissolved in 100 µL of methanol and to this was added 200 µL chloroform to get a clear solution. To this was added 200 µL hexane to form the gel

### **2.3.3 Characterisation of Gels**

#### **2.3.3.1 Scanning Electron Microscopy**

A 10  $\mu\text{l}$  aliquot of the sample solution was added onto a piece of cleaved mica, and allowed to dry in a laminar flowhood. The mica was then attached to an SEM stub via carbon tape and coated with  $\sim 10$  nm of platinum using sputter coater (Quorumtech K757X). SEM images were acquired using a CAMScan MX2500 SEM equipped with a tungsten filament gun operating at working distances of 13 – 20 mm and accelerating voltages of 10 – 15 kV.

#### **2.3.3.2 Transmission Electron Microscopy**

A 2  $\mu\text{l}$  aliquot of the sample solution was placed on a 400 mesh copper grid. After 1 minute, excess fluid was removed and the grid was stained with 2 % phosphotungstate in water. Excess staining solution was removed from the grid after two minutes. Samples were viewed using a JEOL 1200EX electron microscope with the assistance of Mr Kerry Gascoigne.

#### **2.3.3.3 Atomic Force Microscopy**

A 10  $\mu\text{l}$  aliquot of the sample solution was added onto a piece of cleaved mica, and allowed to dry in a laminar flowhood. AFM images were acquired using a Nanoscope IV Multimode SPM (Bruker) operating in TM. TM was used to minimise sample deformation, and reduce probe contamination due to stickiness of the sample. The cantilevers used were NSC15 probes (Mikromasch). The spring constants were between 30 – 60 N/m, while the resonant frequencies were between 310 – 365 kHz. The amplitude setpoint was maintained at 75 – 85 % of the free amplitude, to minimise sample deformation. The images were taken in air at room temperature, with the scan

### *Characterisation of Organogels Formed by Peptide-Based Dendrons and Dendrimers*

speed of 1.5 lines / sec for 512 lines with 512 points per line. A minimum of 10  $\mu\text{m}^2$  was investigated per sample, and each sample was prepared at least twice. The data acquisition was done using Nanoscope v5.30r3sr3 software, while the data analysis was done using Nanoscope v6 software. All images are flattened. Line profiles were used to observe vesicle and fibre heights, and Microsoft® Excel 2010 was used to calculate the average ( $=\text{average}(\text{data})$ ) and standard deviation ( $=\text{stdev}(\text{data})$ ) of height measurements.

#### *2.3.3.4 Photopolymerisation*

Photopolymerisation of the gels from **5a** and **5b** was done under an ultraviolet lamp (Omnicure S1000). **5a** and **5b** were irradiated at 100 W for up to 15 minutes. A colour change from clear/white to pink/red was observed after UV exposure. Longer exposures and increased power did not significantly increase observed colour change, therefore it is assumed photopolymerisation was mostly completed in this time.

#### *2.3.3.5 Fluorescence Microscopy*

A 10  $\mu\text{l}$  aliquot of the sample solution was added onto a clean coverslip, and allowed to dry in a laminar flowhood. Fluorescence images were collected with a Laborlux D fluorescence microscope (Leitz) using filter No 1 (band pass excitation (450 – 490 nm) and 515 nm long pass cut-off emission filters) at 4x objective with an exposure time of 1 s.

#### *2.3.3.6 Confocal Raman Spectroscopy*

A 10  $\mu\text{l}$  aliquot of the sample solution was added onto clean silicon, and allowed to dry in a laminar flowhood. Raman spectra were collected with a

### *Characterisation of Organogels Formed by Peptide-Based Dendrons and Dendrimers*

Confocal Raman Microscope alpha300 R (WiTEC) using a 40x (Numerical Aperture 0.6) and 532 nm laser (Elaser = 2.33 eV) operating up to a possible maximum of approximately 60 mW with the assistance of Dr. Chris Gibson. Raman data was collected by the WiTEC Control software and analysed in the WiTEC Project software, with the surface perpendicular to the excitation source. Standalone spectra were collected using integration times of between 3 to 6 s with 3 accumulations per spectra. The Raman data presented has had cosmic rays removed but no other data processing (e.g. background subtraction, averaging) has been performed.

#### *2.3.3.7 Dynamic Light Scattering*

The sample solution (1 mL) was placed into a 1 mL optically transparent cuvette (Malvern, USA). DLS measurements were performed on a Malvern HPPS (Malvern Instruments, UK) high performance particle sizer at 25°C with the assistance of Professor V Haridas. Software Malvern HTTS version 3.32 was used for data collection, with data exported to Microsoft® Excel 2010 for analysis.

## 2.4 Results & Discussion

### 2.4.1 Characterisation of Organogel Formation from Dendrons

The dendron samples were first dissolved in an appropriate solvent (ethyl acetate and methanol for **3** and **4**, respectively). They were then added to an ultraflat substrate such as mica and imaged under the AFM. No fibres were yet observed, however ‘spots’ of varying sizes were seen (Figure 2:4).

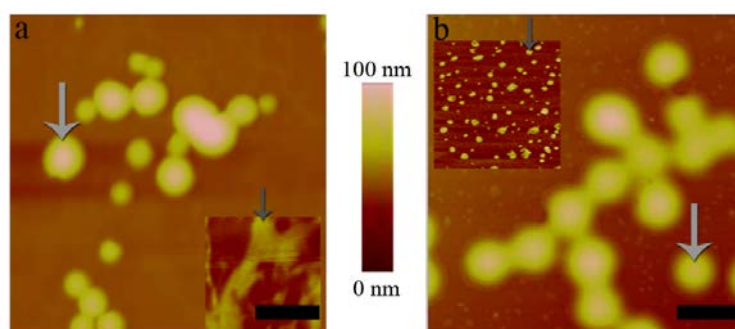


Figure 2:4 – AFM height images in TM of non-gelled sample deposited on mica. (a) Dendron 4 deposited from a solution in methanol (z-scale = 100 nm), with an inset area of higher contrast (z-scale = 7 nm) to highlight dendron ‘islands’. (b) Dendron 3 deposited from a solution in ethyl acetate (z-scale = 100 nm), with an inset area of higher contrast (z-scale = 8 nm) to highlight small spots of dendrons. Light grey arrows show large spots, dark grey arrows show small spots / ‘islands’ of dendrons. X-scale bars = 1  $\mu$ m.

For dendron **3**, smaller spots with height  $3.8 \pm 1.5$  nm, and larger spots with  $39.3 \pm 5.8$  nm heights were observed. Dendron **4** also had large spots with height  $30.1 \pm 13.9$  nm, but had background ‘islands’ around 2.5 nm height instead of smaller spots. Height measurements were used to avoid tip convolution artefacts which are common in AFM of nanoparticles [253]. The smaller spots or ‘islands’ may represent small non-vesicle formations of dendrons. The width of the large spots observed by AFM is  $531 \pm 211$  nm ( $n = 12$ ) and  $329 \pm 215$  nm ( $n = 45$ ) for sample **3** and **4**, respectively, leading to discoid shapes. These flattening effects have been described for AFM imaging of vesicles [254–256] and dendrimers [257]. DLS of the dissolved dendrons

*Characterisation of Organogels Formed by Peptide-Based Dendrons and Dendrimers*

showed nanoparticles between 100 – 300 nm in diameter. These particles seen by DLS and the large discoids seen by AFM are hypothesised to be vesicles, since the discoids may represent a spherical particle with a hollow interior, flattened due to the drying and imaging process by AFM.

Electron microscopy was used to further investigate these potential vesicles, as AFM is unable to determine if the interior of the particles is hollow. In Figure 2:5 b and a, TEM of dissolved dendrons **3** and **4**, respectively, showed circular formations. The uranyl acetate stain is visible in the centre and around the outside of the circles, indicating an interior and exterior component, strongly suggesting that the aggregates are indeed vesicles.

*Characterisation of Organogels Formed by Peptide-Based Dendrons and Dendrimers*

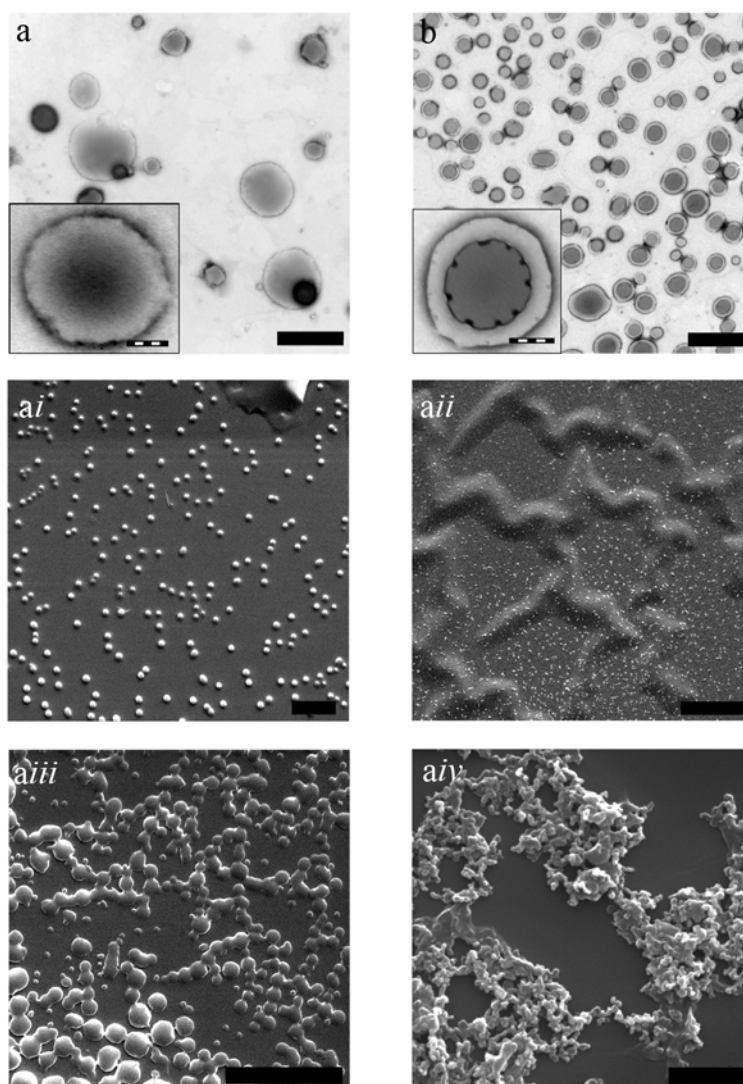


Figure 2:5 – EM micrographs of vesicles from dendrons **3** and **4**.

(a) TEM image of dendron **4** deposited from a solution in methanol onto a copper TEM grid (scale bar 1  $\mu\text{m}$ ), with an inset of a vesicle at higher magnification (scale bar 100 nm). (b) TEM image of dendron **3** deposited from a solution in ethyl acetate onto a copper TEM grid (scale bar 2  $\mu\text{m}$ ), with an inset of a vesicle at higher magnification (scale bar 300 nm). *ai* – *iv* SEM images of dendron **4** (*i*) deposited from a solution in methanol onto mica and coated in 10 nm platinum at 85  $\mu\text{g/mL}$  (scale bar 10  $\mu\text{m}$ ) and (*ii*) 4 mg/mL (scale bar 10  $\mu\text{m}$ ), followed by addition of (*iii*) 10  $\mu\text{L}$  (scale bar 15  $\mu\text{m}$ ) and (*iv*) 100  $\mu\text{L}$  (scale bar 3  $\mu\text{m}$ ) ethyl acetate to partially form the gel.

SEM was also applied to confirm the spherical nature of dendrons prior to gelation. SEM also showed spherical formations for dendron **4** at a low concentration (85  $\mu\text{g/mL}$ , Figure 2:5 *ai*), which appeared to join at higher concentrations (4 mg/mL, Figure 2:5 *aii*). After addition of a minimal amount of the precipitating non-solvent, SEM images of structures formed from

*Characterisation of Organogels Formed by Peptide-Based Dendrons and Dendrimers*

dendron **4** showed ribbons of several microns in length (Figure 2:5 *aiii*). These are larger than the vesicles observed in (*i*) and (*ii*) in width, and most likely represent a fusion of the vesicles during gel formation. These results confirm the spherical particles observed in AFM are representative of the entire sample surface, and provide evidence for vesicle fusion during the gelation process.

The dendrons self-assembled into a dense 3-dimensional network, trapping the non-solvent, to form an organogel [258]. Tube inversion was a method of testing for gelation after introduction of the less polar non-solvent, as the sample became too viscous to flow due to gravity (Figure 2:6, inset of c and f) [256]. AFM and SEM images were then acquired of the gelled substance after depositing it onto an ultraflat substrate such as mica. Dendrons **3** and **4** formed highly tangled networks of fibres, as seen in Figure 2:6 below.

*Characterisation of Organogels Formed by Peptide-Based Dendrons and Dendrimers*

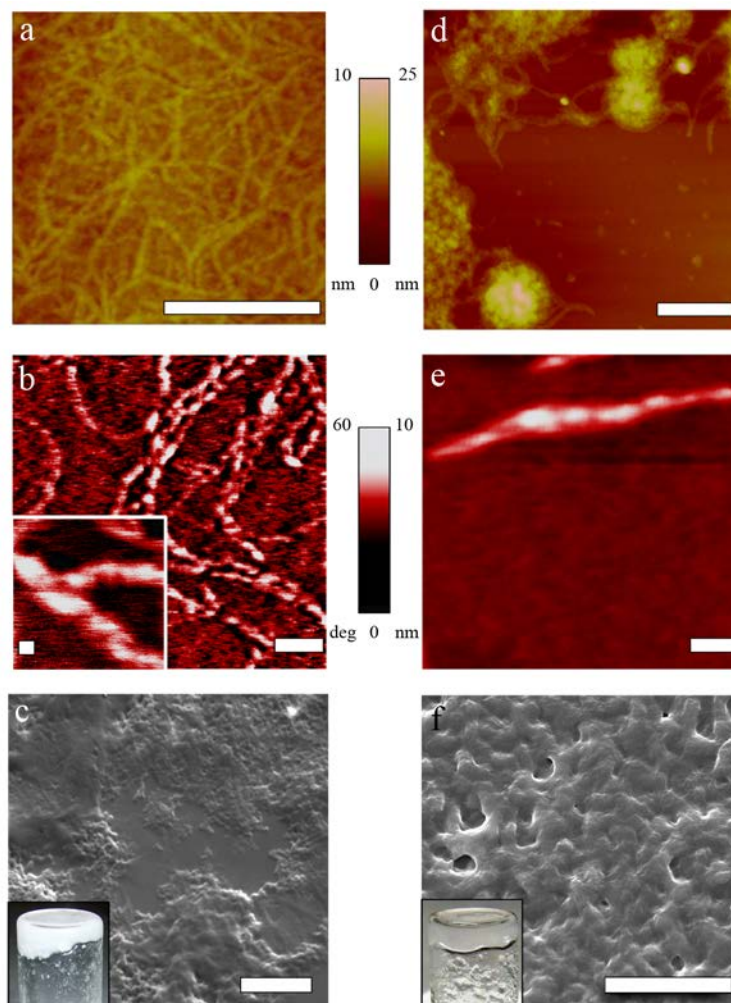


Figure 2:6 – AFM and SEM images of gels formed from (a – c) dendron **3** and (d – f) dendron **4**. (a, d) – AFM TM height images of gels on mica (scale bars 1  $\mu\text{m}$ ). (b) – AFM TM phase image showing the structure of **3** (scale bar 100 nm), with an inset at higher magnification of fibres (scale bar 10 nm). (e) – AFM TM height image showing the structure of a fibre from **4** (scale bar 100 nm). The false colour scheme in (b) and (e) is used to enhance the features of individual fibres. (c, f) – SEM images of platinum-coated gels on mica (scale bars 15  $\mu\text{m}$ ), with inset showing photographs of the gels in inverted tubes.

The fibres formed by **3** were 0.5 – 1.5 nm high and 15 – 45 nm wide. These fibres had a ‘pearls on a string’ beaded appearance, and formed long (300 nm – several microns) flexible chains (Figure 2:6b). The fibres formed by **4** on the other hand were larger at 1.5 – 3 nm high and 50 – 135 nm wide. The fibres of **4** (Figure 2:6d) are less interwoven when compared to **3** (Figure 2:6a), and the beaded architecture is less regular in distribution along the fibre (Figure 2:6e). The difference in the fibres between **3** and **4** can be attributed to the additional

molecular size and steric hindrance caused by the higher generation dendron **4**. Dendrons of increasingly higher generations did not form gels, highlighting the importance of generational control of dendrimer synthesis.

#### **2.4.2 Characterisation of Organogel Formation from Dendrimers**

The dendrimer **5a** dissolved in ethyl acetate, and dendrimer **5b** dissolved in methanol and chloroform. Addition of hexane caused the dendrimers to self-assemble into a dense 3-dimensional network, trapping the non-solvent, to form an organogel [258] similar to those seen for dendrons **3** and **4**.

The dendrimers **5a** and **5b** contained a diacetylene core moiety. This functional group is capable of crosslinking with itself under UV irradiation. Figure 2:7 shows the significant colour change observed, from white to pink/red, after UV exposure. The red colour observed after UV irradiation is an indication of formation of PDA with a non-planar backbone [259]. A non-planar backbone could arise from the structural disturbance caused by the sterically demanding lysine polymethylene chains. Furthermore, the PDA formation also occurred in the solid state at room temperature without any irradiation, albeit at a very slow rate (>5 days).

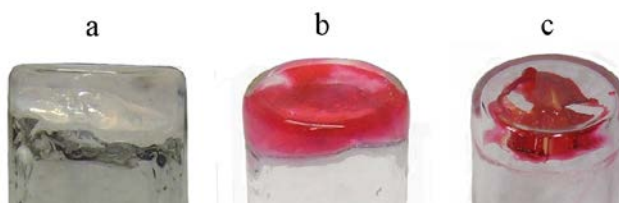


Figure 2:7 – Photographs of the gel formed by **5a** in inverted tubes (a) before UV irradiation, (b) after 5 minutes and (c) 15 minutes of irradiation with an Hg Lamp at 100 W power and 15 cm distance.

*Characterisation of Organogels Formed by Peptide-Based Dendrons and Dendrimers*

A further observation was the ‘shrinking’ of the gel after UV exposure, presumably due to molecular reorientation leading to tighter packing of the gel, and expulsion of trapped solvent molecules. As seen in Figure 2:8 (b and d), the fibres of dendrimers **5a** and **5b** became more tightly packed and ordered than the gels prior to UV exposure (Figure 2:8 a and c). **5a** appeared to be a denser gel than **5b**, observed by both AFM and visual inspection of the gels. This can be attributed to  $\pi$ - $\pi$  interactions from the Z groups, facilitating better packing in the gel state than the Boc-protected **5b**. In support of this hypothesis, the gel transition temperature ( $T_g$ , 59°C) of **5b** was higher than that of **5a** ( $T_g$ , 53°C) as measured by differential scanning calorimetry.

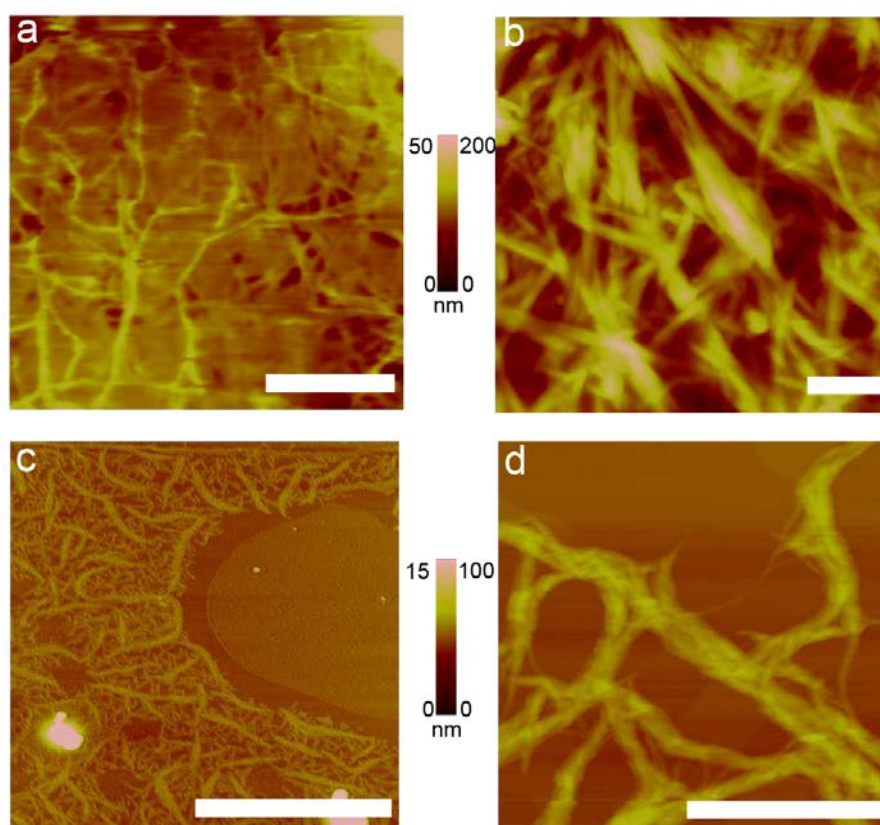


Figure 2:8 – AFM height images in TM of (a) a gel of **5a** and (c) a gel of **5b**, and (b, d) gels after irradiation with an Hg Lamp at 100 W power and 15 cm distance, respectively. Scale bars = 1  $\mu$ m.

*Characterisation of Organogels Formed by Peptide-Based Dendrons and Dendrimers*

The average distance required between acetylene moieties for polymerisation to occur is about 4.9 Å [260]. Given the tight-packed nature of the fibres, it is quite likely that crosslinking via the acetylene groups had occurred. To confirm this, fluorescence and Confocal Raman spectroscopy were performed. There was a significant increase of fluorescence in the gel state after UV exposure for **5b**, and a less significant increase for **5a**, as seen in Figure 2:9. This is consistent with aggregation-induced fluorescence phenomena [261], [262].

*Characterisation of Organogels Formed by Peptide-Based Dendrons and Dendrimers*

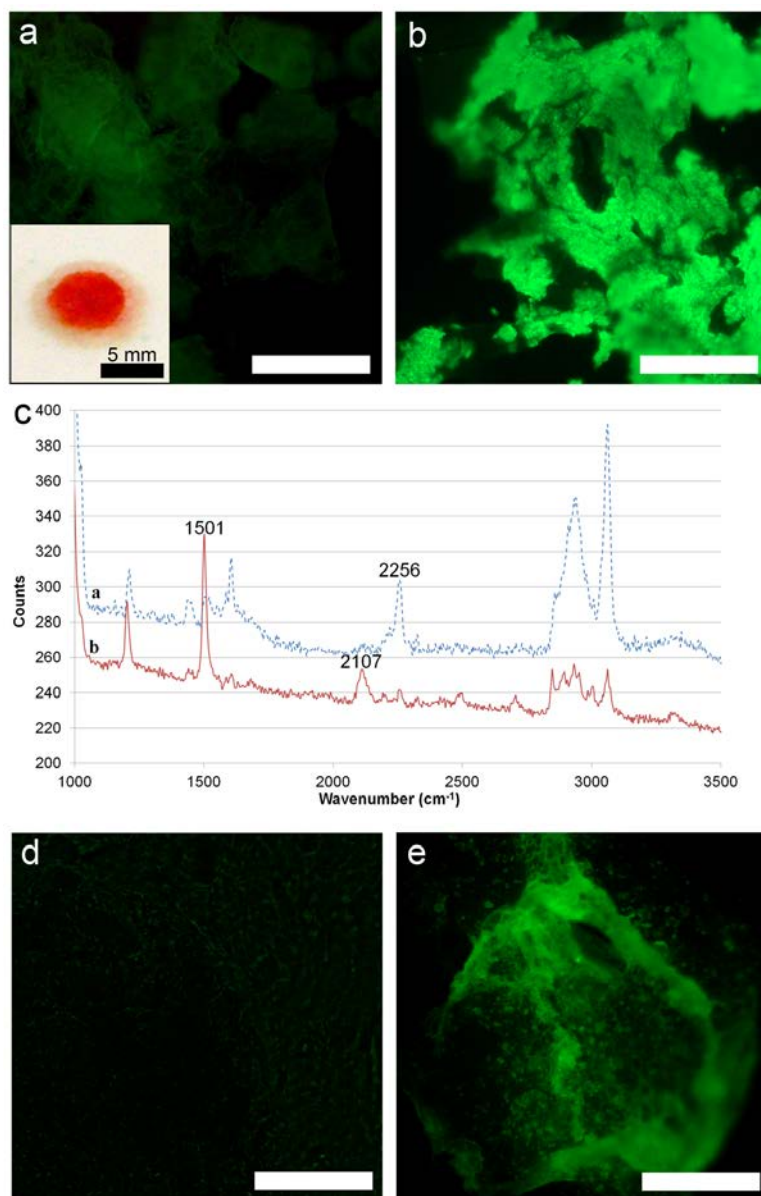


Figure 2:9 – Fluorescence microscopy images of the gels **5a** and **5b**, and the Raman spectra of **5b**, before and after UV irradiation. Fluorescence of **5b** before (a) and after (b) UV irradiation.

The inset in (a) shows a photograph of the gel from **5b** irradiated through a mask with a circular aperture. (c) Raman spectra of the gel from **5b** (a; dotted line) before UV irradiation and (b; solid line) after UV irradiation. (d and e): Fluorescence microscopy images of the gel from **5a** before and after UV irradiation, respectively. Scale bars = 50  $\mu\text{m}$ . The samples were deposited on silicon and dried before recording. Irradiation was done with an Hg Lamp at 100 W power and 15 cm distance. Fluorescence filter band pass excitation (450 – 490 nm) and 515 nm long pass cut-off emission.

Finally, the Raman spectra showed a band at  $2256\text{ cm}^{-1}$  (Figure 2:9c) before UV irradiation, corresponding to the stretching vibration of carbon-carbon triple bonds of the diacetylene group. This band was significantly reduced in intensity in the Raman spectrum acquired after UV irradiation, and a new

absorption band at  $2107\text{ cm}^{-1}$  assigned to the stretching vibration of the carbon-carbon triple bonds of the PDA chain appeared. Furthermore, a C=C vibration at  $1501\text{ cm}^{-1}$  was evident, as has been observed in the literature [263], [264]. These changes in the fluorescence images and Raman spectra for **5b** support my interpretation of photopolymerisation of the acetylene groups. Using UV irradiation through a mask, it is conceivable that this gel could be patterned into sections of crosslinked and non-crosslinked molecules. The inset of Figure 2:9a shows the gel after UV exposure through a circular aperture, resulting in a masked pattern. Nanolithography is a technique utilising spatial control of surfaces at the nanoscale. Conceivably, the dendron gels formed herein could be subjected to nanoscale masks, resulting in nanopatterning of the surface. Nanolithography has been utilised for chemical patterning of microarrays [220], [244], [265], for the localisation of cells or other biomolecules on a substrate. It has also been utilised for peptide amphiphiles containing a photocrosslinkable diacetylene group by Mata *et al.* [266], to study the effects of substrate topography on mesenchymal stem cell culture morphology and differentiation. However, gelation required a long exposure to a harsh basic environment, and the lithography used did not utilise the potential for altering the chemical structure of the surface simultaneously. For example, by masking areas of gel against UV irradiation, the free acetylene groups are available for further click reactions, or can be deprotected for aldehyde reactions. Given the potential for stem cells to be used in regenerative therapies [244], further investigations into material-based control of cell cultures is highly relevant using organogels such as the ones presented here. In particular, the use of dendrimers **5a** or **5b** for UV lithography-based biomaterials presents

*Characterisation of Organogels Formed by Peptide-Based Dendrons and Dendrimers*

a desirable substrate for cell–substrate investigations. Although dendrimer **5b** presented a stronger change in fluorescence and colour following UV irradiation, **5a** is in fact desirable for cell attachment and growth due to the Boc lysine functionality. Following polymerisation, PDA can be washed in 25% TFA in dichloromethane to deprotect the Boc groups for cell growth studies. Such experiments may be utilised for future studies into biomaterial applications.

## **2.5 Conclusions and Future Perspectives**

Organogelation of left-handed lysine-based dendrons was demonstrated, occurring via a vesicle fusion aggregation pathway. The vesicles were observed by AFM, and confirmed as hollow by TEM and DLS. These peptide-based dendrons and dendrimers displayed unique and tuneable gelation properties, forming a dense network of nanofibres, upon addition of a non-solvent. The nanofibres were observed by AFM and SEM, displaying different structural properties based on the number of generations included in the dendron. The diacetylene moieties incorporated into the lysine-based dendrimers were photocrosslinkable using UV irradiation, resulting in PDA formation between the gel fibres. The tighter-packing of fibres was observed using AFM, and formation of PDA was confirmed by colour change, fluorescence microscopy and Raman spectroscopy. The structural repertoire has been expanded by introducing covalent crosslinks into diacetylene-core peptide dendrimers by using UV photopolymerisation.

Lithography was applied using a photomask, leading to gels with distinctly coloured regions, representing crosslinked PDA organogel. A range of potential uses exist for such peptide dendrimer gels, for example as a biomaterial in stem cell differentiation studies utilising UV nanolithography of gels **5a** and **5b**. Further investigation into the host-guest capabilities of dendrons **3** and **4** may find uses in drug delivery, as a target analyte and therapeutic drug may be covalently bound to the different functional groups.

## Chapter 3

---

### **Characterisation of Fibres Formed by Fungal Proteins and Peptides**

This work forms the basis of the following publication:

R. G. Creasey, N. H. Voelcker and C. J. Schultz, 'Investigation of self-assembling P and G-rich recombinant proteins and peptides inspired by proteins from a symbiotic fungus using atomic force microscopy and circular dichroism spectroscopy', *Biochimica Biophysica Acta*, **2012**, 1824 / 5, 711 - 722.

### **3.1 Summary**

Fibre-forming proteins and peptides are being scrutinised as a promising source of building blocks for new nanomaterials. Arabinogalactan-like (AGL) proteins expressed at the symbiotic interface between plant roots and arbuscular mycorrhizal fungi have novel sequences, hypothesized to form polyprolineII (PPII) helix structures. The functional nature of these proteins is unknown but they may form functional structures for the establishment and maintenance of fungal hyphae. Here we show that recombinant AGL1 (rAGL1) and recombinant AGL3 (rAGL3) are extended proteins based upon secondary structural characteristics determined by electronic circular dichroism (CD) spectroscopy and can self-assemble into fibres and microtubes as observed by atomic force microscopy (AFM) and scanning electron microscopy (SEM). CD spectroscopy results suggest that the synthetic peptides contain significant amounts of extended PPII helices and that these structures are influenced by ionic strength and, at least in one case, by concentration. Point mutations of a single residue of the repeat region of AGL3 resulted in altered secondary structures. Self-assembly of these repeats was observed by means of AFM and optical microscopy. Peptide (APADGK)<sub>6</sub> forms structures with similar morphology to rAGL1 suggesting that these repeats are crucial for the morphology of rAGL1 fibres. These novel self-assembling sequences may find applications as precursors for bioinspired nanomaterials.

### **3.2 Introduction**

Self-assembling molecules in nature are responsible for a variety of important biological functions. The extracellular matrix of mammalian cells consists primarily of proteins, glycoproteins and proteoglycans, with fibre-forming proteins such as elastin providing elasticity [267], [268]. The underlying membrane of skin and other basement membranes are composed of a range of fibrous proteins which crosslink to form a dense network, capable of supporting the structure of an organ [269]. Other proteinaceous fibres with important biological functions and structural properties include spider silk [270], wool and hair [271]. By understanding the conditions of protein self-assembly and in particular fibre formation, fibres for specific purposes can be synthesised in a controlled manner. These proteins may reveal useful blueprints for innovative nanomaterials, which may find a variety of uses in medical devices, sensors, implants, microelectronics, and other areas [203], [272], [273].

Structural proteins in fungi and plants are less common, and represent an additional resource of new nanomaterials. The extracellular matrices of fungi and plants are composed predominantly of polysaccharides, rather than proteins. Fungal cell wall polysaccharides include glucans, chitin or chitosan and mannans [274] with a minor amount of protein. Plant cell walls are made from a scaffold of cellulose embedded in a hydrated matrix of noncellulosic polysaccharides with a small amount (<10%) of protein and glycoprotein [275], [276]. Plant extensins are self-assembling glycoproteins that are critical

for scaffold formation during the synthesis of new cell wall material during cell division [277]. A recurring theme found in self-assembling proteins from most organisms is the high proportion of glycine and/or proline [278], or hydroxyproline residues [277], [279], and these residues are frequently found as tandem repeats.

Recently, three genes encoding proline and glycine-rich proteins, AGL1, AGL2 and AGL3, were identified from the arbuscular mycorrhizal (AM) fungus, *Glomus intraradices* [280]. The gene products (proteins) are predicted to be extracellular, based on the presence of an ER signal sequence and a signal for the addition of a GPI-anchor [280], suggesting they could have an important structural role in the symbiosis between *G. intraradices* and most land plants. All three proteins have repeats containing proline and glycine residues (Figure 3:1a–c). The repeats found in AGL1 and AGL3, in addition to proline and glycine, are zwitterionic, containing one positively and one negatively charged amino acid residue; namely lysine and aspartic acid; they also contain alanine. The number of amino acid residues per repeat and the number and arrangement of repeats is different for AGL1 and AGL3. The repeats in AGL1 contain six residues, APADGK, present primarily in one block of eleven tandem repeats (18 repeats in total; Figure 3:1a), whereas the repeats in AGL3 contain five residues, APKDG, in a single tandem block of seven repeats (Figure 3:1c). In contrast AGL2 has with fewer defined repeats, one being GATPPA, and an absence of charged residues in the repeats (Figure 3:1b).

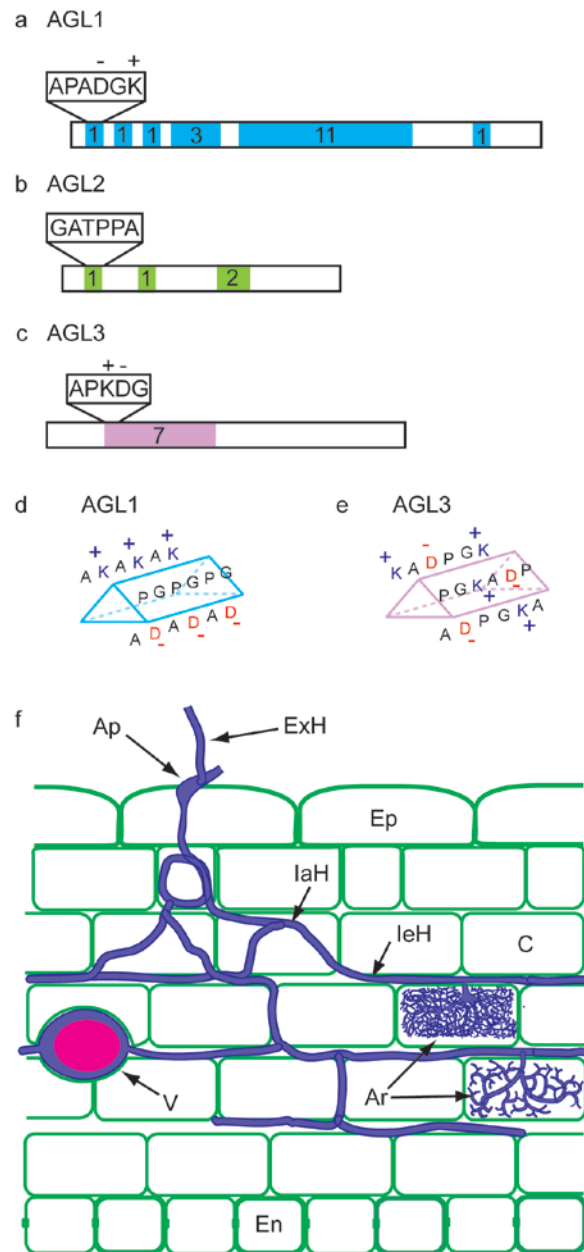


Figure 3:1 – Arbuscular mycorrhizal fungi colonization of roots, and cell wall proteins. Figure prepared by C. J. Schultz.

Schematic diagram of AGL1 (a), AGL2 (b) and AGL3 (c) proteins as predicted from gene sequences [280]. Colour boxes indicate the position (and number) of repeats in each AGL protein. The amino acid sequence (single letter code) of each repeat is indicated above the first repeat. The charge of aspartic acid (D) and lysine (K) is indicated – and + respectively.

Predicted PPII structures are represented as triangular prisms [126] (d and e) showing the different sequence and charge profile along each plane. (f) Schematic representation of a root colonized by an arbuscular mycorrhizal fungal species such as *Glomus intraradices* (*Gi*), showing diverse fungal structures including extracellular hyphae (ExH), appressoria (Ap), intracellular hyphae (IaH), intercellular hyphae (IeH) between cortical (C) cells, extensive dichotomously branched intracellular arbuscules (Ar) in cortical cells and vesicles (V). Plant epidermal (Ep) and endodermal (En) tissues are indicated. Section f is reproduced in modified form with permission from <http://mycorrhizas.info/> (version 2, Mark Brundrett, 2008).

It has been suggested that the AGL proteins have a role in the establishment and/or maintenance of one or more of the diverse fungal structures in the colonized plant root [280], based on some similarities to other naturally occurring structural proteins such as collagen and elastin, many of which can form PPII helices [281]. PPII helices are left-handed, extended helices with three amino acid residues per turn, such that the surface can be represented as a triangular prism (Figure 3:1d and e) [126].

Although the genes encoding the three AGL proteins are expressed in roots colonised with AM fungi, it is not known if the proteins are present in all of the fungal structures of the root (Figure 3:1f). Further understanding of the structural properties of AGL proteins is needed, in order to determine if they have potential to form scaffolds or other functional structures. To the best of our knowledge, there are no known natural proteins identified or characterized with the peptide sequences present in AGL1, AGL2 and AGL3. AGL1 and AGL3 are especially unique in that they contain 'rigid' proline, 'flexible' glycine, and zwitterionic repeats, although there are examples of proteins with one or more of these features [202], [213], [278], [282]. Proteins with PPII helices have been known to aggregate to form fibres [278], [283], [284], and to be important for molecular recognition [285].

If the AGL proteins AGL1 and AGL3 containing the zwitterionic repeats can form PPII helices, then they likely form distinctly different aggregates based on their different charge distribution. We postulate that AGL1 has all the positive residues along one edge, all the negative residues on a second edge, and the

third edge is uncharged and moderately hydrophobic (Figure 3:1d), whereas AGL3 has positive and negative charges on all three edges (Figure 3:1e). Therefore, aggregation of these sequences should be altered by conditions of the buffer, such as ionic strength and concentration [205], [286], [287]. We hypothesize that the two AGLs (AGL1 and AGL3) containing zwitterionic repeats and AGL2 each have unique properties and provide new opportunities both for nanomaterial design and for an improved understanding of the function of proteins involved in AM symbiosis.

### **3.3 Methods and Materials**

#### **3.3.1 Expression of Recombinant AGL Proteins in Escherichia coli**

rAGLs were expressed and purified by C. Schultz, as described in Appendix B.

#### **3.3.2 Peptide Preparation**

Peptides were synthesised by GenScript USA Inc. at >95% purity with the properties described in Table 3:1. Gene source sequences are described by Schultz and Harrison [280]. All peptides were 30 residues in length, such that long peptides of high purity could be readily obtained (based on the manufacturer's recommendations), and be similar to the lengths of the longest repeat found in AGL1 (Figure 3:1a) and AGL3 (Figure 3:1c). This resulted in peptides with six repeats based on AGL1 an AGL2 and five repeats based on AGL3. Amino acid abbreviations will be used when referring to the synthetic peptide sequences (A = alanine, P = proline, D = aspartic acid, G = glycine, K = lysine, T = threonine).

Table 3:1 – Properties of synthetic peptides.

Peptides	Abbreviation	Gene Source	Theoretical mass (Da)	MALDI mass (Da)	Charge
(APADGK) <sub>5</sub>		GiAGL1	2715.94	2715.49	0
(GATPPA) <sub>5</sub>		GiAGL2	2490.73	2490.58	0
(APKDG) <sub>6</sub>		GiAGL3	2829.05	2828.46	0
(APKAG) <sub>6</sub>	DΔA	GiAGL3	2564.99	2564.53	+6
(AAKDG) <sub>6</sub>	PΔA	GiAGL3	2672.83	2672.46	0
(APADG) <sub>6</sub>	KΔA	GiAGL3	2486.48	2486.65	-6

### **3.3.3 Characterisation of Protein and Peptide Samples**

#### **3.3.3.1 *Electronic Circular Dichroism (CD) Spectroscopy and Decomposition***

All CD data was collected and analysed by C. Schultz. The collection and deconvolution of this data is available in Appendix B, with joint discussion in 3.5.1.

#### **3.3.3.2 *Dynamic Light Scattering***

The peptide solution (100  $\mu$ L) was spun at 16,110 x g for 5 min, and the top 90  $\mu$ L of the sample was placed in a low-volume disposable cuvette (Malvern, USA) and sonicated for 15 min. DLS measurements were performed immediately following sonication, then at times of 1 d, 7 d, and 14 d after incubation at room temperature. DLS was performed on a Malvern high performance particle sizer (Malvern Instruments, UK) at 1 mg/mL of sample at 25°C. Software Malvern HTTS version 3.32 was used for data collection, with data exported to Microsoft® Excel 2010 for analysis.

#### **3.3.3.3 *Atomic Force Microscopy***

Desalted rAGLs were diluted to 100  $\mu$ g/mL in 'CD buffer' (100 mM  $(\text{NH}_4)_2\text{SO}_4$ , 10 mM  $\text{KH}_2\text{PO}_4$ ). The CD buffer was selected as one of several recommended buffers compatible with the low wavelengths needed to detect PPII helices by CD spectroscopy [129]. Protein samples were transferred onto freshly cleaved highly ordered pyrolytic graphite (HOPG) in a laminar flowhood at 150  $\mu$ g/mL and incubated for 5 min. The samples were then washed 10 times in Ultrapure MilliQ water, and dried under a gentle stream of filtered nitrogen.

Synthetic peptide samples were resuspended to a concentration of 0.3 mg/ $\mu$ L in a small volume of acetonitrile (<10  $\mu$ L), before diluting to a final concentration of 2 mg/mL (by weight) in Ultrapure MilliQ water (18.2  $\Omega$ ) such that the final concentration of acetonitrile was 0.67% (v/v). Acetonitrile was used based on the manufacturer's recommendation for peptides with zero net charge (GenScript USA). Stock peptide solutions were then further diluted to a working standard of 1 mg/mL. Two salt concentrations were used; 'low salt' (1 mM  $\text{KH}_2\text{PO}_4$ , 10 mM  $(\text{NH}_4)_2\text{SO}_4$ ) and 'high salt' (10 mM  $\text{KH}_2\text{PO}_4$ , 100mM  $(\text{NH}_4)_2\text{SO}_4$ ). Peptide samples were taken from DLS solution immediately following sonication, then after 1 d, 7 d, and 14 d of incubation at room temperature, and placed onto freshly cleaved mica in a laminar flowhood at 1 mg/mL and incubated for 5 min. The samples were then washed 4 times in MilliQ water, and dried under a gentle stream of clean nitrogen. AFM data was collected on a Bruker Multimode with controller V, software version 8.12 (Bruker, USA). TM was used for recombinant proteins, and PeakForce™ imaging mode was used for peptide samples due to an equipment upgrade. NSC-15 probes (Mikromasch, nominal spring constant 40 N/m) were used consistently. The amplitude setpoint was maintained at 75 – 85 % of the free amplitude, to minimise sample deformation when using TM. The images were taken in air at room temperature, with the scan speed of 1.5 lines / sec for 512 lines with 512 points per line. AFM image analysis was performed using Nanoscope Analysis v1.2 (Bruker, USA) offline software. All images are flattened. Line profiles were used to measure fibre heights and lengths, the 'particle analysis' function was used to observe spot heights, and Microsoft®

Excel 2010 was used to calculate the average (=average(*data*)) and standard deviation (=stdev(*data*)) of height measurements.

#### ***3.3.3.4 Scanning Electron Microscopy***

SEM data was collected on a CAMScan MX2500 SEM (Obducat, Sweden) equipped with a tungsten filament gun operating at WD 13 – 20 mm and 10 – 15 kV. Sample precipitates were transferred manually from solution and placed onto freshly cleaved HOPG, and coated in ~10 nm platinum using a Quorumtech K757X sputter coater before SEM image acquisition.

#### ***3.3.3.5 Optical Microscopy***

Optical micrographs were obtained using a Nikon Eclipse 50i microscope equipped with a Nikon Digital Sight CCD captured using NIS-Elements BR 3.2 (Nikon, USA) software. Sample precipitates were transferred manually from solution and placed onto freshly cleaved mica. The samples were then carefully washed once with MilliQ ultrapure water and allowed to dry in a laminar flowhood.

### **3.4 Results**

#### **3.4.1 Secondary Structure and Self-Assembly of Recombinant AGLs**

Recombinant proteins rAGL1 and rAGL3, that contain zwitterionic repeats, were successfully expressed and purified from *E. coli* extracts (Figure B:1a,c). However, rAGL2 was not detected in any of the eluted fractions after metal affinity chromatography (Figure B:1b), suggesting that the protein was not expressed, or was unstable, in *E. coli*. Both rAGL1 and rAGL3 migrate at a higher than expected molecular mass, which is commonly observed for proteins containing proline [288], with  $M_r$  rAGL1 ~30 kDa (expected 16.8 kDa) and  $M_r$  rAGL3 ~25 kDa (expected 13.0 kDa).

CD spectroscopy was used to determine whether rAGL1 and rAGL3 form PPII helices in aqueous solution. The spectra for both rAGL1 and rAGL3 at 25°C lack a positive CD band between 217–225 nm wavelength (Figure 3:2a,b), which is a diagnostic feature of PPII helices [281], [289–291]. However, they do contain localized maxima along the negative shoulder in the range 217–225 nm, considered indicative of PPII by some researchers [281], at 223.5 nm for rAGL1 (Figure 3:2a) and 225 nm for rAGL3 (Figure 3:2b). It is well established that PPII helices can be induced at low temperatures [281], [289–291], so rAGL3 was tested after an overnight incubation at 5°C. The slight upward shift observed, even if the CD value was still negative in the range 217–225 nm, together with the concomitant reduction of the negative band is suggestive of the presence of PPII helices. rAGL1 was not tested at 5°C due to insufficient amounts of recombinant protein.

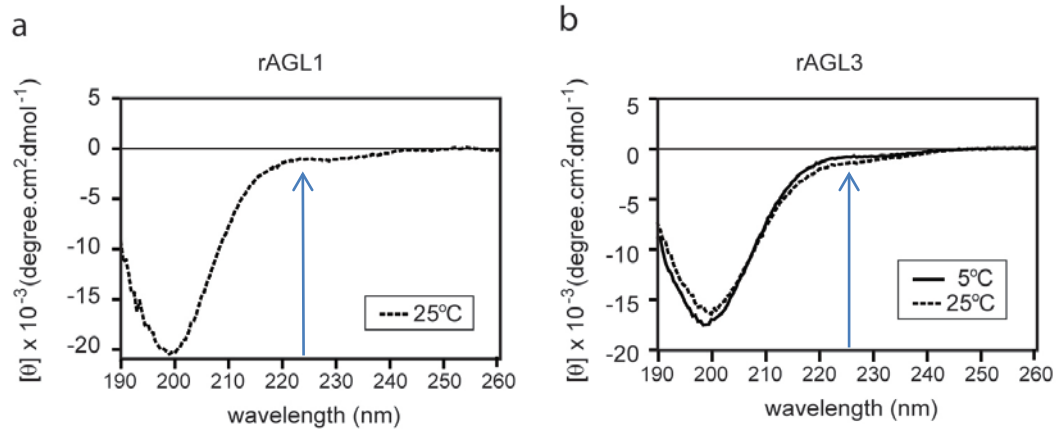


Figure 3:2 – CD of rAGL proteins.  
CD spectra of rAGL1 at 25°C (a), and rAGL3 (b) at 25°C (dashed line) and 5°C (solid line).  
Blue arrows highlight shoulder used for PPII determination. Image by C. J. Schultz.

AFM was the method of choice to observe the self-assembly of rAGL1 and rAGL3. Initially, both recombinant proteins began as unstructured spots of heights (measured on the z-axis)  $5.4 \pm 1.9$  nm and  $3.8 \pm 1.2$  nm for rAGL1 and rAGL3, respectively, as seen in Figure 3:3a and d. The diameter of these spots varied greatly ( $31.5 \pm 20.5$  and  $31.4 \pm 17.4$  nm for rAGL1 and rAGL3, respectively). However, convolution of the images due to tip broadening may have influenced diameter measurements as is commonly observed in AFM [189], [251], [292]. After one week of incubation at room temperature, thread-like structures (hereafter referred to as fibrils) were observed in both protein samples with a variety of morphologies as discerned by AFM. These were classified as rod-like, branching, anfractuous, or ‘other’, based primarily on observable structural characteristics influenced by length, height and width of fibrils.

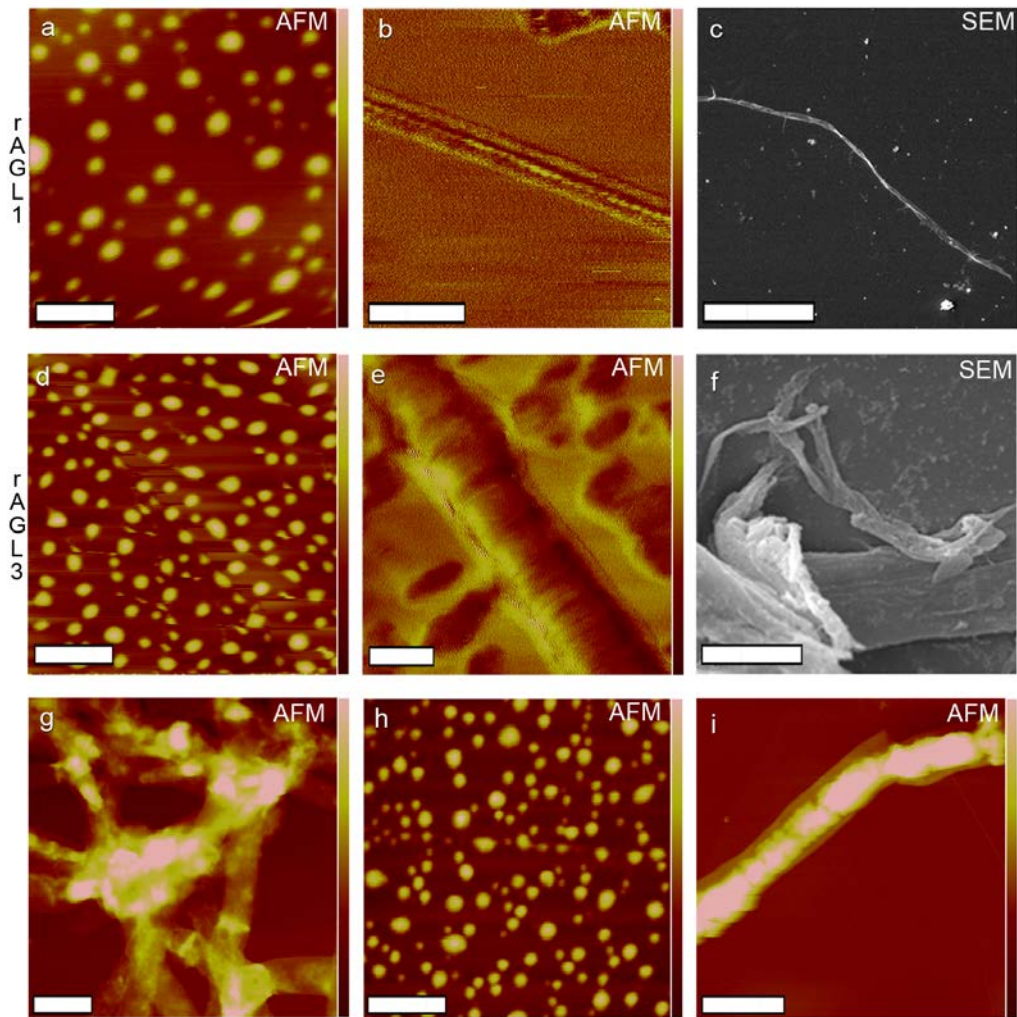


Figure 3:3 – Characterisation of rAGL protein fibre formation.

AFM images of recombinant protein rAGL1 deposited on HOPG (a) immediately following preparation (x-scale = 1  $\mu$ m, z-scale = 20 nm), (b) after 1 wk of incubation (x-scale = 50 nm, z-scale = 10 $^\circ$ ) and SEM image of rAGL1 deposited on HOPG (c) after 6 wks of incubation (x-scale = 25  $\mu$ m). AFM images of recombinant protein rAGL3 deposited on HOPG (d) immediately following preparation (x-scale = 1  $\mu$ m, z-scale = 15 nm), (e) after 1 wk of incubation (x-scale = 50 nm, z-scale = 15 $^\circ$ ) and SEM image of rAGL3 deposited on HOPG (f) after 4 wks of incubation (x-scale = 5  $\mu$ m). AFM images of recombinant protein rAGL3 deposited on HOPG (g) after 4 wks of incubation (x-scale = 2.5  $\mu$ m, z-scale = 260 nm), (h) 15 min sonication to disrupt aggregates (x-scale = 250 nm, z-scale = 7 nm) and (i) after 1 wk of incubation following sonication (x-scale = 2.5  $\mu$ m, z-scale 400 nm). The bottom portion of (a) is distorted due to hysteresis, and does not indicate lengthened features of amorphous rAGL1. Topography AFM channel images are available for comparison to b and e in Figure B:6.

Most commonly seen for rAGL1 were thin rods (n=13, Figure 3:3b) or anfractuous (n=5, data not shown) fibrils, of heights ranging from 0.3 – 80 nm, with an average height of 8.9 nm observed. The lengths of these fibrils ranged from 15 nm to 8  $\mu$ m. The thinnest fibrils had a periodic structure with spacing

of 5 nm, observed in the phase channel (Figure 3:3b), with a final aggregate morphology of large ropey fibres (Figure 3:3c). Periodicity was also observed for rAGL1 fibrils by TEM (Figure B:2) The morphologies seen for rAGL3 were commonly rods (n=9, Figure 3:3e) or ‘other’ (sheet-like, n=6, data not shown) fibrils with heights ranging from 1.4 – 43 nm, with an average height of 15.8 nm and lengths ranging from 400 nm to 5 µm. As seen in Figure 3:3e, the rod-like fibres had corrugations or bands of 0.5 – 0.75 nm in height with irregular spacing.

After 6 wks, rAGL1 began to precipitate into long ropey fibres, as seen in Figure 3:3c. In comparison, rAGL3 precipitated within a month, and produced a network of large flat fibres (Figure 3:3g), appearing much like flattened microtubules (Figure B:3). This aggregation was reversible, as after sonication for 15 min the precipitate was no longer present upon visual inspection of the solution. AFM images of the post-sonication sample showed once again unstructured spots of height 3.8 nm (Figure 3:3h), similar to those seen initially. One week following sonication, precipitates were again observed visually and imaged by AFM. The morphology of the precipitated fibres based on AFM one week after sonication were more linear and dense (Figure 3:3i) than the original fibres observed by SEM (Figure 3:3f).

#### **3.4.2 Characterization of Synthetic Peptides Based on P- and G-rich Repeats of AGL Proteins**

Although the recombinant proteins rAGL1 and rAGL3 self-assembled into fibres, the involvement of PPII helices as structural elements were not strongly

supported. To test whether the absence of clear PPII secondary structure was due to the influence of the non-repetitive regions of the AGL proteins, synthetic peptides were synthesized using the repeat regions only of the recombinant proteins highlighted in Figure 3:1a–c, as shown in Table 3:1. A further rationale to use synthetic peptides was to compare the zwitterionic repeat regions found in AGL1 (APADGK) and AGL3 (APKDG), with the neutral repeat regions found in AGL2 (GATPPA), given that expression of rAGL2 was unsuccessful (Figure B:1b).

CD spectroscopy was performed on peptide solutions in high-salt conditions. At 25°C, none of the peptides exhibited a positive CD band in the relevant range of 217–225 nm (Figure 3:4a–c).

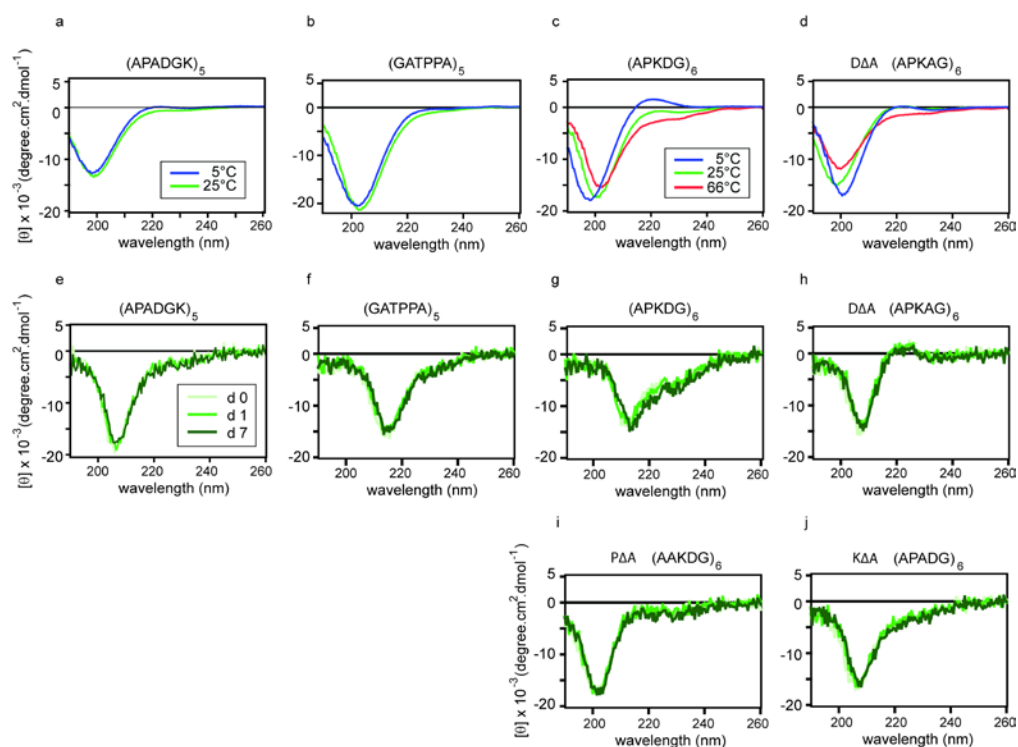


Figure 3:4 – CD spectra of synthetic peptides under different conditions.

(a–d) Peptides at 250  $\mu\text{g/mL}$  in high-salt buffer and different temperatures for (APADGK)<sub>5</sub> (a), (GATPPA)<sub>5</sub> (b), (APKDG)<sub>6</sub> (c) and DΔA (APKAG)<sub>6</sub> (d) at 66 °C (red line), 25 °C (green line) and 5 °C (blue line). (e–j) Peptides at 1 mg/mL in low-salt buffer at 25 °C (APADGK)<sub>5</sub> (e), (GATPPA)<sub>5</sub> (f), (APKDG)<sub>6</sub> (g), DΔA (APKAG)<sub>6</sub> (h), PΔA (AAKDG)<sub>6</sub> (i) and KΔA (APADG)<sub>6</sub> (j). Image by C. J. Schultz.

At 5°C, the peptide (APKDG)<sub>6</sub> had a relatively strong positive CD band at 221 nm (Figure 3:4c), the peptide (APADGK)<sub>5</sub> had a weak positive band at 223 nm (Figure 3:4a), whereas the peptide (GATPPA)<sub>5</sub> had a localized maximum at 225 nm although the ellipticity was still negative (Figure 3:4b). Decomposition of the CD spectra using LINCOMB suggests that all three peptides contain PPII structure with (APADGK)<sub>5</sub> having the least (43.8%) and (APKDG)<sub>6</sub> having the highest proportion of PPII (54.6%) (Table 3:2). Although CD decomposition programs cannot be relied upon for the actual proportions of secondary structures in native proteins, they are particularly useful in providing quantitative estimates of changes that occur with temperature and or different buffer conditions [281], [293]. The peptide (APKDG)<sub>6</sub> and a mutant form

‘DΔA’ (APKAG)<sub>6</sub> were also investigated at a higher temperature 66°C (Figure 3:4c, d, respectively). Both peptides show a loss of PPII structure, and concomitant increase in unstructured, ‘random coil’ at elevated temperatures, as expected. Polyproline and BSA were decomposed as controls (data not shown) and show a predominance of PPII and α-helix, respectively, as expected (Table 3:2).

Table 3:2 – CD deconvolution results for synthetic peptides at different temperatures and in different buffers using the LINCOMB least squares fit method [294], expressed as %. RC, random coil. Table by C. J. Schultz.

Peptide	Temp	α-helix	β-sheet	turn	PPII	RC
(APADGK) <sub>5</sub>	5°C	0	22.5	9.6	43.8	24.1
(GATPPA) <sub>5</sub>	5°C	13.6	0	0	45.3	41.1
(APKDG) <sub>6</sub>	5°C	0	17.5	9.9	54.6	18.1
	25°C	2.6	11.6	0	35.0	50.8
	66°C	8.9	9.2	1.1	29.7	51.1
DΔA, (APKAG) <sub>6</sub>	5°C	0	17.9	0	40.4	41.7
	25°C	0	14.8	8.6	37.0	39.5
	66°C	6.6	10.9	7.2	14.9	67.0
Polyproline	25°C	26.4	0	0	73.4	0
BSA	5°C	61.7	0	10.9	20.5	6.9

Low-salt conditions were tested using CD spectroscopy with the peptides at a higher concentration, conditions chosen to match optimal AFM conditions (see below). Spectra were taken at day 0, 1 d and 7 d, and were essentially unchanged for all peptides tested (Figure 3:4e-j). Several differences were observed between high-salt and low-salt that are almost certainly due to differences in peptide concentration (see 3.5.1, Secondary Structure). Surprisingly, for most peptides there was a shift in the position of the major negative band to a longer wavelength. For example (APKDG)<sub>6</sub> in high-salt at 250 µg/mL had a negative band at 199.5 nm whereas at 1 mg/mL in low-salt buffer, the negative band was observed at 211.5 nm. This apparent red shift

increased the average least squares error obtained when decomposing the CD spectra (data not shown) and this data was not used. Instead, the shape and strength of the positive band at 225 nm was used as an indicator of the relative tendency to form PPII. At high concentration and low salt, peptide (APKDG)<sub>6</sub> (Figure 3:4g) appeared more unstructured than at low concentration (and high salt) (Figure 3:4c), whereas the ‘DΔA’ (APKAG)<sub>6</sub> (Figure 3:4h) peptide appeared to have significant PPII content based on the strong positive band at 224.5 nm. The other two mutant forms were intermediate between the two extremes with ‘PΔA’ (AAKDG)<sub>6</sub> (Figure 3:4i) having more PPII structure than (APKDG)<sub>6</sub> (Figure 3:4j).

Decomposition of the CD spectra of the two peptides containing zwitterionic repeats suggests that there is approximately 20% β-sheet content. Since β-sheet structures are observed in other fibre-forming peptides involved in amyloid plaque formation [207], [295], a Thioflavin T assay was used to detect β-sheets/amyloid structures (Figure B:4). Peptides were tested at the two salt conditions. All of the peptides showed mostly low fluorescence even after 31 d, suggesting a limited tendency to form β-sheets.

In order to determine the propensity for self-assembly in the synthetic peptides and the relevant timeframe, DLS was used to monitor the samples at intermittent times. An indirect measure of self-assembly was used, that is, observation of a large (>100 nm) jump in the primary mode of particle size was considered indicative of self-assembly. The initial sizes of all the peptides was similar (1 – 3 nm) in the two salt conditions used (Table 3:3). All three

peptides showed increases in particle size, which was attributed to self-assembly. (APKDG)<sub>6</sub> grew fastest, while no significant difference was observed in the rate of growth of (APADGK)<sub>5</sub> and (GATPPA)<sub>5</sub>. For all peptides, the low-salt conditions displayed a shorter lag phase before the onset of particle growth than the high-salt condition. Little difference was observed in either particle size or aggregation time for the no-salt condition compared to the low-salt condition (data not shown). As the no-salt condition would not be biologically relevant, these samples were not studied further, or included here.

Table 3:3 – Particle size of synthetic peptides determined by DLS at two salt concentrations; high salt (100mM / 10 mM) and low salt (10mM / 1 mM). Aggregation time was determined by an increase in the particle size by more than 100 nm. Peptide concentration 1 mg/mL.

Sample	Un-aggregated peptide (nm)		Aggregation (d)	
	High salt	Low salt	High salt	Low salt
(APADGK) <sub>5</sub>	2	1	14	7
(GATPPA) <sub>5</sub>	3	3	14	7
(APKDG) <sub>6</sub>	2	2	7	1

As with the recombinant proteins, AFM was used to monitor the process of self-assembly of the synthetic peptides, however it was necessary to use mica as the peptides showed substrate-induced aggregation immediately upon adsorbance to the HOPG surface (see 3.5.2, Self-Assembly of Recombinant Proteins). All peptides were observed as small particles initially with heights  $2.1 \pm 1.9$  nm ( $n = 3,129$ ); Figure 3:5a – c and Figure 3:6a – c), which is consistent with the DLS data. The timeframes chosen for observation of samples by AFM were based on the lag phase determined from DLS for each peptide and salt condition.

In the high-salt condition, (APADGK)<sub>5</sub> fibrils of height 0.3 – 16.6 nm (average  $3.7 \pm 5.1$  nm;) and length 100 nm to 3.0  $\mu$ m were observed after incubation for 14 d at room temperature, as shown in Figure 3:5d. Fibrils were primarily rod-like (n = 12), with some anfractuous (n = 8) morphologies observed (data not shown). (GATPPA)<sub>5</sub> fibrils of height 0.9 – 23.0 nm (average  $7.1 \pm 10.7$  nm) and length 150 nm to 4.0  $\mu$ m were observed as seen in Figure 3:5e after 14 d incubation at room temperature. Some rod-like (n = 6), branched (n = 2) and ‘other’ (n = 2) morphologies were observed, however most fibrils were anfractuous (n = 10). Finally, (APKDG)<sub>6</sub> fibrils of height 5.0 – 59.7 nm (average 21.0 nm,  $\pm 18.5$  nm) and lengths 600 nm to 2.0  $\mu$ m were observed as shown in Figure 3:5f, after 7 d of incubation at room temperature. The morphologies observed were primarily rod-like (n = 17), with smaller anfractuous fibrils also present (n = 6).

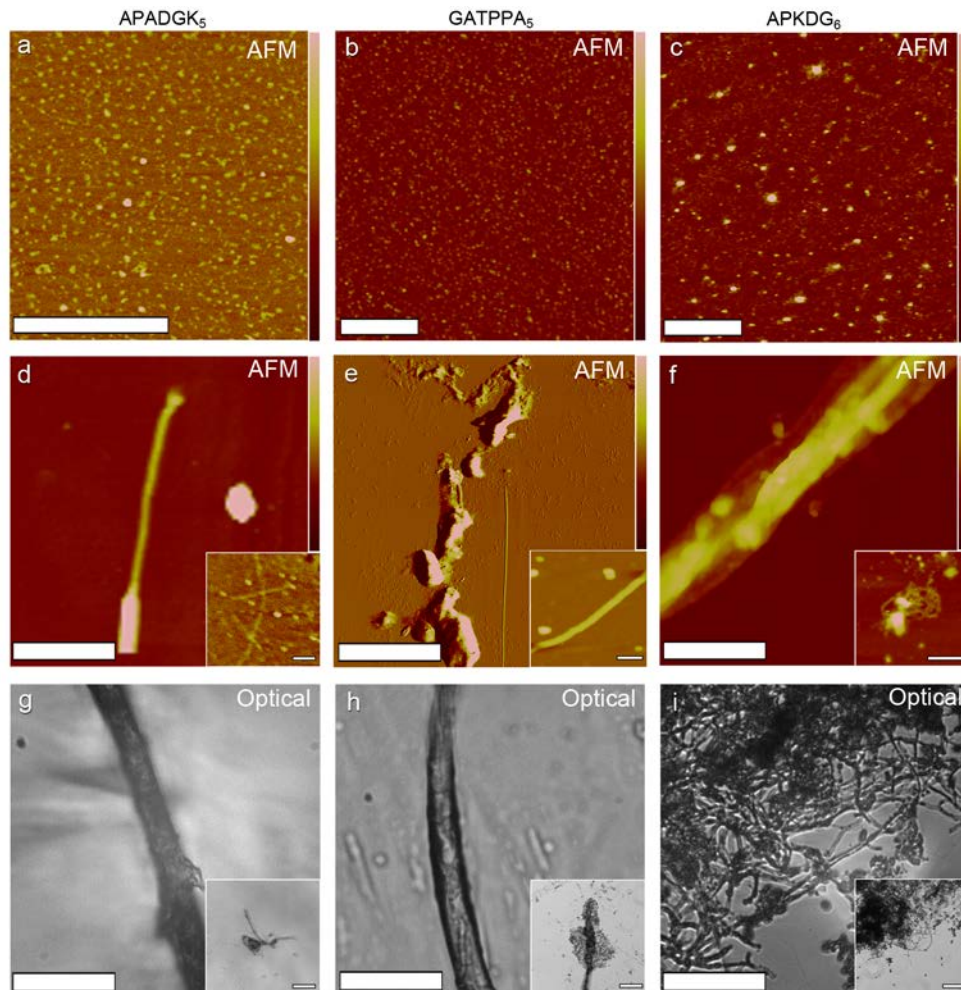


Figure 3:5 – Synthetic peptide self-assembly in high salt conditions  
 AFM height mode images of synthetic peptides in high-salt buffer with sequence (APADGK)<sub>5</sub>, (GATPPA)<sub>5</sub> and (APKDG)<sub>6</sub>, deposited onto mica immediately following preparation (a – c respectively: x-scales = 1  $\mu$ m, z-scales = 3 nm). AFM height / peak error images of fibres formed after 14 d (d – f) from (APADGK)<sub>5</sub> (d: x-scale = 1  $\mu$ m, z-scale = 15 nm, inset: x-scale = 100 nm, z-scale = 1 nm), and (GATPPA)<sub>5</sub> (e: x-scale = 5  $\mu$ m, z-scale = 300 mV, inset: x-scale = 500 nm, z-scale = 6 nm), and after 7 d from (APKDG)<sub>6</sub>. (f: x-scale = 3.5  $\mu$ m, z-scale = 900 nm, inset: x-scale = 500 nm, z-scale = 30 nm). Optical micrographs of precipitates formed after 4 wks from (APADGK)<sub>5</sub>, (GATPPA)<sub>5</sub> and (APKDG)<sub>6</sub>, deposited onto mica (g – i, respectively: scale = 20  $\mu$ m, inset: scale = 50  $\mu$ m). Topography AFM channel image is available for comparison to e in Figure B:6.

After 4 wks incubation, all peptides in the high-salt condition showed aggregates visible with the unaided eye. These precipitates were too large to image using the AFM and the fibrous nature of precipitates were instead observed by optical microscopy as shown in Figure 3:5g – i and Figure 3:6g – i, where insets show the larger structure of the networks at a lower objective magnification. (APADGK)<sub>5</sub> precipitated into large thick fibres with some

networking as seen inset in Figure 3:5. (GATPPA)<sub>5</sub> also showed large thick fibres. However, these were associated with an amorphous cohort of peptides, as seen inset in Figure 3:5h. (APKDG)<sub>6</sub> showed a highly networked precipitate of narrow/thin twisted fibres on the mica surface (Figure 3:5i).

Under low-salt conditions, aggregation of all peptides occurred faster than in the high-salt condition. (APADGK)<sub>5</sub> showed fibrils as well as a fibre made of highly networked fibrils after 7 d. Fibrils had heights 0.5 – 72 nm (average 10.3 nm ± 18.9 nm) and lengths 80 nm to 4.0 µm as seen in Figure 3:6d. These fibrils were generally larger and more anfractuous (n = 10) than those observed for the high-salt condition (Figure 3:5d). (GATPPA)<sub>5</sub> aggregation was also observed after 7 d, with fibril heights observed ranging from 0.5 – 16.9 nm high (average 8.3 nm ± 7.4 nm) and lengths 400 nm – 5.4 µm. In this case, fibrils were of lesser height than those observed for the high-salt condition, and also appeared to contain a lower percentage of anfractuous (n = 12) fibrils as depicted in Figure 3:6e. Additionally, more branched (n = 7) and rod-like (n = 10) morphologies were observed. (APKDG)<sub>6</sub> aggregation was again observed in the low-salt condition, taking 1 d to self-assemble. Fibrils were of smaller height than those seen for the high-salt condition, with height 0.8 – 24.9 nm (average 7.3 nm ± 6.9 nm) and lengths 400 nm – 9.6 µm observed (Figure 3:6f). Compared to the morphologies seen in the high-salt condition, fibrils from the low-salt condition were more commonly anfractuous (n = 6) and branched (n = 5).

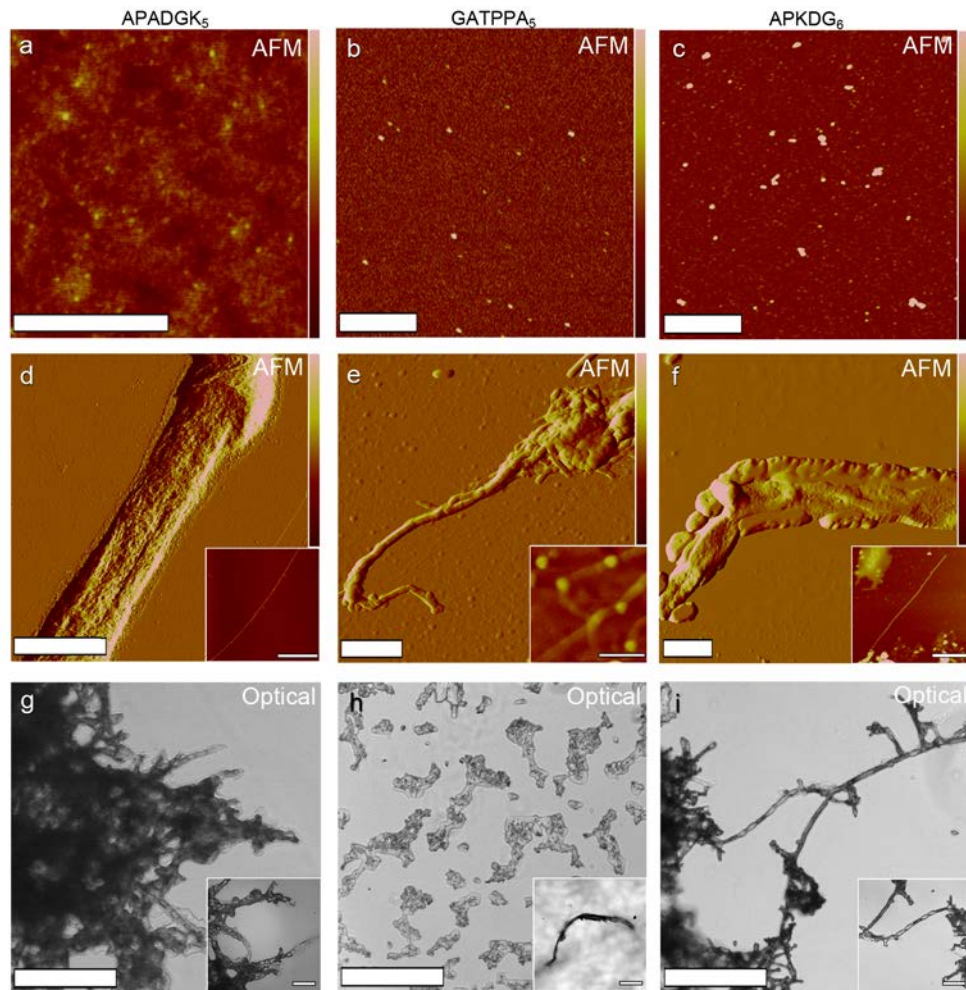


Figure 3:6 – Synthetic peptide self-assembly in low salt conditions. AFM height mode images of synthetic peptides in low-salt buffer with sequence (APADGK)<sub>5</sub>, (GATPPA)<sub>5</sub> and (APKDG)<sub>6</sub>, deposited onto mica immediately following preparation (a – c respectively: x-scales = 1  $\mu$ m, z-scales = 3 nm). AFM height / peak error images of fibres formed after 7 d from (APADGK)<sub>5</sub> (d: x-scale = 1  $\mu$ m, z-scale = 50 mV, inset: x-scale = 2  $\mu$ m, z-scale = 2 nm), (GATPPA)<sub>5</sub> (e: x-scale = 1  $\mu$ m, z-scale = 60 mV, inset: x-scale = 250 nm, z-scale = 3 nm), and after 1 d from (APKDG)<sub>6</sub>. (f: x-scale = 2  $\mu$ m, z-scale = 15 mV, inset: x-scale = 1  $\mu$ m, z-scale = 5 nm). Optical micrographs of precipitates formed after 4 wks from (APADGK)<sub>5</sub>, (GATPPA)<sub>5</sub> and (APKDG)<sub>6</sub>, deposited onto mica (g – i, respectively: scale = 20  $\mu$ m, inset: scale = 50  $\mu$ m). Topography AFM channel images are available for comparison to e – f in Figure B:6.

As with the high-salt condition, 4 wks of incubation also resulted in precipitation in the low-salt condition and optical micrographs were again collected of the precipitated fibres. (APADGK)<sub>5</sub> precipitated into a highly networked structure, composed of thick fibres as seen in Figure 3:6g. These structures were significantly different to those seen for the high-salt condition. (GATPPA)<sub>5</sub> showed smaller fibres than in the high-salt condition (Figure 3:5h

inset), with a larger amount of amorphous peptide present compared to the high-salt condition. (APKDG)<sub>6</sub> again showed a highly networked gel precipitate of twisted fibres. Although the morphology was very similar to that observed in the high-salt condition, the precipitated fibres were longer and appeared to branch more, as displayed in Figure 3:6i.

### **3.5 Discussion**

The data presented clearly show that the AGL proteins and peptides derived from symbiotic fungus, *G. intraradices*, are a new family of self-assembling biomaterials and that they each have different properties, consistent with their different primary sequences, charge profile and, in the case of rAGLs, arrangements of these repeats.

#### **3.5.1 Secondary Structure**

CD spectroscopy demonstrated that all of the peptides had a significant fraction of extended PPII structure, which is known in other proteins and peptides to be an important conformation for molecular recognition [285] and for structural roles as observed with collagen and elastin [278]. Here, a new data set was developed (see Appendix B) to address the often inconsistent assigning of PPII helical and random coil structure. This inconsistency is due in part to non-proline based peptides having PPII structure that was originally assumed to be unstructured or random coil [281], [289–291]. Confusion has led to some authors adopting the term PPII-like [296] while others assume peptides, such as the cell penetrating transactivator TAT protein, adopt a random coil conformation, although TAT clearly shows a positive CD band close to 220 nm [297]. Other researchers suggest that a 'negative shoulder band' [281], as seen in all the CD spectra obtained for rAGLs and AGL derived peptides (Figure 3:4), is indicative of a significant proportion of PPII and this is supported by NMR data [281], [298]. If a negative shoulder band is taken as an indicator of PPII structure, then all of the peptides based on the native AGLs (Figure 3:4a–

c), and rAGL1 (Figure 3:2a) and rAGL3 (Figure 3:2b), contain a significant proportion of PPII. The PPII structure of the repeats based on AGL1 are of particular interest because, in addition to being zwitterionic, they will also be amphipathic. Two edges are hydrophilic, containing the charged residues (alternating A K<sup>+</sup> A K<sup>+</sup>; alternating A D<sup>-</sup> A D<sup>-</sup>; Figure 3:1d), while the third edge is moderately hydrophobic (alternating P G P G).

Synthetic peptides representing the zwitterionic repeats of AGL3 (APKDG), showed the greatest tendency to form PPII helices at low temperature, based on the presence of a positive CD band at 223 nm and decomposition of CD spectra. However, the loss of the PPII structure at higher peptide concentration and lower ionic strength suggests that this peptide is dynamic and capable of forming a variety of structures under different conditions. Further experiments are required to determine if these changes are due to ionic strength, peptide concentration or a synergistic effect of both of these. It is unlikely to be ionic strength alone based on almost identical spectra when 'DAA' (APKAG)<sub>6</sub> at 250 µg/mL is compared in the high- and low-salt buffers (data not shown). The type of salt used may also have an effect on the peptides investigated, based on the very different CD spectra observed when other synthetic peptides, Ac-A<sub>6</sub>DDG<sub>6</sub>-CoNH<sub>2</sub> and Ac-A<sub>6</sub>D-CoNH<sub>2</sub>, were compared in 0.1 M NaCl, phosphate buffered saline (0.058 M Na<sub>2</sub>HPO<sub>4</sub>, 0.017M NaH<sub>2</sub>PO<sub>4</sub>, 0.069 M NaCl, 2 mM Mg<sup>2+</sup>) and water, whereas only relatively minor changes were observed in response to pH [211]. Further investigation of the recombinant AGL proteins and peptides using buffers with different ionic strengths and concentration may be investigated in a future study.

There has been considerable interest in predicting whether or not specific amino acid residues are more likely to favour PPII helix formation. To investigate this, researchers developed PPII propensity scales using host–guest peptides, where different amino acid residues are substituted for proline in polyproline–based peptides [299], [300]. The repeats in AGL1 and AGL3 contain amino acid residues, lysine, glycine and alanine that are favoured in most PPII propensity scales [299], [300] and also found in other established PPII structures [126]. Different repeats in human tropoelastin are known to have low or no proline, yet still form PPII helices (GAGLGALGG (exon 3), PGGLAGAGLGA (exon 5)) [289]. In the present study, the peptide with the most pronounced PPII structure, DΔA mutant peptide (APKAG)<sub>6</sub>, provides another example of this secondary structure in low–proline peptides. These peptides will be of interest to researchers with a theoretical interest in PPII structures.

To further explore the subtle differences between the rAGLs, a more efficient method of obtaining recombinant or native protein is needed in order to investigate biologically relevant conditions, such as those similar to the plant cell wall, but still compatible with CD spectroscopy. Salt conditions in the plant cell wall are not well defined, due to the difficulty in performing these measurements. Most experiments thus far have been performed using leaves, and range from 50 μM to 100 mM K<sup>+</sup> [301], [302], and even up 200 mM K<sup>+</sup> [303]. Ammonium sulphate was used here because of its compatibility for CD spectrometry at wavelengths <190 nm [129]. In addition, NMR could be used

to determine if all of the peptides studied are PPII or unordered. For example, in peptides derived from the sequence of elastic protein titin, containing amino acid residues PEVK, only one of three peptides (PR2) was clearly PPII by CD spectroscopy, but NMR data supported the presence of extended PPII-like structures in two other peptides that did not show bands between 217–225 nm [281], [304].

The CD data supports a low proportion of  $\beta$ -sheet (Table 3:2). These structures, often associated with insoluble aggregate formation, can only be dissolved with chemical cleavage [132]. There are several reasons why the aggregates formed with the AGL derived proteins and peptides, as demonstrated for rAGL3 (Figure 3:3g-i), are more readily disaggregated, at least *in vitro*: 1) The absence of hydrophobic residues such as valine, 2) the regular positioning of proline residues every 5 or 6 residues which limits the extent of sequences able to form  $\beta$ -sheets [284], and 3) the relative positioning of proline to glycine, which leads to a structure less likely to form  $\beta$ -turns. For example, in other proline- and glycine- containing repetitive sequences such as homopolymers based on elastin, the juxtaposition of proline and glycine (PGVGVA) is believed to be responsible for the formation of the corners of the hydrogen-bonded  $\beta$ -turns [284]. As the distance between the proline and glycine  $\beta$ -turns is increased, the propensity for forming insoluble aggregates is also increased, presumably by increasing the length of intervening  $\beta$ -sheet structures [284]. Valine is an abundant amino acid in elastin and is significantly more hydrophobic than alanine, the most hydrophobic residue in the prepeat of all three AGLs, with a value of 4.2 compared to 1.8 on the Kyte

and Doolittle hydrophobicity scale [311]. In the motifs of the peptides based on fungal proteins, the proline and glycine residues are not adjacent to each other and therefore they are unlikely to form  $\beta$ -turns. The absence of  $\beta$ -turns could be tested in future using the  $\beta$ -turns promoting 2,2,2-trifluoroethanol [289]. The presence of lysine opens up the possibility of enzymic cross-linking *in vivo*, as occurs in some elastic proline- and glycine-rich proteins such as elastin [305] and titin [281]. Isolation of the proteins from the fungus would be required to determine their native form.

### **3.5.2 Self-Assembly of Recombinant Proteins**

The morphologies observed for the aggregates of the recombinant proteins are significantly different, suggesting several methods of aggregation for these proteins. The fibrils observed from rAGL1 were often thin and straight (Figure 3:3b), with sections coated in amorphous protein. These thin fibrils resemble the aggregates of the amphipathic peptide sequence observed for (VHLPPP)<sub>8</sub> [219], suggesting a similar method of aggregation. There is some evidence to suggest the fibrils twist together (Figure B:2) as seen for amyloid fibres [306], although it is also possible that the rod-like fibrils are bundling together.

The rAGL1 protein began to precipitate out of solution after 6 wks, forming large fibrous precipitates (Figure 3:3c). These fibres were not heavily networked, and smaller features were still observed surrounding the precipitates, indicating incomplete aggregation. These fibres appeared to have branching segments of thinner filaments, suggesting a formation via a hierarchical assembly of fibrils. Interestingly, these structures were

significantly larger than any fibrils observed, and indeed larger in diameter than many well characterized protein fibres in the literature, such as collagen (~100 nm diameter) [307]. Further, the possibility exists that longer incubation or an increased concentration of protein may result in even larger ropey structures. In any case, the presence of rope-like structures of AGL1 in fungal hyphae likely plays a structural role, much like collagen in mammalian tissues [279].

The fibrils observed from rAGL3 were either straight, with irregular striations resulting in a banded appearance (Figure 3:3e), or flat sheet-like / amorphous aggregates with a spotted appearance (data not shown). Banded structures were observed for natural proteins such as collagen [307] and glycine-rich synthetic peptides [308]. Collagen fibres form via a coiled-coil triple helical structure [309], in which the glycine residues form the raised striations. As with collagen, the repeat regions of rAGL3 also contain glycine and proline, however glycine is positioned every six residues rather than the every third residue which is a mandatory requirement for stable triple helical formation [309]. Another striking difference is the relatively bulky, and charged, lysine residues. These structural differences are likely to be significant but without X-ray diffraction or solid state NMR experiments we can only speculate on the exact supramolecular structure of rAGL3 aggregates.

The different morphologies observed for rAGL3 suggest that aggregation is occurring via multiple potential pathways. Nonetheless, one final fibre morphology is dominant in precipitates (Figure 3:3g). The protein precipitated

out of solution after 4 wks, based on visual inspection, much faster than rAGL1. The precipitated fibres were networked together, and had an appearance of flattened microtubes (Figure B:3a,b). As these experiments were carried out in air, the tube structure may have previously contained buffer that subsequently evaporated leading to a flattened appearance. Such a microtube structure could assist in hyphal growth and/or arbuscule formation (Figure 3:1f) during AM symbioses. Other large ‘sheet-like’ aggregates were also present (Figure 3:3f). A network of aggregates may be beneficial for interactions at the fungal-plant interface during arbuscule formation, or as structural support for expanding hyphae.

The reversibility of rAGL3 assembly suggests that the native protein could play a key role in the cycle of arbuscule development and turnover [310]. Following disruption, the precipitates were observed to reassemble in only one week. This faster aggregation may indicate selective retention of a few smaller aggregates, presumably the most stable ones, due to incomplete disruption of the fibres during sonication. Small aggregates such as these can provide nucleation sites enabling more efficient aggregation as seen in the ‘seeding’ experiments done with amyloid proteins [144], [164]. Support for ‘seeding’ following re-aggregation is gained from the morphology of the fibre following re-aggregation. The fibre width ( $\sim 1 \mu\text{m}$ ) and length ( $< 10 \mu\text{m}$ ) remain relatively unchanged, while the height doubles (Figure 3:3i). This may be due to a new arrangement of proteins. Indeed, limited protein is observed outside of the fibre, suggesting the protein has been entirely consumed due to a more efficient self-assembly. Such rearrangements following sonication have been observed

for fibre-forming ionic self-complementary peptides due to a re-ordering of monomers prior to re-assembly [213]. The other nanostructure observed at all timeframes for both rAGL1 and rAGL3 was an amorphous layer of protein across the surface, similar to those observed for amphiphilic peptide heterodimers [211]. Interestingly, the amorphous layer was less abundant after fibre precipitation. As no fibrils were observed alongside fibres, as with rAGL1, these amorphous and fibril aggregates are assumed to be incorporated to the new fibres. AFM imaging of more samples before and after sonication for various time intervals, or possibly utilising time-lapse AFM, may capture intermediate aggregates / disaggregates [164], [213].

The recombinant proteins did not adsorb efficiently to mica, hence recombinant proteins analysed by AFM were deposited onto HOPG instead. This effect was observed on mica with and without the presence of salts in buffer (data not shown), suggesting that charge is not the primary issue in adsorption. Instead, the better adsorption of the proteins onto HOPG may be due to the hydrophobic nature of the substrate, indicating that the recombinant proteins have exposed hydrophobic residues. Analysis of rAGL1 and rAGL3 using the Kyte and Doolittle hydrophobicity scale (calculated from [311]), shows that the C-terminal region of these recombinant proteins is more hydrophobic than the repeat regions, due to the low proportion of charged residues. This amphipathic type of structure may be beneficial as an interface with fungal or plant cell walls [312–314]. The plant cell wall is composed of several layers, and contains both hydrophobic and hydrophilic surfaces at the interfaces. For example, the surface of the plasma membrane is hydrophilic;

however, plant cell walls contain crystalline cellulose with both hydrophobic and hydrophilic surfaces [275], [315]. Hence, the amphipathic nature of native AGL1 and AGL3 would allow for diverse interactions at the plant cell surface.

Self-assembly resulted in fibrils of multiple morphologies, however the precipitated fibres were dominated by one morphology type per sample, indicating that multiple self-assembly pathways are available for the recombinant proteins, with only one final fibre structure being favourable in the conditions used here.

### **3.5.3 Self-Assembly of Repeat Regions into Fibrous Structures**

Aggregation was observed by DLS in all of the peptide samples investigated. This technique is not ideal for accurate size estimation of ‘rod-like’ fibre-forming peptides, as the calculated hydrodynamic radius is assumed to be due a spherical shape. However, the size of particles in solution increased by over 100 nm, indicating aggregation, as seen in Table 3:3. Based on the timeframes obtained from DLS, aliquots were taken for AFM imaging. Initially, all peptides were observed as discrete spots on the mica surface, with heights comparable to the particle sizes observed in Table 3:3. As the peptides did not adsorb well to mica, Bruker’s PeakForce mode was employed to minimize surface interactions and avoid movement of, or damage to, the samples. No sample damage was observed for initial imaging. However, after aggregation, some rod-like fibrils were observed to be damaged or moved due to imaging (Figure B:5). It is therefore possible that greater numbers of aggregates formed in solution, but were unable to be imaged by AFM under the conditions used.

Following incubation, all peptides in high- and low-salt conditions formed aggregates. Using AFM, these aggregates were observed to be fibrous, with a variety of morphologies seen for each sample. As discussed for recombinant proteins, these variations suggest the possibility of multiple nuclei that could lead to aggregation [134]. A considerable range of lag phases, from 1 to 14 d, was observed before aggregate formation. Following fibril formation, growth into fibres is slow requiring a month for precipitates to be observed visually. Although this slow aggregation could suggest multiple nucleation steps, it is more likely to be an effect of concentration of monomers. A higher concentration would allow for peptides of the required conformation to assemble faster. Due to limitations in the samples available for this study, the effect of concentration was not investigated and should be included in a future study.

#### *3.5.3.1 Ionic Strength Affects Self-Assembly*

Peptide self-assembly is sensitive to a variety of environmental conditions, including temperature, solvent, substrate, pH, and ionic strength [205], [286], [287]. When considering the self-assembly of peptides in aqueous media such as used here, it is the ionic strength which can be considered most important to the mechanism of assembly [205]. Two different ionic strengths were investigated, based upon the expected range of ionic strengths in the apoplast of root cells. Two different salts were used, ammonium sulphate and monopotassium phosphate, due to their low optical activity, rendering them most suitable for CD spectroscopy at low wavelengths. Solutions containing

100 mM NaCl or KCl are not suitable below 195 nm [129]. The three synthetic peptides based upon *GiAGL* repeat regions all formed aggregates faster in the low-salt condition compared to the high-salt condition, as seen by DLS, and a range of morphologies were observed. These are discussed for each peptide in the following paragraphs.

The peptides (APADGK)<sub>5</sub> and (APDGK)<sub>6</sub> both contain charged residues, so a high ionic strength may disrupt intermolecular interactions due to blockage of charged residues. This hypothesis is supported by the DLS data, as peptides in the low-salt condition aggregated faster than in the high-salt condition. The precipitated aggregates, seen after 4 wks for (APADGK)<sub>5</sub> in the high-salt condition (Figure 3:5g), show a few large fibres compared to the dense network of fibres observed with the low-salt condition (Figure 3:6g). However, for (APDGK)<sub>6</sub>, the final precipitate structure appears very similar in both conditions, with a dense network of twisted fibres forming a gel-like substance (Figure 3:5i and Figure 3:6i). As ammonium sulphate has been shown to promote lateral association of fibrils by interaction of sulphate ions with lysine residues of the adjacent fibrils [316], the high-salt condition may assist the growth of larger fibres, while the low-salt conditions results in fully ionized residues to more readily form a stable nucleating fibril for faster aggregation.

The peptide (GATPPA)<sub>5</sub> has no charged residues. Therefore, ionic strength was not expected to have as great an impact on aggregation properties. However, the low-salt condition resulted in smaller and fewer aggregates despite the shorter time to aggregate observed by DLS (Table 3:3). The fibrils observed

tended to be more rod-like in the low-salt condition, with less networking between aggregates (Figure 3:5e and Figure 3:6e). The precipitated fibres, seen after 4 wks, are larger in the high-salt condition with some amorphous peptide observed on or around these fibres (Figure 3:5h). This is in contrast to the low-salt condition, containing smaller fibres and much more amorphous peptide (Figure 3:6h). These results suggest that low ionic strength inhibits networking between peptides. As there are no charged residues for an ionic interaction to occur (Figure 3:1b), it is possible that the salts contained in the buffer are providing thermodynamically favourable hydrogen bonding sites, acting as alternative nucleation sites. In order to test this hypothesis, buffer containing simpler salts, such as sodium chloride, could be used to investigate differences in ionic strength, and this may be the focus of a future study. However, it is more likely that the polar nature of the amide residues is sufficient to act as an ionic interface, in which case altering the type of salt should not affect the observed result.

The aggregation of these peptides is multifaceted, with multiple morphologies under the same conditions. Furthermore, in all salt conditions, incubation times and peptide sequences, the presence of un-aggregated peptides was observed by DLS and AFM, as also seen for recombinant proteins. It is clear that the repeat regions coded by *GiAGLs* are involved, at least in part, in the aggregation of the recombinant proteins. The final fibres precipitated from the peptide (APADGK)<sub>5</sub> are not dissimilar to those seen for rAGL1, suggesting that the repeat regions drive the self-assembly process. These regions are present throughout the protein sequence, without large spacing between most

of the separated repeats. On the other hand, the morphologies of the fibres observed for the peptide (APKDG)<sub>6</sub> are quite different than those seen for rAGL3, suggesting that the relatively large non-repeat regions of the protein also contribute to the self-assembly of rAGL3 because there is only one block of repeat regions seen (Figure 3:1c).

### **3.6 Conclusions and Future Perspectives**

The data provide strong support for peptide repeats found in fungal peptides to form PPII helices and self-assemble. We suggest that in the native proteins the self-assembly in the cell wall contributes to network formation necessary for structural stability. Our data show that the different proteins and peptides are capable of forming different fibres, suggesting distinct functional roles at the diverse fungal-plant interfaces in the symbiotic root (Figure 3:1f). Further studies are needed to correlate these findings with the different fungal cell walls found in the extraradical (hyphae and spores) and various intraradical growth stages (hyphae, arbuscules, vesicles).

The peptide nanostructures investigated here may find various potential applications as nanomaterials [207], [316]. It is the application as a biomaterial which is most relevant here, as current investigations into scaffolds for tissue engineering have focused on amyloid structures [204]. Despite their stability, these  $\beta$ -sheet structures are not usually present in functional tissues and therefore more 'natural' secondary structures are of interest as tissue engineering scaffolds [273], or as use in suture applications [317]. The reversibility of fibrous structures can be important for biomaterial applications, for example as a drug delivery system [205], [318]. Further research is necessary to tune the self-assembly process. Nonetheless, these peptides appear to be ideal for functional nanomaterial applications.

## Chapter 4

---

### **4 Characterisation of Pseudoexfoliation Syndrome Deposits using AFM–Based Antibody Recognition Imaging**

This work forms the basis of the following peer–reviewed publications:

R. Creasey, S. Sharma, J.E. Craig, C. T. Gibson, A. Ebner, P. Hinterdorfer and N. H. Voelcker, ‘Detecting protein aggregates on untreated human tissue samples by atomic force microscopy recognition imaging’, *Biophysical Journal*, **2010**, *99* / 5, 1660 – 1667.

R. Creasey, S. Sharma, J.E. Craig, C. T. Gibson, A. Ebner, T. Becker, P. Hinterdorfer and N. H. Voelcker, ‘Atomic force microscopy–based antibody recognition imaging of proteins in the pathological deposits in Pseudoexfoliation Syndrome’, *Ultramicroscopy*, **2011**, *111* / 8, 1055 – 1061.

## **4.1 Summary**

Protein aggregation is of significant interest to various disciplines including ophthalmology. One ocular disease hallmarked by protein aggregation is known as Pseudoexfoliation (PEX) syndrome. This condition is caused by the formation of insoluble aggregates in the eye, and is clinically characterised by deposition of proteinaceous material on the anterior lens capsule. The ultrastructure of PEX material is poorly characterised, despite numerous proteomic and genomic studies [319–321]. One of the defining issues in studying the PEX material is the difficulty in solubilisation of the material, complicating the identification of proteins in PEX deposits. As the ocular lens capsule is a relatively smooth and thin tissue, it is an ideal candidate for direct AFM imaging of whole tissue without fixation and sectioning.

This chapter addresses the issue of determining the molecular nature of PEX material on lens capsules in the native state by the application of Atomic Force Microscopy (AFM) based antibody recognition imaging techniques. Topographical AFM images and antibody recognition (TREC) images were acquired simultaneously to determine the specific location of clusterin, lysyl oxidase-like 1 (LOXL1) and elastin proteins in and around PEX aggregates to advance the understanding of the PEX pathophysiology, using AFM probes modified with an appropriate antibody. Localisation of protein aggregates on the surface at higher resolution than previously reported is shown for all three proteins. Further understanding of PEX is important for developing diagnostic assays and, ultimately, treatment strategies for this disease.

## **4.2 Introduction**

#### **4.2.1 The Human Eye**

The human eye is a complex organ. Its function is based on a principle similar to the use of a camera, with light entering the eye through the cornea to be focused by the lens onto the retina, where the light signals are transmitted to the brain via the optic nerve for processing [322]. The anatomy of the human eye is shown in Figure 4:1. The anterior segment includes the cornea, the lens and the structures in-between. The posterior segment is the rear of the eye, between the lens and the retina, containing the vitreous humour [322]. This study focuses on the lens capsule surrounding the lens in contact with the aqueous humour.

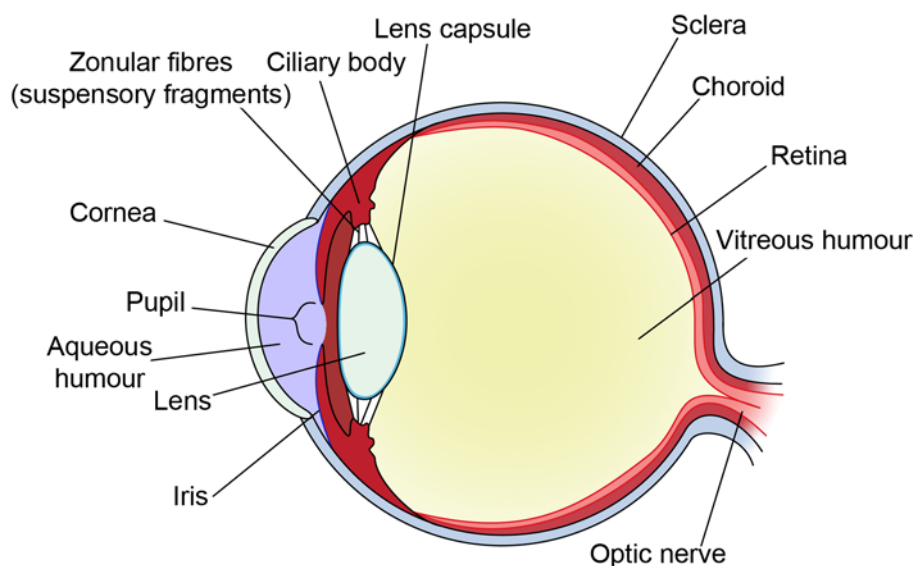


Figure 4:1 – Basic structure of the human eye.

Within the anterior chamber of the eye is the aqueous humour which maintains a certain intraocular pressure (IOP). This fluid is important as it maintains the eye's shape, provides nutrients to the nearby ocular components, and disposes of intraocular waste. The IOP can change from the normal physiological range. A high IOP is closely associated with glaucoma [323], resulting in permanent

damage to the optic nerve in the eye. Glaucoma is the second leading cause of irreversible blindness worldwide, and affects around 3% of Australians over 49 years of age [324], [325]. The most common forms of glaucoma are open-angle glaucoma (OAG) and angle-closure glaucoma (ACG). ACG is diagnosed by the obstruction of the trabecular meshwork, thereby directly preventing the aqueous humour from being drained. The trabecular meshwork is not blocked in OAG. Nonetheless, the drainage of aqueous outflow from the anterior chamber is reduced [323].

#### *4.2.1.1 The Lens Capsule*

The lens capsule is the clear extracellular membrane cover for the ocular lens. Although the lens capsule encapsulates the entire lens, the anterior and posterior facing sides have different properties due to the localised environment. A recent review covers all the current knowledge of the composition, structure and development of the lens capsule [326]; the lens capsule structure will be briefly reviewed here.

Spiro and Fukushi [327], [328] determined that the bovine lens capsule is formed by proteins in the collagen family, and contains around 11% carbohydrates. To study the macromolecular organisation of the lens capsule, Cammarata *et al.* [329] utilised immunofluorescence methods on the undigested bovine lens capsule. Antibodies were used to detect the presence and position of proteins such as type IV collagen, laminin, entactin, fibronectin and heparin sulphate proteoglycan proteins, as these had been previously determined to be basement membrane components. Using a fluorescence

microscope, Cammarata *et al.* determined that only type IV collagen, laminin and entactin had a strong presence, while the more sensitive immunogold EM technique detected type IV collagen, laminin, entactin, fibronectin and heparin sulphate proteoglycan co-localised across the entire capsule. Later studies showed that the bovine lens epithelial cells secrete procollagenous molecules, the fibrillar nature of which is important when considering the structure of the lens capsule. Sawhney [330] immunologically confirmed the production of fibrillar types I and III collagen in the bovine lens epithelium, and identified it also in the anterior lens capsule. Further molecules identified as core proteins in the lens capsule are nidogen, perlecan and, in some areas, fibrillin [326]. Immunological techniques such as those employed above are effective for macromolecular investigations; however they can only be used to find proteins for which an antibody is available.

Mass separation techniques such as gel electrophoresis [331], [332] and mass spectrometry (MS) [333] are able to identify proteins in the lens capsule without the use of an antibody. Recently, Ronci *et al.* [334] applied the MS technique matrix-assisted laser desorption ionisation-mass spectrometry (MALDI-MS)-imaging to whole lens capsules in order to investigate the anterior surface without utilising antibodies. Proteins previously detected in the lens capsule by MS, such as apolipoprotein E and collagen, were also detected by MALDI-MS-imaging. Interestingly, there was a spatial distribution of proteins, suggesting that mechanical strain due to the iris movement, or UV light exposure through the pupil alter the lens capsule composition.

There has been focus on the biomechanical strength of the anterior lens capsule related to factors such as age, capsule thickness, and disease, for instance cataracts [335]. These investigations found that age is the biggest factor influencing physical properties of the lens capsule. This suggests a compositional change in the lens capsule, as seen in earlier studies by Peczon *et al.* [336] who noted a reduction in collagenous amino acids with age. Further, the lens capsule also increases in thickness with age, up to 75 years of age, whereupon it begins to decrease. It is therefore important to consider the age of the patient when investigating the presence of particular proteins. None of the studies include a complete proteomic investigation of the proteins that make up the lens capsule for any age group. Furthermore, cadaver bovine lens capsules were the primary object of study. The study of human lens capsules would obviously be more relevant to human disease.

#### **4.2.1.1.1 Ocular Disease: Pseudoexfoliation Syndrome**

The eye is subject to a variety of protein aggregation diseases. One such disease is cataract [337–339], in which the lens becomes clouded due to aggregation of crystallins [340], [341], leading to impairment of vision, requiring surgery for treatment [342], [343]. PEX is another ocular disease characterised by progressive protein aggregation. The accumulation of proteinaceous material occurs on the surface of the anterior lens capsule, and is also present in other structures of the anterior segment of the eye which are in contact with the aqueous humour [344]. The PEX material affects the flow of aqueous humour as it accumulates in the trabecular meshwork, and is therefore a significant risk factor for OAG. In some patients, it can lead to ACG. PEX is

often also associated with other ocular conditions such as cataracts, and is also a risk factor for heart disease and stroke [345], [346]. Furthermore, the complication rate of cataract surgery is higher in PEX patients [342].

The disease has had many names, initially called ‘senile exfoliation’ and ‘capsular glaucoma’ by Lindberg in 1917 [347], [348]. It was named thus because upon initial observation, the aggregates appeared to be ‘peeling’ off the lens capsule, and therefore were assumed to be an exfoliation. Physical changes are not restricted to the lens capsule, however, and also occur to the cornea, iris, pupil, zonules and ciliary body, anterior chamber angle, vitreous humour and optic disc [344], [348], [349] and even in extraocular areas such as the connective tissues of the vascular system [345], [346], [350]. Additionally, there is another disease which represents true exfoliation of the lens capsule [347], [351]. Hence, Dvorak–Theobald [347] developed the phrase ‘pseudoexfoliation’ to avoid confusion, and this is the term used for this thesis.

#### *4.2.1.1.1.1 Composition of PEX material*

Much like studies on the lens capsule described earlier, immunological techniques have also been carried out on PEX–affected lens capsules. Recently, Sharma *et al.* [321] and Schlötzer–Schrehardt *et al.* [352] confirmed that the LOXL1 protein is present in PEX material and is crucial to the pathophysiology of PEX utilising immunohistochemistry (IHC) on both ocular and other PEX–affected tissues. Antibodies have also been used successfully against fibrillin–1, laminin, entactin/nidogen, fibronectin, vitronectin, elastin, and serum amyloid P component for demonstrating their presence in PEX

material deposited on affected ocular tissues [353–357]; all of which are basement membrane (extracellular matrix) proteins, and some of which have been also shown to be present in normal lens capsules. These proteins were all confirmed to be present in PEX material in the proteomic study by Ovodenko *et al.* [333] that employed differential MS and/or electrophoretic separation of proteins from digested PEX-affected and unaffected capsules. IHC staining was used to further confirm the proteins identified. Although a large amount of proteins are mentioned in this study, the MS data is only shown for clusterin, and IHC data is the primary method of identification. This was used to exclude proteins present in the lens capsule and not the PEX material, however non-staining of the capsule may be due to sensitivity issues associated with IHC.

One of the defining issues in studying the PEX material is the difficulty in solubilisation of the PEX material. In order to run proteomic studies of the material, it is necessary to remove it from the lens capsule, and digest it into fragments for analysis. Ovodenko *et al.* [333] investigated a variety of solvents, such as phosphate buffered saline (PBS), formic acid, hexafluoroisopropanol, guanidine HCl, urea, and acetonitrile / trifluoroacetic acid for solubilisation of PEX on PEX capsules. These solvents were chosen due to their prior success in dissolving amyloid aggregates, although none of the solvents extracted a sufficient amount of protein, and little physical change was observed in the PEX deposits. Hence a solubilisation process in cyanogen bromide / formic acid was used, thereby cleaving the peptide bonds at methionine (M), and aspartic acid – proline (D–P). This process extracted enough protein for further analysis via sodium dodecyl sulphate polyacrylamide gel electrophoresis

(SDS–PAGE) and MS. However, as the physical PEX material could still be observed after solvent extraction, it stands to reason that there still may be proteins which have not been extracted and would need to be identified for a reliable full proteome study.

Sharma *et al.* [321] utilised a similar protein extraction method, however they first isolated the PEX material from the lens capsule tissue during surgery. As mentioned earlier, LOXL1 was detected, along with apolipoprotein E, and shown to be present in PEX material by IHC labelling. It should be noted that LOXL1 was also detected by Schlötzer–Schrehardt using IHC and EM immunogold labelling soon after [352]. In the study by Sharma *et al.*, other proteins known to be present in PEX were identified such as latent transforming growth factor beta binding protein 2, complement 3 and clusterin were also confirmed using this approach. Following chemical cleavage, the PEX material could still be seen microscopically, indicating incomplete protein extraction. MS is a highly sensitive technique for protein identification, and as seen above has been used for PEX investigations. Further advances in sample preparation and MS instrumentation may continue to yield new and interesting results with respect to the protein content of PEX deposits. The use of alternative investigative techniques, such as AFM, will potentially reveal structural insights regarding the development of PEX fibrilopathy.

Genetic investigations have determined that there are risk alleles associated with PEX. Burdon *et al.* [358] and Krumbiegel *et al.* [359] found nominal association of a *CLU* genetic variant with PEX. A high risk association with

### *Characterisation of the Protein Deposits of Pseudoexfoliation Syndrome*

coding variants in the *LOXLI* gene was identified by Hewitt *et al.* [360], and strong associations of the disease with polymorphisms in the *LOXLI* gene have been observed for a variety of populations [360–362]. LOXL1 protein was shown to be expressed in ocular tissues using reverse transcription–polymerase chain reaction and western blotting in this study, then further confirmed by Sharma *et al.* [321] as discussed earlier using MS. *LOXLI* genetic association with PEX has been confirmed worldwide, and ongoing studies into genetic associations with PEX may turn up further ‘risk alleles’, such as contactin–associated protein–like 2 (*CNTNAP2*) [363], apolipoprotein E (*APOE*), glutathione S–transferases (*GSTs*), and tumour necrosis factor–alpha (*TNFA*), in certain study populations [319], [364]. By developing a genetic understanding of PEX, blood screening could become a medical tool to determine patients at risk of developing PEX. Further discussion on the clinical repercussions of genetic associations is available in the literature, along with reviews covering the epidemiology, pathogenesis and treatment of PEX [347–350], [365].

However, genetic analyses alone are not sufficient to describe the PEX pathophysiology, as environmental conditions are also thought to be involved in the development of PEX [352], [360], [366]. As the ultrastructure of protein aggregates and the conditions of aggregation are unknown, further investigation into the proteins and conditions involved is required before the PEX pathophysiology can be understood.

#### **4.2.1.2 Further Investigations in Pseudoexfoliation Syndrome**

AFM is one of the techniques suited for studying the ultrastructure of the protein aggregates on the lens capsule tissue. Most biological tissues would require histological preparation, such as fixation, before imaging studies. Ocular tissues such as the human cornea and sclera have been studied by AFM after fixation and mechanical dissociation of collagen fibrils [367]. Cataract has also been studied using AFM after extensive sample preparation to homogenize and extract the membrane proteins from the lens [368]. However, as the ocular lens capsule is a relatively smooth (roughness <50 nm RMS) and thin (20 – 60  $\mu\text{m}$  [326]) tissue, it is an ideal candidate for direct AFM imaging of whole tissue without fixation and sectioning. Furthermore, modification of the AFM probe with an antibody can lead to antibody–recognition imaging on the nano–scale [50], [93], [369].

In order to further the understanding of PEX aggregates, I used AFM–based techniques on whole mounts of unprocessed lens capsules. AFM was first used on the tissue both with and without PEX. Antibody recognition imaging was then applied to detect clusterin, LOXL1 and elastin proteins on the diseased lens capsules. The ultrastructure and localisation of proteins on unprocessed tissue, extracted during surgery, using AFM is an important methodological advance. This may lead to a greater understanding of the PEX pathophysiology by investigating the proteins directly involved in pathological aggregation.

## **4.3 Materials and Methods**

### **4.3.1 Tissue Samples**

Human lens capsules were collected according to the ethical guidelines of the Southern Adelaide Health/Flinders University Human Research Ethics Committee, Flinders Medical Centre, Australia, from patients with or without PEX undergoing cataract surgery at the Flinders Eye Clinic (Flinders Private Hospital, Bedford Park, South Australia). Samples were stored in sterile MilliQ water or balanced salt solution (BSS; NaCl (0.64%), KCl (0.075%), CaCl<sub>2</sub>•H<sub>2</sub>O (0.048%), MgCl<sub>2</sub>•6H<sub>2</sub>O (0.03%), C<sub>2</sub>H<sub>3</sub>NaO<sub>2</sub>•3H<sub>2</sub>O (0.39%), and C<sub>6</sub>H<sub>5</sub>Na<sub>3</sub>O<sub>7</sub>•2H<sub>2</sub>O (0.17%)) at 4 °C until use.

### **4.3.2 Atomic Force Microscopy**

#### **4.3.2.1 Sample Preparation**

For force spectroscopy measurements, freshly cleaved mica was incubated with 50 µL recombinant human clusterin (Biomedica Medizinprodukte, Austria; 150 µg/mL in phosphate buffered saline (PBS; 150 mM NaCl, 5 mM NaH<sub>2</sub>PO<sub>4</sub>, pH 7.4)) for 1 h, and then rinsed 50 times in 500 µL PBS to remove any loose protein. Freshly prepared clusterin samples were placed into the AFM liquid cell and 600 µL PBS was added.

Lens capsules were carefully washed three times in 1 mL MilliQ water and placed flat on a clean glass coverslip. The coverslip was dried thoroughly under a gentle stream of nitrogen (N<sub>2</sub>) to immobilize the tissue, and then rehydrated in the AFM liquid cell with 600 µL PBS. Interestingly, the tissue detached from the coverslip if allowed to dry with salt present. Hence, the tissue needed to be either stored in fluid or washed thoroughly with MilliQ

before dry storage. Lens capsules were stable for reuse when stored in PBS at 4°C for up to one week. As the AFM experiments were conducted in a non-sterile environment, lens capsules were discarded after use.

#### **4.3.2.2 Probe Functionalisation**

AFM probes were functionalised with antibodies of interest (Table 4:1) as described in detail elsewhere [38], [370]. Probes were washed in a polar solvent (methanol or ethanol) three times for 5 min each then dried gently with N<sub>2</sub>. They were then washed in a non-polar solvent (chloroform or acetone) three times for 5 min each and dried gently with N<sub>2</sub>. Probes were placed into a 5 L desiccator for amino-functionalisation with 30 µL 3-aminopropyl triethoxysilane (APTES, Sigma) and 10 µL triethylamine (TEA, Sigma) for 2 h under argon (Ar) [41]. The desiccator was then flushed with Ar for 15 min, and sealed to cure the APTES layer for 2 days. The probes were washed three times in chloroform for 5 min and dried under N<sub>2</sub>. The heterobifunctional crosslinker NHS-PEG<sub>800</sub>-aldehyde (prepared as per Ebner *et al.* [370] or purchased from Sensopath Technologies, USA) or NHS-dPEG<sub>24</sub>-aldehyde (Quanta BioDesign, USA) was covalently bound to the amine groups on the tips for 2 h at a concentration of 6.6 mg/mL in chloroform with 1 % (vol/vol) TEA. After washing three times in chloroform for 5 min and drying under N<sub>2</sub>, the probes were then immersed in 150 µL PBS containing antibody as per Table 4:1, with 2 µl of sodium cyanoborohydride (NaCNBH<sub>3</sub>, Sigma) solution (1 M NaCNBH<sub>3</sub>, 10 mM sodium hydroxide), for 2 h. The scheme for this reaction can be seen in Figure 1:4, on page 15.

Table 4:1 – Antibodies used for functionalisation of AFM probes.

Antibody specificity	Host organism	Supplier	Purified by	Concentration
Clusterin	Rabbit	Santa Cruz Biotechnology Inc, Germany	HPLC	200 µg/mL
LOXL1	Rabbit	Santa Cruz Biotechnology Inc, Germany	Ultra-centrifugation	150 µg/mL
Elastin	Rabbit	Sapphire Bioscience Pty. Ltd, Australia	Not needed	150 µg/mL

Subsequently, 5 µl of 1 M ethanolamine–hydrochloride was added to the solution for 10 minutes to quench any remaining aldehyde groups. Finally, the probes were washed and stored in PBS at 4°C for no more than a week.

SEM was performed on a CAMScan MX2500 SEM (Obducat, Sweden) equipped with a tungsten filament gun operating at WD 13 – 20 mm and 10 – 15 kV on probes before and after functionalisation (Figure C1) to observe changes to the physical state of the tip. No significant effects were observed.

#### **4.3.2.3 AFM Operation**

##### **4.3.2.3.1 Force Spectroscopy**

For anti–clusterin–functionalised tips, 1000 force spectroscopy curves at a vertical velocity of 300 nm/s were collected in PBS on a Pico–SPM AFM (Molecular Imaging, USA) using silicon nitride probes (MSNL, Bruker, USA, nominal spring constant 0.03 N/m) as detailed by Riener *et al.* [61].

For anti–LOXL1–functionalised tips, force spectroscopy was carried out on a Multimode V SPM (Bruker, USA), using silicon nitride probes (DNP–S, Bruker, USA, 0.12 N/m nominal spring constant) in PBS at a force loading rate of 400 nm/s.

Sensitivity values used were determined using the contact slope of force–distance approach curves in fluid against a glass surface. Spring constant calibration is described in AFM Data Analysis.

#### **4.3.2.3.2 Tapping Mode Imaging**

TM images were acquired using a Nanoscope IV Multimode SPM (Bruker, USA) operating in Acoustic AC (AAC) mode using an e–type scanner (15  $\mu\text{m}$ , Bruker, USA). Images were acquired in air or fluid (PBS or water) as noted per figure. The probes used were OTR8 probes (Bruker, USA, 0.57 and 0.15 N/m nominal spring constant) for normal imaging and DNP–S (Bruker, USA, 0.58 N/m nominal spring constant) functionalised probes for phase imaging. The larger scan size images ( $>20 \mu\text{m}$ ) were acquired using a Dimension 3000 SPM (Bruker, USA), using silicon nitride probes (DNP–S, Bruker, USA, 0.58 N/m nominal spring constant) operating in TM in PBS. All images were collected at a resolution of 512 lines, at 512 points per line, at scan speeds of 0.5 – 2 lines/s depending on scan size. The amplitude setpoint was maintained at 75 – 85% of the free amplitude, to minimise sample deformation while maintaining a stable oscillation.

#### **4.3.2.3.3 Antibody–Recognition Imaging**

For picoTREC<sup>TM</sup> measurements, functionalised MAC probes (Agilent MACLevers Type 6 (N9865b), USA, with nominal spring constant 0.292 N/m) were used for imaging. MAC mode images were acquired using a PicoPlus AFM (Agilent Technologies, USA) fitted with a fluid cell in PBS at room temperature using similar experimental conditions as described by Hinterdorfer *et al.* [96], [109], [371]. TREC measurements were made in regions of interest

of less than  $5 \times 5 \mu\text{m}^2$  and at scanning speeds of  $<1$  line/s (to allow antibody binding) applying full amplitude feedback [109] using a commercially available picoTREC™ box (Agilent Technologies, USA). A very low cantilever drive frequency (3 – 5 kHz) was used for imaging, as cross talk is minimized due to the extra time for topography signal to decay before recognition signal is measured [109]. The amplitude setpoint was maintained at ~95% of the free amplitude, to minimise sample deformation. This smaller setpoint difference is possible due to the MAC mode–driven oscillation of the probe.

Force–volume and phase imaging were carried out on a Multimode V SPM (Bruker, USA), using functionalised silicon nitride probes (DNP–S, Bruker, USA, 0.12 N/m nominal spring constant) operating in TM in PBS. Force–volume images were collected with resolution of 32 lines per image, at 32 points per line.

#### **4.3.2.3.4 Proof of Specificity**

Blocking with free antigen or ligand verifies probe–ligand specificity, as the interaction between the probe receptor and the surface ligand is interrupted, which will only remove signal due to specific interactions. For force spectroscopy, force–volume and phase imaging, blocking was done by introducing free antibody (150  $\mu\text{g}/\text{ml}$  in PBS) into the fluid cell during imaging to block free protein sites on the surface of the sample. For TREC imaging, recognition verification was achieved by amplitude adjustment as described by Preiner *et al.* [109]. One TREC sample was also blocked using antibody (Figure 4:6, page 158) as an additional proof.

#### **4.3.2.4 AFM Data Analysis**

For clusterin force spectroscopy data, MatLAB 7.1 (MathWorks, Natick, MA, USA) was used for force curve analysis and spring constant determination as described by Riener *et al.* [61].

For LOXL1 force spectroscopy data, SPIP™ 5.1.3 (Image Metrology, Denmark) was used for force curve analysis using the batch processing plug-in and generation of adhesion (force–volume) images. Only data which was more than 15 nm from the contact point were included, as the linker must be stretched to analyse the unbinding force of the antibody–antigen interaction. Forces over 300 pN were removed from analysis as they do not reflect single antibody–antigen interactions.

Spring constants were determined using both the Sader [35] and the thermal noise [32], [372] methods for Bruker probes, and were found to be between 0.013 – 0.090 N/m. For the MAC mode probes the thermal noise method was used for calibration, and spring constants were found to be between 0.2 and 0.9 N/m. Sensitivity values were calculated using the slope of cantilever deflection against a hard surface, resulting in photodiode voltage per nanometre of deflection.

AFM topography, force–volume and phase images acquired using Bruker SPMs were analysed using Nanoscope Analysis v1.2 (Bruker, USA) offline software. All images were plane–fitted, and topography data for some images had noise removed using the low–pass filter and ‘clean’ function (streak and

spike  $\sigma_3$  cutoff). RMS roughness was determined on images of  $5 \mu\text{m}^2$  using the 'roughness' tool.

AFM TREC images acquired using Agilent SPMs were analysed using freeware Gwyddion data analysis software (<http://gwyddion.net/>). All images were plane levelled and line corrected using standard Gwyddion tools. Some images were also filtered using the 'scar' correction tool (similar to Bruker's 'clean' function). Recognition images were then analysed using freeware ImageJ v.1.43 analysis software (<http://rsb.info.nih.gov/ij/>): Images were converted to 8-bit, and then the threshold was adjusted so that recognition spots were black against a white background. Then the particle analysis function was used to determine recognition spot size, count, and area. The data was exported to Microsoft® Excel software for statistical analysis.

Masking was done using the 'add mask' function in Gwyddion onto topography images using the recognition channel, and the 'subtract mask' function was used to remove amplitude error channel crosstalk. Recognition and amplitude error channels were median filtered to 2 pixels, to reduce noise while preserving edges, before masking to make visualisation easier.

#### **4.3.3 Immunofluorescence Labelling**

Lens capsules were carefully cut into pieces and immobilized in wells of 6-well tissue culture plate (Iwaki, Bibby–Sterlin Ltd, UK) using 30 Gauge PrecisionGlide syringe needles (Benton Dickinson & Co, USA). For immunolabelling of the ZO–1 protein, the samples were washed three times in

### *Characterisation of the Protein Deposits of Pseudoexfoliation Syndrome*

PBS, blocked in 150  $\mu$ L 5% donkey serum/PBS for 15 min, hybridized with 150  $\mu$ L rabbit anti-ZO-1 primary antibody (Zymed Laboratories; 1:400 dilution) in 1% donkey serum/PBS for 1 h, and then with 150  $\mu$ L Alexa Fluor-488 conjugated goat anti-rabbit IgG secondary antibody (Molecular Probes; 1:1000 dilution) in PBS for 1 h. After each incubation, the samples were washed three times in PBS. The negative control sample was incubated with 1% donkey serum/PBS instead of a primary antibody. After labelling, the samples were mounted on microscope glass slides in buffered glycerol (2 : 1; Glycerol, NaHCO<sub>3</sub> (0.5 M). pH adjusted to 8.6 using Na<sub>2</sub>CO<sub>3</sub> (0.5 M)). Clusterin was similarly labelled with the rabbit anti-clusterin primary antibody (Santa Cruz Biotechnology Inc.; 1:250 dilution) in PBS without blocking the samples with donkey serum. Images in z-plane optical sections of 1  $\mu$ m intervals were taken on a Leica SP5 Confocal Microscope with Leica Application software using the Argon laser (excitation 488 nm, emission 525 nm). Image analysis was done using freeware ImageJ v.1.43 analysis software (<http://rsb.info.nih.gov/ij>).

## **4.4 Results & Discussion**

### **4.4.1 Pilot Study: Detection of Clusterin**

#### *4.4.1.1 Summary*

The investigation of PEX on the anterior lens capsule is an ongoing subject of international scientific research. Light microscopy has been used to observe tissue sections, however the resolution was insufficient to examine protein ultrastructure, and there is no 3-dimensional information available for the anterior lens capsule surface. SEM has also been used to observe the PEX lens capsule [373]. However, the sample must be dehydrated and coated with a conductive layer before imaging for standard SEM. Although a newer application of SEM called ‘environmental SEM’ is capable of viewing samples without a conductive coating, it is still not possible to use near-physiological environments. Hence, another technique was required to further investigate the anterior lens capsule in a physiological environment at high-resolution. AFM was considered as an ideal technique for this investigation. To determine the usefulness of AFM, control and PEX-affected lens capsules were first imaged under standard AC-driven TM conditions in fluid. Antibody-recognition imaging was then considered as a protein identification method as it had not been applied to unprocessed tissue before. Clusterin was used to test this system since it is more abundant in PEX-affected lens capsules compared to unaffected capsules and is known to be present in PEX material [333], [358]. AFM imaging yielded high-resolution topographical images of the capsule ultrastructure. AFM antibody recognition imaging detected the presence of clusterin on both control and PEX-affected lens capsules, but with a distinct distribution pattern. This pilot study demonstrates the potential of AFM

antibody recognition imaging for the analysis of unprocessed human tissue samples.

#### **4.4.1.2 Atomic Force Microscopy Imaging**

Since lens capsule tissue has not been previously used for AFM analysis, imaging (using a non-functionalised tip) was performed to optimize the technique of lens capsule mounting and to establish the relevant AFM parameters. Mounting using an adhesive surface was attempted, but this was unreliable, and raised concerns about contamination. As dehydration is often used in protein studies by AFM [189] and immunofluorescence [374], AFM measurements were attempted on a clean coverslip to simply dry the tissue in order to immobilize it, followed by rehydration for imaging. The surface of the control lens capsule was not observed to be affected by dehydration (Figure C2). Hence, drying of the lens capsule was used since this tissue adhered strongly to a clean glass substrate upon dehydration. Even after rehydration in MilliQ water for 24 h or more, the tissue remained tightly attached to the substrate. TM AFM imaging of the rehydrated lens capsule tissue with a non-functionalised tip, gave high-resolution surface images of both control and PEX lens capsules (Figure 4:2).

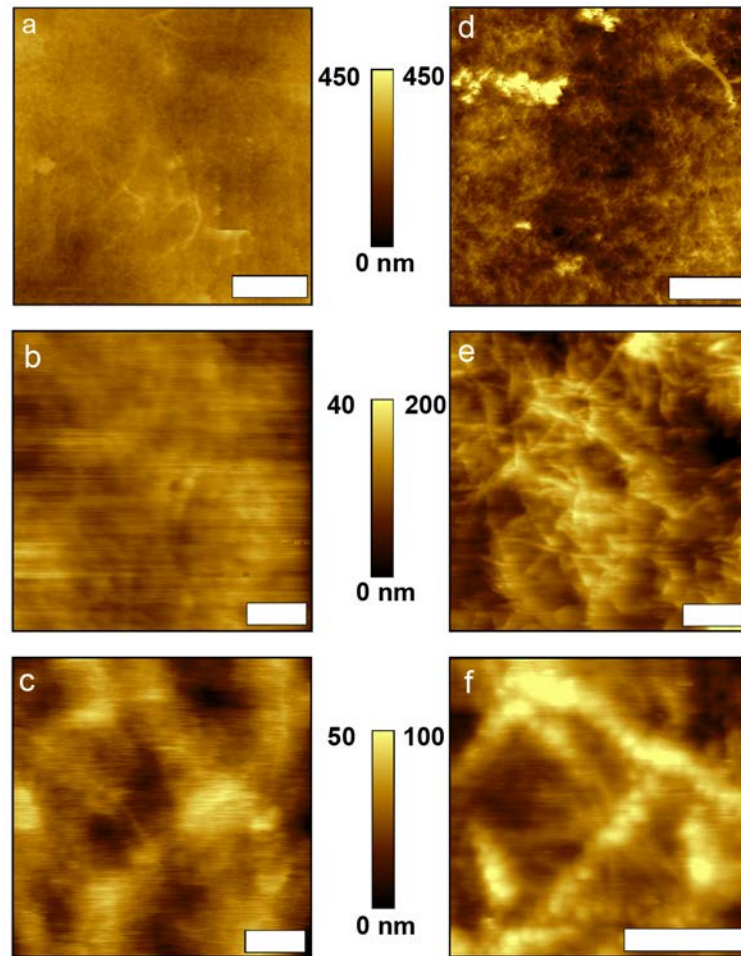


Figure 4:2 – TM AFM images acquired in PBS of (a–c) control and (d–f) PEX–affected lens capsules, at increasing magnification. a, d: Scale = bar 5  $\mu\text{m}$ . b, e: Scale bar = 1  $\mu\text{m}$ . c, f: Scale bar = 400 nm.

The control lens capsule surface was very soft, and many of the features were distorted or not resolved. However, the sample topography was mostly smooth, with small (1 – 10 nm high and 1 – 100 nm wide, Figure 4:2 b and c fibres seen across the surface. Large (25 – 50 nm high and 300 – 500 nm wide, Figure 4:2 a) fibres were also occasionally observed. These fibre–like surface features were expected, since the lens capsule is predominantly composed of the fibrous basement membrane proteins collagen IV and laminin. These fibrous proteins are networked with nidogen and perlecan [326] to form the basement membrane matrix.

On the other hand, the PEX lens capsules imaged in MilliQ water showed large (100 – 500 nm high and 400 nm – 8  $\mu$ m diameter, Figure 4:2 d) ‘bushy’ aggregates, similar to those seen by electron microscopy [375], [376]. The large aggregates appeared to be surrounded by and composed of fibres, a variety of which were observed when imaging at smaller scan areas such as seen in Figure 4:2 e and f. These fibres on PEX affected capsules were observed to be thicker and denser than on control capsules. These fibres ranged from large fibres 22 – 166 nm in height and up to 11  $\mu$ m in length to small smooth fibres in between the large ones 5 – 21 nm in height and up to 388 nm in length. On both control and PEX capsules granular fibres were occasionally observed, producing an effect similar to a string-of-pearls. This effect was pronounced in PEX images, as seen in Figure 4:2 f. Measurements for control lens capsules gave RMS roughnesses of 5 – 50 nm, whilst the PEX capsules were significantly rougher with values of 20 – 200 nm RMS. It should be pointed out that some areas of the PEX capsule contained large aggregates of PEX material which were unable to be imaged, leading to a large variability in roughness values. Hence, PEX images were acquired only on the areas of the capsule with moderate roughness. PEX deposits are not uniformly distributed across the lens capsule, and more deposits are seen in the peripheral area. This effect is known as the ‘bullseye’ pattern, and is likely due to physical rubbing of the overlying iris. Nevertheless, PEX is expected to be present across all areas of the lens capsule [373], [377], [378].

EM images [326], [349], [373], [379] of these tissues are incomparable in topography to the AFM images due to the completely different sample

preparation and scales. However, they do confirm the flat nature of the tissue and the presence of a fibrous protein network. This is another good example of how AFM has the distinct advantage over the majority of EM techniques since it is able to analyse samples in their native environment. Cryo-EM should be mentioned, however, as it has been used to successfully study hydrated elastic tissues [403]. Topography AFM images obtained using non-functionalised tips showed that the lens capsule is a suitable tissue for TREC imaging, since areas of less than 50 nm RMS roughness were easily found [109].

#### ***4.4.1.3 Force Spectroscopy on Free Clusterin***

Clusterin was selected as a model protein for the testing of applicability of TREC imaging to the human lens capsule, as it has been clearly implicated in the PEX pathology [321], [333], [358], and both the protein and antibody are readily commercially available. Further discussion on the biological role of clusterin follows in *The Biological Significance*, page 176.

The NHS-PEG<sub>800</sub>-aldehyde crosslinker was chosen since it allows easy and stable binding of (lysine containing) proteins to aminofunctionalised tips. This crosslinker has also been previously used for antibody experiments [370], and the published protocol was followed.

To verify the specificity of the antibody-protein interaction, force spectroscopy was carried out using recombinant human clusterin adsorbed on mica and an anti-clusterin coated AFM tip. Pull-off forces were between 12 – 85 pN with an average unbinding force of 40 pN. These values are slightly lower than other reported antibody-antigen forces [45]. However, they are within

experimental uncertainty. After incubation of the tip with clusterin to block the antibody, the number of unbinding events dropped from 7% to 2% at 300 nm/s tip velocity, indicating that the adhesion is occurring primarily due to the antibody–protein interaction, and validating the specificity of the modified probe. Force spectroscopy can also be used to determine the stretched linker length before unbinding. The average linker length was calculated as 20 nm ( $\pm$  4 nm), which is expected as the theoretical length of the linker combined with an antibody is 20 nm [63]. This information from the force spectroscopy data is useful for calculation of amplitudes necessary for TREC data collection.

#### **4.4.1.4 Topography and Recognition Imaging**

TREC imaging was applied successfully to both control and PEX–affected lens capsules in PBS buffer using anti–clusterin antibody functionalised AFM tips. PBS buffer has similar pH and ionic strength as the aqueous humour that bathes the lens capsule *in vivo*, and was therefore an ideal fluid for imaging conditions. Measurements were made in regions of interest of less than 5 x 5  $\mu\text{m}^2$  at a scanning speed of 1 line/s to allow for molecular reorientation and binding. The tip oscillation amplitude was adjusted to allow the linker to stretch, but not unbind, to dampen the upper motion of the cantilever oscillation (this amplitude varied from 10 to 50 nm). As seen in Figure 4:3 (right panels), the clusterin protein was detected on control lens capsules. In the following recognition images, dark spots represent amplitude dampening (*green arrows*), and these spots are correlated with topographical features in the same region of interest (*blue arrows*).

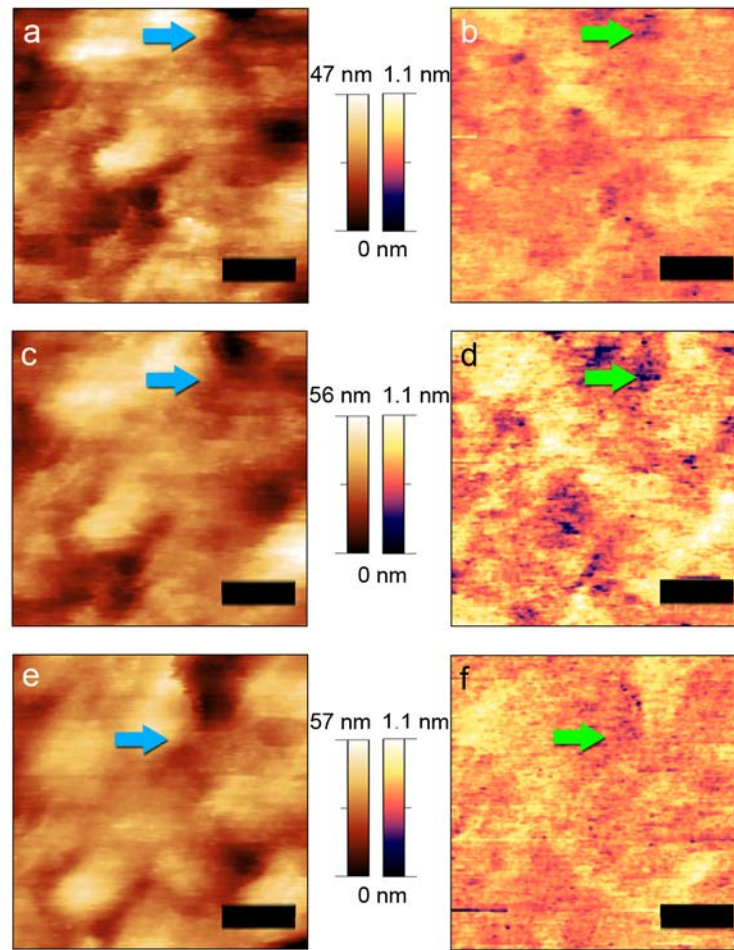


Figure 4:3– AFM images of control lens capsule mounted on a glass slide using MAC mode in PBS.

The left panels show topography images while the panels on the right show the corresponding TREC images. a and b are acquired with a tip oscillation amplitude of 22 nm, c and d with 33 nm, and e and f with 44 nm. These amplitude variations are a method for confirming antibody specificity. The blue arrows point out topographical features and the green arrows point out corresponding recognition features. Scale bars = 100 nm.

Recognition spots averaged  $240 \text{ nm}^2$  in area, representing small patches across the scanned regions, but did not seem to follow a specific distribution pattern. When compared to PEX capsule imaging, a difference in detection was observed: The dark spots corresponding to recognition (Figure 4:4, right panels) formed in larger patches, showing an increased localization of protein. Furthermore, these patches were observed frequently in-between large fibres or around the junction of multiple fibres.

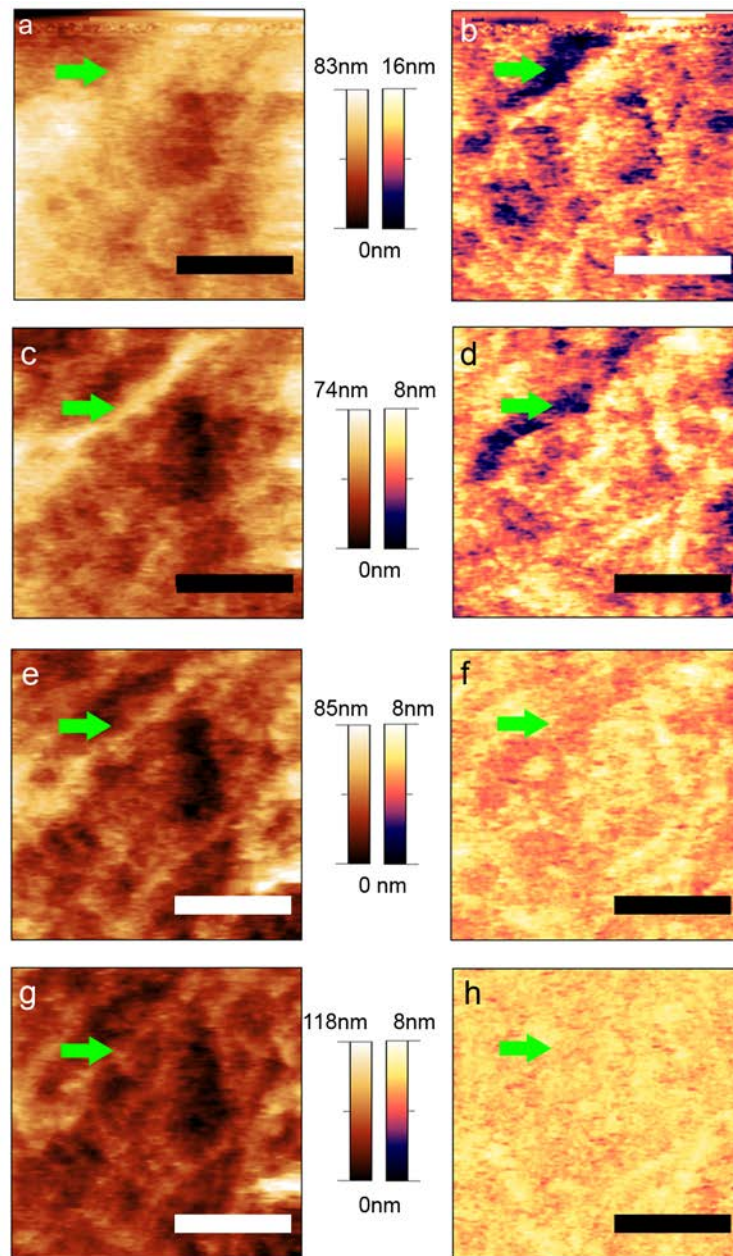


Figure 4:4 – AFM images of PEX lens capsule on glass using MAC mode in PBS. On the left are topography images while the right side is the corresponding recognition images. a and b are acquired with a tip oscillation amplitude of 15 nm, c and d with 30 nm, e and f with 45 nm, and g and h with 60 nm. These amplitude variations are a method for confirming antibody specificity. The blue arrows point out topographical features and the green arrows point out corresponding recognition features, for added visualization assistance see Figure C:6. Scale bars = 400 nm.

On the PEX-affected lens capsules, the area of recognition spots averaged 1791 nm<sup>2</sup>, with a general trend of having significantly larger areas of recognition than on normal lens capsules (Figure 4:5). An independent t-test verified the statistical difference in the mean recognition spot area between

normal and PEX capsules ( $t(1119) = 2.7$ , two-tail  $p < 0.007$ ), confirming the visually observed differences.

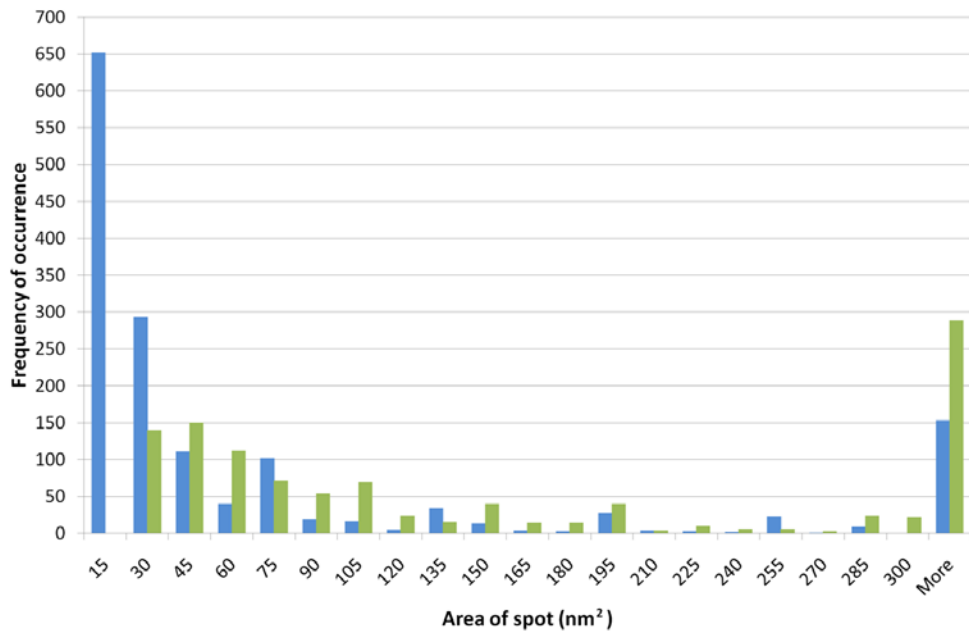


Figure 4:5– Frequency distribution histogram of TREC recognition spots observed across control (■) and PEX (■) lens capsule samples measured as a unit of area (nm<sup>2</sup>).

It is important to note that to determine clinical significance, one would require a far larger number of samples (two normal and two PEX capsules were analysed) than were used here. Furthermore, these results only reflect a qualitative difference in distribution of clusterin, and not a quantitative difference on the whole tissue.

Similar topography was observed using TREC imaging on both control and PEX capsules as were seen previously in Figure 4:2 using non-functionalised tips. Some difference in features in the topographical images acquired with TREC may appear broader than those acquired with a non-functionalised tip [109]. This may be attributed to the length of the linker used to immobilize the

antibody to the AFM tip, or to a tip broadening due to magnetic coating. One way of increasing image resolution is the use of a shorter linker. However, a shorter, less flexible linker may reduce or eliminate immuno-recognition, depending on the antibody orientation. Alternatively, fixation has been reported to enhance TREC image resolution [67], [111], [380]. Fixation was not attempted here, since the objective was to study the PEX aggregates in their native state.

Two control methods designed to remove the antibody binding event confirmed that recognition was specific for clusterin and not due to a topographical artefact. First, the introduction of free antibody into the solution, blocking surface-bound clusterin, resulted in a significant decrease in recognition as observed by the reduction in dark pixels (*green arrows*) in the TREC images (Figure 4:6).

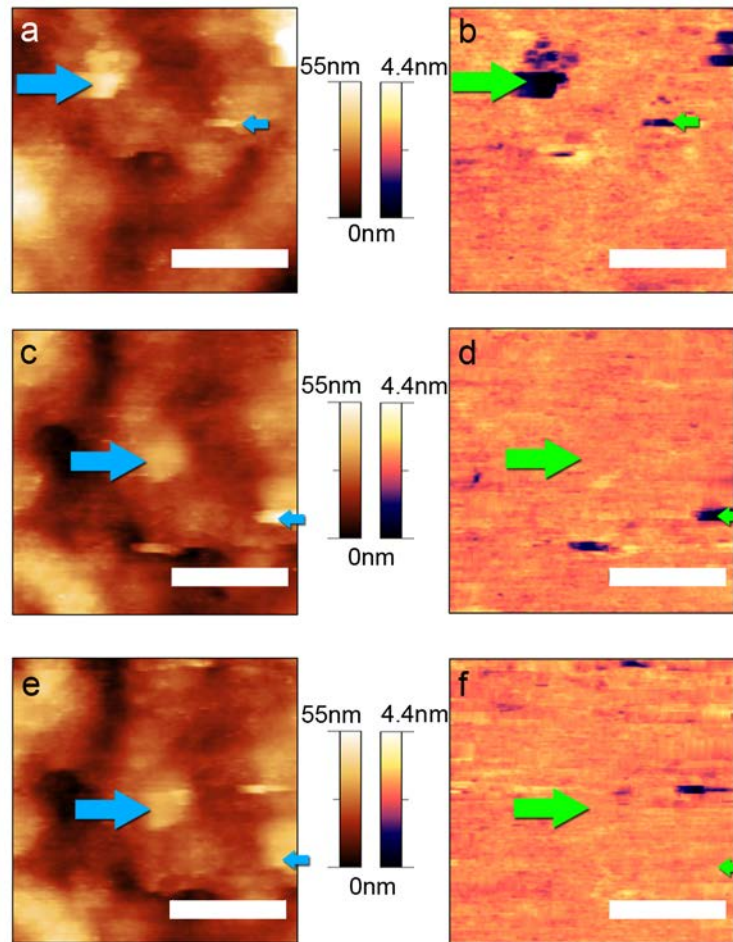


Figure 4:6 – AFM images of normal lens capsule mounted on a glass slide using MAC mode in PBS with injection of anti-clusterin antibody (150  $\mu\text{g}/\text{ml}$ ) to block surface-bound clusterin. On the left are topography Images whereas the right side is the corresponding recognition images. All images are acquired at a tip oscillation amplitude of 44 nm. (a and b) acquired before addition of antibody. (c and d) acquired 30 min after injection. (e and f) acquired 50 min after injection. The arrows point out corresponding topographical (left, blue) and recognition (right, green) features. Scale bars = 300 nm.

This method of blocking is not ideal since it contaminates the system [109] and does not allow further TREC measurements on the same sample. For this reason, it was only performed once. Second, a more convenient control method was applied for every area analysed. Recognition imaging is based on the use of the appropriate oscillation amplitude. If the linker is insufficiently stretched at low oscillation amplitudes or, alternatively, if the receptor–ligand–bond is broken at each oscillation cycle when using amplitudes greater than the stretched linker length, no pronounced and stable recognition events can be

observed. We therefore increased the amplitude (while keeping the ratio of amplitude setpoint and free amplitude constant) to values above a threshold value to prove the specificity of the interactions. Increasing the amplitude above the stretched length of the linker resulted in a breakage of the specific antibody–antigen bonds in the upper part of the oscillation [109] (Figure 4:3 e, f, and Figure 4:4 g, h); the disappearance of the recognition spots upon increasing the oscillation amplitude clearly demonstrates the specificity of the recognition. From force spectroscopy analysis, one would predict the threshold amplitude for this effect to be around 20 nm, the stretched length of the linker and the antibody. Note that the experimentally determined threshold amplitude while imaging was higher, up to 50 nm. This discrepancy may occur due to deformation of the lens capsule surface, contributing to the break–off length by acting as an additional spring. We also examined the amplitude error images (Figure C3) since these indicate any feedback artefacts (known as topographical cross talk) that can occur due to inadequate signal decay. However, by using a frequency lower than the cantilever resonant frequency at the surface, topographical cross talk can be minimised by allowing the topography signal to decay before the recognition signal is detected [109]. Therefore, it can be concluded that the features seen in the TREC images are due to recognition events between the antibody on the tip and the sample.

#### **4.4.1.5 Immunofluorescence Labelling**

IHC studies performed by Ovodenko *et al.* [333] confirmed a significant presence of the clusterin protein in PEX aggregates on sections of PEX–affected lens capsule. Such optical microscopy methods are limited in

resolution and are not able to distinguish individual proteins or fibres in the PEX aggregates. However, these are established procedures for confirmation of presence of a protein and potential distribution patterns. Immunofluorescent labelling was performed on whole lens capsules to further confirm the specificity of the antibody used, while also providing a technique to compare the TREC results to. Initially, clusterin was detected in fresh control lens capsules, as it is known to be present in the lens epithelial cells that remain attached to the posterior surface of the anterior lens capsule after surgery. Propidium iodide counterstaining revealed the nuclei, and clusterin was observed within the cells in the cytoplasm (Figure C4). However, this protocol required permeabilisation with methanol, which was not part of the AFM protocol. This treatment may cause antibody trapping leading to non-specific labelling. Therefore, further experiments were done without permeabilisation.

The negative control samples (without a primary antibody) did not show significant fluorescence on the anterior side of the lens capsule suggesting the signal obtained with the anti-clusterin antibody to be specific. These samples were immunolabelled with and without permeabilisation, with no difference seen. Additional control labelling performed with antibody against ZO-1, an intracellular protein, did not detect this protein on the anterior side of the capsule. Instead ZO-1 was seen on the posterior side in the remnants of damaged lens epithelial cells (Figure C5).

Clusterin was detected as a nearly homogenous layer across the anterior surface of the control lens capsule (Figure 4:7 a). It should be noted that in

PEX, the pathological material forms a layer across the lens capsule before it is clinically recognizable; as these controls come from cataract patients, there is a chance that the patient has sub-clinical PEX at the time of cataract surgery when lens capsule is collected. For this reason, two capsules from different patients were used to confirm this clusterin layer across the control anterior capsule, verifying that the clusterin is present in non-PEX cases. Yet, clusterin showed a significantly stronger immunofluorescence signal on the anterior side of the PEX lens capsule, indicating higher expression is coincident with PEX deposits (Figure 4:7 b).

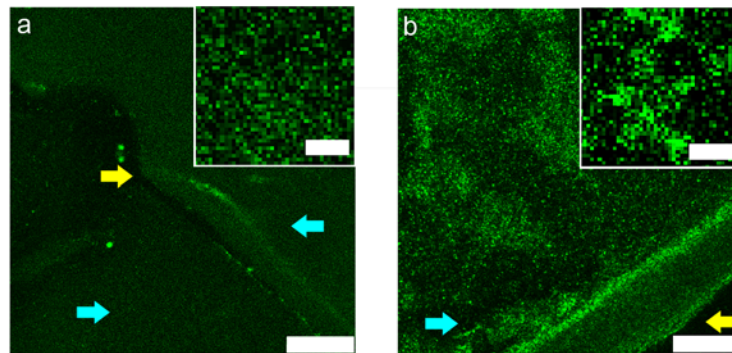


Figure 4:7 – Confocal microscopy images of the anterior side of (a) a control lens capsule (scale bar 20  $\mu\text{m}$ ) with inset of digital zoom (scale bar = 500 nm), and (b) a PEX-affected lens capsule (scale bar 10  $\mu\text{m}$ ) with inset of digital zoom (scale bar = 500 nm) immunolabelled with the anti-clusterin primary antibody and labelling detected with Alexa fluor-488 conjugated anti-rabbit IgG secondary antibody.

Image brightness curves adjusted for fluorescence visibility. Yellow arrows denote the edge of the tissue, and the cyan arrows denote the area of the image occupied by tissue. In a, this edge is due to the pinning procedure used during labelling, while b is the edge of the surgical cut of the lens capsule.

In particular, clusterin protein aggregates were more prevalent in PEX capsules. These results confirm that the PEX lens capsules have a different pattern of spatial clusterin distribution across capsule compared to control capsules. The immunofluorescence data is consistent with TREC results, as patches of clusterin were present on PEX-affected the lens capsules. However,

this technique is clearly insufficient for molecular topographical studies. TREC images acquired contain 512 points per  $\mu\text{m}$ , while fluorescence images contained only 40 points per  $\mu\text{m}$  at best, and are also unable to show the topography of PEX deposits. Furthermore, clusterin does not appear to be permeating the lens capsule from the lens epithelial cells in control or diseased capsules (Figure C4). This may be an important piece of the PEX pathophysiology puzzle.

#### ***4.4.1.6 Conclusions and Future Perspectives***

In this study, the AFM recognition imaging technique TREC was used for the first time to detect a protein on a human tissue sample. No fixation or processing of the tissue was applied. The pattern of apolipoprotein clusterin in the human lens capsule associated with the condition PEX, that increases the risk of developing glaucoma, a blinding condition, was investigated. After proving the specificity of clusterin to anti-clusterin antibody binding by force spectroscopy, the clusterin protein was demonstrated to be present on the surface of lens capsules using TREC and immunofluorescence. It was observed by both methods that clusterin aggregation patterns differed between normal and PEX lens capsules. This distribution pattern may be due to a chaperone response by the clusterin protein in response to the protein aggregation observed in PEX. Further investigations are warranted to confirm the pathological implications. However, this study successfully demonstrates the feasibility of TREC imaging of biological tissues, and may be used to analyse protein aggregates in a physiological environment.

Investigation of fixed tissue sections may also be conducive to TREC imaging which would expand the scope of this approach to the study of other diseases such as neurodegenerative disorders or cancers. The possibilities of TREC imaging are far-reaching and go beyond the exploration of proteins implicated in diseases. For example, this approach can be applied to the characterization of protein or tissue interactions with synthetic biomaterials. Likewise, physiological processes such as the formation of new basement membranes can be explored. These applications deserve further investigation given this successful proof-of-principle.

#### **4.4.2 AFM–Based Antibody Recognition Imaging: Technique Comparison for the Detection of LOXL1**

##### **4.4.2.1 Summary**

Following the success of the pilot study utilising clusterin, LOXL1 was considered a protein of high interest to the PEX investigations, due to the genetic association of the gene encoding this protein with the disease. Given the amino oxidase function of LOXL1, involved in the crosslinking of elastin fibres, it is conceivable that the protein may be intrinsically involved in the protein aggregates. Further discussion of the biological role of LOXL1 follows in *The Biological Significance*, page 176.

AFM antibody recognition is not limited to TREC as seen in the pilot study, however, and a variety of techniques are available for AFM antibody recognition imaging. Hence, three different AFM–based antibody recognition techniques are compared for the detection of LOXL1 on PEX–affected lens capsules; force–volume imaging, phase imaging, and TREC. TREC was identified as the best technique for investigations of unprocessed tissue samples such as the lens capsule.

##### **4.4.2.2 Force Spectroscopy**

Force–distance curves were collected on the PEX lens capsules. Figure 4:8 (a) shows a typical approach and retract force curve on a PEX–affected lens capsule with an anti–LOXL1 antibody functionalised AFM tip where no binding event was detected (purple curve). Offset from that curve, another force curve is shown in red, obtained on the same sample where a snap–off event is clearly seen due to unbinding of the AFM–bound antibody from the

tissue surface after the PEG crosslinker has fully extended.

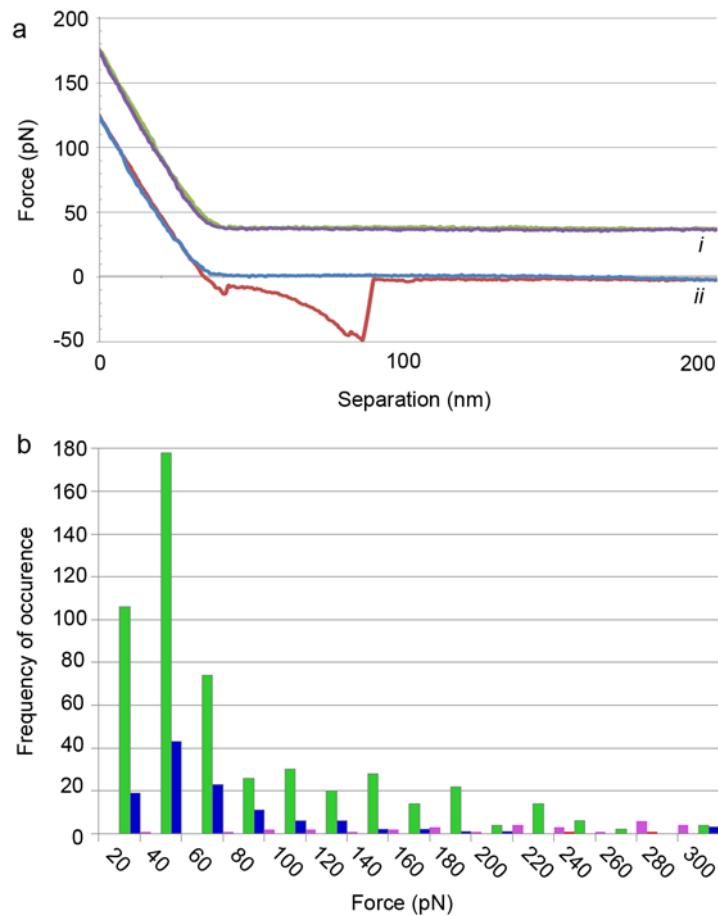


Figure 4:8 – Force spectroscopy detection of adhesion between sample and functionalised probe.

(a) Sample force-of-deflection vs. tip-sample separation curves are displayed, where the lower retract curve (ii) shows an unbinding event, offset from a retract curve showing no adhesion (i).

(b) Frequency distribution histogram of the force of unbinding detected using (■) a non-functionalised tip, (■) an APTES-functionalised tip, (■) an anti-LOXL1 antibody functionalised tip and (■) the same tip after blocking of surface LOXL1 sites with free anti-LOXL1 antibody in solution.

When using a non-functionalised tip on the surface of a PEX-affected lens capsule, the frequency of binding events due to non-specific adhesion was 3.14%. In turn, AFM tips which were functionalised first with an APTES coating resulted in 0.23% binding events, whilst those further functionalised with anti-LOXL1 antibody via the PEG<sub>800</sub> crosslinker showed up to 27.62% binding events. The percentage of binding events was reduced to 12.23% on

addition of antibody in solution into the AFM fluid cell. Incomplete blocking may occur due to mobility of free antibodies in solution, allowing dissociation of ligand–receptor pairs. Furthermore, insufficient antibody may be present to block all ligands; therefore, increasing concentration of free antibody may reduce binding events further. Nonetheless, the significant reduction of binding events seen here demonstrated the effect of blocking of recognition of ligand sites.

Figure 4:8 (b) shows a frequency distribution histogram of forces represented in the positive binding events. The mode of the unbinding forces seen in Figure 4:8 (b) was 40.5 pN and 40 pN for the antibody–functionalised tip and functionalised tip on the blocked surface, respectively. The unbinding force for the functionalised tip was within the expected range for an antibody–antigen unbinding [18], [45]. For the bare and the APTES–functionalised tip, infrequent higher force events peaking at 280 pN and 240 pN, respectively, were observed. Those were attributed to tissue elasticity (causing non–specific adhesion to be included despite the exclusion of <15 nm unbinding lengths), non–specific adhesions [381], multiple tip–surface interactions [382], sample roughness [29], alternative protein or surface conformations [67] or due to environmental noise. Although this technique is robust and reliable for investigating antibody–antigen interactions, it is not possible by itself to determine the location of proteins across a surface. The use of force spectroscopy for lateral recognition imaging is performed and discussed further in Force–Volume Imaging, page 171.

#### **4.4.2.3 Topography and Recognition Imaging**

Two lens capsules from patients diagnosed with PEX were imaged using the PicoTREC system with an AFM tip functionalised with anti-LOXL1 antibodies using a heterobifunctional PEG<sub>800</sub> crosslinker. The targeted areas contained fibrous material similar to that seen in Figure 4:2, page 150. LOXL1 was detected on the PEX-affected lens capsule as seen in Figure 4:9 b (i), represented by the dark areas of the image. These dark recognition areas correspond to the topography image shown in Figure 4:9 a (i). Therefore, LOXL1 was detected on the fibres shown in the topography image, as these images are collected simultaneously.

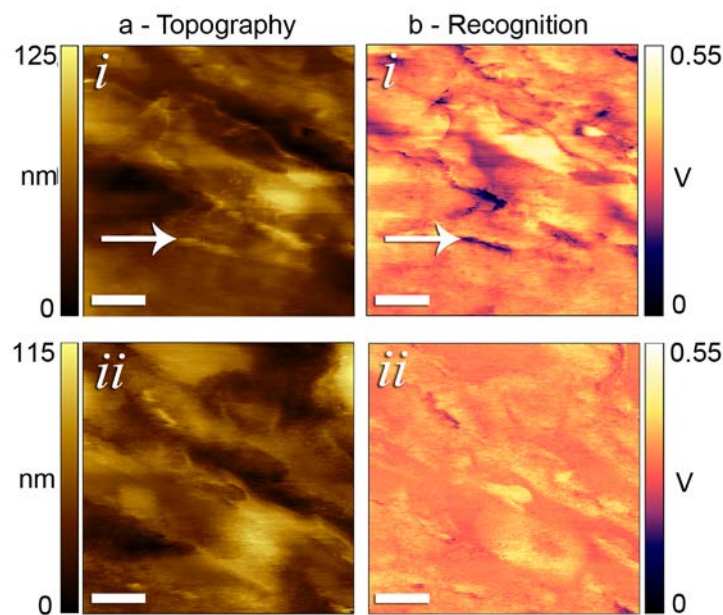


Figure 4:9 – AFM (a) topography and (b) recognition images of a lens capsule from a PEX patient acquired using an anti-LOXL1 antibody functionalised tip. Images acquired (i) with a tip oscillation amplitude of 30 nm (arrows denote the relative position of a recognition area in relation to the topography features), and (ii) with a tip oscillation amplitude of 54 nm display a reduction in recognition which affords proof of recognition specificity (scale bars = 200 nm).

All recognition data presented were confirmed by tip oscillation amplitude adjustment to remove LOXL1 recognition [109]. As the amplitude was

increased, the crosslinker no longer stretched to stunt the recognition signal as the antigen–antibody bond breaks. This effect was seen through Figure 4:9 b (ii), where the tip amplitude oscillation is increased up to 60 nm, removing dark areas representing recognition in the image. The amplitude oscillation at which recognition is removed should include the length of the linker and antibody (15 – 20 nm). However, the tissue is a heavily cross–linked basement membrane and will therefore provide some elasticity, acting as an additional spring.

This study is by no means exhaustive, and further research into the localisation of LOXL1 on the surface fibres of PEX may reveal associations with particular sizes or shapes of fibres, and may co–localise differently across the capsule (further experiments and discussion in 4.4.3 The Biological Significance of TREC results, page 176). It is also possible that there is more LOXL1 present on the PEX material than detected by TREC, as only available epitopes at the surface can be detected with this method. However, TREC is shown here to be a fast technique to apply to protein aggregation investigation on whole tissue samples with high lateral resolution. It is also easily verified by the amplitude oscillation modification technique, making it a preferable methodology compared to other AFM antibody–recognition techniques.

#### **4.4.2.4 Phase Imaging**

Phase imaging using antibody–modified probes is an alternative method to TREC. A specialized AFM accessory is not required, and any modern AFM capable of AC mode imaging is already equipped with phase detection.

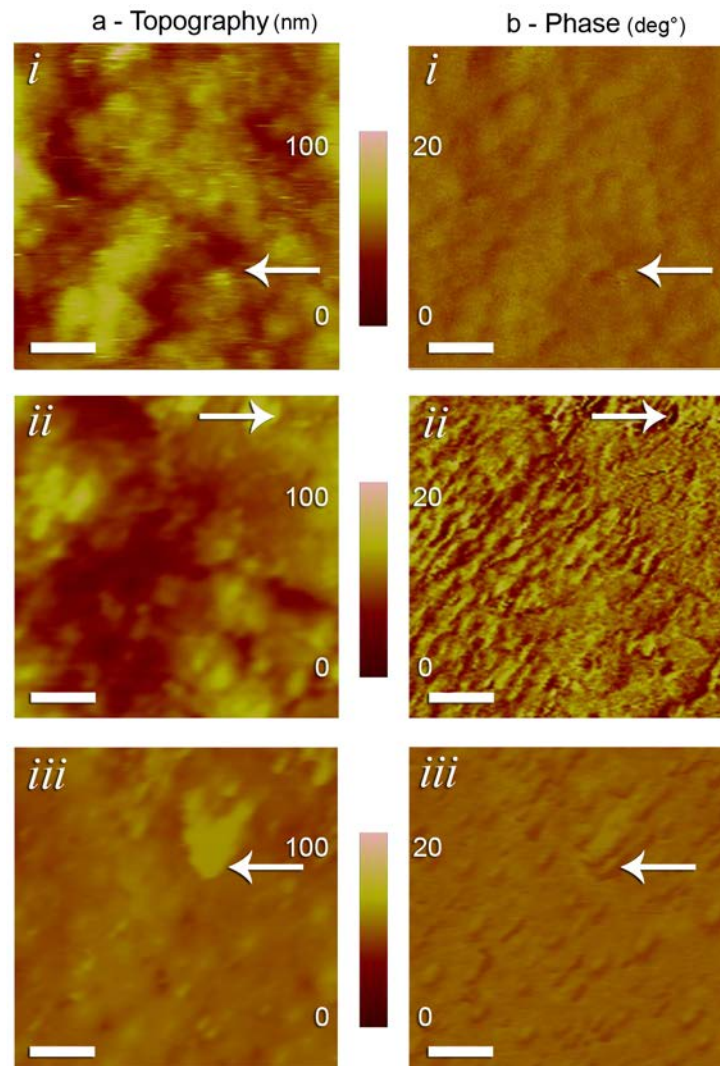


Figure 4:10 – AFM (a) topography and (b) phase images of a lens capsule from a PEX patient acquired in TM in PBS, using (i) a non-functionalised tip, (ii) a functionalised tip and (iii) the same tip after blocking of surface LOXL1 sites with free anti-LOXL1 antibody in solution. White arrows denote the relative position of phase contrasting areas in relation to topographical features (scale bars = 200 nm).

The PEX capsule was first imaged with non-functionalised tip, yielding the topography and phase images seen in Figure 4:10 a and b (i). As there should be no immunorecognition in this case, this response reflects topography-influenced phase shifts, surface adhesion and material stiffness. It is clear when comparing the phase image to the corresponding topography image (Figure 4:10 a (i)) that much of the phase signal is influenced by the surface roughness

[383]. When using another tip, this time functionalised with anti-LOXL1 antibody using the same crosslinker as before (Figure 4:10 b (ii)), the image contrast increased, reflecting increased tip-surface interactions. By blocking free LOXL1 epitopes on the surface of the tissue with an injection of anti-LOXL1 antibody into the AFM's fluid cell, the change of the phase signal upon blocking the ligand sites on the sample was observed. Due to the system feedback being affected, the topography image (Figure 4:10 a (iii)) had drifted and the introduction of the anti-LOXL1 antibody appeared to have changed the topography. However, it can be seen that the contrast in the phase image in Figure 4:10 b (iii) decreases, indicating a disruption of the tip-surface interactions due to the protein blocking. This blocking method has certain disadvantages, as it contaminates the sample and can only be done once per sample, therefore severely limiting the area that can be investigated per sample. Also, the introduction of new solution into the fluid cell affects the feedback system, introducing thermal drift in the piezoelectric scanner. Furthermore, inter-experimental variation due to tip shape, amplitude set point and sample softness give rise to phase variations and artefacts. This AFM antibody-recognition technique is not applicable to whole tissue samples, or any rough biomaterial which may contain multiple surface attributes detectable by phase imaging. This is due to the difficulty in excluding the influence of parameters such as sample topography or changes in sample stiffness contributing to the phase signal.

#### **4.4.2.5 Force–Volume Imaging**

Force–volume imaging using antibody–modified probes utilises force spectroscopy (as seen with clusterin characterisation, page 152) to map the tip interactions across a surface. As with phase imaging, a specialized AFM accessory is not usually required, and any modern AFM capable of acquiring force curves can be used for force–volume imaging.

The adhesion forces were mapped in Figure 4:10 b (*i – iii*), for a non–functionalised, an antibody–functionalised and a functionalised AFM tip after epitope blocking, at a resolution of 32 x 32 pixels. The corresponding topography maps at the same resolution are shown in Figure 4:11 a (*i – iii*).

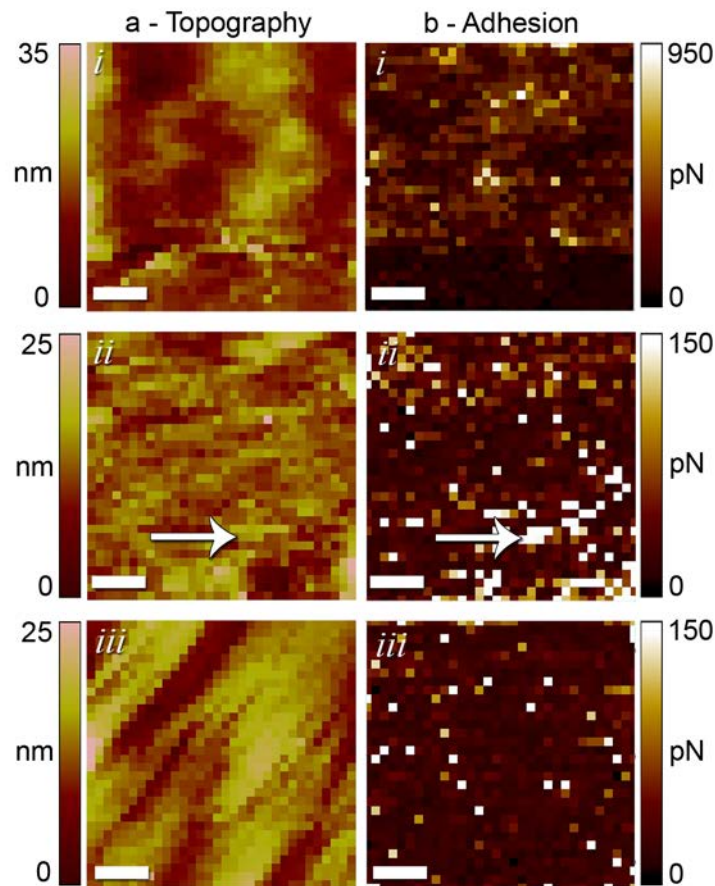


Figure 4:11 –AFM (a) topography and (b) adhesion map images with 32 x 32 pixel resolution, using (i) a non-functionalised tip, (ii) an anti-LOXL1 antibody functionalised tip and (iii) the same tip after blocking of LOXL1 epitopes on the tissue surface with anti-LOXL1 antibody in solution. The white arrow denotes an area of strong adhesion relative to corresponding topographical features, for added visualization assistance see Figure C:6 (scale bars = 100 nm).

The comparison between the adhesion and topography maps shows clearly where immunorecognition events occurred; the percentage of pixels showing maximum adhesion forces between 0 – 150 pN are 1 %, 12 % and 11 %, for the non-functionalised tip, LOXL1-functionalised tip and functionalised tip with blocked surface, respectively (n = 1024 for each tip). In Figure 4:11 b (ii), LOXL1 is co-localised with the fibrous surface features, as seen in the corresponding topography image (Figure 4:11 a (ii), white arrow, or Figure C:6 (cyan outline)). Some z-drift was observed in the shifting of the force curve baselines, however a baseline correction was employed to equalise this effect,

and some x,y drift also occurred due to the timeframe of the experiment. This drift is obvious when comparing Figure 4:11 a (ii) and (iii).

The downsides of this technique as compared to TREC imaging, besides the higher probability of drift-related artefacts, are that the image acquisition in force volume imaging is far more time consuming and that the resolution is limited. For example, a 1  $\mu\text{m}$  TREC image acquired with 512 x 512 pixels will take 4.3 min to acquire at 2 lines/s, whereas a 500 nm force-volume image acquired with only 32 x 32 pixels takes around 30 min to acquire. Also, careful data analysis is required to ensure that adhesion forces from antibody-antigen snap-off events are plotted rather than other features in the force curve due to changes in the sample surface softness and adhesion. Over the timeframe of the experiment, drift in the x,y,z position is difficult to exclude, and this severely limits the resolution of the technique. Again, blocking of the immunorecognition needs to be performed by injecting free antibody or, alternatively, by injecting LOXL1 into solution to block the antibody on the AFM tip. The latter was not done since we did not have access to a commercial source of LOXL1 protein. In any case, this method of blocking contaminates the system and introduces thermal drift.

#### ***4.4.2.6 Conclusions and Future Perspectives***

LOXL1 was detected on lens capsules affected by PEX syndrome by three different AFM-based antibody recognition techniques; TREC, phase and force-volume imaging. The protein was found in localised regions, associated with fibres on the surface, supporting an important role in the formation of the

filamentous protein aggregates, which are the hallmark of the PEX pathology. As the LOXL1 protein has been shown to be an integral component of PEX material [321], [352], it may be implicated in the pathological formation of PEX deposits. In particular, it is conceivable that given its amino oxidase function, LOXL1 may become embedded into or remain attached to the elastic fibres that eventually form part of the PEX material after performing cross-linking of elastin. This function is further discussed in the next chapter.

The data also show that AFM-based antibody recognition techniques are well suited to detect the presence of specific proteins on human lens capsule tissue in a near-physiological environment at a molecular level, whilst other protein-identifying methods, such as immunogold labelling, IHC or immunofluorescence, are often either of insufficient resolution, require excessive sample preparation, or require imaging in non-native environments [353], [384], [385]. Admittedly, the results presented here need to be viewed in the context of a proof-of-principle study having used a small number of PEX-affected capsules and concentrating on a single protein. However, the results are encouraging to integrate this technique into a detailed study of PEX in combination with genomic and proteomic analyses.

In terms of differentiating the three techniques, phase imaging and force-volume imaging can be performed on conventional AFM instruments using common AFM probes. However, in phase imaging, it was difficult to exclude the influence of parameters such as sample topography, tip geometry, or changes in sample stiffness contributing to the phase signal. Force-volume

imaging in turn was slow and of low-resolution in comparison to the other two techniques. In both cases, control experiments required the use of free antibody in solution to block epitopes on the tissue surface, contaminating the sample in the process and introducing thermal drift in the AFM experiment.

Overall, TREC was the most suitable technique for studies of this type. As TREC data were collected simultaneously at high-resolution, recognition maps are easily comparable to the topography of the surface. Furthermore, blocking of the recognition signal could be done by tip oscillation amplitude adjustment without contaminating the sample or introducing drift. TREC is a relatively new technique, with data collected on biological specimens only emerging in recent years [120], [380]. However, the applications of this technique in the biosciences are far-reaching and go well beyond the analysis of protein aggregation on tissues.

#### **4.4.3 The Biological Significance of TREC results**

##### **4.4.3.1 Summary**

The application of topography and recognition imaging to whole tissue samples is an important methodological advancement for the investigation of human diseases. To investigate the pathophysiological basis for the ocular disease PEX, the proteins clusterin, LOXL1 and elastin were detected on lens capsules from human patients undergoing cataract surgery. The lateral localisation on the surface at higher resolution than previously reported was shown for all three proteins. In this next section, the biological function and expression of each protein is briefly introduced, and the relevance of the TREC recognition patterns discussed with reference to the function of each protein. Although none of the proteins were found to co-localise with each other using this technique, the roles of clusterin, LOXL1 and elastin in the pathological accumulation of PEX material are suggested based on the recognition features observed.

##### **4.4.3.2 Proteins Detected by TREC in Pseudoexfoliation Material**

###### **4.4.3.2.1 Clusterin**

Clusterin has been implicated in pathology of the neurodegenerative Alzheimer's disease [357]. The protein is expressed as a 449 amino acid chain, and is then proteolytically cleaved to remove the 22 amino acid secretory signal peptide. Further cleavage between residues 227/228 generates the so-called alpha and beta chains, which arrange in anti-parallel fashion via disulphide linkages to produce the final heterodimeric protein [386]. Clusterin's primary known function is as a molecular chaperone, in response to cellular stress and to inhibit apoptosis [386], [387]. It is

down-regulated in anterior segment tissues of PEX affected eyes and is an integral component of PEX deposits [333], [344], [358], [374], [388].

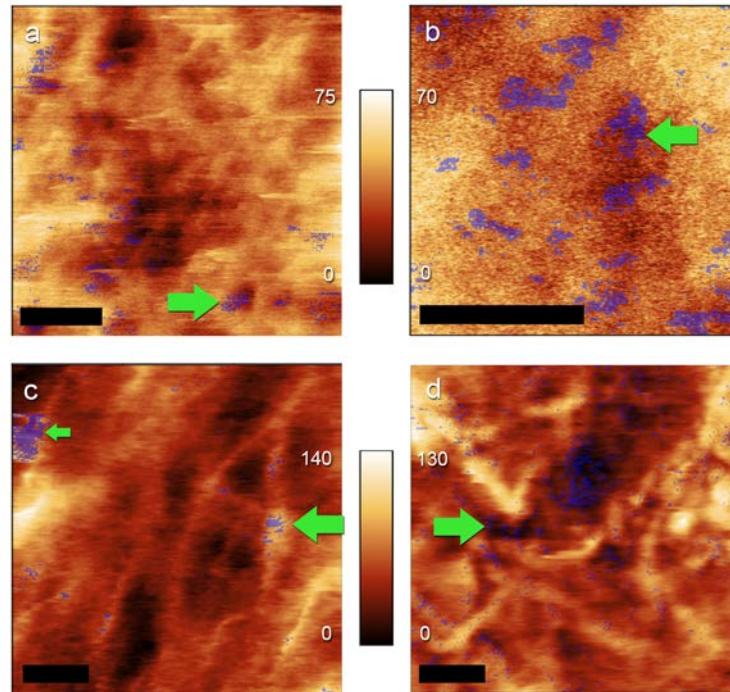


Figure 4:12 – AFM topography images of (a, b) control and (c, d) PEX-affected lens capsules acquired using an anti-clusterin antibody functionalised tip, overlaid with TREC recognition in blue.

Green arrows denote recognition of (a, b) pits, (c) junction of two fibres (large arrow) and a large spot (small arrow), and (d) a pit adjacent to a junction of fibres.

As seen in Figure 4:12 (a, b) and in Figure 4:12 (page 155), clusterin recognition was most commonly observed associated with pits and large (>50 nm width) spots. For the control capsules, there were smaller recognition patches which did not always reflect a specific topographical feature. PEX-affected capsules showed recognition associated with large (>50 nm width) fibres (Figure 4:4, page 155, green arrows). Recognition was often observed on or near the junctions of fibres, as seen in Figure 4:12 (c, d – large green arrows), and on large (>50 nm width) spots (Figure 4:12 c – small green arrow). Although, some small (<50 nm width) fibres were observed in the

topography images for which recognition was not observed. A total of 4 samples were investigated for clusterin detection; 2 control and 2 PEX-affected lens capsules.

#### **4.4.3.2.2 Lysyl Oxidase-Like 1**

LOXL1 is an extracellular enzyme with a copper-dependent amine oxidase function, catalysing the first step in the formation of crosslinks in fibre formation of collagens and elastin – an integral part of the basement membrane forming the lens capsule [389]. According to the literature, LOXL1 is also involved in developmental regulation, senescence, tumour suppression, cell growth control, and chemotaxis, indicating that it has multiple physiological roles [389–392]. Given the fibrillar nature of PEX pathology, it is the fibre formation function of LOXL1 that is relevant here.

Although LOXL1 is produced as a 417-amino acid pro-protein, post-translational modification cleaves the N-terminus, leaving a 249-amino acid active enzyme [393]. Before cleavage, the N-terminus is glycosylated and the protein is folded to contain at least three disulfide bonds [394], along with incorporation of copper [395] and lysyltyrosine quinone [396]. Finally, the pro-protein is secreted, and the glycosylated N-terminus is cleaved once the extracellular matrix is detected to reveal the mature enzymatically active LOXL1 protein [389], [397], [398].

The lysine residues in the C-terminal region of elastin monomers (tropoelastin) are de-aminated by the mature LOXL1 enzyme, resulting in aldehyde groups

capable of forming covalent cross-linkages with adjacent lysine residues. LOXL1 also binds with fibulin-5, assisting in the regulation of growth and deposition of tropoelastin onto extracellular matrix scaffolds for elastic fibre homeostasis [390]. *LOXLI* mRNA expression in ocular tissues is increased in the early stages of PEX, then significantly decreased in advanced PEX [399] with reference to control tissue expression.

Two coding single nucleotide polymorphisms in the *LOXLI* gene confer higher susceptibility to PEX [352], [360], [362], and LOXL1 has been shown to be present in PEX deposits using both MS and IHC [321]. It is therefore known that LOXL1 has a role in the pathophysiology of PEX. LOXL1 has been shown to be localised to mature PEX fibres using immunofluorescence and EM immunogold labelling on PEX-affected capsule sections [399], however the lateral distribution of LOXL1 is unknown.

AFM-based antibody recognition imaging was successful in detecting LOXL1 and clusterin on PEX-affected lens capsules, with TREC imaging determined to be of most use in investigating this disease. However, the initial studies seen in 4.4.2 AFM-Based Antibody Recognition Imaging: Technique Comparison for the Detection of LOXL1, page 164, used only one PEX-affected capsule, hence further imaging was done to increase the significance of LOXL1 data on PEX-affected lens capsules by increasing the sample number to four capsules. Furthermore, four control capsules were included in order to determine if LOXL1 is present in non-diseased tissue, and to observe any differences in localisation in the diseased state.

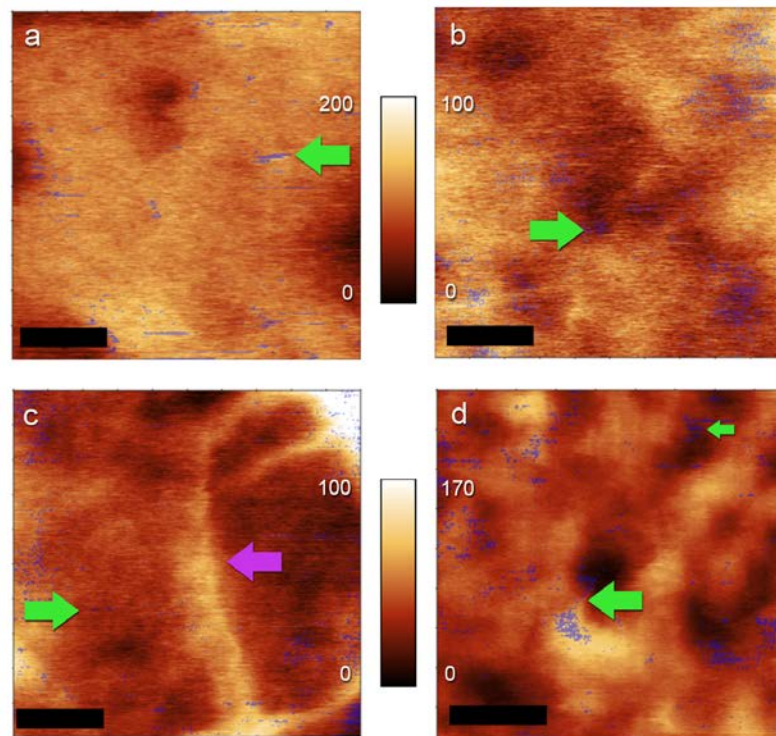


Figure 4:13 – AFM topography images of (a, b) control and (c, d) PEX-affected lens capsules acquired using an anti-LOXL1 antibody functionalised tip, overlaid with TREC recognition in blue.

Green arrows denote recognition of (a) a small fibre, (b) the edge of a pit, (c) a small fibre, and (d) a small fibre (large arrow) and the edge of a pit (small arrow). The purple arrow in (c) denotes a large fibre showing no recognition.

As seen in Figure 4:13 above, and in Figure 4:9 on page 167, LOXL1 was detected on both control and PEX-affected lens capsules. It was most commonly associated with small (<50 nm width) fibres and the edges of pits, regardless of disease status, as shown by the green arrows in Figure 4:13. LOXL1 was also detected on large (>50 nm width) spots and fibres on PEX-affected lens capsules. Very little inter-sample variation was seen with respect to recognition features on PEX-affected lens capsules, whilst recognition on or beside pits (Figure 4:13 a, d) on control capsules did not follow any trends, even on the same sample. There was comparatively less association with topographical features in the control capsules, with more recognition spots not

being clearly associated with topographical features. Given its involvement in extracellular matrix production, the detection of minimal LOXL1 in control capsules is expected.

#### **4.4.3.2.3 Elastin**

As collagen has not been identified as a major component of PEX, and elastin epitopes have been detected in PEX material, elastin is therefore the most likely candidate for LOXL1 cross-linking in PEX. Hence, elastin was targeted on PEX-affected lens capsules using TREC to investigate potential associations between LOXL1 and elastin in PEX deposits.

As discussed in the previous section, LOXL1 is responsible for cross-linking tropoelastin monomers into fibrous arrays. Tropoelastin is an 830 amino acid protein with alternating hydrophobic and lysine-rich domains [400]. This monomer is water soluble, however the deamination of the lysine residues leading to cross-linking changes the structure such that some of the hydrophobic residues are available, hence the cross-linked protein becomes insoluble. Elastin forms the core of elastic fibres in connective and supportive tissues and is a major component of the extracellular matrix and PEX [356], [384], along with fibrillin [401] .

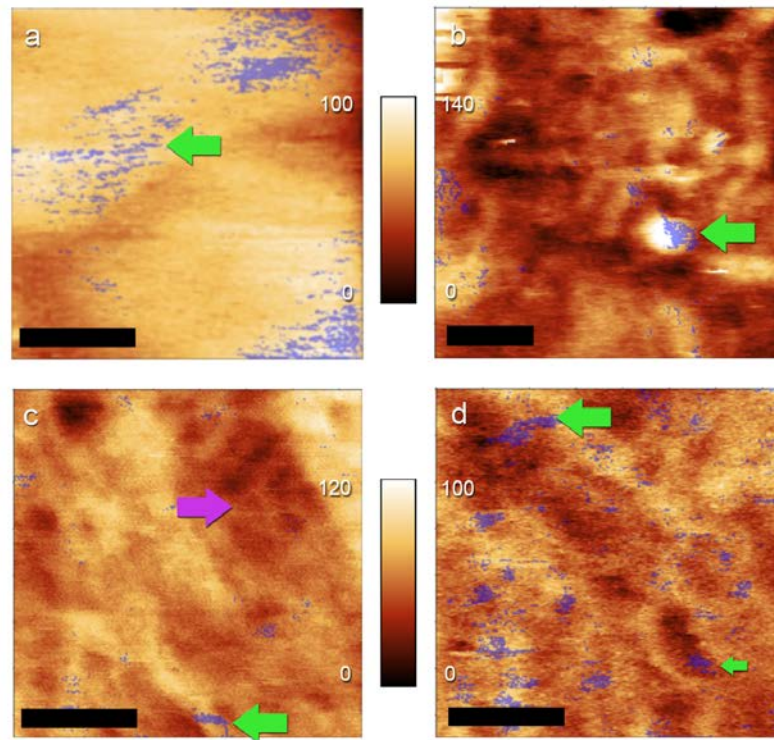


Figure 4:14 – AFM topography images of (a) control and (b – d) PEX-affected lens capsules acquired using an anti-elastin antibody functionalised tip, overlaid with TREC recognition. Green arrows denote recognition of (a) no specific topographical features, (b) the side of a large spot, (c) a large fibre, and (d) a large fibre (large arrow) and the edge of a pit (small arrow). The purple arrow in (c) denotes a small fibre showing no recognition.

Only one control capsule was imaged using the anti-elastin modified probe, in which no fibres were observed (Figure 4:14 a). The presence of elastin in extracellular matrices such as the lens capsule is well established [326], [400], [402], [403], and it is the comparison of elastin to LOXL1 in PEX-affected tissue that is of interest in this case.

In PEX-affected lens capsules, elastin was most commonly associated not with the small (<50 nm width) fibres as seen with LOXL1, but with large (>50 nm width) fibres and spots instead, as seen in Figure 4:14 (b – d). There is also a large amount of recognition observed without association to specific topographical features. This may be due to detection of lamellar elastin, or the pre-crosslinked monomer, tropoelastin. As seen with LOXL1 recognition on

normal capsules, detection of elastin on or beside pits is not consistent either between samples or on the same sample. Interestingly, detection on the sides of large spots (Figure 4:14 b) was observed primarily on one sample, while the other PEX-affected capsule showed detection on top of large spots. A larger sample size would be required to further investigate this pattern of recognition.

#### **4.4.3.3 Comparison of Protein Co-Localisation in PEX**

As seen in Table 4:2, and in 4.4.1 Pilot Study: Detection of Clusterin (page 148), the recognition spot sizes are both larger ( $1791 \pm 573 \text{ nm}^2$ ) and more frequent ( $n = 1517$ ) on PEX-affected capsules compared to control capsules ( $240 \pm 34 \text{ nm}^2$ ,  $n = 1112$ ) for detection of clusterin. The presence of large spots of clusterin in PEX material could be due to clusterin associating with aggregates as a response to cellular stress or an attempt by the natural system to clear abnormal aggregation of other proteins through its chaperone function [387], [404], [405]. If so, the natural system may be being overwhelmed, leading to an increased accumulation of clusterin. Another possibility is the inhibition of the chaperone function of clusterin by another molecule. Clusterin is known to bind to a variety of biological molecules, including those involved in the fibre-forming amyloidosis such as beta-amyloid [406]. However, amyloid proteins are not known to be expressed in ocular tissue. Three proteins known to be present in ocular tissues which also bind to clusterin are and apolipoprotein A1 [407], heparin [408] and paraoxinase, involved in lipid metabolism, anticoagulation and oxidative damage protection, respectively. It is well known that oxidative stress plays a role in the pathogenesis of PEX [366], [409], [410], therefore it is possible that clusterin binding and

aggregation is a key role in this process. Alternatively, interactions with another misfolded protein may be inducing aggregation of clusterin itself. Due to the multifaceted nature of the protein, however, its presence may actually represent several functions, including involvement in lipid movement, matrix stabilization, or other hitherto unknown functions [386], [404], compounding the complex nature of PEX pathophysiology.

Clusterin has been reported to co-localise with LOXL1 in immunofluorescence studies [399]. However, as seen in the morphological characterisation of recognition data in previous sections (Pilot Study: Detection of Clusterin – page 148, and AFM-Based Antibody Recognition Imaging: Technique Comparison for the Detection of LOXL1 – page 164, Figure 4:12 – page 177 and Figure 4:13, page 180), no co-localisation was observed in the TREC data of clusterin and LOXL1. Due to the resolution limitations of immunofluorescence on sections, the results cannot be compared with TREC data, as both proteins may simply be associated with PEX material at that resolution.

Similarly to clusterin, LOXL1 detection shows more spots of larger area on PEX-affected ( $89 \pm 8 \text{ nm}^2$ ,  $n = 3793$ ) compared to control ( $56 \pm 7 \text{ nm}^2$ ,  $n = 2918$ ) capsules, seen in Table 4:2. In general, however, the spot sizes are much smaller than those seen for clusterin indicating less ‘gathering’ of protein. The increased detection of LOXL1 in PEX-affected capsules may indicate an increased presence, as expected from IHC results [321], on diseased capsules. However, TREC is not a quantitative technique, and solubility and

homogenisation issues inhibit confirmation via a proteomic technique.

Table 4:2 – Comparison of recognition spot sizes between control and PEX-affected lens capsules seen for clusterin, elastin and LOXL1 proteins.

The % recognition describes the amount of pixels due to recognition with respect to the total number of pixels imaged. The P value describes the statistical significance of spot size comparisons between normal and PEX data for each antibody (where  $P > 0.05$  indicates no statistical difference). Note that the small image area of controls for elastin makes this calculation insignificant.

<i>Clusterin</i>	Spot size (nm <sup>2</sup> )	Spot count	Total image area (μm <sup>2</sup> )	% Recognition	P(T<=t) two-tail
PEX	1791 ± 573	1517	26.21	7.60	0.0070
control	240 ± 34	1112	26.21	1.39	
<i>LOXL1</i>					
PEX	89 ± 8	3793	20.24	1.66	0.0031
control	56 ± 7	2918	20.5	0.80	
<i>Elastin</i>					
PEX	47 ± 2	5492	17.25	1.49	0.6809
control	51 ± 10	1437	5.5	1.34	

Given that the recognition spots for LOXL1 were observed associated with small fibres in TREC images on the PEX-affected lens capsule, it is conceivable that the LOXL1 protein is becoming trapped or embedded in the elastin fibres it enables to crosslink, or is unable to dissociate from the ECM substrate. This may be a result of the sequence variant detected in the genetic associations with PEX, as these variants occur in the enzyme-activation and substrate-recognition portions of LOXL1 [352]: However, the LOXL1 genotypes of the patients from whom these samples were acquired are unknown, and so determination of this potential hypothesis is not possible with this data. If it is true that LOXL1 is becoming trapped with elastin, it follows that the elastin detected in PEX-affected capsules should chart a similar trend of recognition to LOXL1 as evidence of co-localisation. As only a small area of control capsule was investigated using an anti-elastin antibody modified probe, no significance can be attributed to the comparison between control and PEX-affected capsules. However, the percentage of recognition between PEX-

affected capsules of elastin and LOXL1 are comparable, yet a smaller spot size ( $47 \pm 2 \text{ nm}^2$ ) and increased spot count ( $n = 5492$ ) was seen for elastin on PEX-affected capsules in Table 4:2.

These results suggest that elastin and LOXL1 do not co-localise as hypothesised, as elastin is not significantly observed on the smaller fibres of PEX.

Interestingly, clusterin and elastin both associated with the larger ( $>50 \text{ nm}$ ) topographical features on PEX-affected capsules. However, the spots observed were not comparable in size or frequency (Table 4:2). Although these two proteins have not been reported to co-localise, both have been suggested to co-localise with LOXL1 in PEX deposits using IHC and immunogold TEM [352], [399]. However, these techniques require extensive sample preparation which would alter the native state of PEX fibres. Furthermore, the tissue is sectioned, hence laterally-oriented fibres would not be visible as fibres, and may become indistinguishable due to the resolution limitation of EM. TREC can be affected by large variations in topography, due to insufficient decay of the topography signal before collection of recognition data. Hence, the areas investigated by AFM were the relatively flat regions surrounding the larger PEX deposits. These areas certainly contain PEX material, but in smaller amounts than seen in IHC and TEM experiments. Whilst unlikely that the fibres would significantly differ in the relatively larger deposits, it is a consideration in the comparison of these co-localisation results. Ultimately, however, it is not entirely possible to compare these methodologies, due to sample preparation and resolution differences.

It is worth noting that due to a limitation of the TREC technique, the ligand epitopes must be available at the surface of the material to be detected [411]. As elastin has been observed as the central core of elastic fibres with a fibrillin coating [401], it is not surprising that the epitopes may not be available for TREC detection. Furthermore, mature PEX fibres may in fact be composed of multiple proteins, or may be oriented so that the elastin binding epitope becomes hidden during PEX fibre formation. It is also possible that epitopes for the protein may not be detectable with the utilised antibody. However, all antibodies used were confirmed to detect their respective proteins in control capsules using Western Blotting [321], [358] (Martin and Sharma, unpublished data). Admittedly, the number of PEX-affected lens capsules investigated using the anti-elastin antibody functionalised probes is half that investigated for LOXL1; however, there is no indication of co-localisation even in this small sample number. Due to the rarity and expense of reagents and samples, further investigations into elastin were not pursued as no new insights were becoming apparent.

#### ***4.4.3.4 Conclusions and Future Perspectives***

AFM antibody-based topography and recognition imaging has been applied to the whole tissue samples from cataract patients undergoing surgery. In clinically diagnosed PEX, fibrillar proteinaceous deposits build up on the lens capsule, among other ocular tissues. This material is thought to be composed of fibres from excessive production and abnormal aggregation of extracellular matrix proteins.

Three proteins involved in the production and homeostasis of extracellular matrices, clusterin, LOXL1 and elastin, were investigated using the AFM–based antibody–recognition imaging technique, TREC. The localisation of these proteins with respect to PEX fibres has been achieved at a higher resolution than previously observed. Increased aggregations of clusterin and LOXL1 are observed in the diseased state. The detection of large patches of clusterin in the diseased tissue was most likely due to the protein’s chaperone function. Despite its presence, there is still an accumulation of fibrous material. LOXL1 is responsible for the cross–linking of tropoelastin monomers into elastic fibres. However, evidence for co–localisation of these proteins was not found by TREC. Co–localisation of LOXL1 with elastin and clusterin has been observed previously in the literature using IHC and EM techniques [399], The conflicting results may be due to the variation in techniques used, or it may reflect the highly complicated pathophysiology of PEX.

The use of TREC in PEX investigations allows for analysis of the tissue surface in a physiological environment. Further, it offers a higher resolution than other immuno–based techniques utilising EM or optical/fluorescence microscopy. However, TREC has some drawbacks as a technique for investigations of protein aggregation disease:

- Time; the time to acquire images is limited by the kinetics of antibody binding as the probe approaches and withdraws from the surface. Hence, a maximum tip speed of 2  $\mu\text{m/s}$  limits the speed at which images can be acquired. Further time is taken to acquire each image multiple times at different probe oscillation amplitudes as a proof. At 5 min per 1  $\mu\text{m}$  image, the

minimum time to acquire an amplitude set for one area is 20 min, without accounting for sensitivity calibrations and optimising imaging parameters. Hence, the total area investigated can be severely limited by overall time of acquisition. Using EM and IHC, much larger (>15  $\mu\text{m}$ ) areas can be observed in one frame. It should be noted that sample preparation is less time consuming for TREC experiments.

- Sample choice; the sample size is limited by the confines of the equipment, and the sample roughness must be minimised to avoid topography and recognition crosstalk. The sample also must be immobilised to prevent movement.
- Immunorecognition; TREC operation relies upon the protein epitopes naturally being accessible at the tissue surface.

Further studies investigating the effects of tissue preparation to expose protein epitopes or utilising of alternate antibodies for probe functionalisation are recommended. Such future studies could be used to identify and localise more proteins on the tissue surface involved in PEX. Initially, fibulin and fibrillin protein investigations may reveal the reason for the delocalisation of LOXL1 and elastin by revealing the pathway leading from the small fibres that LOXL1 is associated with to the larger fibres and non-structured recognition of elastin. More proteins that are of interest in the ultrastructural studies of PEX are haemoglobin, CNTNAP2, and apolipoprotein E, as detected by MS or implicated in genome-wide associations. The potential function of these proteins in PEX pathophysiology is completely unknown, and any data

regarding the ultrastructural association with PEX material could yield new insights.

Additionally, investigation of further AFM antibody–recognition techniques, such as Bruker’s HarmoniX™ and Peakforce QNM™ may prove useful in the study of PEX syndrome. Although systems for proving recognition specificity may not be as robust as TREC, these systems are capable of faster acquisition times, and may employ a wider range of tip functionalisation procedures.

# Chapter 5

---

## **Conclusions and Future Perspectives**

## *Conclusions and Future Perspectives*

The goal of this thesis was to utilise and optimise AFM as a tool for protein investigations. Initially, the use of AFM in the literature for investigation of protein and peptide aggregation – such as the prion aggregation, and peptide-based organogel formation – was reviewed. Importantly, AFM was often not used in isolation but rather in conjunction with other analytical techniques such as EM, DLS, CD spectroscopy, immunofluorescence, and optical microscopy. By running experiments either in parallel, or examining the same sample by multiple techniques, the self-assembly mechanisms of fibre-forming molecules can be revealed.

Fibre-forming molecules are of interest for a variety of applications, including but not limited to microelectronics, tissue engineering, nanomaterials, and drug delivery. Novel controllable chemistries are in high demand, particularly those incorporating biological or biocompatible moieties for medical applications. The characterisation of self-assembling structures by AFM allows for morphological elucidation of the self-assembly pathways and is essential for the future development of controllable materials.

Peptide-based dendrons and dendrimers were analysed using TM AFM in air, in parallel with EM, fluorescence microscopy and Raman spectroscopy. A unique vesicle-driven pathway was observed by transmission electron microscopy for gelation of the L-lysine-based <sup>3rd</sup>- and <sup>4th</sup>-generation dendrons into a dense network of nanofibres. Symmetrical L-lysine dendrimers also formed nanofibre-based gels, which would turn pink upon UV irradiation due to the formation of tightly-packed gels with altered optical, Raman and

### *Conclusions and Future Perspectives*

fluorescence properties. This was shown to be due to topochemical polymerisation of the acetylene core of the dendrimers. Utilising a UV-blocking mask, the polymerisation was restricted to areas exposed to UV light, generating a pattern. These self-assembling gels might find applications in drug delivery and as tissue engineering scaffolds.

The morphological characterisation of surfaces is not limited to synthetic molecules incorporating biological moieties; indeed, recombinant proteins sequenced from the interface of the fungal symbiont *G. intraradices* also form fibres, and were characterised by AFM. rAGL1 was seen to form large ropey structures, while rAGL3 formed tube-like structures after incubation for one month. These proteins contained characteristic repeat regions, which were synthesised and shown to form fibrous structures. Interestingly, the structure of rAGL1 aggregates was quite similar to those formed by peptides based on rAGL1 repeat regions, suggesting that the repeat regions drive the self-assembly process. However, the same is not true of rAGL3, as the repeat regions did not form the tube-like structures observed for the full protein. This was hypothesised to be due to differences in the hydrophobicity of the non-repeat regions of the protein sequences. The structural properties of the fungal proteins are vital to the understanding of AM symbiosis, and also represent an opportunity to develop innovative self-assembling biomaterials, utilising the novel amphipathic repeat regions identified.

Molecular recognition is traditionally limited by the microscopic techniques available for detecting immuno-responses, such as immunogold EM which can

### *Conclusions and Future Perspectives*

only be performed in a vacuum or immunofluorescence which is limited in resolution by the diffraction limit of light. However, functionalisation of an AFM probe allows for molecular resolution of ligands in a physiological environment. This technique is ideal for investigation of protein aggregation diseases, such as PEX.

There are multiple techniques now available for AFM-based antibody recognition, such as force-volume, phase, and TREC imaging. Although all three techniques can be applied to the study of PEX, TREC was found to be the most suitable methodology, resulting in high-resolution antibody recognition of both control and PEX lens capsule surfaces. Topographical AFM images and antibody recognition images were obtained simultaneously to determine the specific location of clusterin, LOXL1, and elastin proteins in and around PEX aggregates using AFM probes modified with the appropriate antibody. Despite literature showing the co-localisation of LOXL1 with elastin and clusterin using EM techniques, TREC did not show the same co-localisation. This may be due to differences in sample preparation, resulting in epitope unavailability in the native state, or resolution differences in the lateral measure of the lens capsule. Nevertheless, AFM allowed the high-resolution study of fibres of PEX on whole unprocessed tissue samples. TREC could be further optimised for investigating protein aggregation disease by improving current sample preparation techniques. Ideally, AFM would be used in future to find the relationship between normal basement membrane fibres such as elastin and the mature form of PEX fibres. Incorporation of other proteins found to be genetically implicated in the disease, such as CNTNAP2, and proteins found

### *Conclusions and Future Perspectives*

by mass spectrometry such as haemoglobin, could also be investigated to further advance the understanding of the PEX pathophysiology. Additionally, the application of other AFM–antibody recognition techniques such as Bruker’s Peakforce QNM is sure to lead to interesting combinations of mechanical and compositional data.

# Reference List

---

- [1] G. Binnig, C. Quate, and C. Gerber, "Atomic force microscope," *Physical Review Letters*, pp. 930–3, 1986.
- [2] V. J. Morris, A. R. Kirby, and A. P. Gunning, *Atomic force microscopy for biologists*, 2nd ed. Imperial College Press, 2009.
- [3] H. Hansma and J. Hoh, "Biomolecular imaging with the atomic force microscope," *Review of Biophysics and Biomolecular Structure*, vol. 23, pp. 115–39, 1994.
- [4] M. Firtel and T. J. Beveridge, "Scanning probe microscopy in microbiology," *Micron*, vol. 26, no. 4, pp. 347–62, 1995.
- [5] D. J. Müller and Y. F. Dufrêne, "Atomic force microscopy as a multifunctional molecular toolbox in nanobiotechnology," *Nature Nanotechnology*, vol. 3, no. 5, pp. 261–9, 2008.
- [6] S. Cohen and A. Bitler, "Use of AFM in bio-related systems," *Current Opinion in Colloid & Interface Science*, vol. 13, no. 5, pp. 316–25, 2008.
- [7] L. W. Francis, P. D. Lewis, C. J. Wright, and R. S. Conlan, "Atomic force microscopy comes of age," *Biology of the Cell / under the Auspices of the European Cell Biology Organization*, vol. 102, no. 2, pp. 133–43, 2010.
- [8] N. C. Santos and M. R. B. Castanho, "An overview of the biophysical applications of atomic force microscopy," *Biophysical Chemistry*, vol. 107, no. 2, pp. 133–49, 2004.
- [9] H. Hansma and L. Pietrasanta, "Atomic force microscopy and other scanning probe microscopies," *Current Opinion in Chemical Biology*, pp. 579–84, 1998.
- [10] L. P. Silva, "Imaging proteins with atomic force microscopy: an overview," *Current Protein & Peptide Science*, vol. 6, no. 4, pp. 387–95, 2005.
- [11] C. Ascoli, "Normal and lateral forces in scanning force microscopy," *Journal of Vacuum Science & Technology B: Microelectronics and Nanometer Structures*, vol. 12, no. 3, p. 1642–5, 1994.
- [12] R. García, "Dynamic atomic force microscopy methods," *Surface Science Reports*, vol. 47, no. 6–8, pp. 197–301, 2002.
- [13] C. Putman, K. V. der Werf, B. G. D. Grooth, N. F. V. Hulst, and J. Greve, "Tapping mode atomic force microscopy in liquid," *Applied Physics Letters*, vol. 64, no. 18, pp. 2454–6, 1994.
- [14] S. N. Magonov, V. Elings, and M.-H. Whangbo, "Phase imaging and stiffness in tapping-mode atomic force microscopy," *Surface Science*, vol. 375, no. 2–3, p. L385–L391, 1997.
- [15] J. Tamayo and R. García, "Relationship between phase shift and energy dissipation in tapping-mode scanning force microscopy," *Applied Physics Letters*, vol. 73, no. 20, pp. 2926–8, 1998.
- [16] F. J. Giessibl, "Atomic resolution of the silicon (111)-(7x7) surface by atomic force microscopy," *Science*, vol. 267, no. 5194, pp. 68–71, 1995.
- [17] F. J. Giessibl, "Advances in atomic force microscopy," *Reviews of Modern Physics*, vol. 75, no. 3, pp. 949–83, 2003.
- [18] U. Dammer, M. Hegner, D. Anselmetti, P. Wagner, M. Dreier, W. Huber, and H. J. Güntherodt, "Specific antigen/antibody interactions measured by force microscopy," *Biophysical Journal*, vol. 70, no. 5, pp. 2437–41, 1996.

## Reference List

- [19] A. Alessandrini and P. Facci, "AFM: a versatile tool in biophysics," *Measurement Science and Technology*, vol. 16, no. 6, pp. R65–R92, 2005.
- [20] J. Tansock and C. Williams, "Force measurement with a piezoelectric cantilever in a scanning force microscope," *Ultramicroscopy*, vol. 42–44, pp. 1464–9, 1992.
- [21] B. Cappella and G. Dietler, "Force–distance curves by atomic force microscopy," *Surface Science Reports*, vol. 34, no. 1–3, pp. 1–104, 1999.
- [22] B. Bhushan, J. N. Israelachvili, and U. Landman, "Nanotribology: friction, wear and lubrication at the atomic scale," *Nature*, vol. 374, no. 6523, pp. 607–16, 1995.
- [23] C. T. Gibson, G. S. Watson, and S. Myhra, "Determination of the spring constants of probes for force microscopy/spectroscopy," *Nanotechnology*, vol. 7, no. 3, pp. 259–62, 1996.
- [24] C. T. Gibson, G. S. Watson, and S. Myhra, "Scanning force microscopy–calibrative procedures for 'best practice'," *Scanning*, vol. 19, no. 8, pp. 564–81, 2006.
- [25] J. Zlatanova, S. M. Lindsay, and S. H. Leuba, "Single molecule force spectroscopy in biology using the atomic force microscope," *Progress in Biophysics and Molecular Biology*, vol. 74, no. 1–2, pp. 37–61, 2000.
- [26] V. Muller, B. Derjaguin, and Y. P. Toporov, "On two methods of calculation of the force of sticking of an elastic sphere to a rigid plane," *Colloids and Surfaces*, vol. 7, no. 3, pp. 251–59, 1983.
- [27] B. V. Derjaguin, V. M. Muller, and Y. P. Toporov, "Effect of contact deformations on the adhesion of particles," *Journal of Colloid and Interface Science*, vol. 53, no. 2, pp. 314–26, 1975.
- [28] K. L. Johnson, K. Kendall, and A. D. Roberts, "Surface Energy and the Contact of Elastic Solids," *Proceedings of the Royal Society of London. Series A, Mathematical and Physical Sciences*, vol. 324, no. 1558, pp. 301–13, 1971.
- [29] H. Butt, B. Cappella, and M. Kappl, "Force measurements with the atomic force microscope: Technique, interpretation and applications," *Surface Science Reports*, vol. 59, no. 1–6, pp. 1–152, 2005.
- [30] M. Radmacher, "Measuring the elastic properties of biological samples with the AFM," *Engineering in Medicine and Biology Magazine, IEEE*, vol. 16, no. 2, pp. 47–57, 1997.
- [31] J. P. Cleveland, S. Manne, D. Bocek, and P. K. Hansma, "A nondestructive method for determining the spring constant of cantilevers for scanning force microscopy," *Review of Scientific Instruments*, vol. 64, no. 2, p. 403, 1993.
- [32] J. L. Hutter and J. Bechhoefer, "Calibration of atomic–force microscope tips," *Review of Scientific Instruments*, vol. 64, no. 7, p. 1868, 1993.
- [33] M. L. B. Palacio and B. Bhushan, "Normal and lateral force calibration techniques for AFM cantilevers," *Critical Reviews in Solid State and Materials Sciences*, vol. 35, no. 2, pp. 73–104, 2010.
- [34] N. A. Burnham, X. Chen, C. S. Hodges, G. A. Matei, E. J. Thoreson, C. J. Roberts, M. C. Davies and S. J. B. Tendler, "Comparison of calibration methods for atomic–force microscopy cantilevers," *Nanotechnology*, vol. 14, no. 1, pp. 1–6, 2003.
- [35] J. E. Sader, J. W. M. Chon, and P. Mulvaney, "Calibration of rectangular atomic force microscope cantilevers," *Review of Scientific Instruments*, vol. 70, no. 10, p. 3967, 1999.
- [36] M. Munz, "Force calibration in lateral force microscopy: a review of the experimental methods," *Journal of Physics D: Applied Physics*, vol. 43, no. 6, p. 063001, 2010.
- [37] P. Cumpson, C. Clifford, and J. Portoles, "Cantilever Spring–Constant Calibration in Atomic Force Microscopy," *Probe Methods VIII*, 2008.

## Reference List

- [38] A. Ebner, L. Wildling, R. Zhu, C. Rankl, T. Haselgrübler, P. Hinterdorfer and H. J. Gruber, "Functionalisation of probe tips and supports for single-molecule recognition force microscopy," *STM and AFM Studies*, 2008.
- [39] G. Chen, X. Ning, B. Park, G.-J. Boons, and B. Xu, "Simple, clickable protocol for atomic force microscopy tip modification and its application for trace ricin detection by recognition imaging," *Langmuir*, vol. 25, no. 5, pp. 2860–4, 2009.
- [40] A. S. M. Kamruzzahan, A. Ebner, L. Wildling, F. Kienberger, C. K. Riemer, C. D. Hahn, P. D. Pollheimer, P. Winklehner, M. Holzl, B. Lackner, D. M. Schorkl, P. Hinterdorfer and H. J. Gruber, "Antibody linking to atomic force microscope tips via disulfide bond formation," *Bioconjugate Chem*, vol. 17, no. 6, pp. 1473–1481, 2006.
- [41] A. Ebner, P. Hinterdorfer, and H. Gruber, "Comparison of different aminofunctionalisation strategies for attachment of single antibodies to AFM cantilevers," *Ultramicroscopy*, vol. 107, pp. 922–927, 2007.
- [42] R. Barattin and N. Voyer, "Chemical modifications of AFM tips for the study of molecular recognition events," *Chemical Communications*, vol. 7, no. 13, pp. 1513–32, 2008.
- [43] H. Clausen-Schaumann, M. Seitz, R. Krautbauer, and H. E. Gaub, "Force spectroscopy with single bio-molecules," *Current Opinion in Chemical Biology*, vol. 4, no. 5, pp. 524–30, 2000.
- [44] B. Heymann and H. Grubmüller, "Dynamic force spectroscopy of molecular adhesion bonds," *Physical Review Letters*, vol. 84, no. 26, pp. 6126–9, 2000.
- [45] C. K. Lee, Y. M. Wang, L. S. Huang, and S. Lin, "Atomic force microscopy: determination of unbinding force, off rate and energy barrier for protein-ligand interaction," *Micron*, vol. 38, no. 5, pp. 446–61, 2007.
- [46] E. Evans and K. Ritchie, "Dynamic strength of molecular adhesion bonds," *Biophysical Journal*, vol. 72, no. 4, pp. 1541–55, 1997.
- [47] O. H. Willemsen, M. M. Snel, A. Cambi, J. Greve, B. G. De Groot, and C. G. Figdor, "Biomolecular interactions measured by atomic force microscopy," *Biophysical Journal*, vol. 79, no. 6, pp. 3267–81, 2000.
- [48] D. Leckband and J. Israelachvili, *Intermolecular forces in biology*, vol. 34, no. 2. 2001, pp. 105–267.
- [49] F. Kienberger, A. Ebner, H. J. Gruber, and P. Hinterdorfer, "Molecular recognition imaging and force spectroscopy of single biomolecules," *Accounts of chemical research*, vol. 39, no. 1, pp. 29–36, 2006.
- [50] P. Hinterdorfer and Y. F. Dufrene, "Detection and localization of single molecular recognition events using atomic force microscopy," *Nature methods*, vol. 3, no. 5, pp. 347–55, 2006.
- [51] S. Izrailev, S. Stepaniants, M. Balsera, Y. Oono, and K. Schulten, "Molecular dynamics study of unbinding of the avidin-biotin complex," *Biophysical Journal*, vol. 72, no. 4, pp. 1568–81, 1997.
- [52] M. Ludwig, W. Dettmann, and H. Gaub, "Atomic force microscope imaging contrast based on molecular recognition," *Biophysical Journal*, vol. 72, no. 1, pp. 445–448, 1997.
- [53] a Chilkoti, T. Boland, B. D. Ratner, and P. S. Stayton, "The relationship between ligand-binding thermodynamics and protein-ligand interaction forces measured by atomic force microscopy," *Biophysical Journal*, vol. 69, no. 5, pp. 2125–30, 1995.
- [54] Y.-shiu Lo, J. Simons, and T. P. Beebe, "Temperature Dependence of the Biotin-Avidin Bond-Rupture Force Studied by Atomic Force Microscopy," *Journal of Physical Chemistry B*, vol. 106, no. 38, pp. 9847–52, 2002.
- [55] A. Chen and V. T. Moy, "Cross-linking of cell surface receptors enhances cooperativity of molecular adhesion," *Biophysical Journal*, vol. 78, no. 6, pp. 2814–20, 2000.

## Reference List

- [56] J. Wong, A. Chilkoti, and V. T. Moy, "Direct force measurements of the streptavidin–biotin interaction," *Biomolecular engineering*, vol. 16, no. 1–4, pp. 45–55, 1999.
- [57] M. Grandbois, M. Beyer, M. Rief, H. Clausen–Schaumann, and H. Gaub, "How strong is a covalent bond?," *Science*, vol. 283, no. 5408, pp. 1727–30, 1999.
- [58] K. C. Langry, T. V. Ratto, R. E. Rudd, and M. W. McElfresh, "The AFM measured force required to rupture the dithiolate linkage of thiocetic acid to gold is less than the rupture force of a simple gold–alkyl thiolate bond," *Langmuir*, vol. 21, no. 26, pp. 12064–7, 2005.
- [59] T. V. Ratto, K. C. Langry, R. E. Rudd, R. L. Balhorn, M. J. Allen, and M. W. McElfresh, "Force spectroscopy of the double–tethered concanavalin–A mannose bond," *Biophysical Journal*, vol. 86, no. 4, pp. 2430–7, 2004.
- [60] A. Touhami, M. H. Jericho, and T. J. Beveridge, "Molecular recognition forces between immunoglobulin G and a surface protein adhesin on living *Staphylococcus aureus*," *Langmuir*, vol. 23, no. 5, pp. 2755–60, 2007.
- [61] C. Riemer, "Simple test system for single molecule recognition force microscopy," *Analytica Chimica Acta*, vol. 479, no. 1, pp. 59–75, 2003.
- [62] H. Lee, N. F. Scherer, and P. B. Messersmith, "Single–molecule mechanics of mussel adhesion," *Proceedings of the National Academy of Sciences of the United States of America*, vol. 103, no. 35, pp. 12999–3003, 2006.
- [63] C. M. Stroh, A. Ebner, M. Geretschlager, G. Freudenthaler, F. Kienberger, A. S. M. Kamruzzahan, S. J. Smith–Gill, H. J. Gruber and P. Hinterdorfer, "Simultaneous topography and recognition imaging using force microscopy," *Biophysical Journal*, vol. 87, no. 3, pp. 1981–90, 2004.
- [64] C. Stroh, H. Wang, R. Bash, B. Ashcroft, J. Nelson, H. Gruber, D. Lohr, S. M. Lindsay and P. Hinterdorfer, "Single–molecule recognition imaging microscopy," *Proceedings of the National Academy of Sciences of the United States of America*, vol. 101, no. 34, pp. 12503–7, 2004.
- [65] O. H. Willemsen, M. M. E. Snel, K. O. van der Werf, B. G. de Groot, J. Greve, P. Hinterdorfer, H. J. Gruber, H. Schindler, Y. van Kooyk and C. G. Figdor, "Simultaneous height and adhesion imaging of antibody–antigen interactions by atomic force microscopy," *Biophysical Journal*, vol. 75, no. 5, pp. 2220–8, 1998.
- [66] A. Ebner, F. Kienberger, G. Kada, C. M. Stroh, M. Geretschlager, A. S. M. Kamruzzahan, L. Wildling, W. T. Johnson, B. Ashcroft, J. Nelson, S. M. Lindsay, H. J. Gruber and P. Hinterdorfer, "Localization of single avidin–biotin interactions using simultaneous topography and molecular recognition imaging," *Chemphyschem: a European journal of chemical physics and physical chemistry*, vol. 6, no. 5, pp. 897–900, 2005.
- [67] W. Baumgartner, P. Hinterdorfer, W. Ness, A. Raab, D. Vestweber, H. Schindler, and D. Drenckhahn, "Cadherin interaction probed by atomic force microscopy," *Proceedings of the National Academy of Sciences of the United States of America*, vol. 97, no. 8, pp. 4005–10, 2000.
- [68] R. Nevo, C. Stroh, F. Kienberger, D. Kaftan, V. Brumfeld, M. Elbaum, Z. Reich, and P. Hinterdorfer, "A molecular switch between alternative conformational states in the complex of Ran and importin  $\beta$ 1," *Nature Structural & Molecular Biology*, vol. 10, no. 7, pp. 553–557, 2003.
- [69] J. A. Wieland, A. A. Gewirth, and D. E. Leckband, "Single molecule adhesion measurements reveal two homophilic neural cell adhesion molecule bonds with mechanically distinct properties," *The Journal of Biological Chemistry*, vol. 280, no. 49, pp. 41037–46, 2005.
- [70] M. Etienne and A. Walcarius, "Analytical investigation of the chemical reactivity and stability of aminopropyl–grafted silica in aqueous medium," *Talanta*, vol. 59, no. 6, pp. 1173–88, 2003.

## Reference List

- [71] J. H. Moon, J. W. Shin, S. Y. Kim, and J. W. Park, "Formation of Uniform Aminosilane Thin Layers : An Imine Formation To Measure Relative Surface Density of the Amine Group," *Society*, vol. 7463, no. 12, pp. 4621–4624, 1996.
- [72] S. Flink, F. C. J. M. van Veggel, and D. N. Reinhoudt, "Functionalisation of self-assembled monolayers on glass and oxidized silicon wafers by surface reactions," *Journal of Physical Organic Chemistry*, vol. 14, no. 7, pp. 407–415, 2001.
- [73] Y. Lyubchenko, L. Shlyakhtenko, R. Harrington, and P. Odent, "Atomic force microscopy of long DNA : Imaging in air and under water," *Biophysics*, vol. 90, no. March, pp. 2137–2140, 1993.
- [74] M. Bergkvist, J. Carlsson, T. Karlsson, and S. Oscarsson, "TM–AFM Threshold Analysis of Macromolecular Orientation: A Study of the Orientation of IgG and IgE on Mica Surfaces," *Journal of Colloid and Interface Science*, vol. 206, no. 2, pp. 475–481, 1998.
- [75] L. a Chtcheglova, L. Wildling, J. Waschke, D. Drenckhahn, and P. Hinterdorfer, "AFM functional imaging on vascular endothelial cells," *Journal of Molecular Recognition*, vol. 23, no. 6, pp. 589–96, 2010.
- [76] R. Creasey, S. Sharma, J. E. Craig, C. T. Gibson, A. Ebner, P. Hinterdorfer and N. H. Voelcker, "Detecting protein aggregates on untreated human tissue samples by atomic force microscopy recognition imaging," *Biophysical Journal*, vol. 99, no. 5, pp. 1660–7, 2010.
- [77] S. Lee, "Chemical functionalisation of AFM cantilevers," Thesis (S.M.)—*Massachusetts Institute of Technology*, 2005.
- [78] M. Bergkvist and N. C. Cady, "Chemical functionalisation and bioconjugation strategies for atomic force microscope cantilevers," in *Methods in Molecular Biology*, vol. 751, S. S. Mark, Ed. Totowa, NJ: Humana Press, 2011, pp. 381–400.
- [79] P. Grütter, W. Zimmermann–Edling, and D. Brodbeck, "Tip artefacts of microfabricated force sensors for atomic force microscopy," *Applied Physics Letters*, vol. 60, no. 22, p. 2741, 1992.
- [80] P. Niedermann, W. Hänni, D. Morel, A. Perret, N. Skinner, P. F. Indermühle, N. F. de Rooij, and P. A. Buffat, "CVD diamond probes for nanotechnology," *Applied Physics A: Materials Science & Processing*, vol. 66, no. 7, p. S31–S34, 1998.
- [81] J. H. Hafner, C. L. Cheung, a T. Woolley, and C. M. Lieber, "Structural and functional imaging with carbon nanotube AFM probes," *Progress in Biophysics and Molecular Biology*, vol. 77, no. 1, pp. 73–110, 2001.
- [82] G. Ge, D. Han, D. Lin, W. Chu, Y. Sun, L. Jiang, W. Ma and C. Wang, "MAC mode atomic force microscopy studies of living samples, ranging from cells to fresh tissue," *Ultramicroscopy*, vol. 107, no. 4–5, pp. 299–307, 2007.
- [83] S. Kumar and M. S. Li, "Biomolecules under mechanical force," *Physics Reports*, vol. 486, no. 1–2, pp. 1–74, 2010.
- [84] A. Sikora and L. Bednarz, "Direct measurement and control of peak tapping forces in atomic force microscopy for improved height measurements," *Measurement Science and Technology*, vol. 22, no. 9, p. 094005, 2011.
- [85] A. Yacoot, L. Koenders, and H. Wolff, "An atomic force microscope for the study of the effects of tip–sample interactions on dimensional metrology," *Measurement Science and Technology*, vol. 18, no. 2, pp. 350–359, 2007.
- [86] D. Keller, "Reconstruction of STM and AFM images distorted by finite–size tips," *Surface Science*, vol. 253, no. 1–3, pp. 353–364, 1991.
- [87] A. Relini, R. Rolandi, M. Bolognesi, M. Aboudan, G. Merlini, V. Bellotti and A. Gliozzi, "Ultrastructural organization of ex vivo amyloid fibrils formed by the apolipoprotein A–I Leu174Ser variant: an atomic force microscopy study," *Biochimica et biophysica acta*, vol. 1690, no. 1, pp. 33–41, 2004.

## Reference List

- [88] V. Bykov, a Gologanov, and V. Shevyakov, “Test structure for SPM tip shape deconvolution,” *Applied Physics A: Materials Science & Processing*, vol. 66, no. 5, pp. 499–502, 1998.
- [89] A. Noy, D. V. Vezenov, and C. M. Lieber, “Chemical force microscopy,” *Annual review of materials science*, vol. 27, no. 1, pp. 381–421, 1997.
- [90] C. D. Frisbie, L. F. Rozsnyai, A. Noy, M. S. Wrighton, and C. M. Lieber, “Functional group imaging by chemical force microscopy,” *Science*, vol. 265, no. 5181, pp. 2071–4, 1994.
- [91] Z. Ye and X. Zhao, “Phase imaging atomic force microscopy in the characterization of biomaterials,” *Journal of Microscopy*, vol. 238, no. 1, pp. 27–35, 2010.
- [92] M. Radmacher, J. Cleveland, M. Fritz, H. Hansma, and P. Hansma, “Mapping interaction forces with the atomic force microscope,” *Biophysical Journal*, vol. 66, no. 6, pp. 2159–2165, 1994.
- [93] W. T. Johnson, G. Kada, C. Stroh, H. Gruber, H. Wang, F. Kienberger, A. Ebner, S. Lindsay and P. Hinterdorfer, “Simultaneous Topography and RECOgnition mapping with PicoTREC<sup>TM</sup>: A powerful new technology that can be used to map nanometer-scale molecular binding sites on a variety of surfaces,” *NSTI-Nanotech*, vol. 2, pp. 679–682, 2005.
- [94] K. Sweers, K. van der Werf, M. Bennink, and V. Subramaniam, “Nanomechanical properties of  $\alpha$ -synuclein amyloid fibrils: a comparative study by nanoindentation, harmonic force microscopy, and Peakforce QNM,” *Nanoscale Research Letters*, vol. 6, no. 1, p. 270, 2011.
- [95] J. Adamcik, A. Berquand, and R. Mezzenga, “Single-step direct measurement of amyloid fibrils stiffness by peak force quantitative nanomechanical atomic force microscopy,” *Applied Physics Letters*, vol. 98, no. 19, p. 193701, 2011.
- [96] A. Ebner, L. A. Ctcheglova, J. Preiner, J. Tang, L. Wildling, H. J. Gruber and P. Hinterdorfer, “Simultaneous Topography and Recognition Imaging,” in *Scanning Probe Microscopy in Nanoscience and Nanotechnology*, Springer, 2010, pp. 325–362.
- [97] W. Baumgartner, P. Hinterdorfer, and H. Schindler, “Data analysis of interaction forces measured with the atomic force microscope,” *Ultramicroscopy*, vol. 82, no. 1–4, pp. 85–95, 2000.
- [98] J. Yu, J. Warnke, and Y. L. Lyubchenko, “Nanoprobng of  $\alpha$ -synuclein misfolding and aggregation with atomic force microscopy,” *Nanomedicine : nanotechnology, biology, and medicine*. Sep–2010.
- [99] H. Takahashi, Y. R. Silberberg, M. Kumeta, J. M. Edwardson, and K. Takeyasu, “Force spectroscopy addresses fundamental problems in cell physiology,” in *Microscopy: Science, Technology, Applications and Education*, no. c, 2010, pp. 478–488.
- [100] Y. Martin, C. C. Williams, and H. K. Wickramasinghe, “Atomic force microscope-force mapping and profiling on a sub 100-Å scale,” *Journal of Applied Physics*, vol. 61, no. 10, p. 4723, 1987.
- [101] V. Dupres, F. D. Menozzi, C. Locht, B. H. Clare, N. L. Abbott, S. Cuenot, C. Bompard, D. Raze and Y. F. Dufrêne, “Nanoscale mapping and functional analysis of individual adhesins on living bacteria,” *Nature Methods*, vol. 2, no. 7, 2005.
- [102] F. Gaboriaud, B. S. Parcha, M. L. Gee, J. A. Holden, and R. A. Strugnell, “Spatially resolved force spectroscopy of bacterial surfaces using force-volume imaging,” *Colloids and Surfaces. B: Biointerfaces*, vol. 62, no. 2, pp. 206–13, 2008.
- [103] M. R. Nussio, N. H. Voelcker, M. J. Sykes, B. S. Flavel, J. O. Miners, and J. G. Shapter, “High resolution chemical mapping of biomimetic membranes by force volume imaging,” *2008 International Conference on Nanoscience and Nanotechnology*, vol. 1m, pp. 121–124, 2008.

## Reference List

- [104] H. An, M. R. Nussio, M. G. Huson, N. H. Voelcker, and J. G. Shapter, "Material Properties of Lipid Microdomains: Force–Volume Imaging Study of the Effect of Cholesterol on Lipid Microdomain Rigidity," *Biophysical Journal*, vol. 99, no. 3, pp. 834–844, 2010.
- [105] S. Chirasatitsin and A. J. Engler, "Detecting cell–adhesive sites in extracellular matrix using force spectroscopy mapping," *Journal of Physics: Condensed Matter*, vol. 22, no. 19, p. 194102, 2010.
- [106] M. Radmacher, M. Fritz, J. P. Cleveland, D. A. Walters, and P. K. Hansmat, "Imaging Adhesion Forces and Elasticity of Lysozyme Adsorbed on Mica with the Atomic Force Microscope," *Society*, vol. VII, no. 23, pp. 3809–3814, 1994.
- [107] G. Li, N. Xi, and D. H. Wang, "Investigation of angiotensin II type 1 receptor by atomic force microscopy with functionalised tip," *Nanomedicine: nanotechnology, biology, and medicine*, vol. 1, no. 4, pp. 306–12, 2005.
- [108] G. Li, N. Xi, and D. H. Wang, "Probing membrane proteins using atomic force microscopy," *Journal of Cellular Biochemistry*, vol. 97, no. 6, pp. 1191–7, 2006.
- [109] J. Preiner, A. Ebner, L. Chtcheglova, R. Zhu, and P. Hinterdorfer, "Simultaneous topography and recognition imaging: physical aspects and optimal imaging conditions," *Nanotechnology*, vol. 20, no. 21, p. 215103, 2009.
- [110] J. L. Tang, A. Ebner, H. Badelt–Lichtblau, C. Vollenkle, C. Rankl, B. Kraxberger, M. Leitner, L. Wildling, H. J. Gruber, U. B. Sleytr, N. Ilk and P. Hinterdorfer, "Recognition imaging and highly ordered molecular templating of bacterial S–layer nanoarrays containing affinity–tags," *Nano Letters*, vol. 8, no. 12, pp. 4312–9, 2008.
- [111] L. A. Chtcheglova, F. Atalar, U. Ozbek, L. Wildling, A. Ebner, and P. Hinterdorfer, "Localization of the ergtoxin–1 receptors on the voltage sensing domain of hERG K+ channel by AFM recognition imaging," *Pflügers Archiv: European Journal of Physiology*, vol. 456, no. 1, pp. 247–54, 2008.
- [112] A. Ebner, D. Nikova, T. Lange, J. Haberle, S. Falk, A. Dubbers, R. Bruns, P. Hinterdorfer, H. Oberleithner and H. Schillers, "Determination of CFTR densities in erythrocyte plasma membranes using recognition imaging," *Nanotechnology*, vol. 19, no. 38, p. 384017, 2008.
- [113] B. B. Pittenger, N. Erina, and C. Su, *Quantitative Mechanical Property Mapping at the Nanoscale with PeakForce QNM – Application Notes*. Veeco Instruments Inc, 2010.
- [114] F. Rico, C. Su, and S. Scheuring, "Mechanical mapping of single membrane proteins at submolecular resolution," *Nano Letters*, vol. 11, no. 9, pp. 3983–6, 2011.
- [115] K. Mitsuoka, T. Hirai, K. Murata, A. Miyazawa, A. Kidera, Y. Kimura and Y. Fujiyoshi, "The structure of bacteriorhodopsin at 3.0 Å resolution based on electron crystallography: implication of the charge distribution," *Journal of Molecular Biology*, vol. 286, no. 3, pp. 861–82, 1999.
- [116] S. Husale, H. H. J. Persson, and O. Sahin, "DNA nanomechanics allows direct digital detection of complementary DNA and microRNA targets," *Nature*, vol. 462, no. 7276, pp. 1075–8, 2009.
- [117] J. Adamcik, J.–M. Jung, J. Flakowski, P. De Los Rios, G. Dietler, and R. Mezzenga, "Understanding amyloid aggregation by statistical analysis of atomic force microscopy images," *Nature nanotechnology*, vol. 5, no. 6, pp. 423–8, 2010.
- [118] E. Adams, "The combined application of AFM and LSCM: Changing the way we look at innate immunity," *Modern Research and Educational Topics in Microscopy*, pp. 68–76, 2007.
- [119] S. Mangold, K. Harneit, T. Rohwerder, G. Claus, and W. Sand, "Novel combination of atomic force microscopy and epifluorescence microscopy for visualization of leaching bacteria on pyrite," *Applied and environmental microbiology*, vol. 74, no. 2, pp. 410–5, 2008.

## Reference List

- [120] M. Duman, M. Pflieger, R. Zhu, C. Rankl, L. A. Chtcheglova, I. Neundlinger, B. L. Bozna, B. Mayer, M. Salio, D. Shepherd, P. Polzella, M. Moertelmaier, G. Kada, A. Ebner, M. Dieudonne, G. J. Schütz, V. Cerundolo, F. Kienberger and P. Hinterdorfer, "Improved localization of cellular membrane receptors using combined fluorescence microscopy and simultaneous topography and recognition imaging," *Nanotechnology*, vol. 21, no. 11, p. 115504, 2010.
- [121] M. M. Apetri, N. C. Maiti, M. G. Zagorski, P. R. Carey, and V. E. Anderson, "Secondary structure of alpha-synuclein oligomers: characterization by raman and atomic force microscopy," *Journal of Molecular Biology*, vol. 355, no. 1, pp. 63–71, 2006.
- [122] A. H. Zhou, G. D. Mcewen, and Y. Z. Wu, "Combined AFM / Raman microspectroscopy for characterization of living cells in near physiological conditions," *Exposure*, pp. 515–522, 2010.
- [123] C. Prater, K. Kjoller, D. Cook, R. Shetty, G. Meyers, C. Reinhardt, J. Felts, W. King, K. Vodopyanov and A. Dazzi, "Nanoscale Infrared Spectroscopy of Materials by Atomic Force Microscopy," *Microscopy and Analysis*, no. c, pp. 5–8, 2010.
- [124] W. Kabsch and C. Sander, "Dictionary of protein secondary structure: pattern recognition of hydrogen-bonded and geometrical features," *Biopolymers*, vol. 22, no. 12, pp. 2577–637, 1983.
- [125] E. R. Blout, "Polypeptides and Proteins," *In Fundamental Aspects and Recent Developments in Optical Rotatory Dispersion and Circular Dichroism*, pp. 352–372, 1973.
- [126] A. Rath, A. R. Davidson, and C. M. Deber, "The structure of 'unstructured' regions in peptides and proteins: role of the polyproline II helix in protein folding and recognition," *Biopolymers*, vol. 80, no. 2–3, pp. 179–85, 2005.
- [127] S. Kakinoki, Y. Hirano, and M. Oka, "On the Stability of Polyproline-I and II Structures of Proline Oligopeptides," *Polymer Bulletin*, vol. 53, no. 2, pp. 109–115, 2004.
- [128] O. N. Antzutkin, "Amyloidosis of Alzheimer's Abeta peptides: solid-state nuclear magnetic resonance, electron paramagnetic resonance, transmission electron microscopy, scanning transmission electron microscopy and atomic force microscopy studies," *Magnetic Resonance in Chemistry*, vol. 42, no. 2, pp. 231–46, 2004.
- [129] N. J. Greenfield, "Using circular dichroism spectra to estimate protein secondary structure," *Nature protocols*, vol. 1, no. 6, pp. 2876–90, 2006.
- [130] C. M. Dobson, "Protein misfolding, evolution and disease," *Trends in Biochemical Sciences*, vol. 24, no. 9, pp. 329–32, 1999.
- [131] A. Mitraki, "Protein aggregation from inclusion bodies to amyloid and biomaterials," *Advances in protein chemistry and structural biology*, vol. 79, pp. 89–125, 2010.
- [132] H. Ecroyd and J. A. Carver, "Unraveling the mysteries of protein folding and misfolding," *IUBMB life*, vol. 60, no. 12, pp. 769–74, 2008.
- [133] F. Chiti and C. M. Dobson, "Protein Misfolding, Functional Amyloid, and Human Disease," *Annual Review of Biochemistry*, vol. 75, no. 1, pp. 333–366, 2006.
- [134] A. M. Morris, M. a Watzky, and R. G. Finke, "Protein aggregation kinetics, mechanism, and curve-fitting: a review of the literature," *Biochimica et biophysica acta*, vol. 1794, no. 3, pp. 375–97, 2009.
- [135] W. Wang, S. Nema, and D. Teagarden, "Protein aggregation—pathways and influencing factors," *International Journal of Pharmaceutical Sciences and Research*, vol. 390, no. 2, pp. 89–99, 2010.
- [136] I. W. Hamley, "Peptide fibrillization," *Angewandte Chemie (International ed. in English)*, vol. 46, no. 43, pp. 8128–47, 2007.

## Reference List

- [137] G. Bhak, Y.-J. Choe, and S. R. Paik, "Mechanism of amyloidogenesis: nucleation-dependent fibrillation versus double-concerted fibrillation," *BMB reports*, vol. 42, no. 9, pp. 541–51, 2009.
- [138] Merriam-Webster.com, "'Fiber,'" 2011. [Online]. Available: <http://www.merriam-webster.com/dictionary/fiber?show=0&t=1317942787>. [Accessed: 07–Oct–2011].
- [139] O. S. Makin and L. C. Serpell, "Structures for amyloid fibrils," *The FEBS journal*, vol. 272, no. 23, pp. 5950–61, 2005.
- [140] M. Fändrich, "On the structural definition of amyloid fibrils and other polypeptide aggregates," *Cellular and Molecular Life Sciences*, vol. 64, no. 16, pp. 2066–78, 2007.
- [141] G. McKhann, D. Drachman, M. Folstein, R. Katzman, D. Price, and E. M. Stadlan, "Clinical diagnosis of Alzheimer's disease," *Neurology*, vol. 34, no. 7, p. 939, 1984.
- [142] J. Yu and Y. L. Lyubchenko, "Early stages for Parkinson's development: alpha-synuclein misfolding and aggregation," *Journal of Neuroimmune Pharmacology*, vol. 4, no. 1, pp. 10–6, 2009.
- [143] M. J. Volles and P. T. Lansbury, "Zeroing in on the pathogenic form of alpha-synuclein and its mechanism of neurotoxicity in Parkinson's disease," *Biochemistry*, vol. 42, no. 26, pp. 7871–8, 2003.
- [144] J. D. Harper, C. M. Lieber, and P. T. Lansbury Jr, "Atomic force microscopic imaging of seeded fibril formation and fibril branching by the Alzheimer's disease amyloid- $\beta$  protein," *Chemistry & Biology*, vol. 4, no. 12, pp. 951–959, 1997.
- [145] A. Quist, L. Doudevski, H. Lin, R. Azimova, D. Ng, B. Frangione, B. Kagan, J. Ghiso and R. Lal, "Amyloid ion channels: a common structural link for protein-misfolding disease," *Proceedings of the National Academy of Sciences of the United States of America*, vol. 102, no. 30, pp. 10427–32, 2005.
- [146] K. Conway, S. J. Lee, J. C. Rochet, T. Ding, and R. Williamson, "Acceleration of oligomerization, not fibrillization, is a shared property of both a-synuclein mutations linked to early-onset Parkinson's disease: Implications for pathogenesis and therapy," *Proceedings of the National Academy of Sciences*, vol. 99, no. 2, pp. 571–576, 2000.
- [147] W. Hoyer, D. Cherny, V. Subramaniam, and T. M. Jovin, "Rapid self-assembly of alpha-synuclein observed by in situ atomic force microscopy," *Journal of Molecular Biology*, vol. 340, no. 1, pp. 127–39, 2004.
- [148] F. Zhang, X. J. Lin, L. N. Ji, H. N. Du, L. Tang, J. H. He, J. Hu and H. Y. Hu, "Assembly of alpha-synuclein fibrils in nanoscale studied by peptide truncation and AFM," *Biochemical and biophysical research communications*, vol. 368, no. 2, pp. 388–94, 2008.
- [149] R. J. O'Brien and P. C. Wong, "Amyloid precursor protein processing and Alzheimer's disease," *Annual review of neuroscience*, vol. 34, pp. 185–204, 2011.
- [150] M. Fändrich, M. Schmidt, and N. Grigorieff, "Recent progress in understanding Alzheimer's  $\beta$ -amyloid structures," *Trends in Biochemical Sciences*, vol. 36, no. 6, pp. 338–45, 2011.
- [151] D. G. Lynn and S. C. Meredith, "Review: model peptides and the physicochemical approach to beta-amyloids," *Journal of Structural Biology*, vol. 130, no. 2–3, pp. 153–73, 2000.
- [152] S. B. Prusiner, "Molecular biology of prion diseases," *Science*, vol. 252, no. 5012, pp. 1515–22, 1991.
- [153] L. A. Stewart, L. H. M. Rydzewska, G. F. Keogh, and R. S. G. Knight, "Systematic review of therapeutic interventions in human prion disease," *Neurology*, vol. 70, no. 15, pp. 1272–81, 2008.
- [154] D. Selkoe, "Alzheimer's disease: genes, proteins, and therapy," *Physiological reviews*, pp. 741–766, 2001.

## Reference List

- [155] W. B. Stine, S. W. Snyder, U. S. Ladrör, W. S. Wade, M. F. Miller, T. J. Perun, T. F. Holzman and G. A. Krafft, "The nanometer-scale structure of amyloid-beta visualized by atomic force microscopy," *Journal of Protein Chemistry*, vol. 15, no. 2, pp. 193–203, 1996.
- [156] B. H. Toyama and J. S. Weissman, "Amyloid structure: conformational diversity and consequences," *Annual review of biochemistry*, vol. 80, pp. 557–85, 2011.
- [157] M. F. Perutz, J. T. Finch, J. Berriman and A. Lesk, "Amyloid fibers are water-filled nanotubes," *Proceedings of the National Academy of Sciences of the United States of America*, vol. 99, no. 8, pp. 5591–5, 2002.
- [158] O. V. Bocharova, L. Breydo, A. S. Parfenov, V. V. Salnikov, and I. V. Baskakov, "In vitro conversion of full-length mammalian prion protein produces amyloid form with physical properties of PrP(Sc)," *Journal of Molecular Biology*, vol. 346, no. 2, pp. 645–59, 2005.
- [159] M. Anderson, O. V. Bocharova, N. Makarava, L. Breydo, V. V. Salnikov, and I. V. Baskakov, "Polymorphism and ultrastructural organization of prion protein amyloid fibrils: an insight from high resolution atomic force microscopy," *Journal of Molecular Biology*, vol. 358, no. 2, pp. 580–96, 2006.
- [160] S. A. Petty, T. Adalsteinsson, and S. M. Decatur, "Correlations among morphology, beta-sheet stability, and molecular structure in prion peptide aggregates," *Biochemistry*, vol. 44, no. 12, pp. 4720–6, 29–Mar–2005.
- [161] A. Podestà, G. Tiana, P. Milani, and M. Manno, "Early events in insulin fibrillization studied by time-lapse atomic force microscopy," *Biophysical Journal*, vol. 90, no. 2, pp. 589–97, 2006.
- [162] A. Relini, S. Torrasa, R. Rolandi, A. Gliozzi, C. Rosano, C. Canale, M. Bolognesi, G. Plakoutsi, M. Bucciandini, F. Chiti and M. Stefani, "Monitoring the process of HypF fibrillization and liposome permeabilization by protofibrils," *Journal of Molecular Biology*, vol. 338, no. 5, pp. 943–57, 2004.
- [163] C. Goldsbury, J. Kistler, U. Aebi, T. Arvinte, and G. J. Cooper, "Watching amyloid fibrils grow by time-lapse atomic force microscopy," *Journal of Molecular Biology*, vol. 285, no. 1, pp. 33–9, 1999.
- [164] C. Goldsbury, P. Frey, V. Olivieri, U. Aebi, and S. a Müller, "Multiple assembly pathways underlie amyloid-beta fibril polymorphisms," *Journal of Molecular Biology*, vol. 352, no. 2, pp. 282–98, 2005.
- [165] J. D. Harper, S. S. Wong, C. M. Lieber, and P. T. Lansbury, "Observation of metastable A $\beta$  amyloid protofibrils by atomic force microscopy," *Chemistry & Biology*, vol. 4, no. 2, pp. 119–25, 1997.
- [166] M. Polano, A. Bek, F. Benetti, M. Lazzarino, and G. Legname, "Structural insights into alternate aggregated prion protein forms," *Journal of Molecular Biology*, vol. 393, no. 5, pp. 1033–42, 2009.
- [167] Y. Sun, N. Makarava, C.-I. Lee, P. Laksanalamai, F. T. Robb, and I. V. Baskakov, "Conformational stability of PrP amyloid fibrils controls their smallest possible fragment size," *Journal of Molecular Biology*, vol. 376, no. 4, pp. 1155–67, 2008.
- [168] P.-C. Klöhn, L. Stoltze, E. Flechsig, M. Enari, and C. Weissmann, "A quantitative, highly sensitive cell-based infectivity assay for mouse scrapie prions," *Proceedings of the National Academy of Sciences of the United States of America*, vol. 100, no. 20, pp. 11666–71, 2003.
- [169] S. Wegmann, M. Miesbauer, K. F. Winklhofer, J. Tatzelt, and D. J. Müller, "Observing fibrillar assemblies on scrapie-infected cells," *Pflügers Archiv: European Journal of Physiology*, vol. 456, no. 1, pp. 83–93, 2008.
- [170] S. H. Ku and C. B. Park, "Highly accelerated self-assembly and fibrillation of prion peptides on solid surfaces," *Langmuir*, vol. 24, no. 24, pp. 13822–7, 2008.

## Reference List

- [171] C. Ha and C. B. Park, "Ex situ atomic force microscopy analysis of beta-amyloid self-assembly and deposition on a synthetic template," *Langmuir*, vol. 22, no. 16, pp. 6977–85, 2006.
- [172] C. E. Giacomelli and W. Norde, "Influence of hydrophobic Teflon particles on the structure of amyloid beta-peptide," *Biomacromolecules*, vol. 4, no. 6, pp. 1719–26, 2003.
- [173] M. Zhu, P. O. Souillac, C. Ionescu-Zanetti, S. A. Carter, and A. L. Fink, "Surface-catalyzed amyloid fibril formation," *The Journal of Biological Chemistry*, vol. 277, no. 52, pp. 50914–22, 2002.
- [174] T. Kowalewski and D. M. Holtzman, "In situ atomic force microscopy study of Alzheimer's  $\beta$ -amyloid peptide on different substrates: New insights into mechanism of  $\beta$ -sheet formation," *Proceedings of the National Academy of Sciences*, vol. 96, no. 7, p. 3688, 1999.
- [175] Z. Wang, C. Zhou, C. Wang, L. Wan, X. Fang, and C. Bai, "AFM and STM study of beta-amyloid aggregation on graphite," *Ultramicroscopy*, vol. 97, no. 1–4, pp. 73–9, 2003.
- [176] X. Ma, L. Liu, X. Mao, L. Niu, K. Deng, W. Wu, Y. Li, Y. Yang and C. Wang, "Amyloid beta (1–42) folding multiplicity and single-molecule binding behavior studied with STM," *Journal of Molecular Biology*, vol. 388, no. 4, pp. 894–901, 2009.
- [177] P. M. Gorman, C. M. Yip, P. E. Fraser, and A. Chakrabarty, "Alternate aggregation pathways of the Alzheimer beta-amyloid peptide: Abeta association kinetics at endosomal pH," *Journal of Molecular Biology*, vol. 325, no. 4, pp. 743–57, 2003.
- [178] J.D. Greena, L. Kreplaka, C. Goldsburya, X. Li Blatterb, M. Stolza, G.S. Cooperc, A. Seeligb, J. Kistlerc and U. Aebia, "Atomic force microscopy reveals defects within mica supported lipid bilayers induced by the amyloidogenic human amylin peptide," *Journal of Molecular Biology*, vol. 342, no. 3, pp. 877–87, 2004.
- [179] M. L. DeMarco, J. Silveira, B. Caughey, and V. Daggett, "Structural properties of prion protein protofibrils and fibrils: an experimental assessment of atomic models," *Biochemistry*, vol. 45, no. 51, pp. 15573–82, 2006.
- [180] M. R. H. Krebs, L. A. Morozova-roche, K. Daniel, C. V. Robinson, and C. M. Dobson, "Observation of sequence specificity in the seeding of protein amyloid fibrils," *Protein Science*, vol. 13, pp. 1933–1938, 2004.
- [181] K. N. Dahlgren, A. M. Manelli, W. B. Stine, L. K. Baker, G. a Krafft, and M. J. LaDu, "Oligomeric and fibrillar species of amyloid-beta peptides differentially affect neuronal viability," *The Journal of Biological Chemistry*, vol. 277, no. 35, pp. 32046–53, 30-Aug-2002.
- [182] V. Zamotin, A. Gharibyan, N. V. Gibanova, M. A. Lavrikova, D. A. Dolgikh, M. P. Kirpichnikov, I. A. Kostanyan, and L. A. Morozova-Roche, "Cytotoxicity of albebetin oligomers depends on cross-beta-sheet formation," *FEBS Letters*, vol. 580, no. 10, pp. 2451–7, 2006.
- [183] R. Kaye, Y. Sokolov, B. Edmonds, T. M. McIntire, S. C. Milton, J. E. Hall and C. G. Glabe, "Permeabilization of lipid bilayers is a common conformation-dependent activity of soluble amyloid oligomers in protein misfolding diseases," *The Journal of Biological Chemistry*, vol. 279, no. 45, pp. 46363–6, 2004.
- [184] D. L. Pountney, N. H. Voelcker, and W. P. Gai, "Annular alpha-synuclein oligomers are potentially toxic agents in alpha-synucleinopathy. Hypothesis," *Neurotoxicity research*, vol. 7, no. 1, pp. 59–67, 2005.
- [185] S. M. Butterfield and H. a Lashuel, "Amyloidogenic protein-membrane interactions: mechanistic insight from model systems," *Angewandte Chemie (International ed. in English)*, vol. 49, no. 33, pp. 5628–54, 2010.

## Reference List

- [186] R. Lowe, D. L. Pountney, P. H. Jensen, W. P. Gai, and N. H. Voelcker, "Calcium (II) selectively induces alpha-synuclein annular oligomers via interaction with the C-terminal domain," *Protein Science*, vol. 13, no. 12, pp. 3245–3252, 2004.
- [187] S. Rivera-Mancía, I. Pérez-Neri, C. Ríos, L. Tristán-López, L. Rivera-Espinosa, and S. Montes, "The transition metals copper and iron in neurodegenerative diseases," *Chemico-biological interactions*, vol. 186, no. 2, pp. 184–99, 2010.
- [188] A. Santner and V. N. Uversky, "Metalloproteomics and metal toxicology of  $\alpha$ -synuclein," *Metallomics: Integrated Biometal Science*, vol. 2, no. 6, pp. 378–92, 2010.
- [189] D. L. Pountney, R. Lowe, M. Quilty, J. C. Vickers, N. H. Voelcker, and W. P. Gai, "Annular alpha-synuclein species from purified multiple system atrophy inclusions," *Journal of Neurochemistry*, vol. 90, no. 2, pp. 502–12, 2004.
- [190] L. Chen, Y. Wei, X. Wang, and R. He, "Ribosylation rapidly induces alpha-synuclein to form highly cytotoxic molten globules of advanced glycation end products," *PLoS one*, vol. 5, no. 2, p. e9052, 2010.
- [191] H.-T. Li, D.-H. Lin, X.-Y. Luo, F. Zhang, L.-N. Ji, H.-N. Du, G.-Q. Song, J. Hu, J.-W. Zhou and H.-Y. Hu, "Inhibition of alpha-synuclein fibrillization by dopamine analogs via reaction with the amino groups of alpha-synuclein. Implication for dopaminergic neurodegeneration," *The FEBS journal*, vol. 272, no. 14, pp. 3661–72, 2005.
- [192] D.-P. Hong, A. L. Fink, and V. N. Uversky, "Smoking and Parkinson's disease: does nicotine affect alpha-synuclein fibrillation?," *Biochimica et Biophysica Acta*, vol. 1794, no. 2, pp. 282–90, 2009.
- [193] B. Winner, R. Jappelli, S. K. Maji, P. A. Desplats, L. Boyer, S. Aigner, C. Hetzer, T. Lohr, M. Vilar, S. Campioni, C. Tzitzilonis, A. Soragni, S. Jessberger, H. Mira, A. Consiglio, E. Pham, E. Masliah, F. H. Gage, and R. Riekac, "In vivo demonstration that alpha-synuclein oligomers are toxic," *Proceedings of the National Academy of Sciences of the United States of America*, vol. 108, no. 10, pp. 4194–9, 2011.
- [194] J. R. Silveira, G. Raymond, A. G. Hughson, R. E. Race, V. L. Sim, S. F. Hayes and B. Caughey, "The most infectious prion protein particles," *Nature*, vol. 437, no. 7056, p. 257, 2005.
- [195] D. A. Harris and H. L. True, "New insights into prion structure and toxicity," *Neuron*, vol. 50, no. 3, pp. 353–7, 2006.
- [196] V. N. Uversky, "Mysterious oligomerization of the amyloidogenic proteins," *The FEBS journal*, vol. 277, pp. 2940–2953, 2010.
- [197] K. A. Dasilva, J. E. Shaw, and J. McLaurin, "Amyloid-beta fibrillogenesis: structural insight and therapeutic intervention," *Experimental Neurology*, vol. 223, no. 2, pp. 311–21, 2010.
- [198] H. A. Lashuel and P. T. Lansbury, "Are amyloid diseases caused by protein aggregates that mimic bacterial pore-forming toxins?," *Quarterly reviews of biophysics*, vol. 39, no. 2, pp. 167–201, 2006.
- [199] M. J. Volles and P. T. Lansbury, "Vesicle Permeabilization by Protofibrillar  $\alpha$ -Synuclein Is Sensitive to Parkinson's Disease-Linked Mutations and Occurs by a Pore-like Mechanism †," *Biochemistry*, vol. 41, no. 14, pp. 4595–4602, 2002.
- [200] L. A. Chtcheglova, J. Waschke, L. Wildling, D. Drenckhahn, and P. Hinterdorfer, "Nano-scale dynamic recognition imaging on vascular endothelial cells," *Biophysical Journal*, vol. 93, no. 2, p. L11–L13, 2007.
- [201] S. Zhang, "Fabrication of novel biomaterials through molecular self-assembly," *Nature biotechnology*, vol. 21, no. 10, pp. 1171–8, 2003.
- [202] C. A. E. Hauser and S. Zhang, "Designer self-assembling peptide nanofiber biological materials," *Chemical Society reviews*, no. March, pp. 2780–2790, 2010.

## Reference List

- [203] S. J. Eichhorn, "Cellulose nanowhiskers: promising materials for advanced applications," *Soft Matter*, vol. 7, no. 2, p. 303, 2011.
- [204] S. Mankar, A. Anoop, S. Sen, and S. K. Maji, "Nanomaterials: amyloids reflect their brighter side," *Nano Reviews*, vol. 2, pp. 1–12, 2011.
- [205] H. Cui, M. J. Webber, and S. I. Stupp, "Self-assembly of peptide amphiphiles: from molecules to nanostructures to biomaterials," *Biopolymers*, vol. 94, no. 1, pp. 1–18, 2010.
- [206] J. Kopecek and J. Yang, "Peptide-directed self-assembly of hydrogels," *Acta biomaterialia*, vol. 5, no. 3, pp. 805–16, 2009.
- [207] X. Zhao, F. Pan, H. Xu, M. Yaseen, H. Shan, C. A. E. Hauser, S. Zhang and J. R. Lu, "Molecular self-assembly and applications of designer peptide amphiphiles," *Chemical Society reviews*, vol. 39, no. 9, pp. 3480–98, 2010.
- [208] F. Meersman, R. Q. Cabrera, P. F. McMillan, and V. Dmitriev, "Structural and mechanical properties of TTR105–115 amyloid fibrils from compression experiments," *Biophysical Journal*, vol. 100, no. 1, pp. 193–7, 2011.
- [209] M. R. Caplan, P. N. Moore, S. Zhang, R. D. Kamm, and D. a Lauffenburger, "Self-assembly of a beta-sheet protein governed by relief of electrostatic repulsion relative to van der Waals attraction," *Biomacromolecules*, vol. 1, no. 4, pp. 627–31, 2000.
- [210] D. M. Marini, W. Hwang, D. A. Lauffenburger, S. Zhang, and R. D. Kamm, "Left-Handed Helical Ribbon Intermediates in the Self-Assembly of a  $\beta$ -Sheet Peptide," *Nano Letters*, vol. 2, no. 4, pp. 295–299, 2002.
- [211] Z. Luo, B. Åkerman, S. Zhang, and B. Nordén, "Structures of self-assembled amphiphilic peptide-heterodimers: effects of concentration, pH, temperature and ionic strength," *Soft Matter*, vol. 6, no. 10, p. 2260, 2010.
- [212] M. R. Tiné, M. Alderighi, C. Duce, L. Ghezzi, and R. Solaro, "Effect of temperature on self-assembly of an ionic tetrapeptide," *Journal of Thermal Analysis and Calorimetry*, vol. 103, no. 1, pp. 75–80, 2010.
- [213] H. Yokoi, T. Kinoshita, and S. Zhang, "Dynamic reassembly of peptide RADA16 nanofiber scaffold," *Proceedings of the National Academy of Sciences of the United States of America*, vol. 102, no. 24, pp. 8414–9, 2005.
- [214] Z. Luo, X. Zhao, and S. Zhang, "Self-organization of a chiral D-EAK16 designer peptide into a 3D nanofiber scaffold," *Macromolecular Bioscience*, vol. 8, no. 8, pp. 785–91, 2008.
- [215] J. Sun and Q. Zheng, "Experimental study on self-assembly of KLD-12 peptide hydrogel and 3-D culture of MSC encapsulated within hydrogel in vitro," *Journal of Huazhong University of Science and Technology*, vol. 29, no. 4, pp. 512–6, 2009.
- [216] J. Dai, "Characterization of self-assembling peptide nanofibers of KLD12 and RID 12," Thesis (M. Eng.)—*Massachusetts Institute of Technology*, 2004.
- [217] L. Wang and X.-J. Zhao, "Investigation of Self-assembly Structure and Properties of a Novel Designed Lego-type Peptide with Double Amphiphilic Surfaces," *Bulletin of the Korean Chemical Society*, vol. 31, no. 12, pp. 3740–3744, 2010.
- [218] M. J. Kogan, I. Dalcol, P. Gorostiza, C. López-Iglesias, M. Pons, F. Sanz, D. Ludevid, and E. Giralt, "Self-assembly of the amphipathic helix (VHLPPP)<sub>8</sub>. A mechanism for zein protein body formation," *Journal of Molecular Biology*, vol. 312, no. 5, pp. 907–13, 2001.
- [219] M. J. Kogan, I. Dalcol, P. Gorostiza, C. Lopez-Iglesias, R. Pons, M. Pons, F. Sanz and E. Giralt, "Supramolecular properties of the proline-rich gamma-Zein N-terminal domain," *Biophysical Journal*, vol. 83, no. 2, pp. 1194–204, 2002.
- [220] M. Grinstaff, "Dendritic macromers for hydrogel formation: Tailored materials for ophthalmic, orthopedic, and biotech applications," *Journal of Polymer Science Part A: Polymer*, vol. 46, pp. 383–400, 2008.

## Reference List

- [221] S.-C. Lo, N.A.H. Male, J.P.J. Markham, S.W. Magennis, P.L. Burn, O.V. Salata and I.D.W. Samuel, "Green phosphorescent dendrimer for light-emitting diodes," *Advanced Materials*, vol. 14, no. 13–14, pp. 975–979, 2002.
- [222] V. Haridas, Y. K. Sharma, R. Creasey, S. Sahu, C. T. Gibson, and N. H. Voelcker, "Gelation and topochemical polymerization of peptide dendrimers," *New Journal of Chemistry*, vol. 35, no. 2, p. 303, 2011.
- [223] A. R. Hirst, D. K. Smith, M. C. Feiters, H. P. M. Geurts, and A. C. Wright, "Two-component dendritic gels: easily tunable materials," *Journal of the American Chemical Society*, vol. 125, no. 30, pp. 9010–1, 2003.
- [224] D. K. Smith, "Dendritic Gels—Many Arms Make Light Work," *Advanced Materials*, vol. 18, no. 20, pp. 2773–2778, 2006.
- [225] R. Mammadov, A. B. Tekinay, A. Dana, and M. O. Guler, "Microscopic characterization of peptide nanostructures," *Micron*, 2011.
- [226] H. Cui, T. Muraoka, A. G. Cheetham, and S. I. Stupp, "Self-Assembly of Giant Peptide Nanobelts 2009," *Nano*, 2009.
- [227] M. Ghadiri, J. Granja, R. Milligan, and D. McRee, "Self-assembling organic nanotubes based on a cyclic peptide architecture," *Nature*, 1993.
- [228] R. J. Brea, C. Reiriz, and J. R. Granja, "Towards functional bionanomaterials based on self-assembling cyclic peptide nanotubes," *Chemical Society reviews*, vol. 39, no. 5, pp. 1448–56, 2010.
- [229] H. G. Börner, "Strategies exploiting functions and self-assembly properties of bioconjugates for polymer and materials sciences," *Progress in Polymer Science*, vol. 34, no. 9, pp. 811–851, 2009.
- [230] R. Hourani and A. Kakkar, "Advances in the elegance of chemistry in designing dendrimers," *Macromolecular Rapid Communications*, vol. 31, no. 11, pp. 947–74, 2010.
- [231] A. Jain, S. Dubey, and A. Kaushik, "Dendrimer: A complete drug carrier," *International Journal of Pharmaceutical Sciences and Research*, vol. 1, no. 4, pp. 38–53, 2010.
- [232] E. Buhleier, W. Wehner and F. Vögtle, "'Cascade'- and 'Nonskid-Chain-like' Syntheses of Molecular Cavity Topologies," *Synthesis*, vol. 1978, no. 2, pp. 155–158, 1978.
- [233] C. J. Hawker and J. M. J. Fréchet, "Preparation of polymers with controlled molecular architecture. A new convergent approach to dendritic macromolecules," *Journal of the American Chemical Society*, vol. 112, no. 21, pp. 7638–7647, 1990.
- [234] a W. Bosman, H. M. Janssen, and E. W. Meijer, "About dendrimers: Structure, physical properties, and applications," *Chemical Reviews*, vol. 99, no. 7, pp. 1665–1688, 1999.
- [235] C. C. Lee, J. A. MacKay, J. M. J. Fréchet, and F. C. Szoka, "Designing dendrimers for biological applications," *Nature biotechnology*, vol. 23, no. 12, pp. 1517–26, 2005.
- [236] M. A. Mintzer and M. W. Grinstaff, "Biomedical applications of dendrimers: a tutorial," *Chemical Society reviews*, vol. 40, no. 1, pp. 173–90, 2011.
- [237] R. Prakash, B. Soni, S. Jain, and A. Bhandari, "Dendrimer: A polymer of 21st century dendrimer," *Review Literature And Arts Of The Americas*, vol. 1, no. 9, pp. 1–15, 2010.
- [238] V. Haridas, Y. K. Sharma, S. Sahu, R. P. Verma, S. Sadanandan, and B. G. Kacheshwar, "Designer peptide dendrimers using click reaction," *Tetrahedron*, vol. 67, no. 10, pp. 1873–1884, 2011.
- [239] H. C. Kolb, M. G. Finn, and K. B. Sharpless, "Click Chemistry: Diverse Chemical Function from a Few Good Reactions," *Angewandte Chemie (International ed. in English)*, vol. 40, no. 11, pp. 2004–2021, 2001.

## Reference List

- [240] D. Astruc, E. Boisselier, and C. Ornelas, "Dendrimers designed for functions: from physical, photophysical, and supramolecular properties to applications in sensing, catalysis, molecular electronics, photonics, and nanomedicine," *Chemical Reviews*, vol. 110, no. 4, pp. 1857–959, 2010.
- [241] B. K. Nanjwade, H. M. Bechra, G. K. Derkar, F. V. Manvi, and V. K. Nanjwade, "Dendrimers: emerging polymers for drug–delivery systems," *European Journal of Pharmaceutical Sciences*, vol. 38, no. 3, pp. 185–96, 2009.
- [242] P. Niederhafner, J. Sebestík, and J. Jezek, "Peptide dendrimers," *Journal of Peptide Science*, vol. 11, no. 12, pp. 757–88, 2005.
- [243] J. B. Matson, R. H. Zha, and S. I. Stupp, "Peptide self–assembly for crafting functional biological materials," *Current Opinion in Solid State and Materials Science*, pp. 1–11, 2011.
- [244] E. Dawson, G. Mapili, K. Erickson, S. Taqvi, and K. Roy, "Biomaterials for stem cell differentiation," *Advanced drug delivery reviews*, vol. 60, no. 2, pp. 215–28, 2008.
- [245] A. L. Hook, D. G. Anderson, R. Langer, P. Williams, M. C. Davies, and M. R. Alexander, "High throughput methods applied in biomaterial development and discovery," *Biomaterials*, vol. 31, no. 2, pp. 187–98, 2010.
- [246] D. Charych, Q. Cheng, A. Reichert, G. Kuziemko, M. Stroh, J. O. Nagy, W. Spevak, and R. C. Stevens, "A 'litmus test' for molecular recognition using artificial membranes," *Chemistry & Biology*, vol. 3, no. 2, pp. 113–20, 1996.
- [247] S. Kolusheva, T. Shahal, and R. Jelinek, "Peptide–membrane interactions studied by a new phospholipid/polydiacetylene colorimetric vesicle assay," *Biochemistry*, vol. 39, no. 51, pp. 15851–9, 2000.
- [248] L. Silbert, I. Ben Shlush, E. Israel, A. Porgador, S. Kolusheva, and R. Jelinek, "Rapid chromatic detection of bacteria by use of a new biomimetic polymer sensor," *Applied and environmental microbiology*, vol. 72, no. 11, pp. 7339–44, 2006.
- [249] J. Song, Q. Cheng, and S. Zhu, "'Smart' Materials for Biosensing Devices: Cell–Mimicking Supramolecular Assemblies and Colorimetric Detection of Pathogenic Agents," *Biomedical Microdevices*, pp. 213–221, 2002.
- [250] A.–M. Caminade, R. Laurent, and J.–P. Majoral, "Characterization of dendrimers," *Advanced drug delivery reviews*, vol. 57, no. 15, pp. 2130–46, 2005.
- [251] L. W. Hoffman, G. G. Andersson, A. Sharma, S. R. Clarke, and N. H. Voelcker, "New insights into the structure of PAMAM dendrimer/gold nanoparticle nanocomposites," *Langmuir*, vol. 27, no. 11, pp. 6759–67, 2011.
- [252] V. Haridas, Y. K. Sharma, and S. Naik, "Multi–Tier Dendrimers with an Aromatic Core," *European Journal of Organic Chemistry*, no. 10, pp. 1570–1577, 2009.
- [253] T. Junno, K. Deppert, L. Montelius, and L. Samuelson, "Controlled manipulation of nanoparticles with an atomic force microscope," *Applied Physics Letters*, vol. 66, no. 26, p. 3627, 1995.
- [254] X. Liang, G. Mao, and K. Y. Simon Ng, "Probing small unilamellar EggPC vesicles on mica surface by atomic force microscopy," *Colloids and Surfaces. B: Biointerfaces*, vol. 34, no. 1, pp. 41–51, 2004.
- [255] I. Reviakine and A. Brisson, "Formation of Supported Phospholipid Bilayers from Unilamellar Vesicles Investigated by Atomic Force Microscopy," *Langmuir*, vol. 16, no. 4, pp. 1806–1815, 2000.
- [256] W. Cai, G.–tao Wang, Y.–xiang Xu, X.–kui Jiang, and Z.–ting Li, "Vesicles and organogels from foldamers: a solvent–modulated self–assembling process," *Journal of the American Chemical Society*, vol. 130, no. 22, pp. 6936–7, 2008.
- [257] Y. H. I. E. Kim, W. T. Ford, and T. H. Mourey, "Branched Poly ( styrene–b–tert–butyl acrylate ) and Poly ( styrene–b–acrylic acid ) by ATRP from a Dendritic Poly ( propylene imine )( NH 2 ) 64 Core," *Polymer*, pp. 4623–4634, 2007.

## Reference List

- [258] R. Wang, C. Geiger, L. Chen, B. Swanson, and D. G. Whitten, "Direct Observation of Sol–Gel Conversion: The Role of the Solvent in Organogel Formation," *Journal of the American Chemical Society*, vol. 122, no. 10, pp. 2399–2400, 2000.
- [259] M. Schott, "The colors of polydiacetylenes: A commentary," *The journal of physical chemistry. B*, vol. 110, no. 32, pp. 15864–8, 2006.
- [260] F. W. Fowler and J. W. Lauher, "A rational design of molecular materials," *Journal of Physical Organic Chemistry*, vol. 13, no. 12, pp. 850–857, 2000.
- [261] J. Luo, Z. Xie, J. W. Y. Lam, L. Cheng, H. Chen, C. Qiu, H. S. Kwok, X. Zhan and Y. Liu, "Aggregation–induced emission of 1–methyl–1,2,3,4,5–pentaphenylsilole," *Chemical Communications*, vol. 381, no. 18, pp. 1740–1741, 2001.
- [262] B.–K. An, S.–K. Kwon, S.–D. Jung, and S. Y. Park, "Enhanced emission and its switching in fluorescent organic nanoparticles," *Journal of the American Chemical Society*, vol. 124, no. 48, pp. 14410–5, 2002.
- [263] S. Yin, C. Wang, B. Song, S. Chen, and Z. Wang, "Self–organization of a polymerizable bolaamphiphile bearing a diacetylene group and L–aspartic acid group," *Langmuir*, vol. 25, no. 16, pp. 8968–73, 2009.
- [264] G. Wegner, "Solid–state polymerization mechanisms," *Pure & Applied Chemistry*, vol. 49, pp. 443–454, 1977.
- [265] A. L. Hook, H. Thissen, and N. H. Voelcker, "Advanced substrate fabrication for cell microarrays," *Biomacromolecules*, vol. 10, no. 3, pp. 573–9, 2009.
- [266] A. Mata, L. Hsu, R. Capito, C. Aparicio, K. Henrikson, and S. I. Stupp, "Micropatterning of bioactive self–assembling gels," *Soft matter*, vol. 5, no. 6, pp. 1228–1236, 2009.
- [267] R. O. Hynes, "The extracellular matrix: not just pretty fibrils," *Science*, vol. 326, no. 5957, pp. 1216–9, 2009.
- [268] P. Singh, C. Carraher, and J. E. Schwarzbauer, "Assembly of Fibronectin Extracellular Matrix," *Annual review of cell and developmental biology*, 2010.
- [269] R. Timpl and J. C. Brown, "Supramolecular assembly of basement membranes," *Bioessays*, vol. 18, no. 2, pp. 123–132, 1996.
- [270] F. Vollrath, "Strength and structure of spiders' silks," *Journal of biotechnology*, vol. 74, no. 2, pp. 67–83, 2000.
- [271] J. W. Hearle, "A critical review of the structural mechanics of wool and hair fibres," *International journal of biological macromolecules*, vol. 27, no. 2, pp. 123–38, 2000.
- [272] J. He, X. Qi, Y. Miao, H. L. Wu, N. He, and J. J. Zhu, "Application of smart nanostructures in medicine," *Nanomedicine*, vol. 5, no. 7, pp. 1129–1138, 2010.
- [273] N. Higashi, "Self–Assembled Peptide Nanofibers," *Advanced Computer Simulation Approaches For Soft Matter Sciences I*, no. July, pp. 27–68, 2008.
- [274] J. E. Coronado, S. Mneimneh, S. L. Epstein, W.–G. Qiu, and P. N. Lipke, "Conserved processes and lineage–specific proteins in fungal cell wall evolution," *Eukaryotic cell*, vol. 6, no. 12, pp. 2269–77, 2007.
- [275] M. S. Doblin, F. Pettolino, and A. Bacic, "Evans Review : Plant cell walls: the skeleton of the plant world," *Functional Plant Biology*, vol. 37, no. 5, p. 357, 2010.
- [276] L. Taiz and E. Zieger, "Cell Walls: Structure, Biogenesis and Expansion," in *Plant Physiology*, Sinauer Associates, Inc, 2010.
- [277] M. C. Cannon, K. Terneus, Q. Hall, L. Tan, Y. Wang, B. L. Wegenhart, L. Chen, D. T. A. Lampert, Y. Chen and M. J. Kieliszewski, "Self–assembly of the plant cell wall requires an extensin scaffold," *Proceedings of the National Academy of Sciences of the United States of America*, vol. 105, no. 6, pp. 2226–31, 2008.

## Reference List

- [278] S. Rauscher, S. Baud, M. Miao, F. W. Keeley, and R. Pomès, “Proline and glycine control protein self-organization into elastomeric or amyloid fibrils,” *Structure*, vol. 14, no. 11, pp. 1667–76, 2006.
- [279] M. D. Shoulders and R. T. Raines, “Collagen structure and stability,” *Annual review of biochemistry*, vol. 78, p. 929, 2009.
- [280] C. J. Schultz and M. J. Harrison, “Novel plant and fungal AGP-like proteins in the *Medicago truncatula*–*Glomus intraradices* arbuscular mycorrhizal symbiosis,” *Mycorrhiza*, vol. 18, no. 8, pp. 403–412, 2008.
- [281] K. Ma and K. Wang, “Malleable conformation of the elastic PEVK segment of titin: non-co-operative interconversion of polyproline II helix, beta-turn and unordered structures,” *Biochemical Journal*, vol. 374, no. 3, p. 687, 2003.
- [282] N. Matsushima, T. Tanaka, and R. H. Kretsinger, “Non-globular structures of tandem repeats in proteins,” *Protein and Peptide Letters*, vol. 16, no. 11, pp. 1297–322, 2009.
- [283] Y. Mansiaux, A. P. Joseph, J.-C. Gelly, and A. G. de Brevern, “Assignment of PolyProline II conformation and analysis of sequence–structure relationship,” *PLoS one*, vol. 6, no. 3, p. e18401, 2011.
- [284] L. D. Muiznieks and F. W. Keeley, “Proline periodicity modulates the self-assembly properties of elastin-like polypeptides,” *The Journal of Biological Chemistry*, vol. 285, no. 51, pp. 39779–89, 2010.
- [285] G. Siligardi and A. F. Drake, “The importance of extended conformations and, in particular, the PII conformation for the molecular recognition of peptides,” *Biopolymers*, vol. 37, no. 4, pp. 281–92, 1995.
- [286] R. V. Pappu, X. Wang, A. Vitalis, and S. L. Crick, “A polymer physics perspective on driving forces and mechanisms for protein aggregation,” *Archives of biochemistry and biophysics*, vol. 469, no. 1, pp. 132–41, 2008.
- [287] D. A. White, A. K. Buell, T. P. J. Knowles, M. E. Welland, and C. M. Dobson, “Protein aggregation in crowded environments,” *Journal of the American Chemical Society*, vol. 132, no. 14, pp. 5170–5, 2010.
- [288] G. Gutierrez-Cruz, a H. Van Heerden, and K. Wang, “Modular motif, structural folds and affinity profiles of the PEVK segment of human fetal skeletal muscle titin,” *The Journal of Biological Chemistry*, vol. 276, no. 10, pp. 7442–9, 2001.
- [289] A. M. Tamburro, B. Bochicchio, and A. Pepe, “Dissection of human tropoelastin: exon-by-exon chemical synthesis and related conformational studies,” *Biochemistry*, vol. 42, no. 45, pp. 13347–62, 2003.
- [290] Z. Shi, K. Chen, Z. Liu, and N. R. Kallenbach, “Conformation of the backbone in unfolded proteins,” *Chemical Reviews*, vol. 106, no. 5, pp. 1877–97, 2006.
- [291] R. Woody, *Advances in Biophysical Chemistry, Volume 2*. JAI Press, 1992, pp. 37 – 79.
- [292] L. A. Bottomley, “Scanning probe microscopy,” *Analytical chemistry*, vol. 70, no. 12, p. 425R–475R, 1998.
- [293] N. J. Greenfield, “Analysis of circular dichroism data,” *Methods in Enzymology*, vol. 383, pp. 282–317, 2004.
- [294] A. Perczel, K. Park, and G. D. Fasman, “Analysis of the circular dichroism spectrum of proteins using the convex constraint algorithm: A practical guide,” *Analytical biochemistry*, vol. 203, no. 1, pp. 83–93, 1992.
- [295] D. W. P. M. Löwik and J. C. M. van Hest, “Peptide based amphiphiles,” *Chemical Society reviews*, vol. 33, no. 4, pp. 234–45, 2004.
- [296] G. Darnell, J. P. R. O. Orgel, R. Pahl, and S. C. Meredith, “Flanking polyproline sequences inhibit beta-sheet structure in polyglutamine segments by inducing PPII-like helix structure,” *Journal of Molecular Biology*, vol. 374, no. 3, pp. 688–704, 2007.

## Reference List

- [297] E. Eiríksdóttir, K. Konate, U. Langel, G. Divita, and S. Deshayes, “Secondary structure of cell-penetrating peptides controls membrane interaction and insertion,” *Biochimica et biophysica acta*, vol. 1798, no. 6, pp. 1119–28, 2010.
- [298] B. Bochicchio, A. Pepe, and A. M. Tamburro, “Investigating by CD the molecular mechanism of elasticity of elastomeric proteins,” *Chirality*, vol. 20, no. 9, pp. 985–94, 2008.
- [299] A. L. Rucker, C. T. Pager, M. N. Campbell, J. E. Qualls, and T. P. Creamer, “Host-guest scale of left-handed polyproline II helix formation,” *Proteins*, vol. 53, no. 1, pp. 68–75, 2003.
- [300] M. Moradi, V. Babin, C. Sagui, and C. Roland, “PPII propensity of multiple-guest amino acids in a proline-rich environment,” *The journal of physical chemistry. B*, vol. 115, no. 26, pp. 8645–56, 2011.
- [301] B. Sattelmacher, “The apoplast and its significance for plant mineral nutrition,” *New Phytologist*, vol. 149, no. 2, pp. 167–192, 2001.
- [302] C. Grignon and H. Sentenac, “pH and ionic conditions in the apoplast,” *Annual Review of Plant Biology*, vol. 42, no. 1, pp. 103–128, 1991.
- [303] M. J. Canny, “Apoplastic Water and Solute Movement: New Rules for an Old Space,” *Annual Review of Plant Physiology and Plant Molecular Biology*, vol. 46, no. 1, pp. 215–236, 1995.
- [304] K. Ma, L. Kan, and K. Wang, “Polyproline II helix is a key structural motif of the elastic PEVK segment of titin,” *Biochemistry*, vol. 40, no. 12, pp. 3427–38, 2001.
- [305] J. F. Almine, D. V. Bax, S. M. Mithieux, L. Nivison-Smith, J. Rnjak, A. Waterhouse, S. G. Wise and A. S. Weiss, “Elastin-based materials,” *Chemical Society reviews*, vol. 39, no. 9, pp. 3371–9, 2010.
- [306] P.-E. Milhiet, D. Yamamoto, O. Berthoumieu, P. Dosset, C. Le Grimellec, J.-M. Verdier, S. Marchal and T. Ando, “Deciphering the structure, growth and assembly of amyloid-like fibrils using high-speed atomic force microscopy,” *PloS one*, vol. 5, no. 10, p. e13240, 2010.
- [307] I. Revenko, F. Sommer, D. T. Minh, R. Garrone, and J. M. Franc, “Atomic force microscopy study of the collagen fibre structure,” *Biology of the cell / under the auspices of the European Cell Biology Organization*, vol. 80, no. 1, pp. 67–9, 1994.
- [308] A. M. Salvi, P. Moscarelli, G. Satriano, B. Bochicchio, and J. E. Castle, “Influence of amino acid specificities on the molecular and supramolecular organization of glycine-rich elastin-like polypeptides in water,” *Biopolymers*, vol. 95, no. 10, pp. 702–21, 2011.
- [309] A. Bhattacharjee and M. Bansal, “Collagen structure: the Madras triple helix and the current scenario,” *IUBMB life*, vol. 57, no. 3, pp. 161–72, 2005.
- [310] H. Javot, R. V. Penmetsa, N. Terzaghi, D. R. Cook, and M. J. Harrison, “A Medicago truncatula phosphate transporter indispensable for the arbuscular mycorrhizal symbiosis,” *Proceedings of the National Academy of Sciences of the United States of America*, vol. 104, no. 5, pp. 1720–5, 2007.
- [311] J. Kyte, R. F. Doolittle, S. Diego, and L. Jolla, “A Simple Method for Displaying the Hydrophobic Character of a Protein,” *Structure*, pp. 105–132, 1982.
- [312] C. T. Brett and K. Waldron, *Physiology and biochemistry of plant cell walls*, 2nd ed. London: Chapman & Hall, 1996, pp. 64, 73, 152.
- [313] T. Castellanos, F. Ascencio, and Y. Bashan, “Cell-surface hydrophobicity and cell-surface charge of *Azospirillum* spp.,” *FEMS Microbiology Ecology*, vol. 24, no. 2, pp. 159–172, 1997.
- [314] Y.-R. Yoon, Y.-beom Lim, E. Lee, and M. Lee, “Self-assembly of a peptide rod-coil: a polyproline rod and a cell-penetrating peptide Tat coil,” *Chemical Communications*, no. 16, pp. 1892–4, 2008.

## Reference List

- [315] N. C. Carpita, "Structure and Biogenesis of the Cell Walls of Grasses," *Annual review of plant physiology and plant molecular biology*, vol. 47, pp. 445–476, 1996.
- [316] D. E. Wagner, C. L. Phillips, W. M. Ali, G. E. Nybakken, E. D. Crawford, A. D. Schwab, W. F. Smith and R. Fairman, "Toward the development of peptide nanofilaments and nanoropes as smart materials," *Proceedings of the National Academy of Sciences of the United States of America*, vol. 102, no. 36, pp. 12656–61, 2005.
- [317] C. K. S. Pillai, W. Paul, and C. P. Sharma, "Chitin and chitosan polymers: Chemistry, solubility and fiber formation," *Progress in Polymer Science*, vol. 34, no. 7, pp. 641–678, 2009.
- [318] B. Law, R. Weissleder, and C.–H. Tung, "Peptide–based biomaterials for protease–enhanced drug delivery," *Biomacromolecules*, vol. 7, no. 4, pp. 1261–5, 2006.
- [319] U. Schlötzer–Schrehardt, "Genetics and genomics of pseudoexfoliation syndrome/glaucoma," *Middle East African journal of ophthalmology*, vol. 18, no. 1, pp. 30–6, 2011.
- [320] K. F. Damji, "Progress in understanding pseudoexfoliation syndrome and pseudoexfoliation–associated glaucoma," *Canadian Journal of Ophthalmology*, vol. 42, no. 5, p. 657, 2007.
- [321] S. Sharma, T. Chataway, K. P. Burdon, L. Jonavicius, S. Klebe, A. W. Hewitt, R. A. Mills and J. E. Craig, "Identification of LOXL1 protein and Apolipoprotein E as components of surgically isolated pseudoexfoliation material by direct mass spectrometry," *Experimental Eye Research*, vol. 89, no. 4, pp. 479–485, 2009.
- [322] N. A. Campbell and J. B. Reece, *Biology*, 6th ed. Benjamin Cummings, 2002.
- [323] A. L. Coleman, "Glaucoma," *The Lancet*, vol. 354, no. 9192, pp. 1803–1810, 1999.
- [324] P. Mitchell, W. Smith, K. Attebo, and P. R. Healey, "Prevalence of open–angle glaucoma in Australia: The blue mountains eye study," *Ophthalmology*, vol. 103, no. 10, pp. 1661–1669, 1996.
- [325] J. K. Schmier, M. T. Halpern, and M. L. Jones, "The economic implications of glaucoma," *PharmacoEconomics*, vol. 25, no. 4, pp. 287–308, Jan–2007.
- [326] B. P. Danysh and M. K. Duncan, "The lens capsule," *Experimental Eye Research*, vol. 88, no. 2, pp. 151–64, 2009.
- [327] R. Spiro and S. Fukushi, "The Lens Capsule," *Journal of Biological Chemistry*, vol. 244, no. 8, 1969.
- [328] S. Fukushi and R. G. Spiro, "The lens capsule. Sugar and amino acid composition," *The Journal of Biological Chemistry*, vol. 244, no. 8, pp. 2041–8, 1969.
- [329] P. R. Cammarata, D. Cantu–Crouch, L. Oakford, and a Morrill, "Macromolecular organization of bovine lens capsule," *Tissue & Cell*, vol. 18, no. 1, pp. 83–97, 1986.
- [330] R. S. Sawhney, "Immunological identification of types I and III collagen in bovine lens epithelium and its anterior lens capsule," *Cell Biology International*, vol. 29, no. 2, pp. 133–7, 2005.
- [331] J. M. Brinker, M. T. Pegg, P. S. Howard, and N. A. Kefalides, "Immunochemical characterization of type IV procollagen from anterior lens capsule," *Collagen and Related Research*, vol. 5, no. 3, pp. 233–44, 1985.
- [332] M. Muraoka and T. Hayashi, "Three polypeptides with distinct biochemical properties are major alpha chain–size components of type IV collagen in bovine lens capsule," *Journal of Biochemistry*, vol. 114, no. 3, pp. 358–62, 1993.
- [333] B. Ovodenko, A. Rostagno, T. A. Neubert, V. Shetty, S. Thomas, A. Yang, J. Liebmann, J. Ghiso and R. Ritch, "Proteomic analysis of exfoliation deposits," *Investigative Ophthalmology & Visual Science*, vol. 48, no. 4, pp. 1447–57, 2007.

## Reference List

- [334] M. Ronci, S. Sharma, T. Chataway, K. P. Burdon, S. Martin, J. E. Craig, and N. H. Voelcker, "MALDI-MS-Imaging of Whole Human Lens Capsule," *Journal of Proteome Research*, pp. 3522–29, 2011.
- [335] S. Krag, T. Olsen, and T. T. Andreassen, "Biomechanical characteristics of the human anterior lens capsule in relation to age," *Investigative Ophthalmology & Visual Science*, vol. 38, no. 2, pp. 357–63, 1997.
- [336] B. D. Peczon, J. Peczon, C. Cintron, and B. G. Hudson, "Changes in chemical composition of anterior lens capsules of cataractous human eyes as a function of age," *Experimental Eye Research*, vol. 30, no. 2, pp. 155–165, 1980.
- [337] H. Shichi, "Cataract formation and prevention," *Expert Opinion on Investigational Drugs*, vol. 13, no. 6, pp. 691–701, 2004.
- [338] J. J. Harding, "Physiology, biochemistry, pathogenesis, and epidemiology of cataract," *Current Opinion in Ophthalmology*, vol. 2, no. 1, pp. 3–15, 1991.
- [339] J. M. Jefferis, U. P. Mosimann, and M. P. Clarke, "Cataract and cognitive impairment: a review of the literature," *The British Journal of Ophthalmology*, vol. 95, no. 1, pp. 17–23, 2011.
- [340] M. S. Kosinski-Collins and J. King, "In vitro unfolding, refolding, and polymerization of human gamma crystallin, a protein involved in cataract formation," *Protein Science*, vol. 12, no. 3, pp. 480–490, 2003.
- [341] O. Weinreb, A. F. V. Rijk, A. Dovrat, and H. Bloemendal, "In vitro filament-like formation upon interaction between lens alpha-crystallin and beta L-crystallin promoted by stress," *Investigative Ophthalmology & Visual Science*, vol. 41, no. 12, pp. 3893–3897, 2000.
- [342] L. Drolsum, A. Ringvold, and B. Nicolaissen, "Cataract and glaucoma surgery in pseudoexfoliation syndrome: a review," *Acta ophthalmologica Scandinavica*, vol. 85, no. 8, pp. 810–21, 2007.
- [343] A. Bockelbrink, S. Roll, K. Ruether, A. Rasch, W. Greiner, and S. N. Willich, "Cataract surgery and the development or progression of age-related macular degeneration: a systematic review," *Survey of ophthalmology*, vol. 53, no. 4, pp. 359–67, 2008.
- [344] U. Schlötzer-Schrehardt and G. O. H. Naumann, "Ocular and systemic pseudoexfoliation syndrome," *American journal of ophthalmology*, vol. 141, no. 5, pp. 921–937, 2006.
- [345] M. R. Praveen, S. K. Shah, A. R. Vasavada, R. P. Diwan, S. M. Shah, B. R. Zumkhawala and R. Thomas, "Pseudoexfoliation as a risk factor for peripheral vascular disease: a case-control study," *Eye*, vol. 25, no. 2, pp. 174–9, 2011.
- [346] P. Mitchell, J. J. Wang, and W. Smith, "Association of pseudoexfoliation syndrome with increased vascular risk," *American journal of ophthalmology*, vol. 124, no. 5, pp. 685–7, 1997.
- [347] G. Dvorak-Theobald, "Pseudoexfoliation of the lens capsule: relation to true exfoliation of the lens capsule as reported in the literature, and role in the production of glaucoma capsulocuticularis," *Transactions of the American Ophthalmological Society*, vol. 51, pp. 385–407, 1953.
- [348] R. Ritch and U. Schlötzer-Schrehardt, "Exfoliation syndrome," *Survey of Ophthalmology*, vol. 45, no. 4, pp. 265–314, 2001.
- [349] E. Vesti and T. Kivelä, "Exfoliation syndrome and exfoliation glaucoma," *Progress in Retinal and Eye Research*, vol. 19, no. 3, pp. 345–368, 2000.
- [350] B. W. Streeten, Z. Li, R. N. Wallace, R. C. Eagle, and A. A. Keshgegian, "Pseudoexfoliative fibrilopathy in visceral organs of a patient with pseudoexfoliation syndrome," *Archives Of Ophthalmology*, Vol. 110, No. 12, Pp. 1757–1762, 1992.

## Reference List

- [351] N. Yamamoto and A. Miyagawa, "True exfoliation of the lens capsule following uveitis," *Graefe's Archive for Clinical and Experimental Ophthalmology*, vol. 238, no. 12, pp. 1009–10, 2000.
- [352] U. Schlötzer–Schrehardt, "Molecular pathology of pseudoexfoliation syndrome/glaucoma—new insights from LOXL1 gene associations," *Experimental Eye Research*, vol. 88, no. 4, pp. 776–85, 2009.
- [353] Z.–Y. Li, B. W. Streeten, and R. N. Wallace, "Association of elastin with pseudoexfoliative material: an immunoelectron microscopic study," *Current Eye Research*, vol. 7, no. 12, pp. 1163–1172, 1988.
- [354] U. Schlotzer–Schrehardt, K. Von Der Mark, L. Y. Sakai, and G. Naumann, "Increased extracellular deposition of fibrillin–containing fibrils in pseudoexfoliation syndrome," *Investigative Ophthalmology & Visual Science*, vol. 38, no. 5, p. 970, 1997.
- [355] B. W. Streeten, S. A. Gibson, and a J. Dark, "Pseudoexfoliative material contains an elastic microfibrillar–associated glycoprotein," *Transactions of the American Ophthalmological Society*, vol. 84, pp. 304–20, 1986.
- [356] U. Schlötzer–Schrehardt, S. Dörfler, G. O. H. O. Naumann, and S. Dorfler, "Immunohistochemical localization of basement membrane components in pseudoexfoliation material of the lens capsule," *Current Eye Research*, vol. 11, no. 4, pp. 343–55, 1992.
- [357] M. Calero, A. Rostagno, E. Matsubara, B. Zlokovic, B. Frangione, and J. Ghiso, "Apolipoprotein J (clusterin) and Alzheimer's disease," *Microscopy Research and Technique*, vol. 50, no. 4, pp. 305–315, 2000.
- [358] M. Krumbiegel, F. Pasutto, C. Y. Mardin, N. Weisschuh, D. Paoli, E. Gramer, M. Zenkel, B. H. F. Weber, F. E. Kruse, U. Schlotzer–Schrehardt and A. Reis, "Genetic analysis of the clusterin gene in pseudoexfoliation syndrome," *Molecular Vision*, vol. 14, no. August, pp. 1727–36, 2008.
- [359] M. Krumbiegel, F. Pasutto, C. Y. Mardin, N. Weisschuh, D. Paoli, E. Gramer, M. Zenkel, B. H. F. Weber, F. E. Kruse, U. Schlotzer–Schrehardt and A. Reis, "Exploring functional candidate genes for genetic association in german patients with pseudoexfoliation syndrome and pseudoexfoliation glaucoma," *Investigative Ophthalmology & Visual Science*, vol. 50, no. 6, pp. 2796–801, 2009.
- [360] A. W. Hewitt, S. Sharma, K. P. Burdon, J. J. Wang, P. N. Baird, D. P. Dimasi, D. A. Mackey, P. Mitchell and J. E. Craig, "Ancestral LOXL1 variants are associated with pseudoexfoliation in Caucasian Australians but with markedly lower penetrance than in Nordic people," *Human Molecular Genetics*, vol. 17, no. 5, pp. 710–6, 2008.
- [361] J. A. Aragon–Martin, R. Ritch, J. Liebmann, C. O'Brien, K. Blaaw, F. Mercieca, A. Spiteri, C. J. Cobb, K. F. Damji, A. Tarkkanen, T. Rezaie, A. H. Child and M. Sarfarazi, "Evaluation of LOXL1 gene polymorphisms in exfoliation syndrome and exfoliation glaucoma," *Molecular Vision*, vol. 14, no. 2007, pp. 533–41, 2008.
- [362] G. Thorleifsson, K. P. Magnusson, P. Sulem, G. B. Walters, D. F. Gudbjartsson, H. Stefansson, T. Jonsson, A. Jonasdottir, G. Stefansdottir, G. Masson, G. A. Hardarson, H. Petursson, A. Arnarsson, M. Motalebipour, O. Wallerman, C. Wadelius, J. R. Gulcher, U. Thorsteinsdottir, A. Kong, F. Jonasson and K. Stefansson, "Common sequence variants in the LOXL1 gene confer susceptibility to exfoliation glaucoma," *Science*, vol. 317, no. 5843, pp. 1397–400, 2007.
- [363] M. Krumbiegel, F. Pasutto, U. Schlotzer–Schrehardt, S. Uebe, M. Zenkel, C. Y. Mardin, N. Weisschuh, D. Paoli, E. Gramer, C. Becker, A. B. Ekici, B. H. F. Weber, P. Nurnberg, F. E. Kruse and A. Reis, "Genome–wide association study with DNA pooling identifies variants at CNTNAP2 associated with pseudoexfoliation syndrome," *European Journal of Human Genetics : EJHG*, vol. 19, no. 2, pp. 186–93, 2011.
- [364] M. Zenkel, E. Pöschl, K. von der Mark, C. Hofmann–Rummelt, G. O. H. Naumann, F. E. Kruse and U. Schlötzer–Schrehardt, "Differential gene expression in pseudoexfoliation syndrome," *Investigative Ophthalmology & Visual Science*, vol. 46, no. 10, pp. 3742–52, 2005.

## Reference List

- [365] R. Lee, "The molecular pathophysiology of pseudoexfoliation glaucoma," *Current Opinion in Ophthalmology*, vol. 19, no. 2, pp. 95–101, 2008.
- [366] M. Zenkel, A. Krysta, F. Pasutto, and A. Juenemann, "Regulation of lysyl oxidase-like 1 (LOXL1) and elastin-related genes by pathogenic factors associated with pseudoexfoliation syndrome," *Investigative Ophthalmology & Visual Science*, vol. 1, pp. 1–30, 2011.
- [367] D. Meller, K. Peters, and K. Meller, "Human cornea and sclera studied by atomic force microscopy," *Cell and Tissue Research*, vol. 288, no. 1, pp. 111–118, 1997.
- [368] N. Buzhynskyy, J.-F. Girmens, W. Faigle, and S. Scheuring, "Human cataract lens membrane at subnanometer resolution," *Journal of Molecular Biology*, vol. 374, no. 1, pp. 162–9, 2007.
- [369] V. Dupres, C. Verbelen, and Y. F. Dufrière, "Probing molecular recognition sites on biosurfaces using AFM," *Biomaterials*, vol. 28, no. 15, pp. 2393–402, 2007.
- [370] A. Ebner, L. Wildling, A. S. Kamruzzahan, C. Rankl, C. D. Hahn, J. Wruss, M. Hölzl, R. Zhu, F. Kienberger, D. Blaas, P. Hinterdorfer and H. J. Gruber, "A new, simple method for linking of antibodies to atomic force microscopy tips," *Bioconjugate Chemistry*, vol. 18, no. 4, pp. 1176–84, 2007.
- [371] H. Gruber, K. Schilcher, and H. Schindler, "Detection and localization of individual antibody-antigen recognition events by atomic force microscopy," *Proceedings of the National Academy of Sciences*, vol. 93, no. April, pp. 3477–3481, 1996.
- [372] C. Rankl, F. Kienberger, H. Gruber, D. Blaas, P. and P. Hinterdorfer, "Accuracy Estimation in Force Spectroscopy Experiments," *Journal of Applied Physics*, vol. 46, no. 8, pp. 5536–5539, 2007.
- [373] M. O. Measure, "Electron Microscopic Investigation of the Lens Capsule and Conjunctival Tissues in Individuals with Clinically Unilateral Pseudoexfoliation Syndrome," *American Academy of Ophthalmology*, vol. 115, no. 4, pp. 614–619, 2008.
- [374] M. Zenkel, F. E. Kruse, A. G. Jünemann, G. O. H. Naumann, and U. Schlötzer-Schrehardt, "Clusterin deficiency in eyes with pseudoexfoliation syndrome may be implicated in the aggregation and deposition of pseudoexfoliative material," *Investigative Ophthalmology & Visual Science*, vol. 47, no. 5, pp. 1982–90, 2006.
- [375] Y. Takei and K. Mizuno, "Electron-Microscopic study of pseudo- exfoliation of the lens capsule," *Albrecht von Graefes Archiv for Klinische und Experimentelle Ophthalmologie*, vol. 205, no. 4, pp. 213–220, 1978.
- [376] A. J. Dark, B. W. Streeten, and C. C. Cornwall, "Pseudoexfoliative disease of the lens: a study in electron microscopy and histochemistry," *The British Journal of Ophthalmology*, vol. 61, no. 7, pp. 462–72, 1977.
- [377] A. J. Dark and B. W. Streeten, "Precapsular film on the aging human lens: precursor of pseudoexfoliation?" *British Journal of Ophthalmology*, vol. 74, no. 12, p. 717, 1990.
- [378] K. Tetsumoto, U. Schlötzer-Schrehardt, M. Küchle, S. Dörfler, and H. N. G. Otto, "Precapsular layer of the anterior lens capsule in early pseudoexfoliation syndrome," *Graefe's Archive for Clinical and Experimental Ophthalmology*, vol. 230, no. 3, pp. 252–257, 1992.
- [379] J. Winkler, H. Lünsdorf, C. Wirbelauer, D. P. Reinhardt, and H. Laqua, "Immunohistochemical and charge-specific localization of anionic constituents in pseudoexfoliation deposits on the central anterior lens capsule from individuals with pseudoexfoliation syndrome," *Graefe's Archive for Clinical and Experimental Ophthalmology*, vol. 239, no. 12, pp. 952–960, 2001.
- [380] L. Chtcheglova and P. Hinterdorfer, "Simultaneous topography and recognition imaging on endothelial cells," *Journal of Molecular Recognition*, vol. 24, no. 5, pp. 788–794, 2011.

## Reference List

- [381] M. R. Nussio, R. D. Lowe, N. H. Voelcker, B. S. Flavel, C. T. Gibson, M. J. Sykes, J. O. Miners and J. G. Shapter “Nanoscale structure of lipid domain boundaries,” *Soft Matter*, vol. 6, no. 10, p. 2193, 2010.
- [382] S. Guo, C. Ray, A. Kirkpatrick, N. Lad, and B. B. Akhremitchev, “Effects of multiple-bond ruptures on kinetic parameters extracted from force spectroscopy measurements: revisiting biotin–streptavidin interactions,” *Biophysical Journal*, vol. 95, no. 8, pp. 3964–76, 2008.
- [383] N. B. Holland and R. E. Marchant, “Individual plasma proteins detected on rough biomaterials by phase imaging AFM,” *Journal of Biomedical Materials Research*, vol. 51, no. 3, pp. 307–15, 2000.
- [384] F. Amari, J. Umihara, M. Nohara, S. Nagata, N. Usuda, K. Segawa and N. Yoshimura, “Electron microscopic immunohistochemistry of ocular and extraocular pseudoexfoliative material,” *Experimental Eye Research*, vol. 65, no. 1, pp. 51–6, 1997.
- [385] T. Kohno, N. Sorgente, T. Ishibashi, R. Goodnight, and S. J. Ryan, “Immunofluorescent studies of fibronectin and laminin in the human eye,” *Investigative Ophthalmology & Visual Science*, vol. 28, no. 3, pp. 506–14, 1987.
- [386] S. E. Jones and C. Jomary, “Clusterin,” *The International Journal of Biochemistry & Cell Biology*, vol. 34, no. 5, pp. 427–31, 2002.
- [387] D. T. Humphreys, J. a Carver, S. B. Easterbrook–Smith, and M. R. Wilson, “Clusterin has chaperone–like activity similar to that of small heat shock proteins,” *The Journal of Biological Chemistry*, vol. 274, no. 11, pp. 6875–81, 1999.
- [388] E. Hardenborg, A. Botling–Taube, J. Hanrieder, M. Andersson, A. Alm, and J. Bergquist, “Protein content in aqueous humor from patients with pseudoexfoliation (PEX) investigated by capillary LC MALDI–TOF/TOF MS,” *Proteomics – Clinical Applications*, vol. 3, no. 3, pp. 299–306, 2009.
- [389] L. Thomassin, C. Werneck, T. Broekelmann, and C, “The Pro–regions of lysyl oxidase and lysyl oxidase–like 1 are required for deposition onto elastic fibers,” *The Journal of Biological Chemistry*, vol. 280, no. 52, pp. 42848–55, 2005.
- [390] X. Liu, Y. Zhao, J. Gao, B. Pawlyk, B. Starcher, J. A. Spencer, H. Yanagisawa, J. Luo, and T. Li, “Elastic fiber homeostasis requires lysyl oxidase–like 1 protein,” *Nature Genetics*, vol. 36, no. 2, pp. 178–82, 2004.
- [391] J. L. Grimsby, H. a Lucero, P. C. Trackman, K. Ravid, and H. M. Kagan, “Role of lysyl oxidase propeptide in secretion and enzyme activity,” *Journal of Cellular Biochemistry*, vol. 111, no. 5, pp. 1231–43, 2010.
- [392] H. M. Kagan and W. Li, “Lysyl oxidase: properties, specificity, and biological roles inside and outside of the cell,” *Journal of Cellular Biochemistry*, vol. 88, no. 4, pp. 660–72, 2003.
- [393] P. C. Trackman, D. Bedell–Hogan, J. Tang, and H. M. Kagan, “Post–translational glycosylation and proteolytic processing of a lysyl oxidase precursor,” *The Journal of Biological Chemistry*, vol. 267, no. 12, pp. 8666–71, 1992.
- [394] M. a Williams and H. M. Kagan, “Assessment of lysyl oxidase variants by urea gel electrophoresis: evidence against disulfide isomers as bases of the enzyme heterogeneity,” *Analytical Biochemistry*, vol. 149, no. 2, pp. 430–7, 1985.
- [395] T. Kosonen, J. Y. Uriu–Hare, M. S. Clegg, C. L. Keen, and R. B. Rucker, “Incorporation of copper into lysyl oxidase,” *The Biochemical Journal*, vol. 327, pp. 283–9, 1997.
- [396] S. X. Wang *et al.*, “A crosslinked cofactor in lysyl oxidase: Redox function for amino acid side chains,” *Science*, vol. 273, no. 5278, pp. 1078–84, 1996.
- [397] A. D. Cronshaw, L. a Fothergill–Gilmore, and D. J. Hulmes, “The proteolytic processing site of the precursor of lysyl oxidase,” *The Biochemical Journal*, vol. 306, pp. 279–84, 1995.

## Reference List

- [398] M. V. Panchenko, W. G. Stetler–Stevenson, O. V. Trubetskoy, S. N. Gacheru, and H. M. Kagan, “Metalloproteinase activity secreted by fibrogenic cells in the processing of prolysyl oxidase. Potential role of procollagen C–proteinase,” *The Journal of Biological Chemistry*, vol. 271, no. 12, pp. 7113–9, 1996.
- [399] U. Schlötzer–Schrehardt, F. Pasutto, P. Sommer, I. Hornstra, F. E. Kruse, G. O. Naumann, A. Reis, and M. Zenkel, “Genotype–correlated expression of lysyl oxidase–like 1 in ocular tissues of patients with pseudoexfoliation syndrome/glaucoma and normal patients,” *The American Journal of Pathology*, vol. 173, no. 6, pp. 1724–35, 2008.
- [400] S. G. Wise and A. S. Weiss, “Tropoelastin,” *The International Journal of Biochemistry & Cell Biology*, vol. 41, no. 3, pp. 494–7, 2009.
- [401] C. M. Kielty, M. J. Sherratt, and C. A. Shuttleworth, “Elastic fibres,” *Journal of Cell Science*, vol. 115, no. 14, pp. 2817–28, 2002.
- [402] E. Cleary and W. Cliff, “The substructure of elastin,” *Experimental and Molecular Pathology*, vol. 28, no. 2, pp. 227–246, 1978.
- [403] M. J. Sherratt, “Tissue elasticity and the ageing elastic fibre,” *Age (Dordrecht, Netherlands)*, vol. 31, no. 4, pp. 305–25, 2009.
- [404] M. R. Wilson and S. B. Easterbrook–Smith, “Clusterin is a secreted mammalian chaperone,” *Trends in Biochemical Sciences*, vol. 25, no. 3, pp. 95–8, 2000.
- [405] J. J. Yerbury, E. M. Stewart, A. R. Wyatt, and M. R. Wilson, “Quality control of protein folding in extracellular space,” *EMBO reports*, vol. 6, no. 12, pp. 1131–6, 2005.
- [406] J. Ghiso *et al.*, “The cerebrospinal–fluid soluble form of Alzheimer’s amyloid beta is complexed to SP–40, 40 (apolipoprotein J), an inhibitor of the complement membrane–attack complex,” *Biochemical Journal*, vol. 293, no. 1, p. 27, 1993.
- [407] D. E. Jenne, B. Lowin, M. C. Peitsch, A. Böttcher, G. Schmitz, and J. Tschopp, “Clusterin (complement lysis inhibitor) forms a high density lipoprotein complex with apolipoprotein A–I in human plasma,” *The Journal of Biological Chemistry*, vol. 266, no. 17, pp. 11030–6, 1991.
- [408] G. J. Pankhurst, C. a Bennett, and S. B. Easterbrook–Smith, “Characterization of the heparin–binding properties of human clusterin,” *Biochemistry*, vol. 37, no. 14, pp. 4823–30, 1998.
- [409] G. J. Kelso, W. D. Stuart, R. J. Richter, C. E. Furlong, T. C. Jordan–Starck, and J. a Harmony, “Apolipoprotein J is associated with paraoxonase in human plasma,” *Biochemistry*, vol. 33, no. 3, pp. 832–9, 1994.
- [410] T. Cumurcu, A. Gunduz, H. Ozyurt, H. Nurcin, O. Atis, and M. Egri, “Increased oxidative stress in patients with pseudoexfoliation syndrome,” *Ophthalmic Research*, vol. 43, no. 4, pp. 169–72, 2010.
- [411] S. Allen *et al.*, “The influence of epitope availability on atomic–force microscope studies of antigen–antibody interactions,” *Biochemical Journal*, vol. 341, no. 1, p. 173, 1999.
- [412] H. Bentz, H. P. Bächinger, R. Glanville, and K. Kühn, “Physical evidence for the assembly of A and B chains of human placental collagen in a single triple helix,” *European Journal of Biochemistry / FEBS*, vol. 92, no. 2, pp. 563–7, 1978.

# Appendices

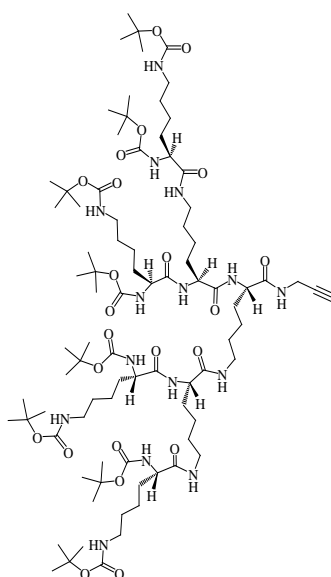
---

## Appendix A

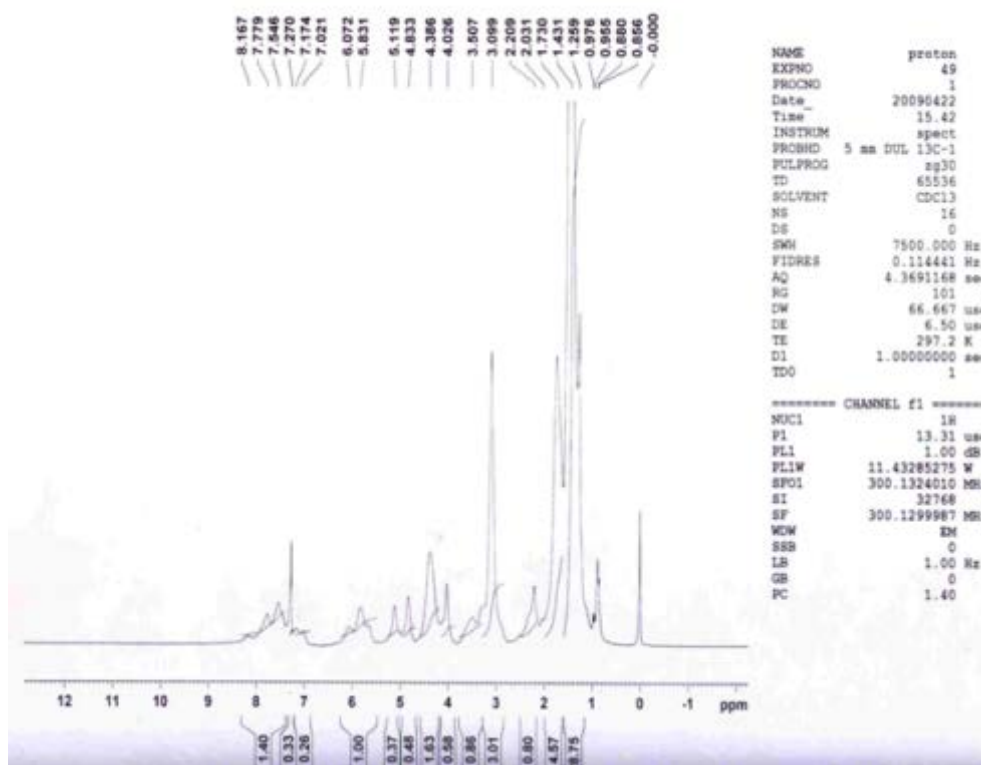
### Supporting data for dendrons and dendrimers

The following characterisations of dendrons and dendrimers used in Chapter 2 were performed and analysed by V. Haridas, Y. Sharma and S. Sahu.

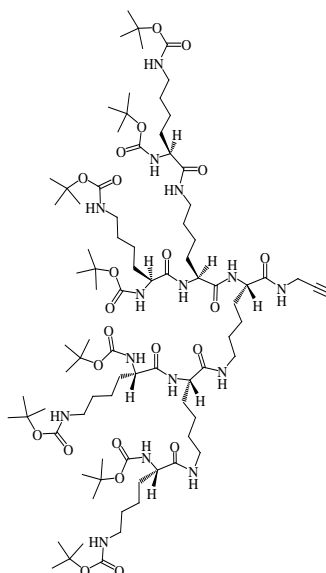
*<sup>1</sup>H NMR (300 MHz, CDCl<sub>3</sub>) of 4*



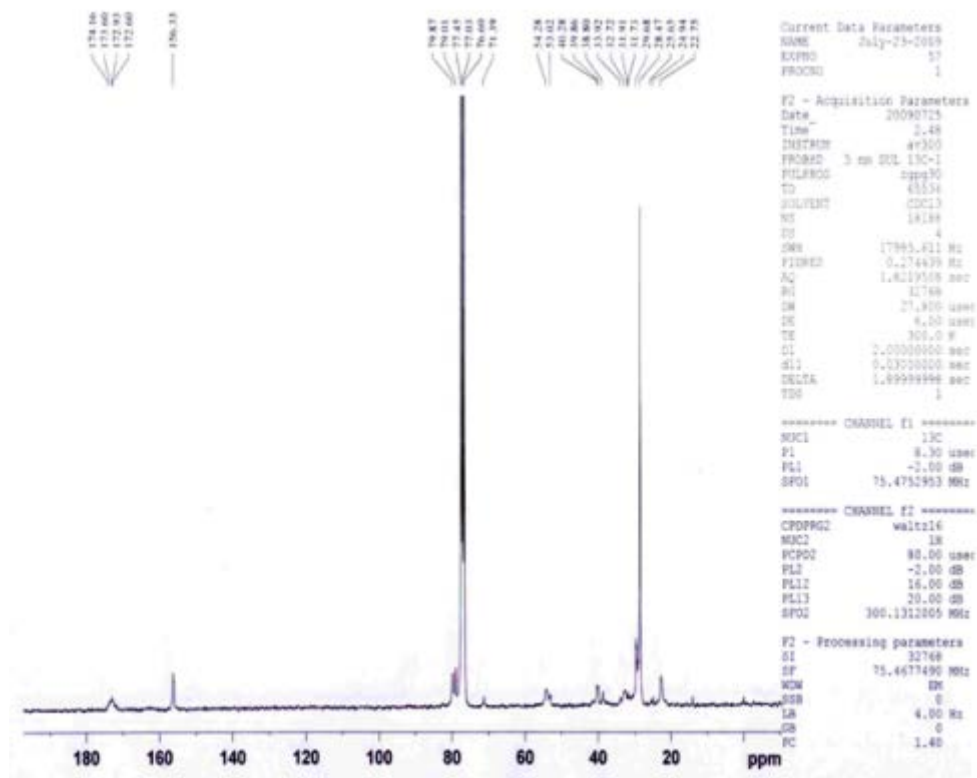
Appendices



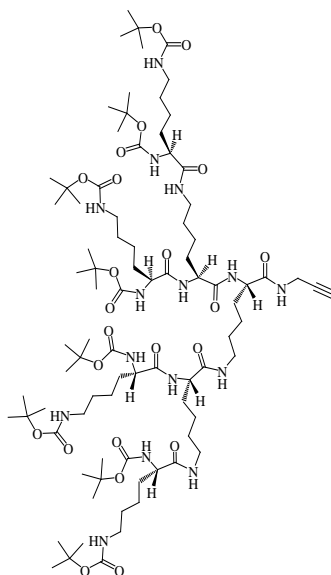
*<sup>13</sup>C NMR (75 MHz, CDCl<sub>3</sub>) of 4*



Appendices



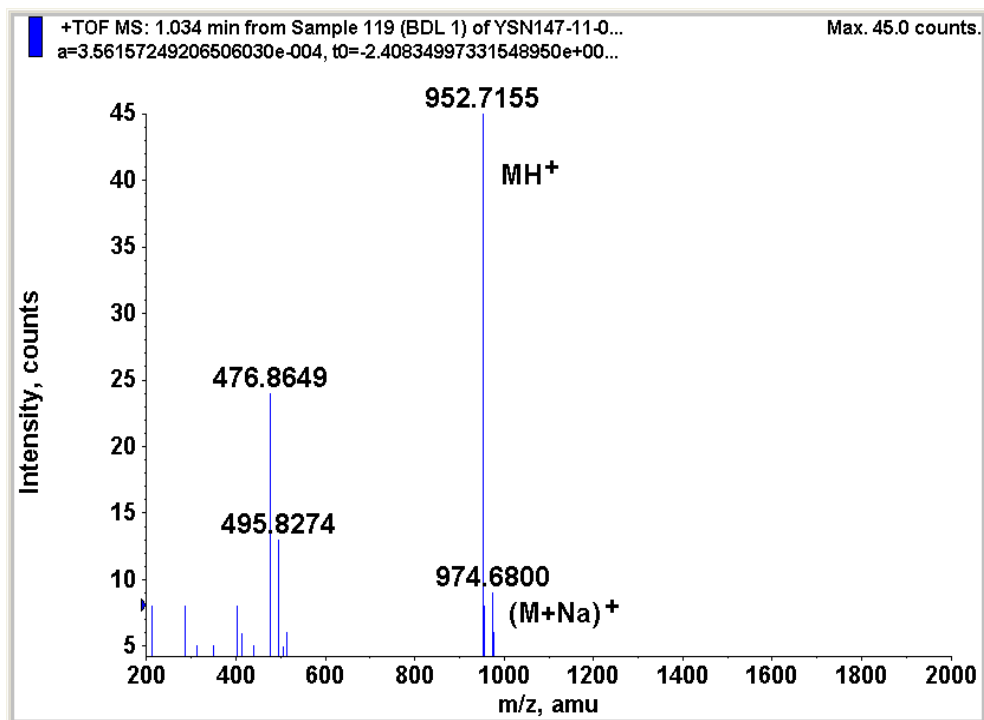
HRMS of 4



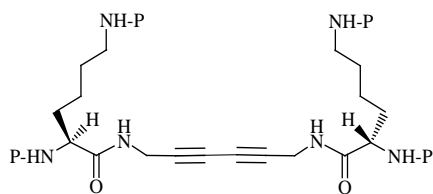




Appendices

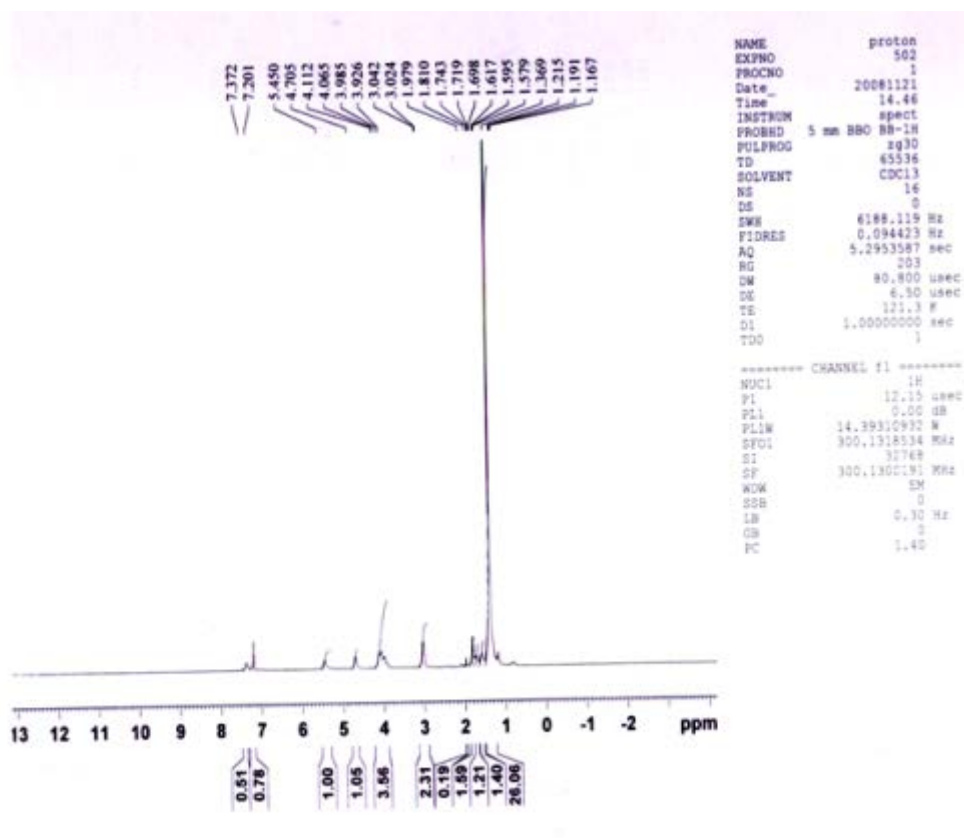


$^1\text{H}$  NMR (300 MHz,  $\text{CDCl}_3$ ) of **5a**

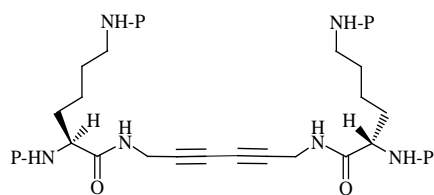


**P = Boc**

Appendices

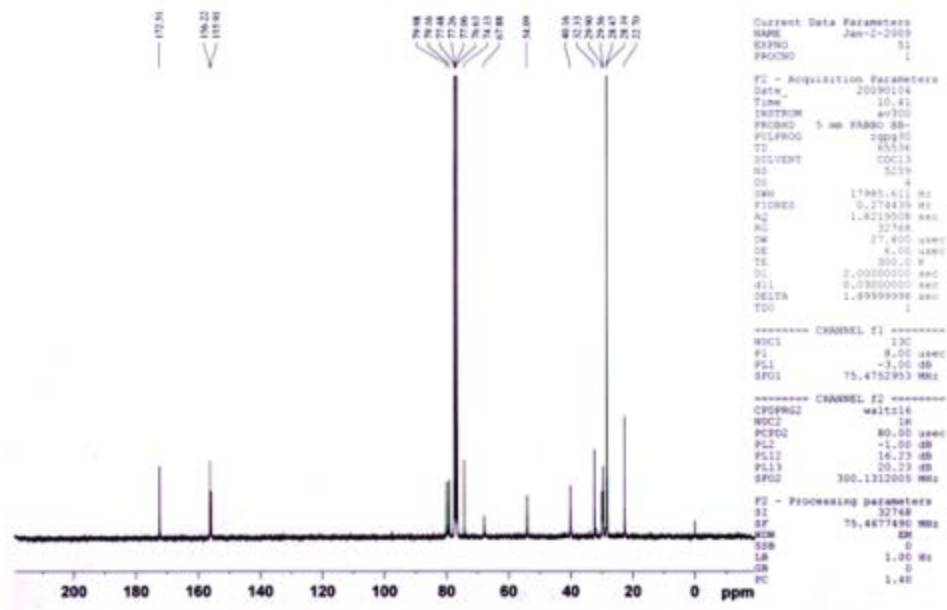


*<sup>13</sup>C NMR (75 MHz, CDCl<sub>3</sub>) of 5a*

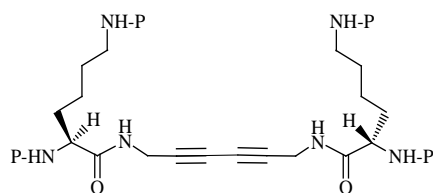


**P = Boc**

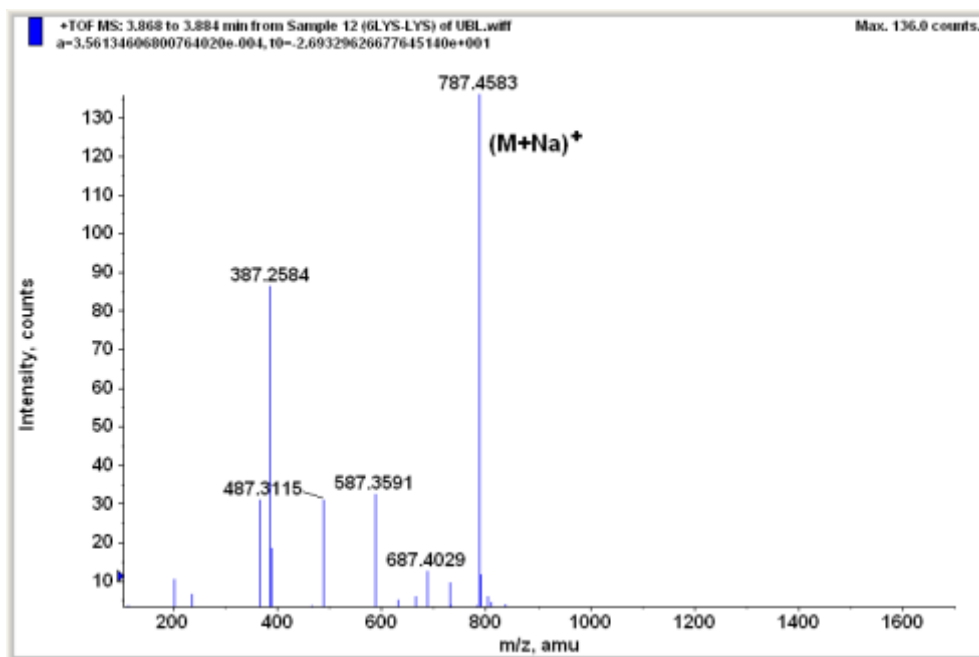
Appendices



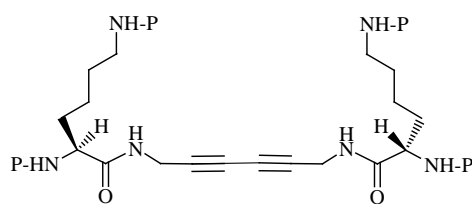
HRMS of 5a



P = Boc

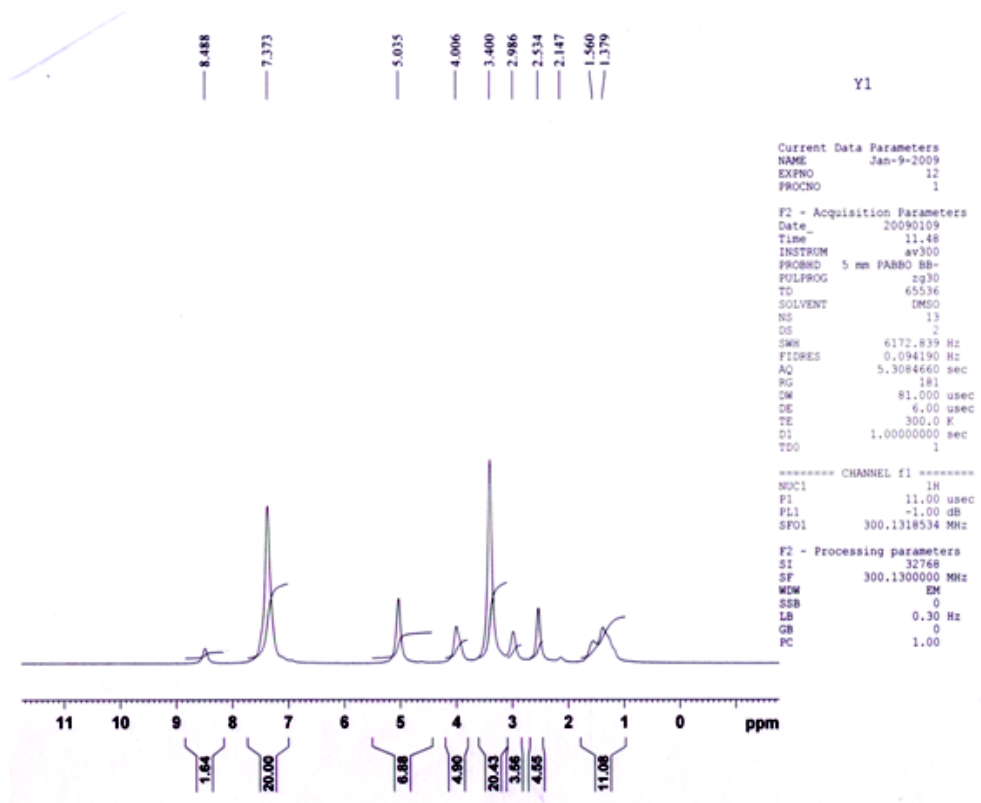


$^1\text{H}$  NMR (300 MHz,  $\text{DMSO}-d_6$ ) of **5b**

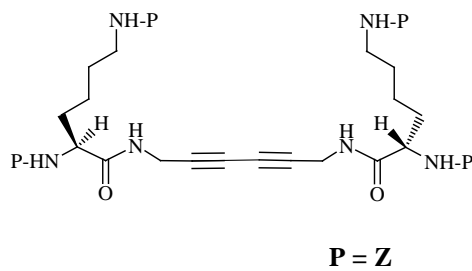


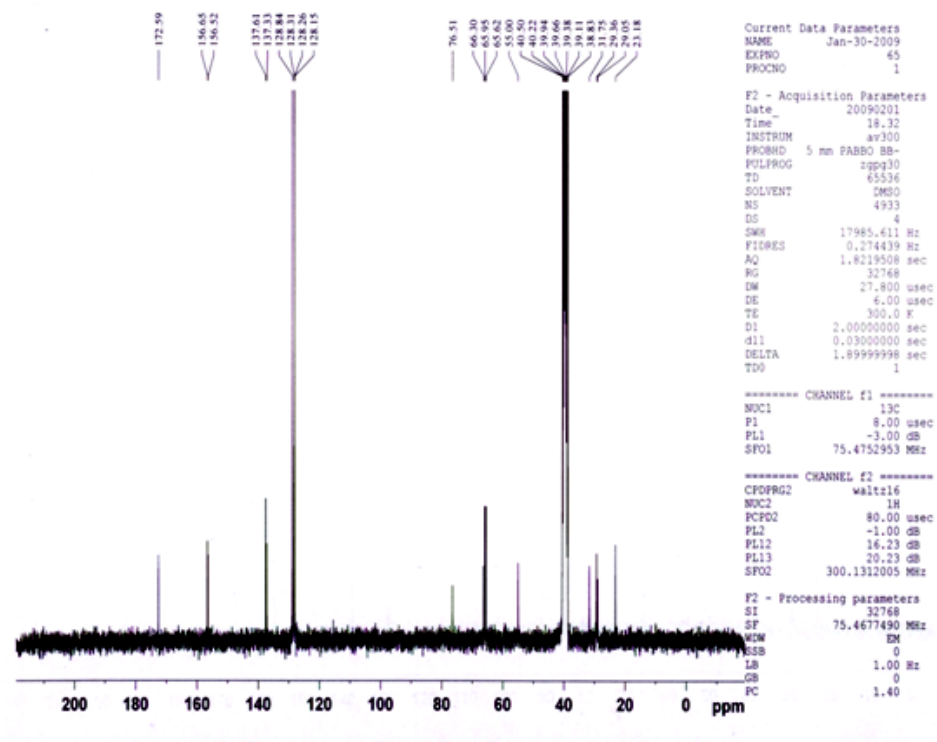
**P = Z**

## Appendices

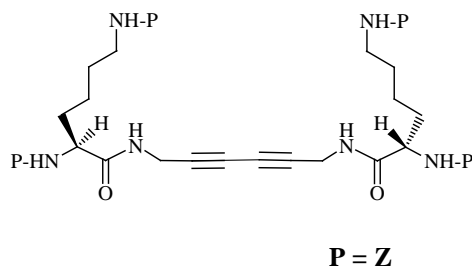


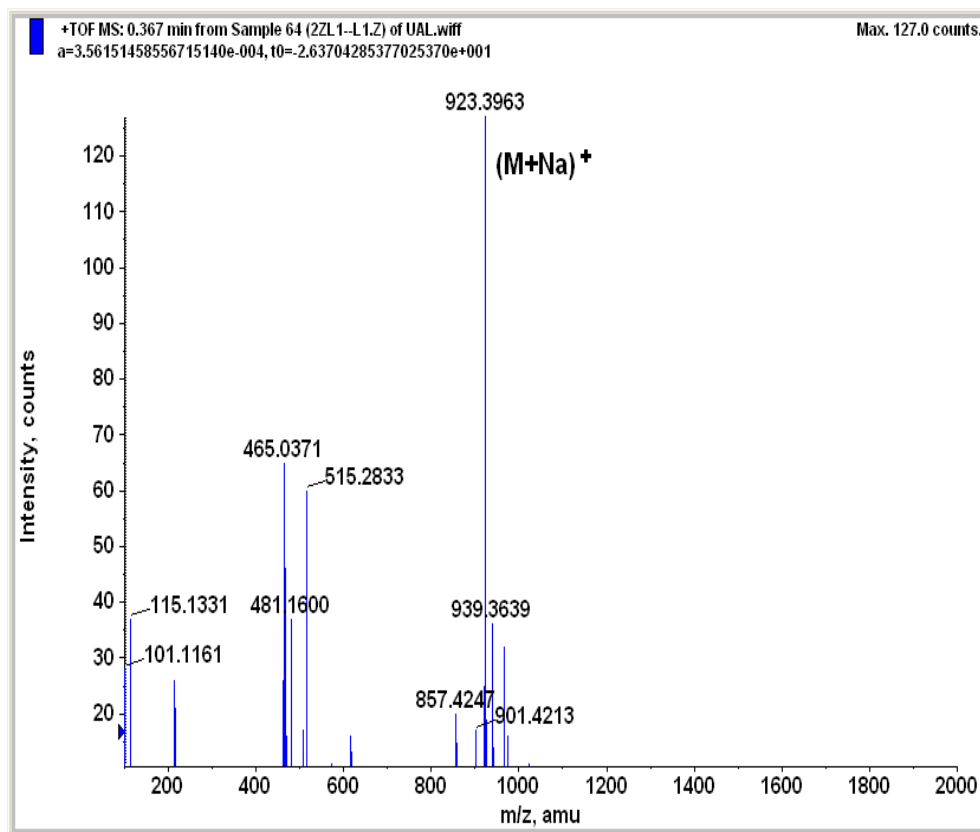
*<sup>13</sup>C NMR (75 MHz, DMSO-*d*<sub>6</sub>) of 5b*





HRMS of 5b





*Gel-transition temperature ( $T_g$ )*

The test tube containing the gel was immersed in a thermostatted water bath and the temperature was raised at a rate of 1°C per minute.  $T_g$  is defined as the temperature at which the gel disappears.

Table A:1 – Gelation Study in various solvent mixtures, extended from Table 2:1, chapter 2.3.2, page 73, including those which were unsuccessful in forming a gel. The dendrons (**3** and **4**) or dendrimers (**5a** and **5b**) were dissolved in the more polar solvent and the less polar non-solvent was then added to initiate gel formation. The gel formation is assessed by the tube inversion method. The symbol ✓ in the table corresponds to formation of the gel and X denotes that no gel formation in that particular solvent has taken place.

Solvent	Sample			
	<b>3</b>	<b>4</b>	<b>5a</b>	<b>5b</b>
Ethyl acetate + hexane (2:3)	✓	X	✓	X
Dichloromethane + hexane (2:3)	X	X	X	X
Chloroform + hexane (2:3)	X	X	X	X
Methanol + hexane (2:3)	X	X	X	X
Acetonitrile + hexane (2:3)	X	X	X	X
Ethanol + hexane (2:3)	X	X	X	X
Acetone + hexane (2:3)	X	X	X	X
Tetrahydrofuran + hexane (2:3)	X	X	X	X
Methanol + ethyl acetate (1:9)	X	✓	X	X
Methanol + dichloromethane (1:9)	X	X	X	X
Methanol + chloroform (1:9)	X	X	X	X
Methanol + acetonitrile (1:9)	X	X	X	X
Methanol + ethanol (1:9)	X	X	X	X
Methanol + acetone (1:9)	X	X	X	X
Methanol + ethyl acetate + hexane (1:2:2)	X	X	X	X
Methanol + chloroform + hexane (1:2:2)	X	X	X	✓

**Acknowledgements**

We thank the Endeavour foundation for an Endeavour Executive Award to VH and gratefully acknowledge support from IIT Delhi, Flinders University, DST (New Delhi) and the Australian Research Council.

## Appendix B

### Supporting data for fungal proteins

#### *Expression and Purification of rAGL proteins*

Construction of expression vectors for recombinant AGL1 (rAGL1) was PCR–amplified from cDNA clones (Genbank #EU931681) using primers (5' to 3') GiAGL1\_matF, GAAGGAGATATACATATGCAAGGACCAGCTGACGG, and GiAGL1\_His6R, CTAGTGATGGTGATGGTGATGTGATGCTGCTGCTTTGG. Recombinant AGL2 (rAGL2) was PCR–amplified from cDNA clone (Genbank #EU931682), using primers GiAGL2 matF, GAAGGAGATATACATATGTCTCCTGAACGATTAGCTGTTC and GiAGL2\_His6R CTAGTGATGGTGATGGTGATGGCCTGTTGCTGCTGGAC. GiAGL3 was PCR–amplified from *G. intraradices* genomic DNA using primers GiAGL3\_matF, GAAGGAGATATACATATGCAGGGACCAGGAGGAGC and GiAGL3\_His6R CTAGTGATGGTGATGGTGATGAGCAAATATAGCACC AAGAATTAC . Reverse primers were designed to produce proteins with a C–terminal His<sub>6</sub>–tag. The PCR product was designed to include a Shine dalgarno sequence, spacer sequence, and a start codon sequence at the N–terminus of the gene and stop codon sequence at the C–terminal end of the gene. PCR products were cloned into an entry vector, pCR8/GW/TOPO vector (Invitrogen) and sequenced. Verified clones were recombined into a destination vector, pDEST14 (Invitrogen). To express the rAGL proteins, clones were

## *Appendices*

transformed into *E. coli* BL21–AI cells (Invitrogen). Expression was induced with 0.2% L–arabinose in 30 mL cultures. Bacterial pellets were resuspended in 1.8 mL of lysis buffer (50 mM NaH<sub>2</sub>PO<sub>4</sub> 300 mM NaCl, pH 7.0) containing lysozyme (1 mg/mL), DNaseI (40 µg/mL) and mini EDTA–free protease cocktail (Roche), lysed with three freeze – thaw cycles (liquid nitrogen, 15 sec followed by 2 min in a 42°C water bath), followed by 20 min at room temperature. Supernatant was loaded onto Talon resin (Clontech) and His–tagged proteins were eluted in low pH buffer (50 mM NaH<sub>2</sub>PO<sub>4</sub> 300 mM NaCl, pH 5.0) according to the resin manufacturer’s instructions. Fractions containing rAGL1 and rAGL3 were pooled, desalted on 1 kDa molecular weight cut off filter device (Microsep, Pall Corporation). Proteins were quantified using Quant–it (Invitrogen), which detects peptide bonds. Final concentration of proteins after desalting was rAGL1 (0.32 mg/mL in ≈ 12 mM Na<sup>+</sup>) and rAGL3 (0.48 mg/mL in ≈ 8 mM Na<sup>+</sup>).

### *CD spectroscopy Data Collection and Decomposition*

Desalted rAGLs were diluted to 100 µg/mL in ‘CD buffer’ (100 mM (NH<sub>4</sub>)<sub>2</sub>S<sub>0</sub><sub>4</sub>, 10 mM KH<sub>2</sub>PO<sub>4</sub>). The CD buffer was selected as one of several recommended buffers compatible with the low wavelengths needed to detect PPII helices by CD spectroscopy [129].

Synthetic peptide samples were resuspended to a concentration of 0.3 mg/µL in a small volume of acetonitrile (<10 µL), before diluting to a final concentration of 2 mg/mL (by weight) in Ultrapure MilliQ water (18.2 Ω) such that the final concentration of acetonitrile was 0.67% (v/v). Acetonitrile was used based on the manufacturer’s recommendation for peptides with zero net charge

## *Appendices*

(GenScript USA). Stock peptide solutions were then further diluted to a working standard of 1 mg/mL. Two salt concentrations were used; 'low salt' (1 mM  $\text{KH}_2\text{PO}_4$ , 10 mM  $(\text{NH}_4)_2\text{SO}_4$ ) and 'high salt' (10 mM  $\text{KH}_2\text{PO}_4$ , 100 mM  $(\text{NH}_4)_2\text{SO}_4$ ).

Control proteins included polyproline (1,000–10,000 Da), Sigma cat # P2254) and bovine serum albumin (BSA, Sigma cat # A4503), stock at 2 mg/mL in 0.67% acetonitrile in Ultrapure MilliQ water. To calculate molar ellipticity for PPII, we used 52 amino acid residues and a MW of 5,068 Da, and for BSA 585 amino acid residues with a MW of 66,776 Da.

CD spectroscopy was performed on a PiStar 180 CD spectrometer. High quality spectra were acquired in the range 190–260 nm, (wavelength interval to 0.5 nm, sample period: 25  $\mu\text{s}$ , adaptive sampling (error  $\pm 0.01$ , max samples: 500,000), number of samples: 200), approx 30 min per scan. For all samples, an average of three scans was used after subtracting average buffer spectra. Samples were prepared and degassed using a vacuum evaporator (1 to 10 min). For the experiment investigating stability of secondary structure, three replicate tubes of each peptide were prepared in low-salt buffer at 1 mg/mL, and samples were sonicated for 5 min (Ultrasonics FXP8M). Acquisition parameters were altered to allow for shorter run times to determine if there were changes in structure over time. One tube for each peptide was sampled immediately, with two consecutive run conditions (3 scans each): very fast (wavelength 190–260 nm, wavelength interval to 1 nm, sample period: 25  $\mu\text{s}$ , adaptive sampling: error  $\pm 0.5$ , max samples: 50,000, number of samples: 200), then fast (wavelength 190–260 nm, wavelength interval to 0.5 nm, sample

period: 25  $\mu$ s, adaptive sampling: error  $\pm$  0.5, max samples: 100,000, number of samples: 100), taking approximately 2 min and 10 min, respectively. The other tubes for each peptide were sampled 1 d and 7 d later using the fast acquisition conditions.

CD spectra were decomposed using the least squares fit method using the program LINCOMB [294]. A custom basis set was developed to distinguish between PPII and random coil structures. It contained the four reference spectra in Brahms.dat, with spectra 4 (poly(P-K-L-K-L)<sub>n</sub>), assumed to be a PPII helix, based on the increasing evidence that a weak positive CD band at 217–225 is evidence of a PPII helix [281], [289–291]. The fifth spectrum in the basis set represents a random coil and was from denatured collagen [412]. The decomposition that produced the lowest average least squares error was used.

Supporting Figures

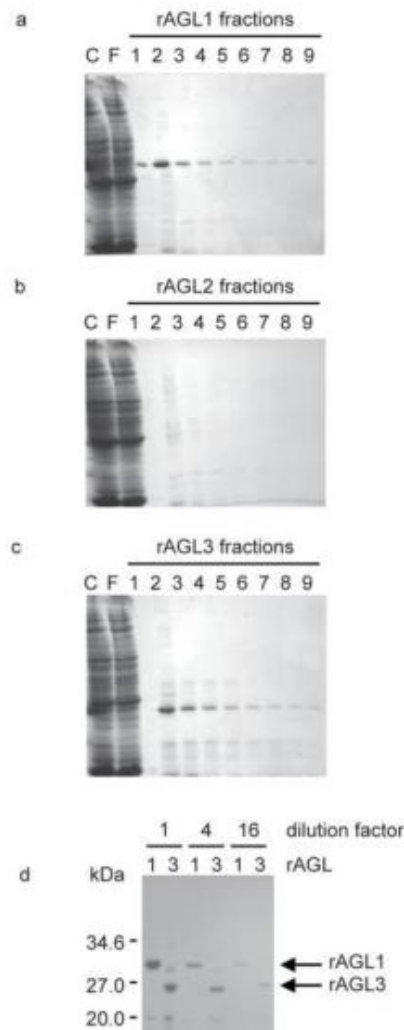


Figure B:1 – Purification of recombinant AGL (rAGL) proteins. (a) Isolation of rAGL1. Lane C, crude soluble proteins from *E. coli*. Lane F, flowthrough (unbound) proteins on Talon resin. Lanes 1 to 9 are 10  $\mu$ L each of sequentially eluted fractions (~1 mL fractions). (b) rAGL2 was not detected in any of the eluted fractions. Lanes as in (a). (c) Isolation of rAGL3. Lanes as in (a). (d) Serial dilutions of desalted rAGL1 and rAGL3 samples. The undiluted samples, Lane 1, contains 7.5  $\mu$ L rAGL (0.32 mg/ml); and Lane 2, contains 7.5  $\mu$ L rAGL3 (0.47 mg/ml). Dilution factors are indicated at the top of the Coomassie stained gel.

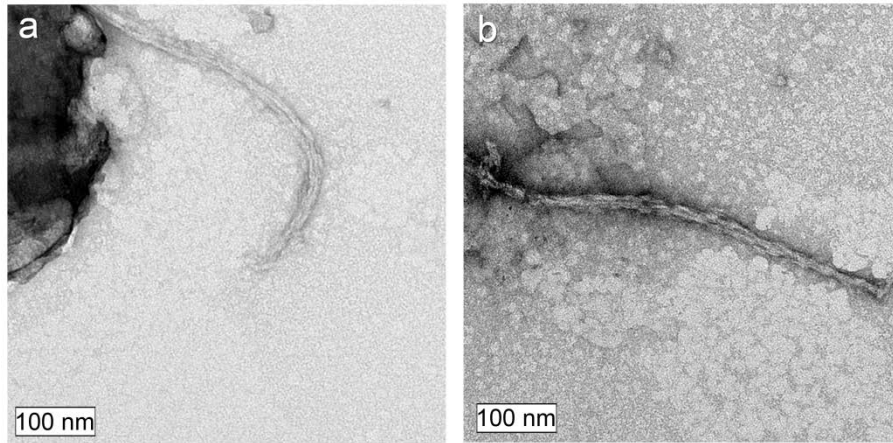


Figure B:2 - Transmission Electron Microscope images of rAGL1 after 6 d incubation at room temperature, followed by storage for 4 wks at 4°C. 20  $\mu$ L of protein solution in low salt (10 mM / 1 mM ammonium sulfate / potassium phosphate) was deposited onto a 400 mesh copper grid and negatively stained with uranyl acetate. Images were acquired on a Philips CM 100 Transmission Electron Microscope.

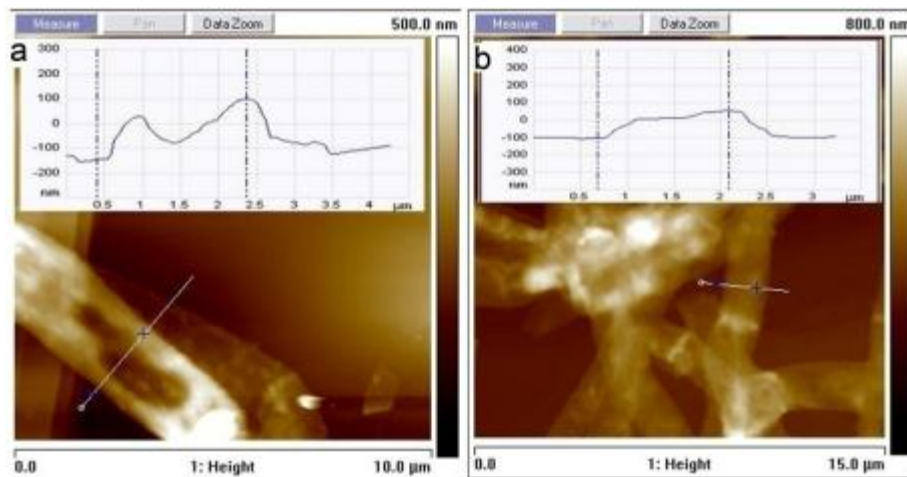


Figure B:3 – AFM height images of the fibres precipitated from rAGL3 (a, b), inset with line profiles highlighting the ‘tube-like’ structure, on HOPG. Image in b is part of image Figure 3:3g.

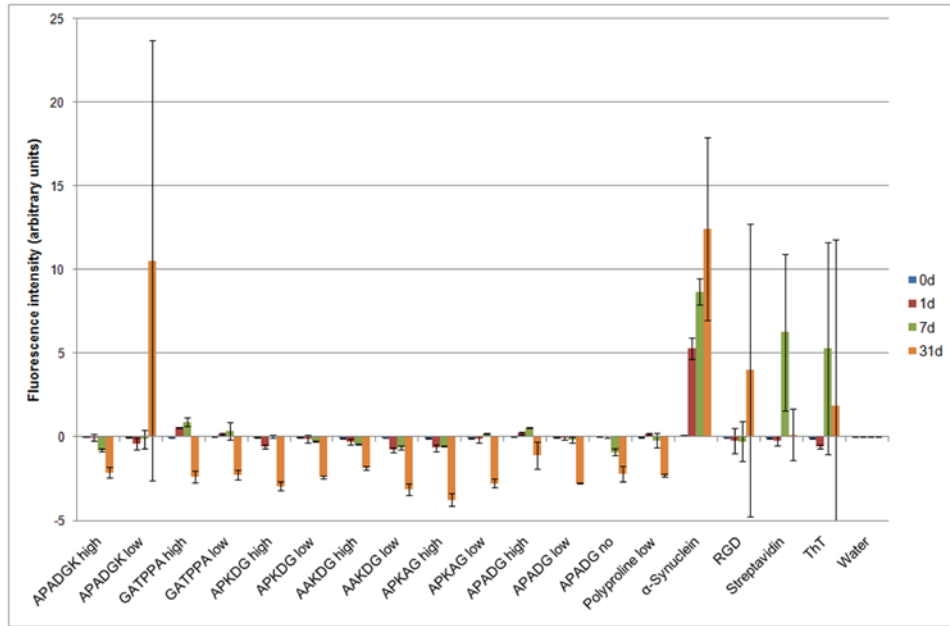


Figure B:4 – Fluorescence intensity of synthetic peptides in the presence of Thioflavin T (ThT) over a 1 month period in high (100 mM / 10m M) and low (10 mM / 1 mM) ammonium sulfate / potassium phosphate salt buffer. Also included is an  $\alpha$ -synuclein positive control, showing an increase in ThT fluorescence. All samples measured in triplicate, and all intensities are normalized against pure water. The large increase seen for APADGK low salt sample and ThT only control after 31 d is due to evaporation of two replicates.

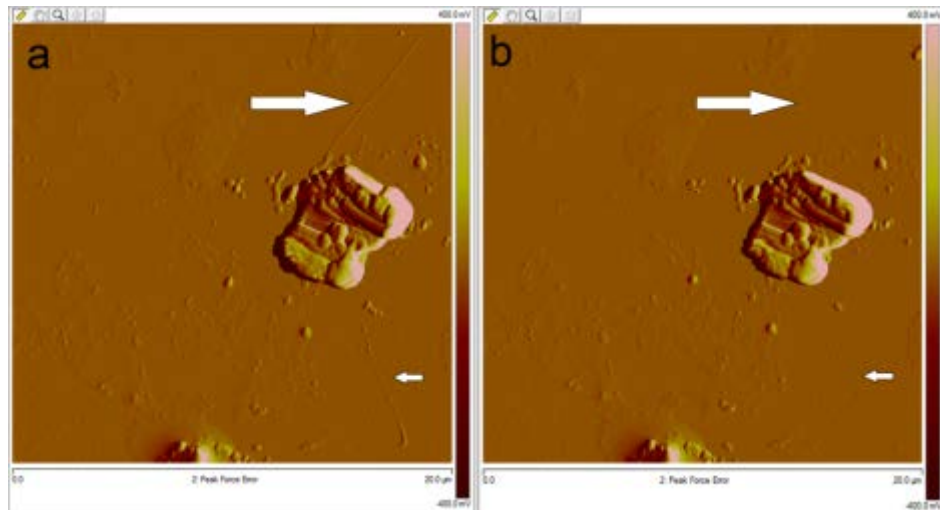


Figure B:5 – AFM peak error images of  $(APKDG)_6$  after 2 wks, showing rod-like fibrils (white arrows) on mica (a) first scan, (b) following scan using identical parameters where fibrils are apparently damaged or removed due to imaging. White arrows indicate the “loss” of fibrils.

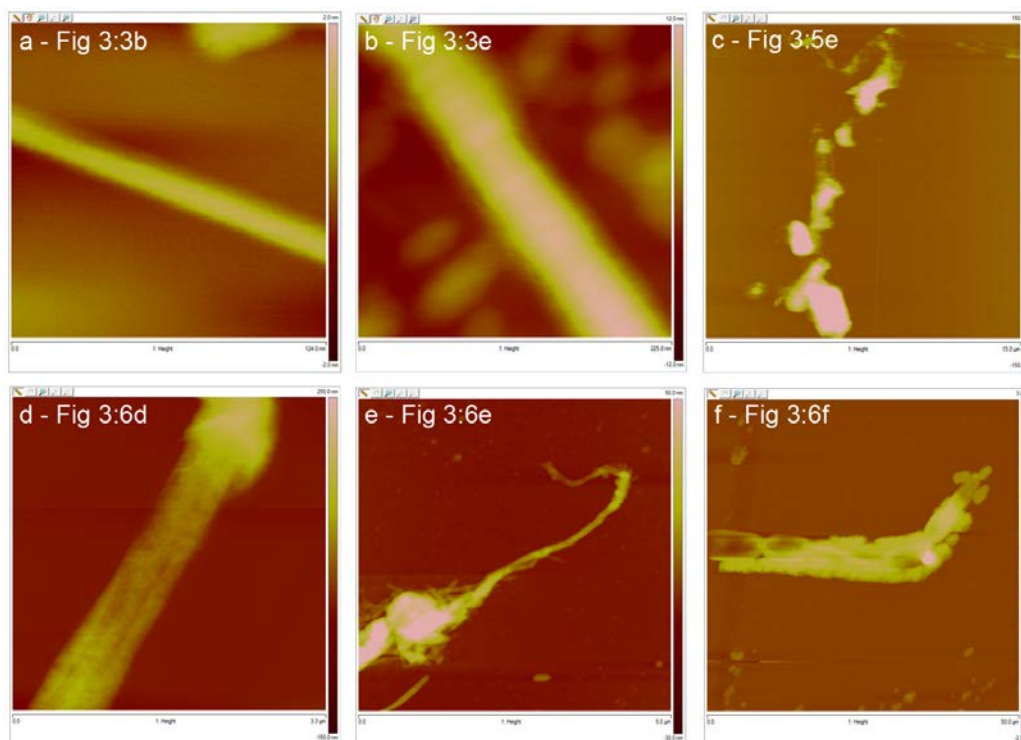


Figure B:6 – AFM topography channel images of phase / amplitude / peak error images from throughout chapter three. (a) Figure 3:3b ( $x = 125 \text{ nm}$ ,  $z = 4 \text{ nm}$ ), (b) Figure 3:3e ( $x = 225 \text{ nm}$ ,  $z = 24 \text{ nm}$ ), (c) Figure 3:5e ( $x = 15 \text{ }\mu\text{m}$ ,  $z = 300 \text{ nm}$ ), (d) Figure 3:6d ( $x = 3.3 \text{ }\mu\text{m}$ ,  $z = 400 \text{ nm}$ ), (e) Figure 3:6e ( $x = 5 \text{ }\mu\text{m}$ ,  $z = 80 \text{ nm}$ ) and (f) Figure 3:6f ( $x = 50 \text{ }\mu\text{m}$ ,  $5.5 \text{ }\mu\text{m}$ ) .

### Acknowledgements

I would like to acknowledge Emeritus Prof Norma Greenfield for helpful discussions on interpreting the CD data, Shazril Zulkipli for designing and construction expression vectors for rAGL clones, Maurizio Ronci for matrix–assisted laser desorption ionization–mass spectrometry data and Martin Sweetman for editing and proofreading assistance. Microscope access was provided by the Australian Microscopy & Microanalysis Research Facility (AMMRF).

Appendix C

Supporting figures for Pseudoexfoliation syndrome

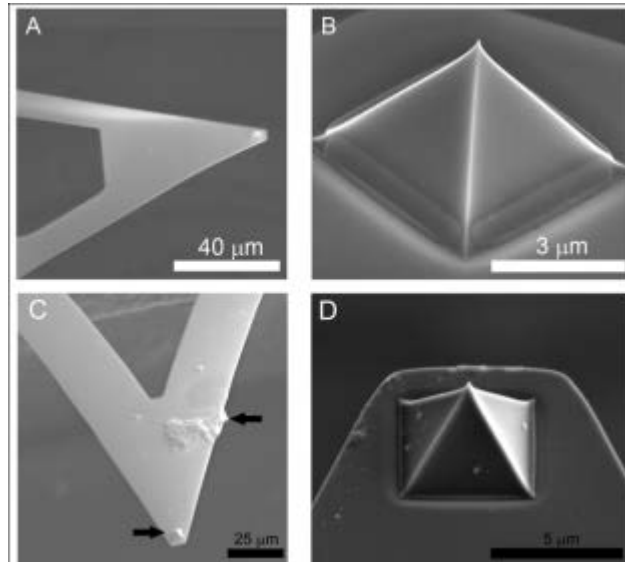


Figure C:1 – A: SEM image of a chemically cleaned AFM cantilever (scale bar 40  $\mu\text{m}$ ) and B: zoom-in on AFM tip (3  $\mu\text{m}$ ). The physical state of the probe is typically similar before and after functionalisation judging by SEM. C: SEM image of an antibody-modified probe (Microlevers, Veeco, USA, with nominal spring constant 0.4 N/m), where the lower arrow is pointing at the AFM tip and the higher one is pointing at material aggregated on the cantilever (scale bar 25  $\mu\text{m}$ ). D: SEM image zoomed to the tip (scale bar 5  $\mu\text{m}$ ).

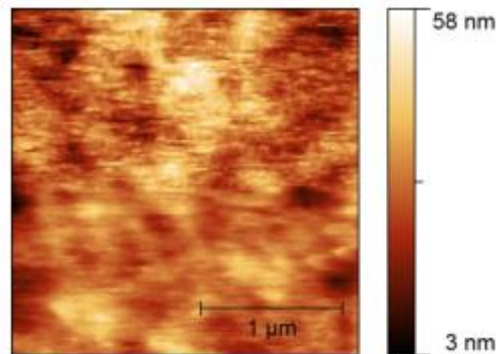


Figure C:2 – AFM topography image of a normal lens capsule immobilised on glass without dehydration. Scale bar = 1  $\mu\text{m}$ .

## Appendices

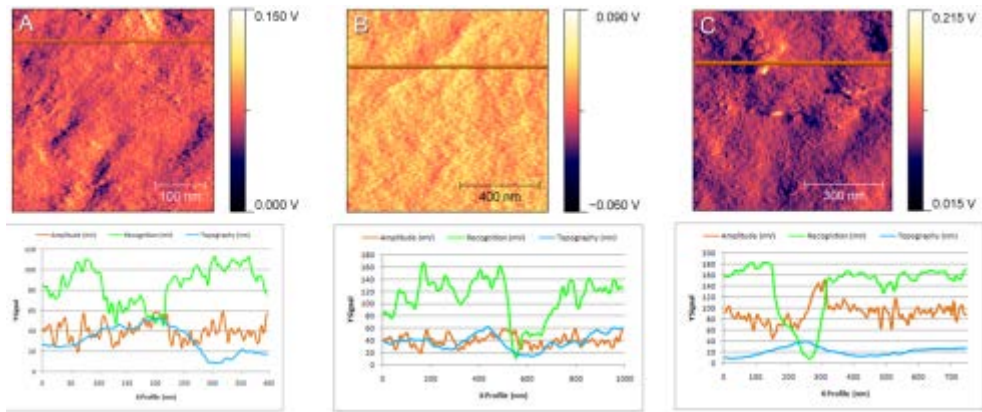


Figure C:3 – Amplitude error images corresponding to TREC images for A: normal lens capsule, B: PEX lens capsule and C: normal lens capsule, acquired using an anti-clusterin modified probe. Below each image is a line profile, showing the amplitude trace (orange) across the lines indicated in the images above. This corresponding recognition (green) and topography (blue) traces are also shown.

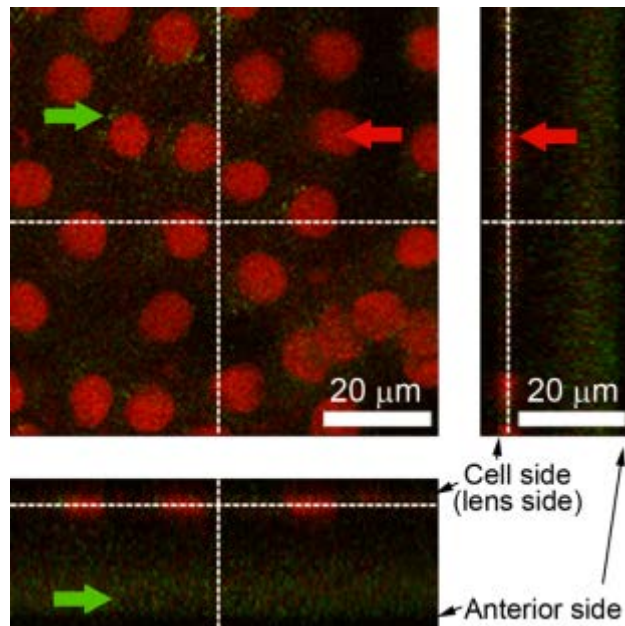


Figure C:4 – (Centre) Fluorescence image of the cell side and (right and below) confocal orthogonal sections of a normal lens capsule permeabilized with methanol and labelled for clusterin with the anti-clusterin primary antibody and Alexa Fluor-488 conjugated anti-rabbit IgG secondary antibody (green arrows). Propidium iodide staining revealed the nuclei (red arrows). The presence of clusterin is observed within the cells and on the anterior side of the lens capsule. The central image is the top-down view of the tissue from the lens side, and the image below and to the right show orthogonal cross-sections of the tissue obtained from optical sections by means of confocal microscopy.

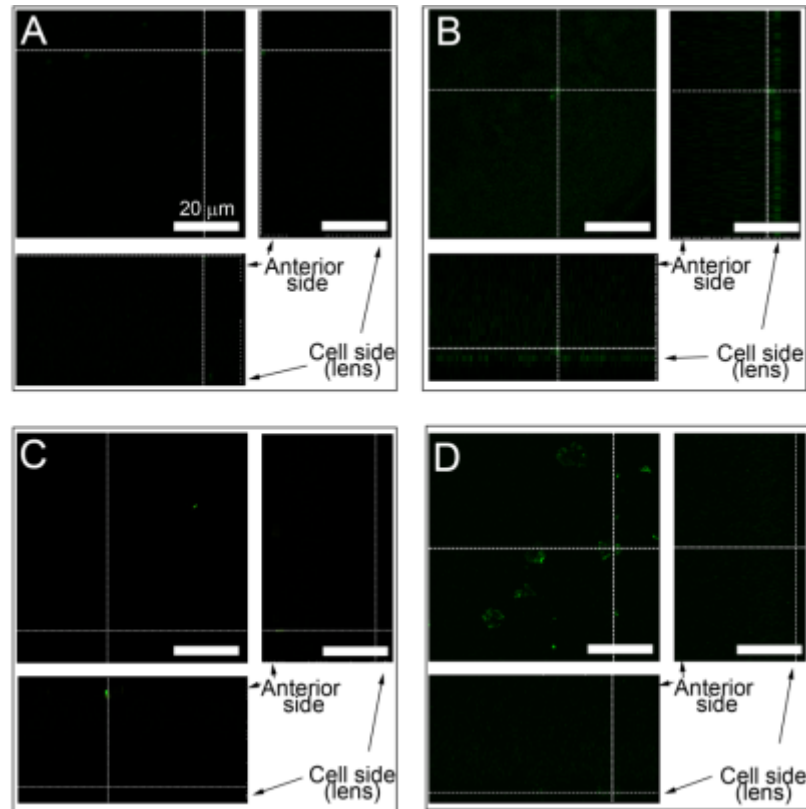


Figure C:5 – Fluorescence images of A: normal lens capsule and C: PEX lens capsule with no primary antibody, and B: normal lens capsule and D: PEX lens capsule labelled with anti-ZO-1 primary antibody and Alexa Fluor-488 conjugated anti-rabbit IgG secondary antibody. To the right and beneath each image is a confocal orthogonal section of the central image through the tissue. Scale bars = 20 μm.

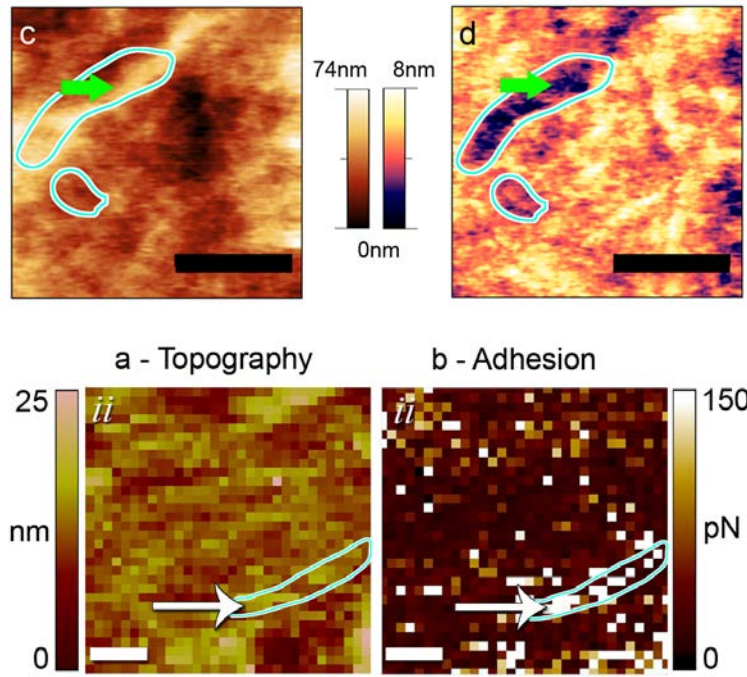


Figure C:6 – Visualisation guides to assist in viewing the highlighted features in recognition and force maps images from Figure 4:2 (above) and 4:11 (below), respectively.

**Acknowledgements**

I would like to thank Dr. Linda Wildling, DI. Barbara Mayer, Dr. Rong Zhu, Dr. Alpana Dave and DI. Markus Kastner for their technical assistance.

This work was funded by the National Health and Medical Research Council (NHMRC), Australia and by the European Community 7th framework program. The work was also partly supported by the Australian Microscopy & Microanalysis Research Facility (AMMRF). Dr Craig is a recipient of the NHMRC practitioner fellowship. Dr Ebner and Dr Hinterdorfer are the recipients of European commission grant ‘Single Molecule Workstation (SMW)’ no. 213717, no. NMP4–SE–2008–213717 and Austrian FFG – MNT–ERA.NET Project IntelliTip (grand 823980).

I was the recipient of travel scholarships from the Fluorescence Applications for Biological Life Sciences (FABLS), the Australian Society for Biomaterials and Tissue Engineering (ASBTE), Flinders University, and the Australian Nanotechnology Network (ANN) for TREC work in Austria and Western Australia.